DTU Energy
Department of Energy Conversion and Storage

Tunable electrons in oxides and hot phonons in silicon: Insights from theory

PhD Thesis

Victor Rosendal

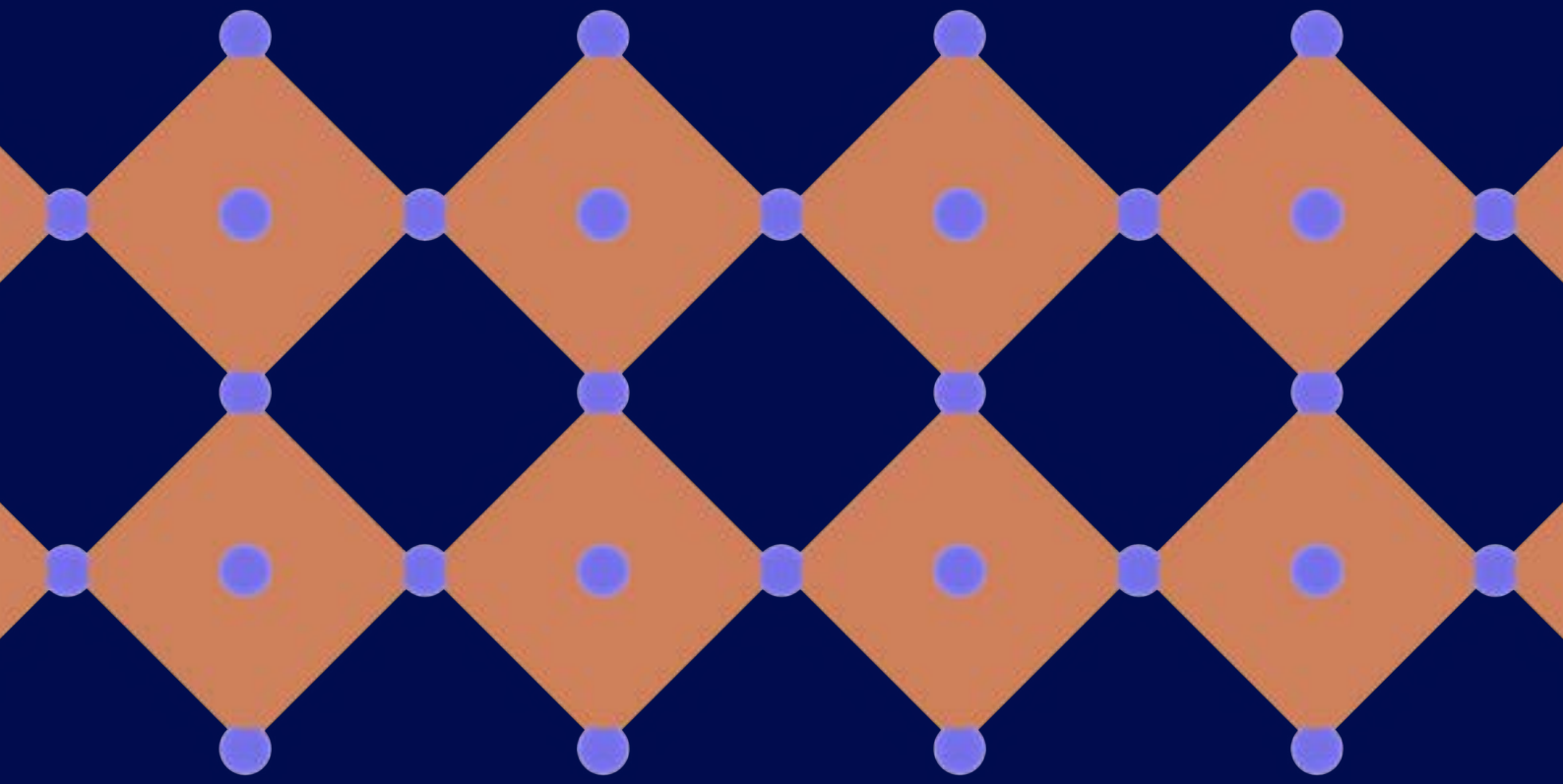

Tunable electrons in oxides and hot phonons in silicon: Insights from theory

PhD Thesis
October, 2023

Author:
Victor Rosendal

Supervisor:
Sr. Researcher Dirch Hjorth Petersen
Department of Energy Conversion and Storage
Technical University of Denmark

Co-supervisors:
Professor Mads Brandbyge
Department of Physics
Technical University of Denmark

Professor Nini Pryds
Department of Energy Conversion and Storage
Technical University of Denmark

Abstract

Computational materials science aims at studying effects or mechanisms that are hard to probe via experiments. Using numerical approaches it is possible to systematically and efficiently study materials with unmatched control and tunability. Density functional theory (DFT) has been the standard method within electronic structure calculations due to to its good balance of low computational cost and high predictability. In this thesis, I describe how I have employed DFT to study the electronic structure and transport properties of $SrNbO_3$, but also the thermal transport in Si.

For $SrNbO_3$, the total energy landscape was mapped as a function of rotations of the NbO_6 octahedra. Here, the effect of biaxial strain was considered. Interestingly, $SrNbO_3$ shows a preference for single in-phase rotation, i.e., $a^0a^0c^+$ in Glazer's notation. This is in contrast to the out-of-phase rotation, $a^0a^0c^-$, which is common in other perovskite oxides. The in-phase (out-of-phase) rotation means that each adjacent octahedra is rotated in the same (alternating) direction. Biaxial compressive strain was found to stabilize the rotations around the out-of-plane axis, while tensile strain stabilizes rotations around the in-plane axes. Due to the interest in using $SrNbO_3$ as a transparent electrode, I then evaluated the optical properties as a function of the likely distortions. The optical excitations are found to be shifted up to ca. 0.25 eV in the visible regime due to octahedral rotations.

By comparing unfolded DFT bands of $SrNbO_3$ with angle-resolved photoemission spectroscopy (ARPES) data, fingerprints of the $a^0a^0c^+$ rotation are observed in the ARPES bands. This further indicates that $a^0a^0c^+$ is a stable rotation in $SrNbO_3$. Motivated by this, I then studied the electronic states of the $a^0a^0c^+$ rotated $SrNbO_3$ with emphasis on Berry phase-related properties. Dirac nodal lines were observed at the boundary of and within the Brillouin zone. Breaking of time-reversal symmetry, using a ferromagnetic spin ordering, leads to large Berry curvatures near the band crossings which are present due to octahedral rotations. This further indicates how octahedral distortions could be leveraged to introduce and tune fascinating physics in oxides.

While it has been understood that oxygen vacancies result in changes to the electronic transport, it is difficult to find quantitative results of how much the vacancies scatter electrons. I, therefore, calculated the reduction in electrical conductance for different oxygen vacancy configurations in $SrNbO_3$. This was done using non-equilibrium Green's functions (NEGFs). As expected, a vacancy blocks the electronic transport, and scattering cross sections of ca $0.8 - 1.5a^2$ were found. A value of $1a^2$ means that one vacancy reduces the effective transport area with one unit cell area. Interestingly, enabling spin-polarization leads to spin-dependent transport, but also to stronger scattering and the effect was enhanced in ultra-thin slabs compared to bulk. This shows that it is reasonable to expect oxygen vacancies to reduce the conductance, especially in ultra-thin samples where the vacancies induce magnetic moments.

Finally, Fourier's law of conduction was put to the test against the more general Boltzmann transport equation (BTE). This was done for the phonons in doped Si at room temperature. DFT was used to calculate the phonon dispersion and anharmonic scattering rates of undoped Si, and the effect of doping was introduced using simple scattering rate models. Comparisons were made between the temperature rise from a nanoscopic heater as predicted using Fourier's law and BTE. At the microscale, the long mean free path phonons in Si carry a substantial part of the heat. Therefore, a length-dependent reduction in the effective thermal conductivity is observed. Doping has a surprisingly small impact on non-diffusive phonon transport. Preliminary experiments on doped Si showed similar length-dependent thermal properties. These results act as a warning against using Fourier's law for modelling phonon transport at the microscale even for doped Si systems.

Preface

This thesis was carried out in the Section for Functional Oxides at the Department of Energy Conversion and Storage, Technical University of Denmark. The project spanned from October 2020 to September 2023. The work has been supported by Independent Research Fund Denmark Grant No. 8048-00088B and Innovation Fund Denmark Grant No. 1045-00029B. I was supervised by Dirch Hjorth Petersen, Mads Brandbyge, and Nini Pryds. During this time I performed electronic structure calculations of perovskite oxides and studied the thermal transport in silicon.

Kongens Lyngby, September 29, 2023

Victor Rosendal

Acknowledgements

First of all, I would like to thank my supervisors Dirch Hjorth Petersen, Nini Pryds and Mads Brandbyge. Dirch for guiding me throughout the whole project, and trying to keep me on track to study relevant material properties that might actually be useful to the real world. Your guidance has helped me navigate through scientific tasks, but also questions such as what to focus on and what not to spend time on. You have also always been available for discussions, which has been very appreciated. Nini for introducing me to the world of oxides, and inspiring me to study these materials using computational techniques. Last but not least, Mads, for supervising many of the computational and theoretical aspects of this project, from density functional theory to non-equilibrium Green's functions.

Next, I want to thank Walber Hugo Brito for the collaboration and numerous discussions we had regarding octahedral distortions in perovskite oxides. Also, for doing calculations beyond density functional theory and sharing those with me.

I also want to thank my experimental colleagues and collaborators, for without their work my calculations have little real value. From the thermal transport part of the study, I want to thank Neetu Lamba, Benny Guralnik and Braulio Beltrán-Pitarch for their micro four-point probe experiments and analysis. I want to thank Alla Chikina and Milan Radovic (and their colleagues at Paul Scherrer Institut) for their angle-resolved photoemission spectroscopy of $SrNbO_3$.

During my external stay, I visited Vladislav Borisov and Olle Eriksson at Uppsala University, and a big thanks goes to them for making my stay a good and educational time.

The people in office 145 at DTU are also worth a thanks for their good spirits and their ample questions about how the thesis writing is going.

My friends throughout the Nordic countries, starting from the earlier years in Finland to Sweden and now Denmark, have been and continue to be very important to me and deserve a shout-out as well.

Finally, I want to thank my family in Finland. A special thanks to my father who, I believe, is responsible for my interest in (trying) to understand how things work.

List of contributions

Below is a list of the published paper and unpublished manuscripts I contributed to during my PhD project:

1. Victor Rosendal, Walber H. Brito, Milan Radovic, Alla Chikina, Mads Brandbyge, Nini Pryds, and Dirch H. Petersen, "Octahedral distortions in $SrNbO_3$: Unraveling the structure-property relation", Phys. Rev. Materials (2023)

2. Alla Chikina, Victor Rosendal, Hang Li, Eduardo B. Guedes, Marco Caputo, Nicholas Clark Plumb, Ming Shi, Dirch H. Petersen, Mads Brandbyge, Walber H. Brito, Ekaterina Pomjakushina, Valerio Scagnoli, Jike Lyu, Marisa Medarde, Felix Baumberger, Nini Pryds, and Milan Radovic, "Band topology induced by octahedral rotation in $SrNbO_3$", To be submitted to Science Advanced

3. Victor Rosendal, Nini Pryds, Dirch H. Petersen, and Mads Brandbyge, "Influence of oxygen vacancies on charge and spin transport in $SrNbO_3$: A DFT-NEGF based study"

4. Victor Rosendal, Neetu Lamba, Benny Guralnik, Braulio Beltran-Pitarch, Mads Brandbyge, Nini Pryds, and Dirch H. Petersen, "Observation of diffusive-to-ballistic phonon transport in boron doped silicon"

Manuscripts I contributed to in a smaller role are listed below. In these studies I mainly contributed with supporting calculations and discussion/analysis.

1. Arindom Chatterjee, Carlos Nunez Lobato, Victor Rosendal, Thomas Aarøe Anhøj, Jean-Claude Grivel, Felix Trier, Dennis Valbjørn Christensen, and Nini Pryds, "Gate-tunable thermoelectric effect in oxide thin films at room temperature", Submitted to Advanced Electronic Materials

2. Hang Li, Shinhee Yun, Alla Chikina, Victor Rosendal, Thomas Tran, Eric Brand, Christina H. Christoffersen, Nicholas C. Plumb, Ming Shi, Nini Pryds, and Milan Radovic, "Heterogeneous integration of $SrTiO_3$ nanomembranes", Submitted to Science Advanced

3. Neetu Lamba, Benny Guralnik, Braulio Beltrán-Pitarch, Victor Rosendal, Nini Pryds, Ole Hansen, and Dirch Hjorth Petersen, "Deconvolution of Heat Sources for Application in Thermoelectric Micro Four-Point Probe Measurements"

My conference contributions are the following:

1. "Band topology induced by strain in $SrNbO_3$", Presentation at Joint Annual Meeting of the Swiss and Austrian Physical Society 2023

2. "Electron-vacancy scattering in thin film oxides: Insights from atomistic modelling", Poster at Quantum Oxide Research Online Meeting 2023

3. "Electronic states and octahedral tilting in $SrNbO_3$", Poster at 28th International Workshop on Oxide Electronics 2022
4. "Strain induced octahedral tilting in $SrNbO_3$ perovskite' Poster at E–MRS Fall Meeting 2022. Awarded for "Best Poster Presentation Award"
5. "Investigating the phonon transport in doped Silicon using micro four-point probe", Poster at Virtual Conference on Thermoelectrics 2021

Acronyms

ARPES angle-resolved photoemission spectroscopy.

BTE Boltzmann transport equation.

BZ Brillouin zone.

DFT density functional theory.

GF Green's function.

GGA generalized gradient approximation.

IFC interatomic force constant.

IP independent-particle.

IS inversion symmetry.

KS Kohn-Sham.

LDA local density approximation.

M4PP micro four-point probe.

MFP mean free path.

NEGF non-equilibrium Green's function.

PBC periodic boundary condition.

RPA random phase approximation.

RTA relaxation time approximation.

SOC spin-orbit coupling.

TB tight binding.

TRS time reversal symmetry.

Contents

Chapter 1

Introduction

Materials science and engineering have been essential to human civilizations over multiple millennia. Many historical epochs are even named after the materials prevalent in that era, e.g., iron and bronze ages, or even the silicon age. Finding new materials or combining previously known materials has been a reoccurring event, and has led to many technological advancements. At times this development has been accidental, while in other cases it has been a sought-after goal. To maximise the rewards, this development should of course be guided and based on our understanding of materials, and the underlying physics and chemistry governing them. Ideally, it is possible to request a certain set of properties, and then using some rules deduce what *stable* atomic structure results in those properties. Unfortunately, this is not possible currently. Alternatively, one can solve the equations that govern physics and chemistry from the atomic level, i.e., the Schrödinger equation, up to the macroscale described by Newtonian physics. In principle this is possible, i.e., for a given configuration of atoms we know the laws of physics that combined result in a set of material properties. In practice, however, this is a huge challenge, and even if one knows the material properties of a given configuration, the inverse problem of finding a material that presents a set of wanted material properties is not trivial.

Computational materials science aims at finding new materials, or use cases, by employing computational techniques. Given the laws of physics, as we know them, one tries to model the behaviour of a material and (hopefully) find properties that can be used in future applications. This also includes finding ways to improve or tune existing materials, or understanding limitations of current materials. The advantage of *computational* materials science is the large throughput and the ability to control every little detail of the simulated material. It is therefore possible to efficiently detangle the different mechanisms in a material by systematically varying relevant parameters, e.g., lattice parameters, defects, doping and so on. It gives us insight into the very core of materials, which is not possible through experiments. On the other hand, while it is in principle possible to include the messy details of reality in the simulations, it can be challenging to bridge the "perfect" material representation used in modelling with real world materials containing complex environments, defects and disorder. Another benefit of *computational* materials science is the possibility of making predictions of properties not (yet) accessible or understood in experimental context. In this context, there is plenty of room for pioneering through *computational* materials science.

Perovskite oxides are a relatively old group of materials that have gathered a growing interest. [1] Due to their wide range of chemical variability, they come with an impressive range of material properties from superconductivity [2] to ferroelectricity [3] and complex magnetic behaviour [4]. Some perovskite oxides are also promising as transparent conductors [5] use-

ful as electrodes in optoelectronic devices. Furthermore, they are very sensitive to external stimuli, such as strain, and oxides can be further tuned via oxygen vacancy engineering. [6, 7] These properties make perovskite oxides relevant for current and potentially many future applications. The conducting oxide $SrNbO_3$ is a material that has gathered interest recently due to its transparent properties in the visible and ultraviolet regime. [8] Furthermore, $SrNbO_3$ has been studied as a possible Dirac semimetal realized due to specific octahedral rotations. [9, 10]

In the present context, silicon is almost synonymous with semiconductors, and the use of silicon is widespread in semiconductor applications such as photovoltaics and electronics. The ongoing miniaturization of transistors has, and continuous to, lead to larger power densities. [11] This requires efficient thermal management, that relies on accurate models of the thermal transport in semiconductors such as silicon. The models must be accurate down to the characteristic length scales of these devices, and potential deviations from macroscopic physics must be captured. The limitations of Fourier's law of conduction have been known for quite some time [12], but there are still unresolved complications in nano- and microscopic thermal transport.

In this thesis, I describe how I have employed numerical methods to study the behaviour of electrons in conducting oxides and phonons in nanoscopic silicon. In the oxide studies, the goal was to both understand how one might engineer the material to gain new properties, but also to understand what the role of imperfections is on the electronic performance. For these studies $SrNbO_3$ was chosen and some comparisons with the well-known $SrTiO_3$ was made. The stability of different octahedral rotations was studied and then electrical and optical properties were investigated as a function of rotation. Furthermore, the effect of oxygen vacancies on the electronic transport was studied in $SrNbO_3$. To my knowledge, quantitative studies of electron-vacancy scattering in conducting oxides has not been performed previously and these values give a first estimate of the importance of vacancy scattering.

The aim of the silicon phonon study was to investigate the breakdown of macroscopic physics, which can have a crucial impact on metrology techniques that rely on accurate models, but also on the performance of electronic devices. Here, my main contribution is that the effect of doping is included in the analysis.

Each manuscript or study is separated into its own self-contained chapters, with all the necessary background, theory, results, and discussions presented in those chapters. The paper or manuscript that the chapter is based on is mentioned and appended at the end of the thesis. The exception of this is the short introduction chapter and the chapter on density functional theory (DFT), since all the studies rely on DFT. Therefore, the information in the chapter on DFT will be taken for granted and will not be treated in the other chapters.

Chapter 2

A brief introduction to density functional theory

In this chapter, I give a short introduction to DFT. All following studies rely on DFT either directly to examine the electronic structure or by evaluating parameters such as force constants that are used as input for other computational frameworks. Details specific to individual stories will be described in the corresponding chapters. Furthermore, this is by no means a complete treatment of DFT, and the main goal is to argue for the need for DFT and point out the different approximations and potential pitfalls of DFT.

Quantum mechanics describes the very small scales of our world where atoms and electrons are the key players. The Schrödinger equation describes the behaviour of these quantum mechanical objects, and it takes the form [13]:

$$i\hbar\frac{d}{dt}\left|\Psi(t)\right\rangle = \hat{H}\left|\Psi(t)\right\rangle, \tag{2.1}$$

where $|\Psi(t)\rangle$ is the state vector as a function of time, t, and $\hat{H}$ is the Hamiltonian operator. Here, i is the imaginary unit, i.e., $i^2 = -1$ and $\hbar = h/2\pi$ is the reduced Planck's constant. The Hamiltonian defines the system and can include, e.g., interactions between particles or between particles and external fields. If the Hamiltonian is independent of time, the time-independent Schrödinger equation can be used:

$$\hat{H}\left|\Psi\right\rangle = E\left|\Psi\right\rangle, \tag{2.2}$$

where E is the corresponding eigenenergy that defines the total energy of the system. Put in words, the time-independent Schrödinger equation is the eigenvalue problem of the quantum mechanical system. A solution of the Schrödinger equation for a given Hamiltonian contains all information to describe the physics of the system. While the above equations both look manageable, it is important to realize that the Hamiltonian (and therefore the states) can be high dimensional. Furthermore, the interaction between particles might be non-zero, like the electrons in atoms and molecules. This makes the problem of calculating the electronic structure of molecules and solids a formidable task.

The first approximation, of many, is to separate the treatment of the electrons and nuclei, which greatly reduces the degrees of freedom. This step is called the Born-Oppenheimer approximation. [14, 15] The justification of this approximation is the fact that the mass of the electron is a tiny fraction of the nucleus mass. In other words, the dynamics of the electrons and nuclei occurs at different scales, and it is reasonable to treat each configuration of the

nuclei as a separate electronic problem. This means that the electronic problem is parametrized by the positions of the nuclei.

Within the Born-Oppenheimer approximation, the Schrödinger equation for the electronic system is written [16]:

$$\left[\hat{T} + \hat{V}_{ee} + \hat{V}_{Ne}\right] \Psi = E\Psi \tag{2.3}$$

$$\left[-\frac{1}{2}\sum_i \nabla_i^2 + \sum_i \sum_{j<i} \frac{1}{|\vec{r}_i - \vec{r}_j|} - \sum_i \sum_I \frac{Z_I}{\left|\vec{r}_i - \vec{R}_I\right|}\right] \Psi = E\Psi \tag{2.4}$$

Here atomic units are employed, and lower (upper) case indices i, j (I) are used for electrons (nuclei). The atomic number of the Ith nucleus is denoted Z_I. The location of electron number i is denoted $\vec{r}_i$. Note, that the wavefunction here is the manybody electron wavefunction, $\Psi(\vec{r}_i, ..., \vec{r}_N)$, parametrized by the nuclei coordinates $\vec{R}_I, ..., \vec{R}_M$ as per the Born-Oppenheimer approximation. Where the number of electrons (nuclei) is denoted N (M). In real molecules and solids, there are multiple nuclei, each contributing with multiple electrons. Therefore, it quickly becomes impossible to even store all the degrees of freedom of the $3N$-particle wavefunction.

A way to tackle this problem is to use DFT. The main goal of DFT is to use the charge density, which only scales with the dimension and not with the number of electrons, as the key variable. Thanks to Hohenberg and Kohn [17], we have the theoretical foundation for doing this switch. Hohenberg and Kohn showed that:

- All ground state properties are determined by the ground state charge density, $\rho(\vec{r}) = N \int d^3\vec{r}_2 ... \int d^3\vec{r}_N \Psi(\vec{r}, ..., \vec{r}_N)^* \Psi(\vec{r}, ..., \vec{r}_N)$
- The ground state charge density minimizes the total energy functional, $E[\rho]$

The theorems, however, do not show how to construct the energy functional, $E[\rho]$. Here, the work by Kohn and Sham come in [18]. Kohn and Sham proposed to move to a fictitious system of non-interacting particles within an effective potential. This is known as Kohn-Sham (KS)-DFT. Crucially, the density of the so-called KS-orbitals is the same as for the interacting electron system. The advantage of moving to the fictitious system is that parts of the functional is known for non-interacting particles:

$$E[\rho] = T_{KS}[\rho] + \int d^3\vec{r} v_{ext}(\vec{r})\rho + E_H[\rho] + E_{xc}[\rho] = \tag{2.5}$$

$$= -\frac{1}{2}\sum_i \int d^3\vec{r} \phi_i^*(\vec{r}) \nabla^2 \phi_i(\vec{r}) - \sum_i \int d^3\vec{r} \sum_I \frac{Z_I}{\left|\vec{r} - \vec{R}_I\right|} |\phi_i(\vec{r})|^2 \tag{2.6}$$

$$+\frac{1}{2}\sum_i \sum_j \int d^3\vec{r}_1 \int d^3\vec{r}_2 |\phi_i(\vec{r}_1)|^2 \frac{1}{|\vec{r}_1 - \vec{r}_2|} |\phi_j(\vec{r}_2)|^2 + E_{xc}[\rho] \tag{2.7}$$

Therefore, by knowing the KS-orbitals, ϕ_i, we can calculate all terms of the energy functional except for the exchange-correlation functional $E_{xc}[\rho]$. This term contains all tricky quantum mechanical effects that are not captured by the simple Coulomb interaction and single particle kinetic term. It is worthwhile to remember that so far DFT is exact. The term that requires approximations is the $E_{xc}[\rho]$, this is where exact DFT ends and practical DFT begins. The accuracy of the DFT calculations rely on accurate approximations of $E_{xc}[\rho]$ [16] and plenty of research has been spent on improving and benchmarking [19] this term. The exchange-correlation functionals come in many different flavors and parametrizations, but they

are typically categorized depending on their dependence on the density. The simplest class of approximations is the local density approximation (LDA), where the exchange-correlation functional only depends locally on the density:

$$E_{xc}^{LDA}[\rho] = \int d^3\vec{r}\varepsilon(\rho)\rho(\vec{r}) \tag{2.8}$$

While the LDA is simple, it is surprisingly accurate. However, improvements can be made by making the functional semi-local in the density. In the generalized gradient approximation (GGA) this is done by introducing the gradient of the density:

$$E_{xc}^{GGA}[\rho] = \int d^3\vec{r}\varepsilon(\rho, \nabla\rho)\rho(\vec{r}) \tag{2.9}$$

Even more information can be included by introducing second derivatives (and so on) of the density, with the cost of computational complexity. The functions $\varepsilon(...)$ are governed by a set of criteria and then the free parameters are optimized.

Finally, one can write the Schrödinger-like KS equation as:

$$\left[-\frac{1}{2}\nabla^2 + v_{ext}(\vec{r}) + v_H(\vec{r}) + v_{xc}(\vec{r})\right]\phi_i = \epsilon_i\phi_i, \tag{2.10}$$

where $v_{xc}(\vec{r}) = \frac{\delta E_{xc}[\rho]}{\delta\rho}$ is the exchange-correlation potential. Using these equations one can self-consistently solve the non-interacting system that generates a charge density equivalent to the interacting system. Therefore quantities such as total energy, forces, etc. that can be expressed by the density are accessible. Again, the quality of these quantities now depend on the approximated exchange-correlation functional $E_{xc}[\rho]$.

There are many different ways to numerically solve the KS equations, but typically one expands the orbitals, ϕ_i, using a set of basis functions. Common choices are localised orbitals, often inspired by atomic orbitals, or plane waves. [20] Having expanded the orbitals using basis functions, the problem turns into a matrix equation which can be solved using a computer. Furthermore, it is common to simplify the electronic structure problem by separating the core electrons from the valence electrons. This is done with the motivation that the core electrons have little impact on the material chemistry. By doing such a separation, and treating the core electrons approximately, the problem becomes numerically less complex. This goes under the name of pseudopotentials. [20]

In crystalline materials, the translational symmetry significantly reduces the complexity of the electronic structure problem. According to Bloch's theorem, a solution to the Schrödinger equation in a periodic potential can then be written:

$$\Psi(\vec{r}) = \exp\Big(i\vec{k}\cdot\vec{r}\Big)u(\vec{r}), \tag{2.11}$$

where $\vec{k}$ is the (crystal) momentum and $u(\vec{r})$ is a function with the same periodicity as the periodic potentials. The 1st Brillouin zone (BZ) contains all unique $\vec{k}$, and the rest of the momentum space can be generated as a combination of the vectors in the 1st BZ. This suggests that it is sufficient to sample the 1st BZ, and the whole electronic structure is known from the information about these states. Furthermore, by the presence of symmetries, one can reduce the BZ to the irreducible BZ, all in the spirit of reducing computational cost.

2.1 Limitations of practical density functional theory

While DFT in principle is exact, one must in practice use approximations that limits the accuracy of the calculations. One of the bigger potential pitfalls of practical DFT is the approximation for the exchange-correlation functional, as mentioned previously. However, besides the quality of the approximation, the fact remains that within KS-DFT, the calculated eigenstates and eigenenergies are that of the fictitious KS system. The auxiliary KS system reproduces the electronic charge density (if the exchange-correlation functional is known), but there are no guarantees that the KS orbitals and energies are indicative of the electronic states. With this said, I will still throughout this thesis examine the KS bands and orbitals and assume that they contain information about the electronic system. This is commonly done now, but it is not obvious that this is reasonable. [21]

The exchange-correlation functionals come in different flavors, and they are often created to fulfill certain needs. Therefore, some functionals are better suited for some materials and properties, while other functionals might perform better in other scenarios. As an example, the Perdew-Burke-Ernzerhof (PBE) functional [22] and the revised PBEsol functional [23] are both GGA-level functionals, but they are parametrized slightly differently. This difference makes PBE better for studying cohesive energies, while PBEsol is better for studying lattice constants. [24]

Furthermore, for a given level of functional (LDA, GGA, and so on) and parametrization (PBE vs. PBEsol etc.), it is also possible to include corrections to the total energy. One such example is the introduction of the so-called Hubbard U. [25] This correction can be relevant for systems with strongly correlated d or f electrons. The idea is to correct for the lack of electron-electron interaction present in the approximate DFT functional. If the orbitals are too delocalised, due to erroneous self-interaction present in the exchange-correlation functional, the additional (repulsive) Coulomb interaction introduced with the Hubbard U correction will localize these states. For some transition metal oxides, it has been believed that this correction is essential for describing the correct electronic and magnetic structure. However, it has also been realised that many of the shortcomings of DFT free of U could be related to insufficient structural and spin degrees of freedom. [4, 26]

In this thesis I have only performed GGA-level DFT calculations. However, I compare my findings with previous theoretical and experimental results of the same or similar materials. Furthermore, through collaborations I have had the possibility of comparing my predictions with experiments, but also with higher level theoretical methods, namely dynamical mean-field theory (DMFT). DMFT is a method for studying the correlated electrons in systems with open d or f shells. In short, the Hubbard model is solved by mapping the lattice problem on to an Anderson impurity model, where the electrons can be created or annihilated via a reservoir. The reservoir describes other electrons, i.e., the impurity model has to be solved self-consistently. [27, 28] Overall, good agreements have been observed between our DFT and DMFT calculations. This indicates that $SrNbO_3$ is weakly correlated. The DMFT calculations won't be discussed further in this thesis but are available in Reference [29] which is appended in this thesis.

Chapter 3

Electrons and octahedral distortions in $SrNbO_3$

Perovskite oxides are a versatile class of materials, showing electrical behaviour ranging from high-κ dielectric, to (semi)conducting and even superconducting phases. [1] Furthermore, some perovskite oxides also show ferroelectric and/or magnetic ordering. The wide range of properties of oxides is due to the large degree of chemical freedom in the ABO_3 structure. As an example, the famous insulating perovskite oxide $SrTiO_3$, can become conducting by doping La on the A-sites [30] or by doping with Nb on the B-sites [31]. Furthermore, these materials can also be tuned via vacancy engineering. [7] Even with a fixed chemical composition, oxides can be tuned further via strain, either directly or by inducing additional distortions. [32, 6]

In this chapter the idea of strain engineering is applied to the perovskite $SrNbO_3$ and the findings are published in Reference [29]. The paper is appended in Section B.1. The goal is to understand the coupling between octahedral tilting and strain in $SrNbO_3$, but also to get insight into the changes in the (primitive cell) band structures due to octahedral tilting. Finally, the optical loss function and Seebeck coefficient are calculated to get a feeling for the influence of octahedral distortions on measurable quantities.

3.1 From $SrTiO_3$ to $SrNbO_3$

In transition metal perovskite oxides, ABO_3, the transition metal atom and oxygen ions form a unit with octahedral symmetry. The BO_6 octahedra form a network which is crucial for the electronic and magnetic properties of this class of materials. To make this less abstract, I will focus on the prototypical perovskite oxide $SrTiO_3$. According to crystal field theory, the titanium $3d$ states will split into two sets of orbitals. The triply degenerate set with lower energy is called t_{2g} and the doubly degenerate set is called e_g. In $SrTiO_3$ the Ti t_{2g} states make up the bottom the (unoccupied) conduction band, hence, upon electron doping, e.g., using Nb, the t_{2g} states start to get occupied. In a simplified picture, $SrNbO_3$ is similar to $SrTiO_3$ with one additional electron per unit cell. Of course, now the t_{2g} states originate from Nb $4d$ states, and therefore one expects the conduction states to be less localized and the overlaps larger, compared to the Ti $3d$ states in $SrTiO_3$. The large Nb ion should also expand the crystal structure, relative to $SrTiO_3$. This is what was found in previous studies of $SrNbO_3$, both from theory and experiments. [33] In powder form, the material has been proposed as a photocatalyst. [34] As a stoichiometric thin film, $SrNbO_3$ has generated interest as a transparent conductor in the visible and ultraviolet regime. [8] While $SrTiO_3$ has been studied thoroughly, there was no systematic theoretical study of $SrNbO_3$. Furthermore, these oxides can typically show a wide range of metastable phases that might be accessible with

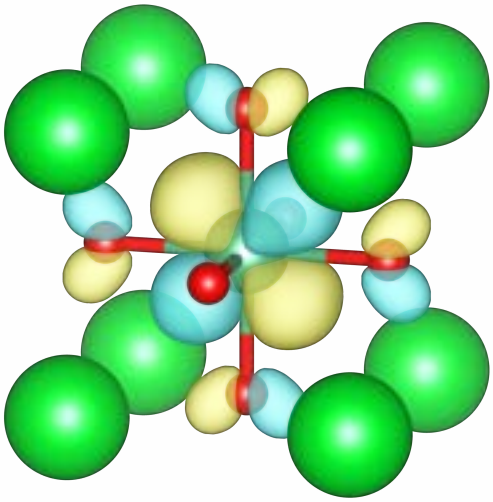

Figure 3.1: Schematic of cubic $SrNbO_3$. The oxygen ions (red) create an octahedral network around Nb (blue). The isosurface shows one (out of the 3 triply degenerate) hybridized states originating from Nb t_{2g} and O $2p$. The t_{2g} character is clearly intact.

potentially different material properties. I try to address this gap in the literature in this chapter, and emphasis is on how the octahedral tilting and biaxial strain is coupled.

3.2 Theory

In this section I will outline the theory essential to this chapter, while relying on the general DFT theory described in Chapter 2. A quick introduction to the dielectric function and Seebeck coefficient is given. Furthermore, a connection between these macroscopic properties and DFT electronic structure is made.

3.2.1 Dielectric function

The (complex) macroscopic dielectric function, $\epsilon(\omega)$, describes the interaction between electromagnetic waves and solids. It relates the electrical field with frequency ω, $\vec{E}(\omega)$, to the displacement field, $\vec{D}(\omega)$, as $\vec{D}(\omega) = \epsilon(\omega)\vec{E}(\omega)$. The dielectric function is a tensor and it can depend on the position $\vec{r}$. Optical excitations can be understood as peaks in the imaginary part of the dielectric function. To a first approximation, it is possible to evaluate the microscopic dielectric function within the independent-particle (IP) picture simply from the KS band structure. The assumption that the excitations are independent and that there is no electron-hole interaction is of course not perfect, but due to the numerical simplicity it is an attractive approximation. Furthermore, by neglecting local field effects, the microscopic and macroscopic dielectric functions become identical. Using these, admittedly crude, approximations it is therefore possible to go from KS-DFT to the optical response of macroscopic crystals. The imaginary part of the optical dielectric function can be evaluated as [35]:

$$\epsilon^{(2)}_{\alpha,\beta}(\omega) = \frac{4\pi^2 e^2}{V} \lim_{q\to 0} \frac{1}{q^2} \sum_{c,v,\vec{k}} 2\omega_{\vec{k}} \delta(\varepsilon_{c\vec{k}} - \varepsilon_{v\vec{k}} - \omega) \left\langle u_{c\vec{k}+\hat{e}_\alpha q} \middle| u_{v\vec{k}} \right\rangle \left\langle u_{c\vec{k}+\hat{e}_\beta q} \middle| u_{v\vec{k}} \right\rangle^*, \quad (3.1)$$

where the optical limit ($\lim_{q\to 0}$) is taken of the transferred momentum q. The Cartesian directions are given by α and β. The variables V, c, v and $\vec{k}$ denote the primitive cell volume, the conduction and valence band indices, and the electron momentum, respectively. The cell periodic part of the state $c\vec{k}$ is denoted $u_{c\vec{k}}$. The real part of the dielectric function is evaluated using a Kramers-Kronig transformation.

Above equation captures only interband transitions. To model intraband transitions a simple Drude term can be added:

$$\epsilon_{\text{intra}}(\omega) = \epsilon^{(1)}_{\text{intra}}(\omega) + i\epsilon^{(2)}_{\text{intra}}(\omega) \tag{3.2}$$

$$\epsilon^{(1)}_{\text{intra}}(\omega) = 1 - \frac{\omega^2_{p,\text{intra}}}{\omega^2 + \gamma^2} \tag{3.3}$$

$$\epsilon^{(2)}_{\text{intra}}(\omega) = \frac{\gamma\omega^2_{p,\text{intra}}}{\omega^3 + \omega\gamma^2} \tag{3.4}$$

where $\omega_{p,\text{intra}}$ is the intraband plasma frequency and γ is the broadening parameter. This type of model introduces a broadening to the dielectric function and the low frequency Drude peak. Note, that the inclusion of the Drude term is not crucial to the conclusions here, it simply makes the dielectric functions more realistic looking.

3.2.2 Seebeck coefficient

Within the relaxation time approximation (RTA) of the Boltzmann transport equation (BTE), the Seebeck coefficient, and other electronic transport coefficients, are the Onsager coefficients of the spectral conductivity [36]:

$$\sigma_{\alpha,\beta}(\varepsilon) = \sum_n \int \frac{d\vec{k}}{8\pi^3} v_{n\vec{k},\alpha} v_{n\vec{k},\beta} \tau_{n\vec{k}} \delta(\varepsilon - \varepsilon_{n\vec{k}}), \tag{3.5}$$

here α and β again denotes Cartesian directions, and $v_{n\vec{k},\alpha}$, $\tau_{n\vec{k}}$, and $\varepsilon_{n\vec{k}}$ denotes the group velocity of state $n\vec{k}$ in the α direction, the relaxation time of state $n\vec{k}$, and the energy of state $n\vec{k}$, respectively. From the spectral conductivity, the general Onsager coefficients are [36]:

$$\mathcal{L}^m_{\alpha,\beta} = -e^2 \int d\varepsilon \sigma_{\alpha,\beta}(\varepsilon)(\varepsilon - \varepsilon_F)^m \frac{\partial f(\varepsilon)}{\partial \varepsilon}, \tag{3.6}$$

where ε_F is the Fermi level and $f(\varepsilon)$ is the Fermi-Dirac distribution:

$$f(\varepsilon) = \frac{1}{e^{(\varepsilon-\varepsilon_F)/k_BT} + 1}, \tag{3.7}$$

for a given thermal energy given by the temperature T and Boltzmann coefficient k_B. Finally the electrical conductivity can be written as:

$$\sigma_{\alpha,\beta} = \mathcal{L}^0_{\alpha,\beta}, \tag{3.8}$$

and the Seebeck coefficient as:

$$S_{\alpha,\beta} = \frac{1}{eT} \frac{\mathcal{L}^1_{\alpha,\beta}}{\mathcal{L}^0_{\alpha,\beta}}. \tag{3.9}$$

Since the integrands in $\mathcal{L}^m_{\alpha,\beta}$ are all proportional to $\tau_{n\vec{k}}$, the ratio of $\frac{\mathcal{L}^1_{\alpha,\beta}}{\mathcal{L}^0_{\alpha,\beta}}$ becomes independent of the scattering rates *if* the scattering is energy independent. Therefore, within the constant (energy) relaxation time approximation, the Seebeck coefficient is independent of the relaxation time, making it a useful probe of the underlying band structure.

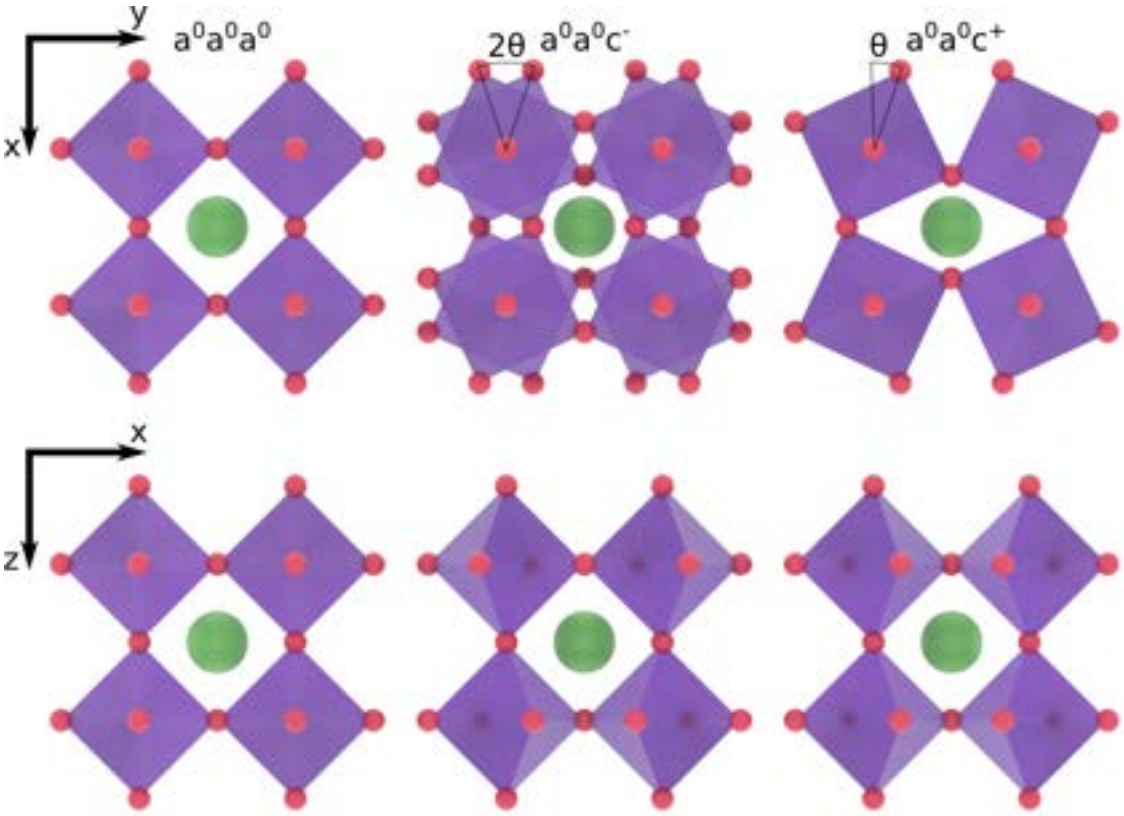

Figure 3.2: Visualization of octahedral rotations in $SrNbO_3$. The O ions (red spheres) form octahedra around the Nb ions. The Sr ions are depicted as green spheres.

3.3 Octahedral rotations and the stabilization under strain

DFT was employed to study the coupling between biaxial strain and octahedral rotations in $SrNbO_3$. Throughout this section, I make comparisons to $SrTiO_3$, since it is a common perovskite oxide. The PBEsol [23] functional was used in this chapter due to its accuracy in describing equilibrium lattice properties. For the exploration of the total energy landscape a Γ-centered k-mesh corresponding to $8 \times 8 \times 8$ in the 5 atom unit cell was used. A plane-wave cutoff of 550 eV was set, and the electronic self-consistency was converged below 1×10^{-6} eV. The ionic degrees of freedom was relaxed below 0.01 eV/Å. All calculations in this chapter was done using *Vienna Ab initio Simulation Package* (VASP). [37] First, the lattice constant of the 5 atom u.c. was optimized, and a value of $a_{\mathrm{DFT}} = 4.0182$ Å was found. This is in very good agreement with the experimental value $a_{\mathrm{exp}} = 4.023$ Å. [33] Using the lattice parameter of the simple high symmetry 5 atom unit cell, the biaxial strain was applied by fixing the in-plane lattice parameters as requested. Strains between $-3\,\%$ and $+3\,\%$ was sampled, and for each in-plane strain, the out-of-plane lattice parameter was found by fitting the equation of states using a third order inverse polynomial [38]. The resulting out-of-plane lattice constants can be found in Table 3.1.

Having found the strained 5 atom u.c. lattice parameters, superstructures of $2 \times 2 \times 2$ u.c. was constructed with varying strain. In these structures the oxygen ions were displaced according to different octahedral rotations described by Glazer's notation [39]. The rotations sampled were $a^0a^0c^-$, $a^0a^0c^+$, $a^0b^-b^-$, $a^0b^+b^+$, $a^-a^-a^-$, $a^+a^+a^+$, $a^+a^-a^+$, $a^-a^-a^+$, and $a^0b^-b^+$. The $+$ ($-$) sign denotes in-phase (out-of-phase) rotation between adjacent octahedra, in the direction given by the position (or index) of the sign. As an example, $a^0b^-b^+$, indicates no

Table 3.1: Predicted lattice parameters, c, using PBEsol in units of Ångström. In the strained cases the relaxed out-of-plane parameter is presented.

Biaxial strain, %	c, $SrNbO_3$	c, $SrTiO_3$
-3.0	4.095	3.974
-2.0	4.073	3.947
-1.0	4.047	3.922
-0.5	4.033	3.910
0.0	4.018	3.896
+0.5	4.007	3.887
+1.0	3.997	3.876
+2.0	3.979	3.855
+3.0	3.964	3.836

rotation around x, out-phase rotation around y and in-phase rotation around z-axis. Three simple cases are visualized in Figure 3.2. Since the displacements were done from scratch, the space groups of the tilted structures were verified using VASPKIT [40].

Applying biaxial strain lowers the symmetry of the lattice, and hence $a^0a^0c^-$ is no longer equivalent with $a^-b^0b^0$. Therefore, both alternatives were sampled. The resulting energy landscape for $SrNbO_3$ under $-2\,\%$, $0\,\%$ and $+2\,\%$ biaxial strain is presented in Figure 3.3. The energies are always related to the untilted cases. There is a striking difference between the compressive strain, i.e., $-2\,\%$ and the other strains. The potential well is getting deeper with compressive strain, while for unstrained and tensile strain the well is shallow. This is the first key finding. It shows that while unstrained and tensile strain might not stabilize octahedral rotations in real conditions (where thermal fluctuations are involved), compressive strain might actually be useful in altering the crystal structure by inducing octahedral rotations. Furthermore, the rotations around the out-of-plane axis are clearly preferred under compressive biaxial strain. In contrast, the rotations around the out-of-plane axis get destabilized during tensile strain. The two relevant modes during compressive strain, e.g., $SrNbO_3$ grown epitaxially on $SrTiO_3$, are $a^0a^0c^-$ and $a^0a^0c^+$. They are almost degenerate for low compressive strain, but they diverge for larger strains, and interestingly $a^0a^0c^+$ is lower in energy compared to $a^0a^0c^-$. This is a drastic difference compared to $SrTiO_3$, which shows a clear preference for out-of-phase rotations, as seen in Figure 3.4. In $SrTiO_3$, the low temperature phase is the tetragonal $a^0a^0c^-$ distortion (see Reference [41] and references therein). The preference for the in-phase rotation, i.e., $a^0a^0c^+$, is rare in oxide perovskites, while common in other perovskites such as iodides and bromides. [42] In many other oxides, if there is an in-phase rotation it is accompanied by an out-of-phase rotation. [43] This makes the predicted stability of $a^0a^0c^+$ in $SrNbO_3$ very unique.

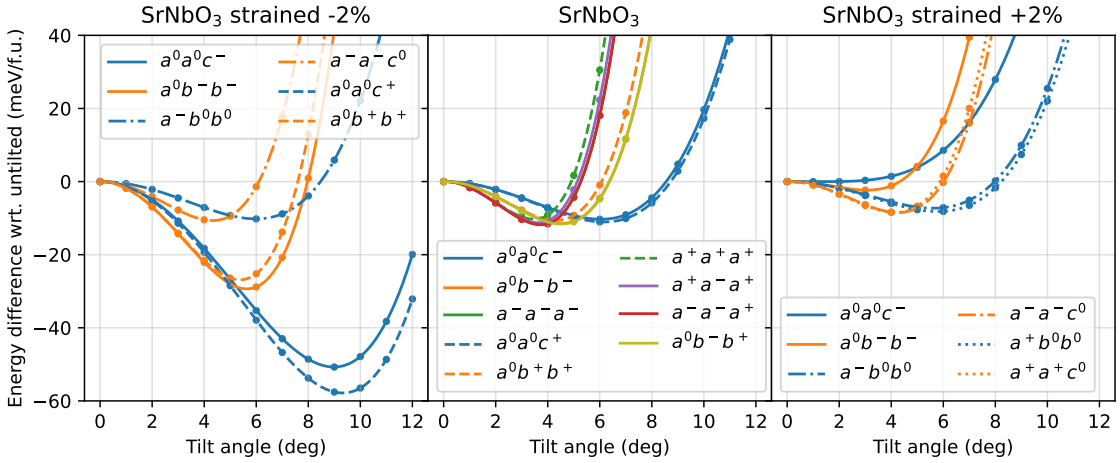

Figure 3.3: Total energy landscape of $SrNbO_3$ for selected strains. The energy difference with respect to the untilted structure is shown.

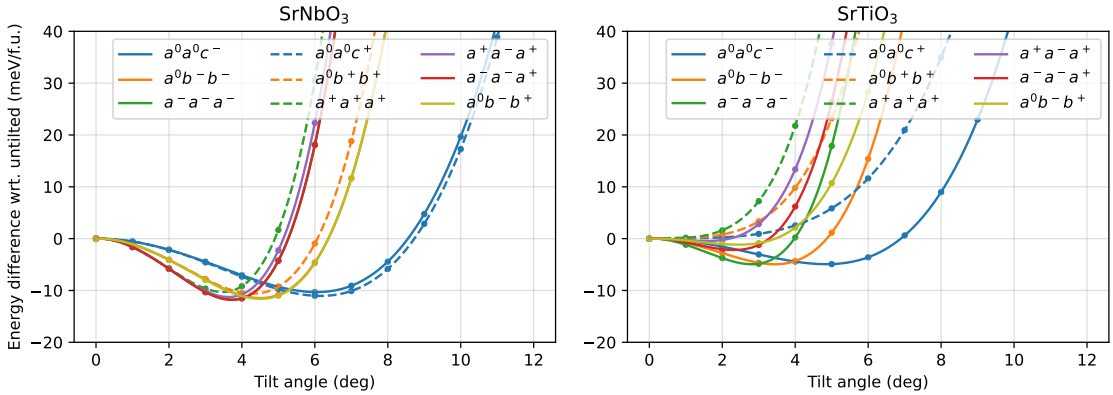

Figure 3.4: Energy landscape of $SrNbO_3$ and $SrTiO_3$ in the unstrained case.

To get some understanding for why the $a^0a^0c^+$ tilt is preferred over $a^0a^0c^-$ in $SrNbO_3$, additional calculations were done for the two tilts with hole doping. This was done based on the simple idea that $SrNbO_3$ should resemble $SrTiO_3$, but with different electron count. Similarly, calculations of $SrTiO_3$ was done with electron doping. The calculations are performed using the background charge method, which adds a constant background charge to counteract the additional charge from the doping. The results are summarized in Figure 3.5 for $-2\,\%$ strain. It is clear that additional electrons in $SrTiO_3$ stabilizes the two modes (like shown in Reference [44]). More importantly, the difference between the two tilts is decreasing with more electrons. By including holes, or removing electrons, in $SrNbO_3$ the two modes are destabilized. In this case, there is a critical doping amount (ca. 0.5 h/f.u.) at which the optimal tilt is changed from $a^0a^0c^+$ to $a^0a^0c^-$. Uchida *et al.* argued that the stabilization of octahedral tilting in electron doped $SrTiO_3$ is related to the increase of the Ti ion due to the filling of the Ti $3d$ states. [44] The distortions are related to the ionic sizes according to the Goldschmidt tolerance factor. [45] A larger B ion decreases the tolerance factor, $t = (r_A + r_O)/(\sqrt{2}(r_B + r_O))$, and a tolerance factor that decreases below 1 hints that octahedral distortions are more likely. The findings presented here are in agreement with theirs, with the addition of the competition between the tilt modes in relation to the doping.

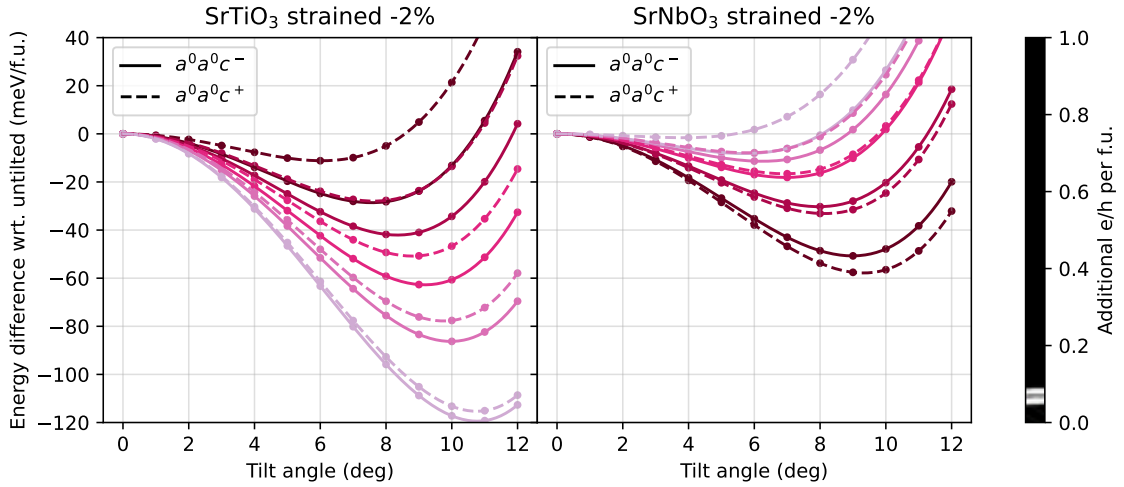

Figure 3.5: Influence of electron (hole) doping on the octahedral tilt stability in compressively strained $SrTiO_3$ ($SrNbO_3$).

To round off this section, I present the optimal tilt modes and angles as a function of strain. This is shown in Figure 3.6. It highlights that the optimal tilt angles are larger in $SrNbO_3$ than in $SrTiO_3$, likely due to the additional electrons as discussed above, but also that compressive strain shows more tunability due to the stronger stabilization of the tilting modes.

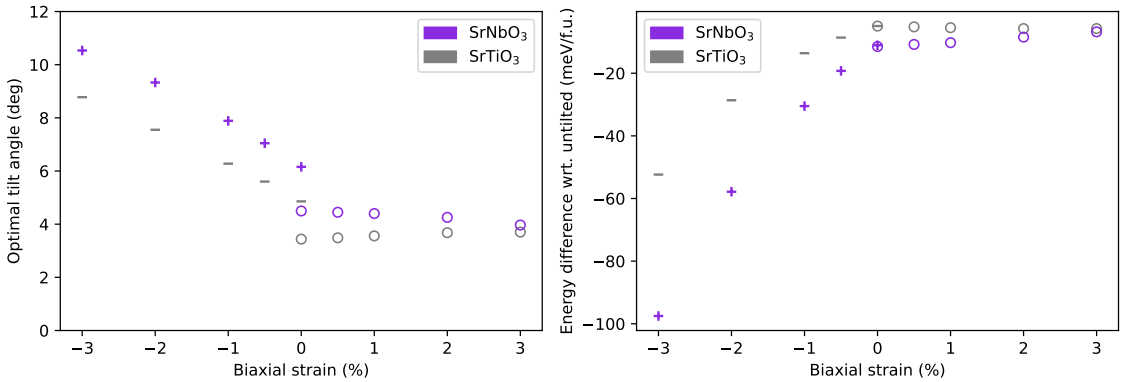

Figure 3.6: Left: Optimal tilt angle vs. strain for $SrNbO_3$ and $SrTiO_3$. Right: Energy difference of the optimal tilt relative to untilted vs. strain. The $+$ ($-$) marker shows that the $a^0a^0c^+$ ($a^0a^0c^-$) tilt is optimal. The open marker shows that $a^-a^-c^0$ is preferred.

3.4 Electronic structure and octahedral tilting

Having studied the energy landscape of octahedral tilting in $SrNbO_3$, it is now possible to examine the electronic structure of likely phases of $SrNbO_3$. The electronic band structure was calculated along different high symmetry points for the different crystals. The same DFT setup is used as before. I here focus on the band structure of $a^0a^0a^0$, $a^0a^0c^-$ and $a^0a^0c^+$, with the motivation that $a^0a^0c^-$ and $a^0a^0c^+$ are stabilized under compressive strain (e.g. $SrNbO_3$ grown epitaxially on $SrTiO_3$). The octahedral tilting changes the lattice, and therefore, space group of the crystal. In Figures 3.7a, 3.7b and 3.7c, the 1st BZ is shown for $a^0a^0a^0$, $a^0a^0c^-$ and $a^0a^0c^+$, respectively. Note, that the coordinate systems are rotated around the z-axis by 45° in $a^0a^0c^-$ and $a^0a^0c^+$ relative to $a^0a^0a^0$.

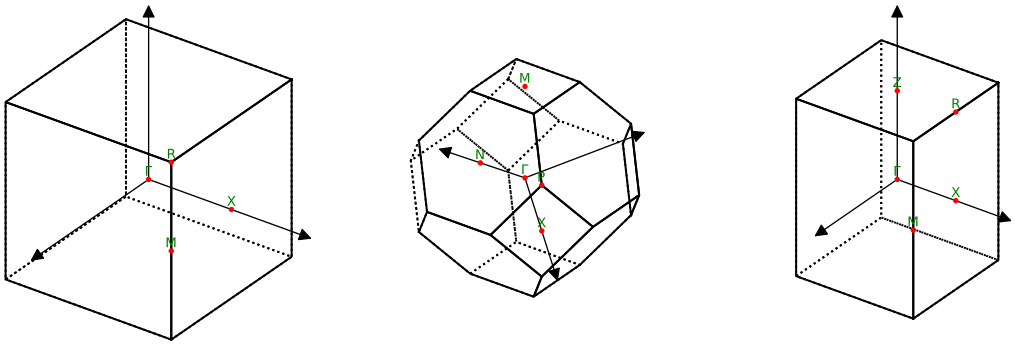

(a) First BZ of $a^0a^0a^0$. (b) First BZ of $a^0a^0c^-$. (c) First BZ of $a^0a^0c^+$.

Figure 3.7: First BZs of different octahedral tilts relevant to compressively strained $SrNbO_3$. Note, that in $a^0a^0c^-$ and $a^0a^0c^+$ the systems are rotated 45° around the z-axis in the $a^0a^0a^0$ system (see Figure A.1 for comparison between the tilted BZs and untilted BZ).

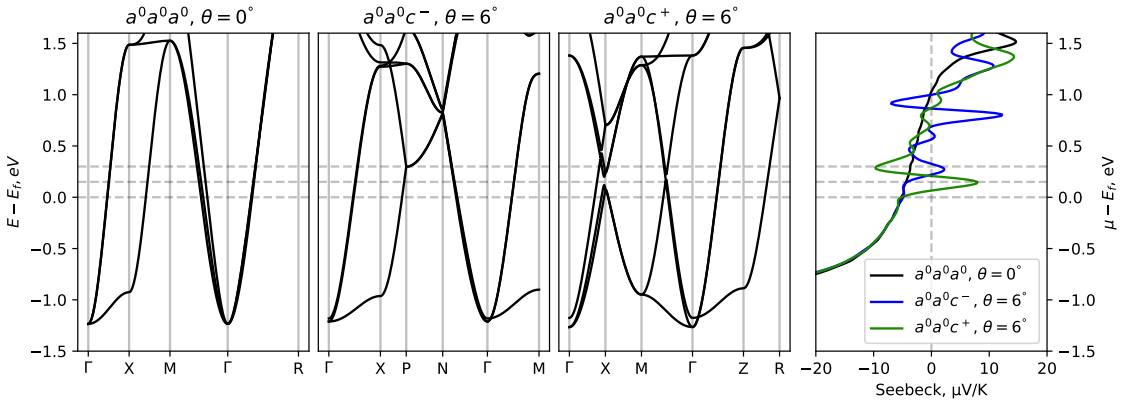

Figure 3.8: Comparison of the band structures of $a^0a^0a^0$, $a^0a^0c^-$ and $a^0a^0c^+$ in unstrained $SrNbO_3$. The room temperature in-plane Seebeck coefficient is presented to the right.

The calculated band structures for unstrained $a^0a^0a^0$, $a^0a^0c^-$ and $a^0a^0c^+$ are presented in Figure 3.8. The simple $a^0a^0a^0$ phase shows the typical Nb $4d$ t_{2g} states, that are all degenerate at Γ and form characteristic cylindrical Fermi surfaces. Introducing the octahedral tilting enlarges the unit cell (in real space), which causes the number of bands to increase in $a^0a^0c^-$ and $a^0a^0c^+$. Furthermore, the distortion of the octahedral network causes the t_{2g} states to split at Γ. The splitting is substantially larger in the case of $a^0a^0c^+$ compared to $a^0a^0c^-$. The $a^0a^0c^-$ distortion show semi-Dirac dispersions at the P and N point, which have gained recent interest. [9, 10] These points are protected by non-symmorphic symmetries and makes the band crossings robust against spin-orbit coupling (SOC). [46] Contrastingly, the $a^0a^0c^+$ distortion shows Dirac lines, e.g., between X and M, on the boundary of the BZ. [46] These are also robust against SOC, and they will be discussed later. In general, both of the octahedral tilting modes reduce the bandwidth of the t_{2g} states, in agreement with findings for other oxides. [47]

3.5 Dielectric function parametrized by octahedral tilting

Since $SrNbO_3$ has been investigated as a transparent conductor, I then investigated the dielectric function as a function of octahedral tilting. This is insightful, since optical excitations are deeply connected to the electronic structure. This was done within the IP random phase

approximation (RPA) using VASP. [35] This treatment neglects any excitonic effects, i.e., it is assumed that the excitations occur from a filled KS state to an empty KS state, where the states are unaffected by the excitation. Furthermore, the RPA neglects any local field effects. These assumptions can be problematic, but comparisons with both experimental and theoretical literature indicate that the assumptions are reasonable for $SrNbO_3$. [48, 8, 49] To model intraband transitions a Drude term was introduced with broadening $\gamma = 0.3\,\text{eV}$ taken to reproduce the experimental values in Reference [49]. The intraband plasma frequency, $\omega_{p,\text{intra}}$, was calculated using VASP. [50] Using the calculated dielectric functions, the optical loss function was evaluated as $-\text{Im}\{\epsilon_{\alpha,\beta}(q \to 0, \omega)^{-1}\}$, where the optical limit, $q \to 0$, is taken of the complex dielectric function, $\epsilon_{\alpha,\beta}$. The loss function is large at frequencies with strong excitations. One such frequency is the plasma frequency which is defined as $\text{Re}\{\epsilon_{ij}(\omega_p)\} = 0$. There can be a slight shift in frequency between the maximum of the loss function and the plasma frequency, due to the imaginary part of the dielectric function. In Figure 3.9, the optical loss function is shown for unstrained $SrNbO_3$ parametrized by the octahedral tilt angle. The results are shown for the diagonal elements in both in-plane (xx) and out-of-plane (zz) directions. The black line represents the untilted phase. The untilted phase is isotropic, and shows a large peak at ca. 2.0 eV followed by a minor bump at ca 2.7 eV. The first peak fits very well with experiments. [48, 8, 49] However, the second peak is missing in experiments, and theoretically it has been connected to transitions from t_{2g} to e_g. [8] Next, the effect of tilting is analysed. By first examining the zz component, which is relevant for experiments with light incident normal to the surface, it is seen that the $a^0a^0c^+$ distortion shows an almost constant peak height, that is blueshifted with a larger tilt angle. In contrast, $a^0a^0c^-$ exhibits a peak with negligible shift, however, now the peak intensity is decreasing with a larger tilt angle. In the case of the xx component, the peak of $a^0a^0c^+$ is almost unchanged in height, however, now there is a redshift with increased tilt angles. In this case, the $a^0a^0c^-$ distortion also redshifts the peak with a larger tilt angle, and there is a clear decrease in peak height with larger tilt angles. Moving on, I would like to emphasis that the region around 2.7 eV is sensitive to the octahedral rotations studied here. This is reasonable since these excitations are associated with transitions from t_{2g} to e_g states [8]. These states are clearly sensitive to the octahedral tilting (Fig. 3.8). While it is unlikely that unstrained $SrNbO_3$ would stabilize any specific octahedral distortions in room temperature, it is possible that the room temperature ellipsometry experiments are sensing $SrNbO_3$ with thermally fluctuating octahedral rotations, and therefore the bump at 2.7 eV is smeared out. Another potential explanation is that the assumptions made to calculate the dielectric function are too crude. In any case, strain and/or temperature dependent ellipsometry would be beneficial for improving the understanding of octahedral distortions in $SrNbO_3$ and potentially other oxide perovskites.

3.6 Seebeck coefficient and octahedral tilting

Due to the band crossings observed in Figure 3.8, it is interesting to consider how the electronic transport is changed in these bands. For this purpose, the Seebeck coefficient was calculated for $SrNbO_3$ with different octahedral tilting. Within the RTA, the Seebeck coefficient is independent of the relaxation time, making it a useful probe of the electronic structure. Here, BoltzTrap2 [36] was used on a non-self-consistent calculation on a $50 \times 50 \times 50$ k-grid. The states were further interpolated on a grid with 15 times denser k-mesh. The Seebeck coefficient was evaluated on this grid within the RTA at 300 K. The in-plane Seebeck coefficient is shown in Figure 3.9. Slightly below the Fermi level, the Seebeck coefficient is negative, although small due to its metallic nature. Interestingly, the thermopower changes sign for both $a^0a^0c^+$ and $a^0a^0c^-$ above the Fermi level in regions where the untilted structure shows a constant negative sign. Furthermore, the peaks and valleys of the Seebeck coefficient is connected to the band features due to octahedral tilting. This is illustrated to the right in Figure 3.8. These

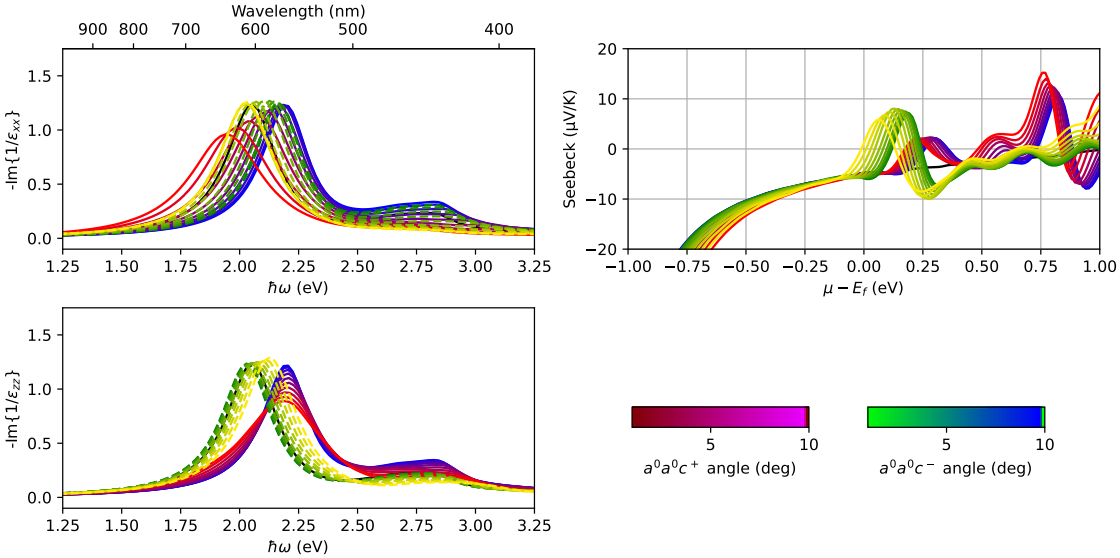

Figure 3.9: Left: Optical loss function of unstrained $SrNbO_3$ parametrized by octahedral tilting. Right: In-plane room temperature Seebeck coefficient of unstrained $SrNbO_3$. Black lines correspond to the untilted structure.

values are small for thermoelectric purposes, but perhaps the Seebeck coefficient could be used to get insight into octahedral tilting in $SrNbO_3$ by systematic gating experiments?

3.7 Summary

The key findings from the study of octahedral rotations in $SrNbO_3$ are the following:

- Biaxial compressive strain stabilizes octahedral rotations around the out-of-plane axis
- The in-phase mode, $a^0a^0c^+$, is preferred over the out-of-phase mode, $a^0a^0c^-$, in $SrNbO_3$
- Both $a^0a^0c^+$ and $a^0a^0c^-$ alter the t_{2g} states, and new band crossings emerge
- The peak position of the optical loss function can be tuned by ca. 0.2 eV by tilting
- While small, the Seebeck coefficient could contain information about octahedral rotations

Chapter 4

Unfolded bands and Dirac physics in tilted $SrNbO_3$

In the previous chapter the coupling between strain, octahedral tilting and electronic structure of $SrNbO_3$ was made. The results were presented in the lattice of the tilted structures, i.e., the band structures were evaluated along high symmetry points of the distorted lattices. This is of course very natural, and perfectly fine, but it can be difficult to compare the electronic structures of the different tilting modes. To ease the comparison, I here *unfold* the band structure of tilted $SrNbO_3$ onto the untilted lattice. Furthermore, this has the additional benefit of making the results more readily comparable to angle-resolved photoemission spectroscopy (ARPES) results. I here focus on compressively strained $SrNbO_3$ with ca. $-2\,\%$ strain, since this is relevant to experiments of $SrNbO_3$ grown epitaxially on $SrTiO_3$. Furthermore, guided by ARPES measurements I also performed a more detailed band structure analysis that is presented here.

Throughout this chapter, I rely on the findings and calculations in the previous chapter and I will only explain the additional theory needed, i.e. the DFT details are taken for granted from previous chapter.

This chapter is based on the unpublished manuscript titled "Band topology induced by octahedral rotation in $SrNbO_3$". The manuscript is appended in Section B.2. In the manuscript, DFT predictions of $SrNbO_3$ is compared with ARPES measurements of $SrNbO_3$. The ARPES measurements were performed by Alla Chikina on ultra thin $SrNbO_3$ grown epitaxially on $SrTiO_3$ at the Paul Scherrer Institute.

4.1 Theory

To be able to compare the effects of different octahedral rotations on the band structure, one can *unfold* the bands from the superstructure (containing the distortion) to a smaller structure without the distortion. The unfolding procedure will be described in the following section. In the subsequent sections, I will describe how Berry phase properties emerge from the electronic bands, and I will also very briefly outline how to fit Wannier functions to DFT results.

4.1.1 Unfolding of bands and Fermi slices

The unfolding of band structures and Fermi slices will be outlined in this section. In essence, the unfolding is a change of reference system, where the character of the states in the superstructure is compared to the states in the undistorted structure. The transformation matrix,

$\bar{M}$, between primitive lattice, $\vec{a}_i$, and supercell lattice $\vec{A}_i$ is defined as:

$$\begin{bmatrix} \vec{A}_1 \\ \vec{A}_2 \\ \vec{A}_3 \end{bmatrix} = \begin{bmatrix} m_{11} & m_{12} & m_{13} \\ m_{21} & m_{22} & m_{23} \\ m_{31} & m_{32} & m_{33} \end{bmatrix} \begin{bmatrix} \vec{a}_1 \\ \vec{a}_2 \\ \vec{a}_3 \end{bmatrix} \tag{4.1}$$

For the Glazer supercell the matrix for going between the unit cell and the $2 \times 2 \times 2$ supercell is $\bar{M} = \mathrm{diag}([2, 2, 2])$. Using the real space transformation matrix, the transformation in reciprocal space can be written as $\bar{M}^{-1}$. Furthermore, the (Bloch) spectral function can be written as [51]:

$$A(\vec{k}, \epsilon) = \sum_m P_{\vec{K}m}(\vec{k}) \delta(\epsilon - \epsilon_m), \tag{4.2}$$

with the spectral weights being:

$$P_{\vec{K}m}(\vec{k}) = \sum_n \left| \langle \Psi_{\vec{K}m} | \Psi_{\vec{k}n} \rangle \right|^2, \tag{4.3}$$

i.e. a projection of supercell states $\left|\Psi_{\vec{K}m}\right\rangle$ onto primitive states $\left|\Psi_{\vec{k}n}\right\rangle$. Here, the momenta in supercell BZ, $\vec{K}$, is unfolded onto the primitive momenta, $\vec{k}$, as:

$$\vec{k}_i = \vec{K} + \vec{G}_i, \ i = 1, ..., \det(\bar{M}) \tag{4.4}$$

This is the original version of band unfolding (or effective band structure) as proposed by Popescu and Zunger. [51]

Next, I describe how to evaluate unfolded Fermi slices (and surfaces). This is simply a generalization of the formulas proposed by Popescu and Zunger from a line in k-space to a surface (or volume). The sampled k-points are denoted by $\vec{k}_s$ corresponding to a list of points in the primitive cell BZ at which the states from the supercell is to be unfolded. The spectral weight, $P_{\vec{K}_s m}(\vec{k}_s)$, denotes the overlap of the *sampled* supercell and primitive states, where m denotes the band index in the supercell. Then the higher dimensional spectral function is written as:

$$\tilde{A}(\vec{k}, \epsilon) = \sum_{\vec{k}_s} \sum_m P_{\vec{K}_s m}(\vec{k}_s) G\left(\left\| \vec{k} - \vec{k}_s \right\|; \sigma_{\vec{k}} \right) G(\epsilon - \epsilon_m; \sigma_\epsilon) \tag{4.5}$$

The Dirac delta functions are approximated by Gaussians with finite widths, σ_ϵ and $\sigma_{\vec{k}}$, that are set rather arbitrarily for visualization purposes. This expression can be understood as the spectral function by Popescu and Zunger, but now the spectral weight is also smeared in momentum.

4.1.2 Berry phase and related properties

The topology of bands are characterized by the Berry phase and related quantities. [52] The Berry phase of Bloch state with band index m is a physical phase obtained as a path integral in momentum space:

$$\gamma_m = \oint_{\mathcal{C}} \mathcal{A}_m(\vec{k}) \cdot d\vec{k}, \tag{4.6}$$

where $\mathcal{C}$ is a closed path and $\mathcal{A}_m(\vec{k})$ is the vector field known as the Berry connection:

$$\mathcal{A}_m(\vec{k}) = \left\langle u_m(\vec{k}) \right| i\nabla_{\vec{k}} \left| u_m(\vec{k}) \right\rangle \tag{4.7}$$

A Berry phase of π along a closed loop indicates that the loop encircles a topological nodal line. [53] Furthermore, the Berry curvature is found by taking the curl of the Berry connection [52]:

$$\Omega_m(\vec{k}) = \nabla_{\vec{k}} \times \mathcal{A}_m(\vec{k}) \tag{4.8}$$

The Berry curvature is odd for time reversal invariant systems:

$$\Omega_m(-\vec{k}) = -\Omega_m(\vec{k}), \tag{4.9}$$

while it is even for inversion invariant systems:

$$\Omega_m(-\vec{k}) = \Omega_m(\vec{k}). \tag{4.10}$$

Therefore, for systems with both time reversal symmetry (TRS) and inversion symmetry (IS), the Berry curvature is constant zero, $\Omega_m(\vec{k}) \equiv 0$. It is therefore essential to break TRS to achieve anomalous transport in centrosymmetric crystals. The total velocity of a particle is a sum of the band velocity and the anomalous velocity [52]:

$$v_m(\vec{k}) = \frac{1}{\hbar}\nabla_{\vec{k}}\epsilon_m(\vec{k}) - \frac{e}{\hbar}\vec{E} \times \Omega_m(\vec{k}), \tag{4.11}$$

where $\epsilon_m(\vec{k})$ is the band dispersion and $\vec{E}$ is an external electric field. It is the anomalous term that can give rise to the transport effects such as the anomalous Hall effect.

4.1.3 Wannier representation

Studying details of band structures, such as the Berry phase related quantities discussed above, typically requires fine sampling of the k-points. While it is in principle possible to evaluate each k-point using DFT, this quickly becomes impractical due to the large computational cost. Instead, it is possible to fit Wannier functions to *one* DFT calculation, then use the resulting Wannier functions to efficiently evaluate the band energies at any point in k-space. The Wannier state of band n in cell $\vec{R}$ is given as a Fourier transform of the Bloch states [54]:

$$\left|\vec{R}n\right\rangle = \frac{V}{8\pi^3}\int d\vec{k} e^{-i\vec{k}\cdot\vec{R}} \left|\Psi_{\vec{k}n}\right\rangle \tag{4.12}$$

The Wannier states contain the same information as the Bloch states, with the additional benefit of being localized. Moving from Bloch states to the Wannier representation is known as Wannierization, and by using the software package Wannier90 [55], it is possible to fit so-called maximally localized Wannier functions to electronic structures calculated from DFT. Using the Wannier states it is then possible to interpolate the dispersion in an efficient manner, e.g., to study the band structure or more complex band related quantities. There are many important details, e.g., how to find a good representation of states that are hybridized with other states and how to define a localization criterion, and for those details I refer to the excellent review in Reference [54].

Like any other fitting problem, there are easier and more difficult systems to Wannierize. The quality of the solution is sensitive to the initial guesses given as input. In Figure 4.1, the resulting Wannier bands of $a^0a^0a^0$ $SrNbO_3$ is shown together with DFT bands. Here, only 3 Wannier functions are fitted and the t_{2g} states are used as initial projections. When introducing octahedral rotations, strain, magnetization, and SOC the fitting becomes more tricky. However, even then it is possible to create high quality Wannierizations as illustrated further down in Figure 4.7.

4.2 Unfolded bands of $a^0a^0c^-$ and $a^0a^0c^+$ onto $a^0a^0a^0$

The electronic structures, as calculated in Chapter 3, of $-2\,\%$ strained $SrNbO_3$ are now unfolded onto the $a^0a^0a^0$ lattice. Here, $a^0a^0a^0$ is included as a benchmark, and the unfolded bands $a^0a^0a^0$ of onto $a^0a^0a^0$ is the trivial case where the spectral weights are Kronecker deltas. In practice the unfolding was done using VASPKIT [40] based on VASP [37] DFT calculations

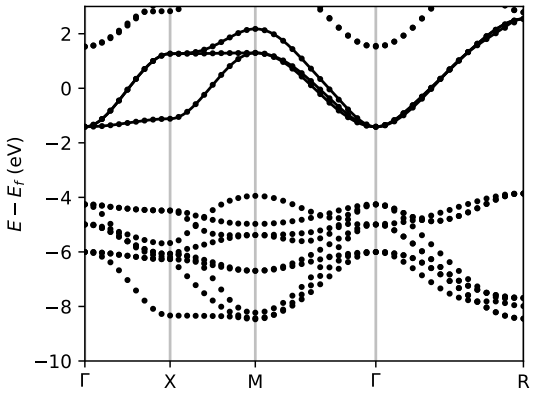

Figure 4.1: Comparison between DFT bands (circles) and Wannier interpolated bands (lines) of $a^0a^0a^0$ $SrNbO_3$.

as in previous chapter. In Figure 4.2, the unfolded bands of $a^0a^0a^0$, $a^0a^0c^-$, and $a^0a^0c^+$ are shown along a high-symmetry path of the $a^0a^0a^0$ lattice. Focus is on $a^0a^0c^-$ and $a^0a^0c^+$ due to the stabilization of these distortions upon biaxial compressive strain, as observed in previous chapter. An artificial smearing, $\sigma_\epsilon = 0.02\,\text{eV}$, is introduced for visualization purposes. This broadening does not have a physical meaning, and should not be interpreted as broadening due to finite lifetime effects. The unfolded bands of $a^0a^0a^0$ show the expected Nb t_{2g} states in the conduction band and a large gap between the t_{2g} and O $2p$ states. A moderately large conduction bandwidth, W, is observed due to the delocalized nature of the Nb $4d$ states, compared to the $3d$ states in $SrTiO_3$ or $SrVO_3$. [8] Furthermore, a small t_{2g} splitting is found due to the tetragonality present in the biaxially strained system. By introducing the $a^0a^0c^-$ rotation, a new band is found centered around M. The energy of the bottom of the band is sensitive to the octahedral tilt angle, but always above the bottom of the bands at Γ and X. Furthermore, the states below the "band gap" also show changes. For $a^0a^0c^-$, there are now states present at Γ with same energy as at M (which in $a^0a^0a^0$ was the "valence" band maximum). This has been predicted for octahedral rotations in $SrTiO_3$, i.e., the tilting can turn an indirect band gap into a direct band gap. [56] As mentioned in the previous chapter, the octahedral tilting breaks the symmetry of the octahedra and enhances the t_{2g} splitting. The $a^0a^0c^+$ also exhibits new bands centered around M. However, in this case, there are multiple non-degenerate bands centered around M. By focusing on the X point, and moving out towards Γ and M, it is evident that the X point is a folding point (see Appendix A for schematics of the folding). The new bands around M originates from the (light and heavy) bands around Γ. Therefore, the bands at M are degenerate with the bands at Γ. This is true for any tilt angle. Furthermore, the t_{2g} splitting is larger in the case of $a^0a^0c^+$ compared to $a^0a^0c^-$ by almost a factor 2. In the case of $a^0a^0c^+$, the O $2p$ states are modified, and now the gaps between O $2p$ and Nb $4d$ is identical at M and Γ. Furthermore, by comparing the bands from Γ to X between the different tilts, it is observed that $a^0a^0c^-$ decreases the bandwidth relative to $a^0a^0a^0$ by ca. 17 %, while $a^0a^0c^+$ has a slightly smaller suppression of ca. 10 % relative to $a^0a^0a^0$. This is in agreement with predictions of other oxides. [47] In other words, the distortions lead to decreases in bandwidths, i.e., increases in effective masses ($m^* \propto 1/W$).

By generalizing the band unfolding to 2D surfaces, one can evaluate the unfolded Fermi slices. This is done in Figure 4.3 at the $k_z = 0$ slice. Here the Gaussian smearing is parametrized by $\sigma_\epsilon = 0.04\,\text{eV}$ and $\sigma_{\mathbf{k}} = 0.005$ in units of primitive reciprocal lattice constant. As expected, the untilted ($a^0a^0a^0$) structure shows cylindrical t_{2g} Fermi shapes centered around Γ. [57] The $a^0a^0c^-$ tilt generates a new pocket around M, as expected from the band structures. Finally,

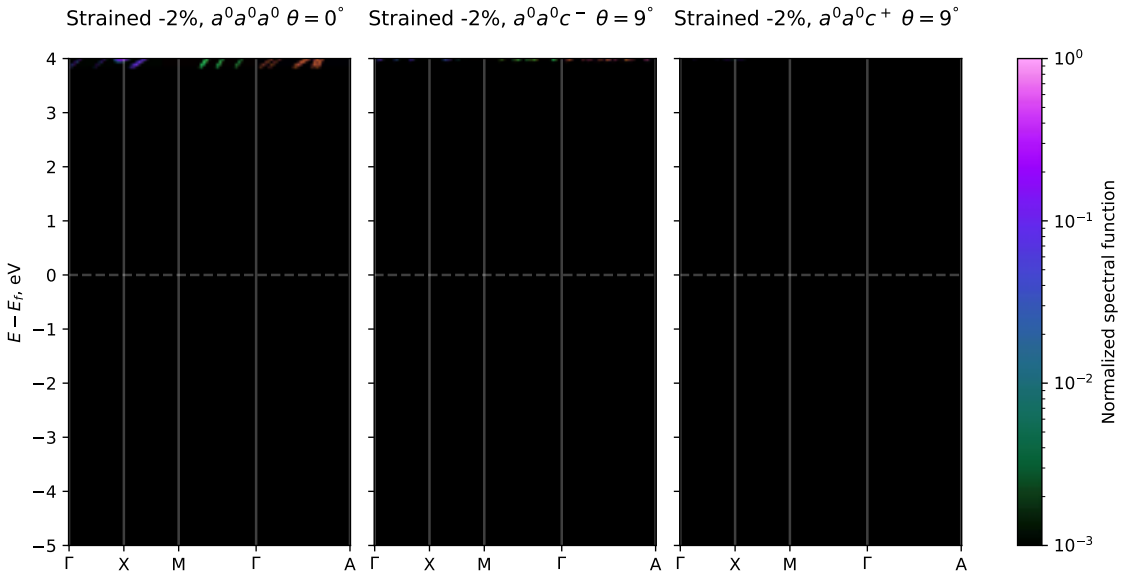

Figure 4.2: Unfolded bands of $-2\,\%$ strained $a^0a^0a^0$, $a^0a^0c^-$, and $a^0a^0c^+$ onto the $a^0a^0a^0$ structure. An artificial smearing is introduced for visualization purposes.

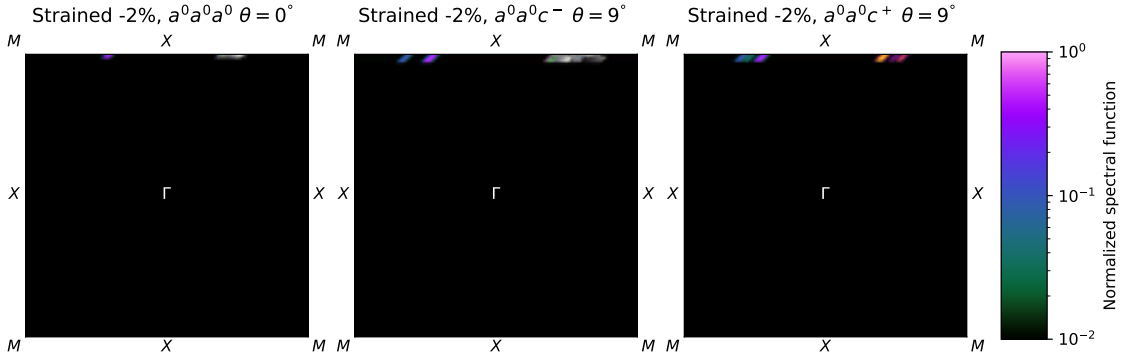

Figure 4.3: Unfolded Fermi slices at $k_z = 0$ of $-2\,\%$ strained $a^0a^0a^0$, $a^0a^0c^-$, and $a^0a^0c^+$. The high symmetry notation of $a^0a^0a^0$ is employed. Artificial smearing in both energy and momentum is included.

$a^0a^0c^+$ tilt forms new bands centered around M, and there is symmetry around the X-X line. The folding is further illustrated in Appendix A.

4.3 ARPES of ultra thin $SrNbO_3$

ARPES gives direct insight into the electronic structure of solids. Via collaboration, I have gotten access to ARPES data of ultra thin $SrNbO_3$ grown on $SrTiO_3$. The ARPES measurements were done by Alla Chikina at the Paul Scherrer Institute. The expected theoretical strain between the two lattices is ca. $-2.8\,\%$, i.e., a large compressive biaxial strain is expected. In Figure 4.4, the ARPES data of 7 u.c. thick $SrNbO_3$ is presented. The DFT bands of $a^0a^0c^+$ are overlain with a shift of 0.6 eV. The cylindrical t_{2g} states are observed both in the Fermi slice and the band structures, as expected. Interestingly, there is a band forming around the M point (in cubic notation), which indicates that there is some periodicity additional to the ones present in $a^0a^0a^0$. The bottom of the band at M is degenerate with the states at Γ, which indicates that the octahedral rotation is of type $a^0a^0c^+$ (see Figure 4.2). The overlain DFT bands of $a^0a^0c^+$, albeit shifted, fit excellent with the ARPES bands. This makes it likely

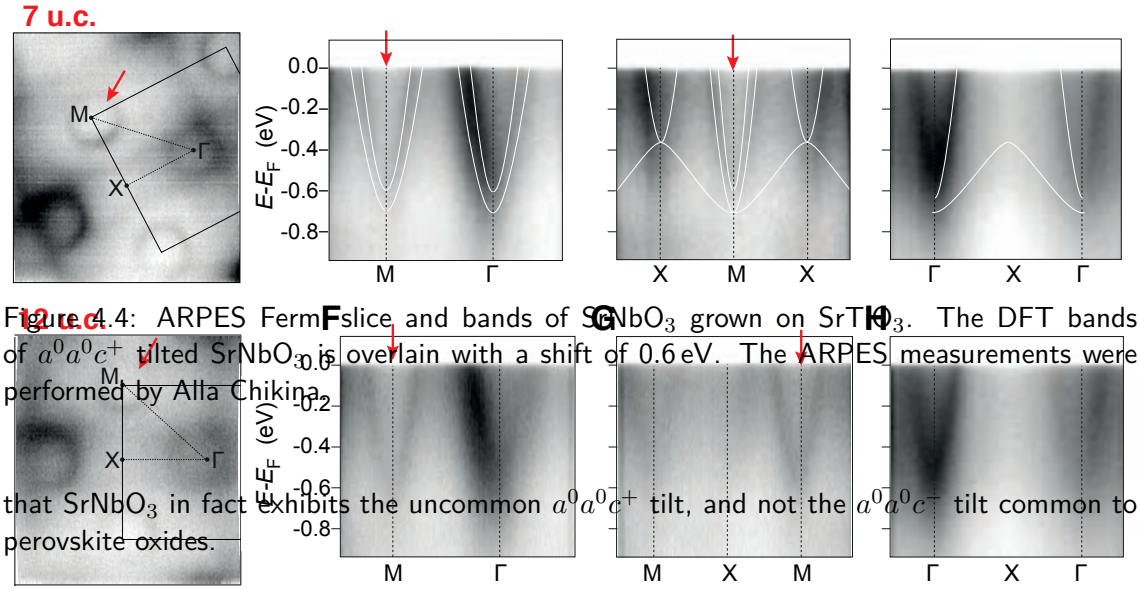

Figure 4.4: ARPES Fermi slice and bands of $SrNbO_3$ grown on $SrTiO_3$. The DFT bands of $a^0a^0c^+$ tilted $SrNbO_3$ is overlain with a shift of 0.6 eV. The ARPES measurements were performed by Alla Chikina.

that $SrNbO_3$ in fact exhibits the uncommon $a^0a^0c^+$ tilt, and not the $a^0a^0c^-$ tilt common to perovskite oxides.

4.4 Details of the $a^0a^0c^+$ tilted band structure

Having predicted that the $a^0a^0c^+$ tilt is the ground state which is stabilized under compressive biaxial strain in $SrNbO_3$, I then take a closer look at the topological properties of the $a^0a^0c^+$ bands. This is inspired by the study of the topological features of the $a^0a^0c^-$ tilt of $SrNbO_3$. [9, 10] In this section all DFT results are from calculations using QuantumESPRESSO [58].

To study the details of electronic structures it is often beneficial to convert the DFT solution into a smaller tight binding (TB) model. The motivation is straightforward: to reduce computational cost. Instead of sampling a very fine k-mesh in DFT (which would be computationally costly), one can construct a set of Wannier functions that describes the bands of interest, and using that small set it is possible to evaluate the dispersion at any k-point with low computational cost. This of course comes with a potential loss in accuracy, since the Wannier functions are fitted to the DFT solution.

Already in Figure 3.8 a nodal line could be observed when going between the high symmetry points $\mathrm{X} \to \mathrm{M}$ of $a^0a^0c^+$ $SrNbO_3$. This nodal line can be identified the easiest when going from Γ to X. In this line (from left to right), there are bands that merge and stay degenerate going towards M. In other words, two states (neglecting spin) meet and form a Dirac degeneracy, this degeneracy is not only a point, but rather a continuous *nodal line* from X to M. This Dirac line is due to the specific space group of the $a^0a^0c^+$ tilt, namely P4/mbm (127). [46] Due to the, so-called, non-symmorphic symmetries present in this space group the SOC vanishes at this path of the boundary of the BZ. In Figure 4.5, a Dirac nodal line that crosses the Fermi level is shown in the vicinity of X. This dispersion is evaluated using Wannier functions generated from a SOC DFT calculation, and the degeneracy is present as predicted by Hirschmann *et al.* in Reference [46]. The linear dispersion is clearly observed in the $\Gamma \to \mathrm{X}$ direction.

Nodal points and lines can also exist away from high-symmetry points or lines. To do a systematic search for these structures, I employed WannierTools [59] to search for nodes in the whole 1st BZ. This is done using the TB Hamiltonian created from a non-SOC DFT calculation. Furthermore, since the Wannierization can fail to capture the correct (lattice and/or global) symmetries present in the system, a symmetrization was performed using WannSymm [60]. Here, the symmetries requested were the ones present in the P4/mbm (127) space group. This step was crucial, since otherwise the nodal lines were found to be "broken" into shorter segments. The resulting nodal structures are visualized in Figure 4.6. Here, there nodal lines from the boundary of the BZ are not drawn for clarity, and only nodal points from the lower

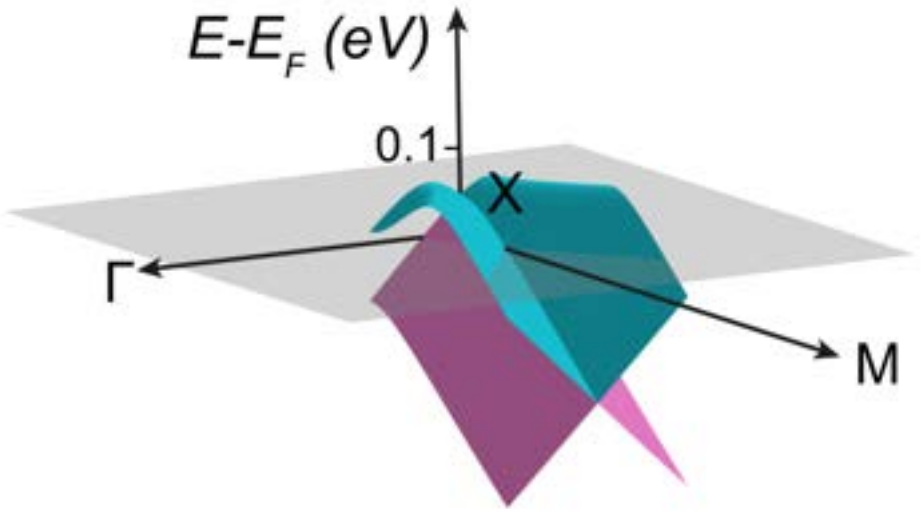

Figure 4.5: Example of a Dirac nodal line at boundary of BZ of $-2\,\%$ strained $a^0a^0c^+$ $SrNbO_3$. The dispersion is shown in vicinity of X. Here, SOC is included, i.e., the degeneracy is stable with respect to SOC.

half of the BZ is shown. I focus on band indices 2 and 3 (out of the 6 t_{2g} states), since they exhibit degeneracies closest to the Fermi level. Interestingly, there exists plenty of nodal lines and many of them are connected forming nodal chains. [61] The small black circles denote paths with π Berry phases calculated using WannierTools, this shows that these states are in fact non-trivial. [62, 53]

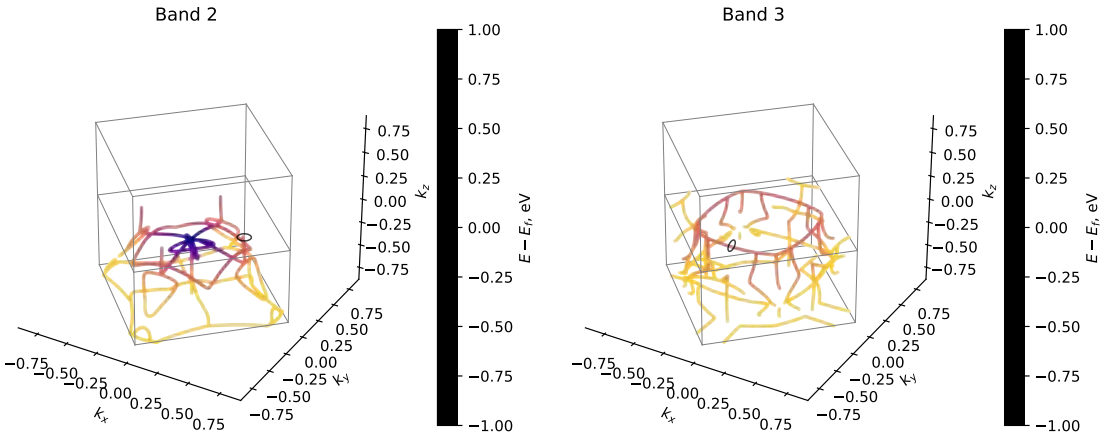

(a) Nodal lines for band 2

(b) Nodal lines for band 3

Figure 4.6: Nodal lines for $-2\,\%$ strained $a^0a^0c^+$ $SrNbO_3$. A tilt angle of 9° was set. Here, SOC was neglected.

To get a feeling for what effect TRS breaking has on the $a^0a^0c^+$ bands, I constrained the DFT solution to converge to a $20\,\%$ spin-polarization in z-direction of the Nb states. Here, SOC was included. This was done in similar fashion as in Reference [10]. In practice this might be

realized using a magnetic field or doping. In absence of TRS, the previously spin degenerate states are now split. In Figure 4.7, the 20 % spin polarized bands of $a^0a^0a^0$ and $a^0a^0c^+$ are shown. The lines correspond to Wannier interpolated bands, and the dots are DFT bands.

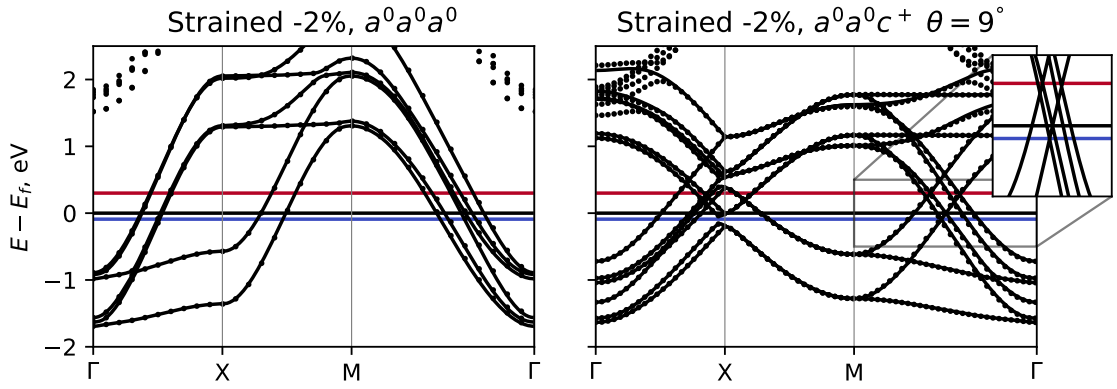

Figure 4.7: The effect of magnetization on the bands of $a^0a^0a^0$ and $a^0a^0c^+$ $SrNbO_3$. A spin polarization of 20 % is constrained onto the Nb states. Excellent agreement between Wannier bands (lines) and DFT bands (dots) is observed.

Using the Wannier fit shown in Figure 4.7, one can then efficiently evaluate the band structure and Berry curvatures on a dense grid. In Figure 4.8, the (Wannier interpolated) band structure of $a^0a^0c^+$ $SrNbO_3$ is shown including SOC and a 20 % spin-polarization. Here, focus is on the crossing between M and Γ. The Berry curvatures at different Fermi levels are also shown in Figure 4.8. Large Berry curvatures are observed at k-points and energies near the band crossings. These crossings are not present without the tilting, and there is therefore a connection between the octahedral distortions and the large Berry curvature signals.

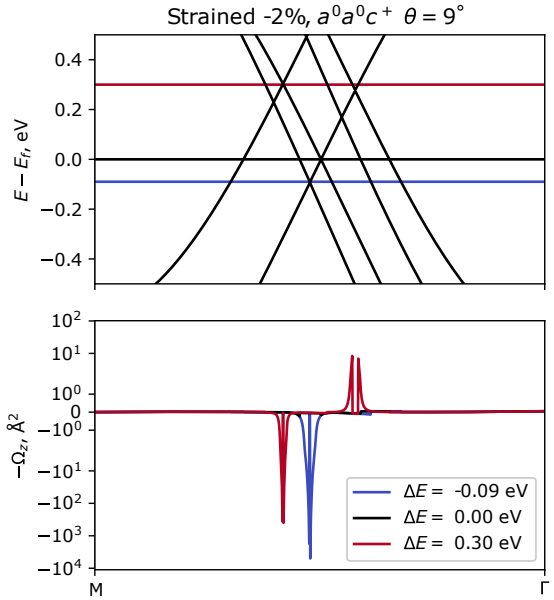

Figure 4.8: Wannier interpolated bands and Berry curvatures of $a^0a^0c^+$ $SrNbO_3$ without TRS. SOC is included and a 20 % spin-polarization in z-direction is constrained. The z-component of the Berry curvature is presented.

To illustrate the difference between $a^0a^0c^+$ and $a^0a^0a^0$ (i.e. untilted), I calculated the Berry curvatures on the $k_z = 0$ slice of the two structures. The results are shown in Figure 4.9. The left (right) column shows the results for $a^0a^0a^0$ ($a^0a^0c^+$). The untilted structure does exhibit non-zero Berry curvatures along the $\Gamma \rightarrow \mathrm{M}$ direction, similarly to ferromagnetic $SrRuO_3$. [63] The Berry curvature is almost unchanged when considering shifts in Fermi level, ΔE. The new crossings due to the band folding in $a^0a^0c^+$ give rise to Berry curvature at k-points previously absent of Berry curvatures. Below and above the Fermi level there are circular regions in the Berry curvatures, which is in agreement with the nodal lines observed in Figure 4.6. These findings illustrate how the octahedral tilting results in new band features that give rise to Berry phase and curvature related properties.

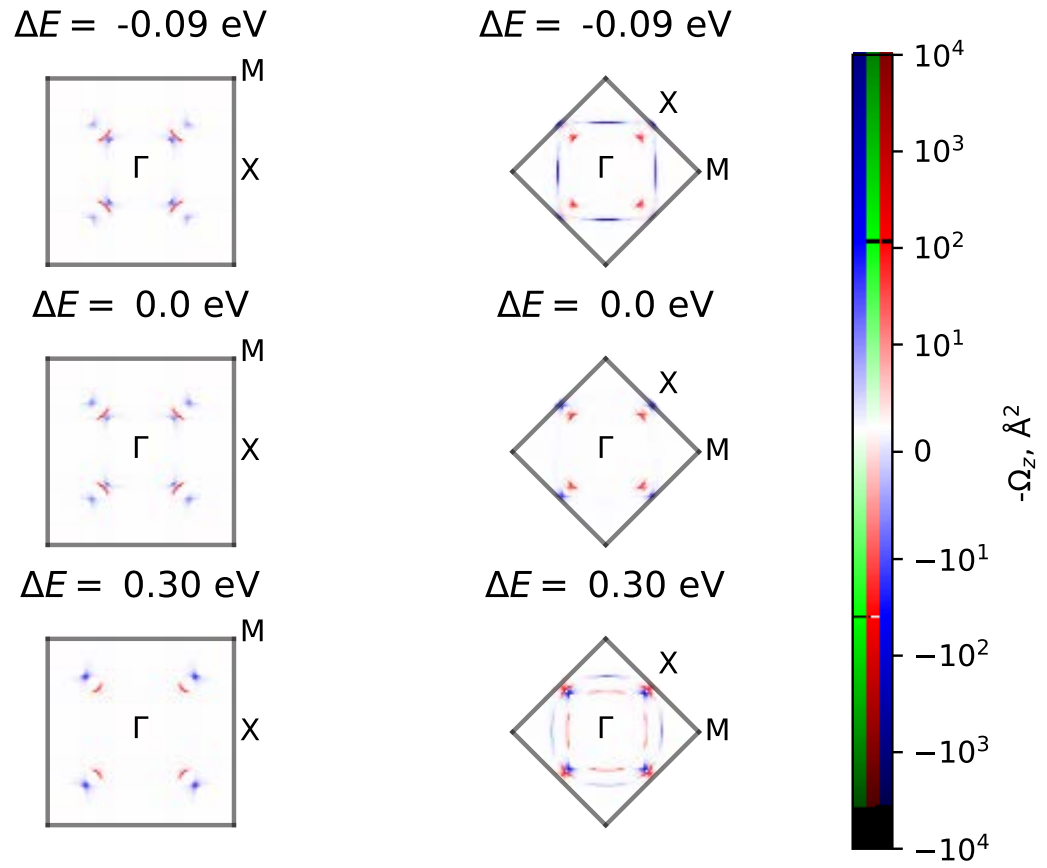

Figure 4.9: Berry curvatures in the $k_z = 0$ plane of $a^0a^0a^0$ ($a^0a^0c^+$) in left (right) columns. SOC is included and the spin polarization is constrained to 20 % in the z-direction on the Nb states.

4.5 Summary

The main takeaways from this chapter are that:

- Unfolded band structures *and* Fermi slices of octahedrally tilted $SrNbO_3$ can be used ease the comparison between different potential tilts
- Comparing DFT and ARPES bands indicates that $SrNbO_3$ exhibits the $a^0a^0c^+$ tilt
- The $a^0a^0c^+$ tilted $SrNbO_3$ exhibits Dirac nodal lines crossing the Fermi level
  - While some degeneracies are unstable against spin-orbit coupling, others are robust even with spin-orbit coupling
- Breaking of time reversal symmetry leads to large Berry curvatures in $a^0a^0c^+$

Chapter 5

Electron-oxygen vacancy scattering in conducting oxides

Materials are not perfect infinite lattices and in reality the crystals contain defects and disorder. Defects are separated into different groups depending on their dimensionality, namely point, line and planar defects. The different types of defects can be important for various material properties, and in some scenarios it is even impossible to separate the defects from the material behaviour. One such example is oxygen vacancies in oxides. [7] Oxygen vacancies are point defects, and like the name suggests, they are simply a missing oxygen ion from the crystal.

Low temperature electron transport is limited by defects, compared to lattice vibration (or phonon) limited transport in higher temperatures. At low temperatures, the phonons are frozen and only the static distortions, such as defects, remains. In this case, without defects, the electrons will flow unhindered in a perfect lattice. Defects will break the perfect periodicity of the ionic potentials, which causes the electrons to scatter and a resistance is formed. In this chapter I will present how oxygen vacancies scatter electrons in the conducting $SrNbO_3$. In related conducting oxides, such as $SrVO_3$ and Nb doped $SrTiO_3$, there is often a degradation in the electrical conductivity with decreased film thickness. [64, 65, 66]. While the understanding that electrons scatter at oxygen vacancies has existed for a long time, I have not found quantitative theoretical analysis of this phenomenon in the literature. I therefore wanted to see how strong the scattering is, but also if there are any differences between bulk and slabs. Perhaps the electrical degradation is partially explained by defects? $SrNbO_3$ is chosen here, since my previous DFT studies were deemed successful and good agreements was observed with ARPES. The study is based on DFT combined with non-equilibrium Green's function (NEGF). The combination of NEGF and DFT will be outlined in the following section. Then the findings are presented and discussed in the subsequent sections.

Note, that while the NEGF allows for studying transport under bias, I here limit the study to the zero-bias problem where the electrodes are in equilibrium.

This chapter is based on the manuscript titled "Influence of oxygen vacancies on charge and spin transport in $SrNbO_3$: A DFT-NEGF based study". The manuscript is appended in Section B.3. Note, that the part about transmission eigenchannels (Section 5.7) is currently not included in the manuscript.

5.1 Theory

DFT is extremely useful for studying the atomic and electronic structure of solids or molecules. However, studying solids requires periodic boundary conditions (PBCs) and molecules can be

modelled using finite domains or by applying PBC with sufficient vacuum surrounding the molecules. This causes a discrepancy between theory and transport experiments, since in reality the systems under study are *coupled* to electrodes, i.e., the systems are *open*. In this section I outline the framework called non-equilibrium Green's function (NEGF) that describes electron transport from an electrode through a central region and out on the other electrode. The two electrodes are separated and can therefore be at different chemical potentials and temperatures, which describes a non-equilibrium problem, such as a transport experiment.

First, the use of Green's functions will be motivated and some useful definitions will be made. I will then outline the combination of the technique with DFT. There are many great resources on the topic of (non-equilibrium) Green's functions, and this section is written based on the following References [67, 68, 69].

5.1.1 Motivating the use of Green's functions and some definitions

A time-independent electronic problem can be generally written as:

$$H(\vec{r})\phi_n(\vec{r}) = E_n\phi_n(\vec{r}) \tag{5.1}$$

Here, a real space representation is used. As an example, this could correspond to the non-interacting KS system or a more complex problem. If the Hamiltonian describes particles on an infinite lattice with translational symmetry, the Bloch's theorem can be applied. This greatly reduces the complexity of the problem and it is then sufficient to study one unit cell and the corresponding BZ. Furthermore, by expanding the wavefunctions, using a basis set, the problem turns into a matrix equation which efficiently can be solved using a computer.

However, what happens if the lattice contains a defect and the translational symmetry is lost? Of course, one could argue that by increasing the cell, to include the defect and "enough" pristine cells around it, the defects would be localised and a solution of this system would be informative. Nonetheless, if the solution relies on the periodicity of the supercells, this still does not enable studying of systems that are at different (local) equilibria separated in space. In other words, the supercell method is incompatible with systems with open boundary conditions. Therefore, to study transport problems another approach must be taken.

Generally, the Green's function (GF) is a solution to the differential equation:

$$[z - H(\vec{r})]G(\vec{r}, \vec{r}_1, z) = \delta(\vec{r} - \vec{r}_1), \tag{5.2}$$

here $z = E + i\delta$ is a complex number. Or in operator form:

$$[z - \hat{H}]\hat{G}(z) = \hat{1} \Rightarrow \hat{G}(z) = \frac{\hat{1}}{z - \hat{H}} \tag{5.3}$$

Furthermore, by multiplying with the unity operator $\hat{1} = \sum_n |\phi_n\rangle \langle\phi_n|$, where $|\phi_n\rangle$ forms a complete set:

$$\hat{G}(z) = \frac{\hat{1}}{z - \hat{H}} \sum_n |\phi_n\rangle \langle\phi_n| = \sum_n \frac{|\phi_n\rangle \langle\phi_n|}{z - E_n} \tag{5.4}$$

This form shows that the Green's function (GF) has poles at the eigenenergies of $\hat{H}$. Next, the retarded (advanced) GFs are defined as:

$$\hat{G}^R(E) = \lim_{\delta \to 0^+} \hat{G}(E + i\delta) \tag{5.5}$$

$$\hat{G}^A(E) = \lim_{\delta \to 0^+} \hat{G}(E - i\delta) \tag{5.6}$$

The advanced and retarded GF are related via the conjugate transpose (†) as $\hat{G}^A(E) = \hat{G}^{R\dagger}(E)$. Furthermore, as an example, the density operator $\hat{\rho}(E) = \delta(E - \hat{H})$ can be evaluated using the (retarded) GF. This can be achieved using the expression:

$$\lim_{\delta \to 0^+} -\frac{1}{\pi} \operatorname{Im} \frac{1}{x + i\delta} = \delta(x) \tag{5.7}$$

Finally the density operator can be written as:

$$\hat{\rho}(E) = -\frac{1}{\pi} \operatorname{Im} \hat{G}^R(E), \tag{5.8}$$

or in the real space representation:

$$\rho(\vec{r}, E) = -\frac{1}{\pi} \operatorname{Im} G^R(\vec{r}, \vec{r}, E), \tag{5.9}$$

which can give information about the total density of states, $D(E)$, as:

$$D(E) = \int d\vec{r} \rho(\vec{r}, E) = -\int d\vec{r} \frac{1}{\pi} \operatorname{Im} G^R(\vec{r}, \vec{r}, E) \tag{5.10}$$

So far the GF contains information about the solution to the (electronic) eigenvalue problem and related properties. The properties could, however, simply be studied be examining the eigenfunctions, $\phi_n(\vec{r})$, directly without the trouble of introducing GFs. The benefit of GFs is the ability to study perturbed systems, $H = H_0 + H_1$, by expressing the GF of the total system with the unperturbed GF G_0 and perturbed Hamiltonian H_1.

Let's now imagine a central region with some Hamiltonian $\bar{H}_C$ expanded in a localised basis set. The $\bar{...}$ denotes that this is a matrix, where the elements are over the different sites. This central region is now connected to a semi-infinite left (right) electrode described by the Hamiltonian $\bar{H}_L$ ($\bar{H}_R$) via the coupling matrix $\bar{V}_{LC}$ ($\bar{V}_{RC}$). Then the Hamiltonian of the total system can be written as:

$$\bar{H} = \begin{bmatrix} \bar{H}_L & \bar{V}_{LC} & 0 \\ \bar{V}_{CL} & \bar{H}_C & \bar{V}_{CR} \\ 0 & \bar{V}_{RC} & \bar{H}_R \end{bmatrix}, \tag{5.11}$$

with $\bar{V}_{CL} = \bar{V}_{LC}^\dagger$. Note, that since the electrodes are semi-infinite, the matrix is in fact infinitely large. In any case, let's formally write down the matrix equation defining the (retarded) Green's function:

$$\begin{bmatrix} (E+i\delta)\bar{I} - \bar{H}_L & -\bar{V}_{LC} & 0 \\ -\bar{V}_{CL} & (E+i\delta)\bar{I} - \bar{H}_C & -\bar{V}_{CR} \\ 0 & -\bar{V}_{RC} & (E+i\delta)\bar{I} - \bar{H}_R \end{bmatrix} \begin{bmatrix} \bar{G}_L & \bar{G}_{LC} & 0 \\ \bar{G}_{CL} & \bar{G}_C & \bar{G}_{CR} \\ 0 & \bar{G}_{RC} & \bar{G}_R \end{bmatrix} = \bar{I} \tag{5.12}$$

From which one can deduce the following matrix equation for the retarded GF of the central region:

$$((E + i\delta)\bar{I} - \bar{H}_C - \bar{\Sigma}^R)\bar{G}_C^R = \bar{I}, \tag{5.13}$$

where the (total) electrode self-energy is introduced as:

$$\bar{\Sigma}^R = \bar{V}_{CL}((E + i\delta)\bar{I} - \bar{H}_L)^{-1}\bar{V}_{LC} + \bar{V}_{CR}((E + i\delta)\bar{I} - \bar{H}_R)^{-1}\bar{V}_{RC} \tag{5.14}$$

$$\bar{\Sigma}^R = \bar{\Sigma}_L^R + \bar{\Sigma}_R^R, \tag{5.15}$$

where the self-energy due to electrode e can be expressed using the electrode GF as:

$$\bar{\Sigma}_e^R = \bar{V}_{Ce}\bar{G}_e^R\bar{V}_{eC} \tag{5.16}$$

To summarize, by separating a large system into subsystems it is possible to calculate the GF of the central region *only* using information about the central region, the coupling between the central region and the electrodes, and the isolated electrodes. Of course, this is only true if the interactions are local. However, the GFs of the semi-infinite electrodes can not simply be found by inversion (remember, they are semi-infinite), but must be calculated using other approaches. The electrode Green's function can be calculated recursively as described in Reference [70].

Finally, in transport problems a useful property is the transmission function:

$$T(E) = \mathrm{Tr}\{\bar{\Gamma}_L(E)\bar{G}^R(E)\bar{\Gamma}_R(E)\bar{G}^A(E)\} \tag{5.17}$$

Above, the broadening matrix for electrode e was introduced:

$$\bar{\Gamma}_e(E) = i(\bar{\Sigma}_e^R - \bar{\Sigma}_e^A) = -2\,\mathrm{Im}\,\bar{\Sigma}_e^R \tag{5.18}$$

Furthermore, in the low temperature limit the transmission function is related to the conductance:

$$G = \frac{e^2}{h}T(E_f) \tag{5.19}$$

A final useful object is the spectral function:

$$\bar{A}(E) = i(\bar{G}^R - \bar{G}^A) = -2\,\mathrm{Im}\,\bar{G}^R, \tag{5.20}$$

which diagonal is proportional to the (local) density of states.

5.1.2 Coupling density functional theory to non-equilibrium Green's function

Having realised that the NEGF framework is useful for studying transport problems, one could resort to a TB description of the electrodes and central region, then evaluate the transport through the system as given by the NEGF method. However, then the question of how to parametrize the Hamiltonians arises. This can be solved by combining DFT and NEGF.[71] The electronic structure is described at a KS-DFT level and then the open boundary conditions are fulfilled via the NEGF method.

The first step of a DFT-NEGF calculation is to calculate the electronic structure of the electrodes at the requested chemical potentials and temperatures. This is done as normal DFT bulk calculations. Then, using these results the self-energies of the electrodes can be evaluated by recursively evaluating the GF of the semi-infinite electrodes. [70] Now, the self-consistent calculation of the device region can be initiated. The charge density is guessed, often using atomic orbitals. Using the guess, the effective KS potential is calculated and the resulting Hamiltonian is diagonalized. Combining the Hamiltonian of the device region with the self-energies of the electrodes, one can calculate the GF of the device region. From the GF (or spectral function), the charge density can now be evaluated. Then, one uses this charge density to evaluate the effective KS potential, and so on. This loop is performed until the change in charge density is below a certain threshold.

5.2 Practicalities of the NEGF calculations

The transport problem was studied using the DFT-NEGF method implemented in Siesta [72] and TranSiesta [71, 73]. Siesta relies on basis sets inspired from atomic orbitals, these are small sets of localized orbitals which makes for efficient numerical techniques. However, compared to plane-wave sets more care has to be used to capture the correct physics. Figure 5.1 shows a comparison between the optimized Siesta $SrNbO_3$ bands and plane-wave $SrNbO_3$ bands. It was important to include triple-zeta polarized functions for the oxygen ions, for the niobium and

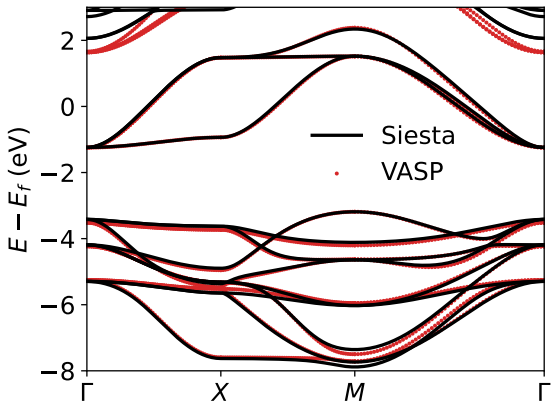

Figure 5.1: Benchmark of the $SrNbO_3$ band structure predicted using Siesta and plane-wave bands from VASP. Note, the valence bands from VASP where shifted to fit the Siesta bands.

strontium ions double-zeta polarized was enough. Excellent agreement was found, which gave me confidence in the following calculations. Oxygen vacancies were modelled using so-called ghost atoms that has no charge but a oxygen basis set.

In all calculations presented here, the PBE [74] functional was used. Furthermore, 12 k-points per 5 atom unit cell was used in the directions with periodic boundary conditions in the self-consistent calculations. This was increased to 60 k-points when the transmission function was evaluated. The Python package SISL [75] was used for post-processing of the data from Siesta and TranSiesta.

Since the perturbation in the central device region (see Figure 5.2) must be localized to the central region, pristine layers of $SrNbO_3$ were extended to the left and right of the defect. This makes the coupling between the leftmost (rightmost) layer in the device region and the left (right) electrode *pristine*. The large amount of electrons present in $SrNbO_3$ makes the screening very efficient and therefore only a small number of layers was required as shown in Figure 5.2.

In the calculations of thin $SrNbO_3$, I used asymmetric slabs and therefore applied a dipole correction to reduce the artificial electrostatic interaction between the two sides of the slabs. Furthermore, I here introduced 10 Å of vacuum to separate the layers.

Finally, while NEGF allows for simulations of biased systems, I here only present results from unbiased calculations. Therefore, the predicted transport conductances are for zero-bias conditions.

5.3 Electron transport in bulk $SrNbO_3$

Electron transport in bulk $SrNbO_3$ was first considered. The lattice parameter obtained in Chapter 3 was set. Due to the symmetry of the bulk transport problem, there are two unique oxygen vacancy positions. The vacancy can be placed between two Nb ions in the transport direction, or between two Nb ions perpendicular to the transport direction. The transport geometry of 2 u.c. thick $SrNbO_3$ is sketched in Figure 5.2. The bulk geometry is similar, but in this case there is no vacuum and an interface area of 3×3 u.c. is used. Ideally, the interface would be infinitely big, so that there is no interaction between the vacancy and its images due to the PBC. I found that the difference between a vacancy in a 3×3 u.c. and 4×4 u.c. interface is negligible compared to the additional computational cost. This indicates that the perturbation of the oxygen vacancy is quite localized.

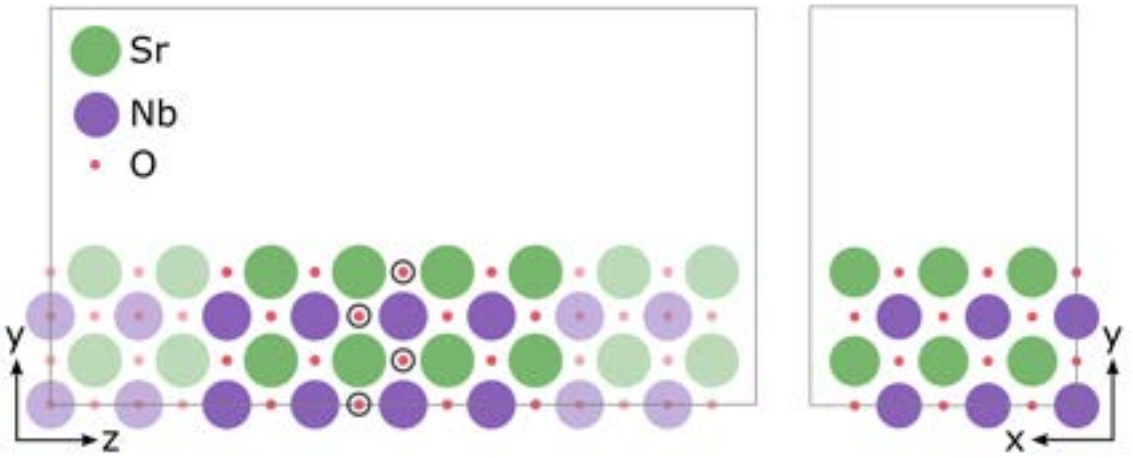

Figure 5.2: Unit cell used for the transport studies. Here the 2 u.c. slab of $SrNbO_3$ is shown. Transport direction is in z, and PBC is applied in x and y-directions. The semi-transparent regions are the electrodes and the opaque region is the central region containing the defect. The black circles correspond to potential vacancy positions (only one location is sampled at a time). The empty region above the slab represents vacuum. To separate the vacancy from its images, 3 u.c. are repeated in the x-direction.

In Figure 5.3 the electrical conductance normalized with the interface area is shown for bulk $SrNbO_3$. The normalized conductance is shown as a function of energy relative to the Fermi level. It is important to remember that electron transport is dominated by the states around the Fermi level. However, I here show a large energy range since the data can still be informative, e.g., in doped or gated systems (assuming rigid bands). As expected, pristine bulk $SrNbO_3$ is conducting, and introducing a oxygen vacancy clearly reduces the conductance. Or alternatively, the oxygen vacancy leads to a resistance for the electrons. The resistance is somewhat larger when the vacancy is placed in the NbO_2 layer compared to SrO layer. This is likely due to the fact that the conduction band is formed by Nb 4d and O 2p states in $SrNbO_3$, and oxygen acts as a bridge between the niobium ions. Therefore, removing an O ion that sits between two Nb ions in the transport direction is expected to cause a large disruption in the transport.

Turning on collinear spin polarization, it is also seen that the two spin channels have different transport properties. Pristine $SrNbO_3$ is non-magnetic and the spin splitting emerges due the O vacancy. This indicates that unpolarized electrons can be polarized when interacting with O vacancies in $SrNbO_3$. The difference between the two spin channels is, however, quite small.

Note that, while good agreement was found between Siesta and plane-wave codes, which in turn agreed well with ARPES data, the oxygen vacancies might complicate the chemistry and the accuracy of the GGA approximation might be questionable. For a related conducting oxide, it was observed that the chemistry of the defect states can be challenging to model using simple GGA functionals. [76] In any case, I here assume that the results obtained using the PBE functional are informative, although discrepancies with more complex functionals (and reality) are possible.

5.4 From bulk to slabs

Next, I moved to ultra thin slabs of pristine $SrNbO_3$. It is expected that forming finite slabs will create discrete states due to the confinement in the out-of-plane direction, while the

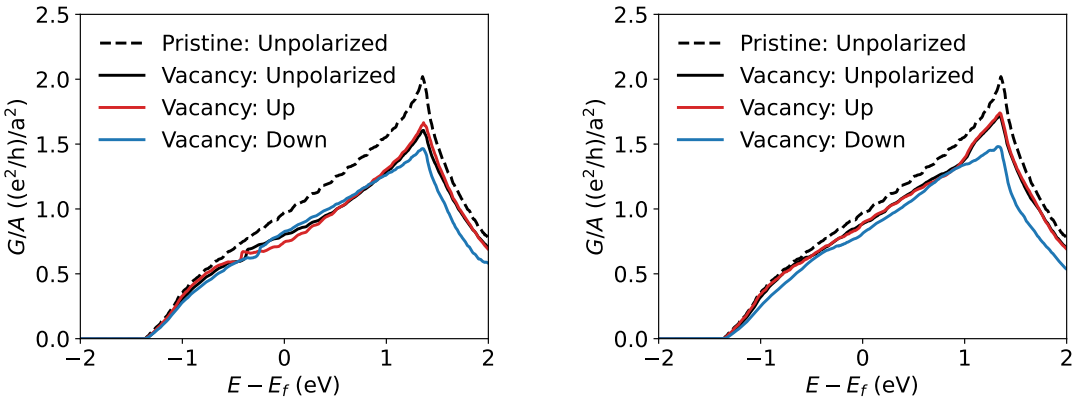

(a) O vacancy in NbO_2 layer

(b) O vacancy in SrO layer

Figure 5.3: Conductance per unit cell area for different configurations of bulk $SrNbO_3$.

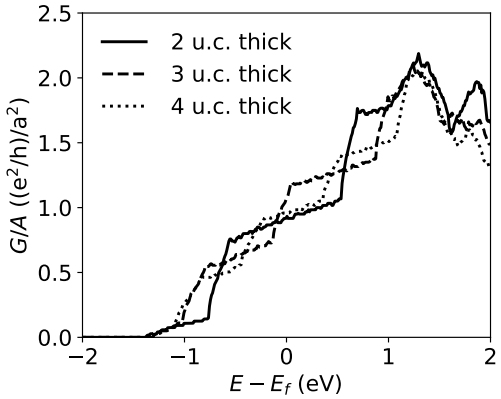

Figure 5.4: Normalized conductance of ultra thin $SrNbO_3$.

periodicity, and hence dispersion, in the in-plane directions remains. Furthermore, as the thickness increases the bulk behaviour should emerge, and the discrete states should form a continuum. This trend is observed in the calculations, see Figure 5.4. The dispersion due to the periodicity in-plane is seen by the "slope" of the steps.

5.5 Impact of relaxation on transport

The influence of ionic relaxation on the electronic transport in 2 u.c. thick $SrNbO_3$ was investigated. This was done in steps: First, the pristine slab was relaxed and compared with the unrelaxed result. Then, an oxygen vacancy was introduced in the unrelaxed slab *and* the relaxed slab. Finally, starting from the relaxed slab an O vacancy was introduced to the structure, then the ions within a radius of $1a$ from the O vacancy was relaxed (named "Fully relaxed" here). The bulk lattice constant is denoted a. Throughout these calculations, the lattice parameter was kept fixed to the bulk value. The results are presented in Figure 5.5. Here, I focus on one oxygen vacancy location, namely the NbO_2 terminated layer. The other locations showed comparable magnitudes in the changes. The impact of ionic relaxation one the conductance of the pristine 2 u.c. slab is minor, especially near the Fermi level. Furthermore, the similarities between the conductances in different levels of relaxed slabs with vacancies are large. There is a minor influence on the conductance near the Fermi level in the defective systems, e.g., the small "dip" or "peak" is modified. Perhaps the scattering is (very weakly) sensitive to the exact shape of defect state, but these are very minor changes and

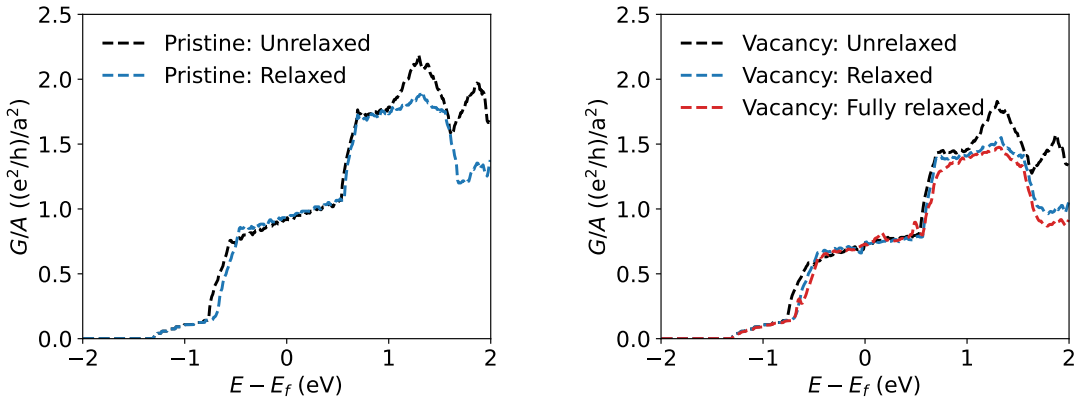

(a) Pristine slab

(b) Slab with O vac.

Figure 5.5: Influence of ionic relaxation on the electronic conductance in 2 u.c. $SrNbO_3$ slab. The vacancy is introduced at the NbO_2 termination layer.

are considered insignificant here. At the GGA level of theory, the role of relaxation is deemed minor and therefore I do not relax the thicker films. I do however present the results of relaxed structures in the 2 u.c. slab in the following sections, since those are available. For thicker films, I present the unrelaxed results.

5.6 Electron-oxygen vacancy scattering in thin $SrNbO_3$

Having set the stage in previous sections I now analyse the electronic transport in defective slabs of $SrNbO_3$. There are 2 unique oxygen vacancy locations per unit cell thickness (see Figure 5.2). For simplicity, I first focus on the 2 u.c. slab and present the energy resolved conductances for each unique configuration. Later I summarize the findings from 3 and 4 u.c. thick $SrNbO_3$, but then only focus on conductances at the Fermi level.

In Figure 5.6, the normalized conductance as a function of energy is shown for 2 u.c. $SrNbO_3$. All four unique oxygen vacancy locations are sampled. By focusing on the spin unpolarized results first (i.e. black lines), it is clear that the location of the O vacancy has a big influence on the resistance. When the vacancy is placed in a NbO_2 layer, there is a large decrease in conductance, however, if the vacancy is located in a SrO layer the influence is vanishingly small near the Fermi level. It is interesting that the resistance due to a O vacancy in a SrO layer is lower in the 2 u.c. slab, compared to the bulk counterpart. This indicates that the current flows largely in the NbO_2 layers in the ultra thin film.

Moving on to the spin polarized results in Figure 5.6. The relative importance of the different layers remains. However, in general, the reduction in conductance is larger compared to the unpolarized cases at the Fermi level. Compared to bulk, the difference between the two spin channels is larger for the 2 u.c. slab, especially when the O vacancy is placed in a NbO_2 layer. This is definitely noteworthy, ultra thin $SrNbO_3$ displays larger variations in the impact of the oxygen vacancies, compared to bulk counterparts. Furthermore, the spin degree of freedom increases the resistance due to the oxygen vacancy, even more so in slab $SrNbO_3$, compared to bulk.

Having examined the conductances of 2 u.c. thick $SrNbO_3$, I then analysed the *scattering cross sections* of 2, 3, and 4 u.c. thick $SrNbO_3$. The scattering cross section is defined as $A(T_0 - T_d)/T_0$, where A is the interface area of the defective system, T_0 is the pristine transmission, and T_d is the transmission of the defective system. [77, 78] It is a measure of how

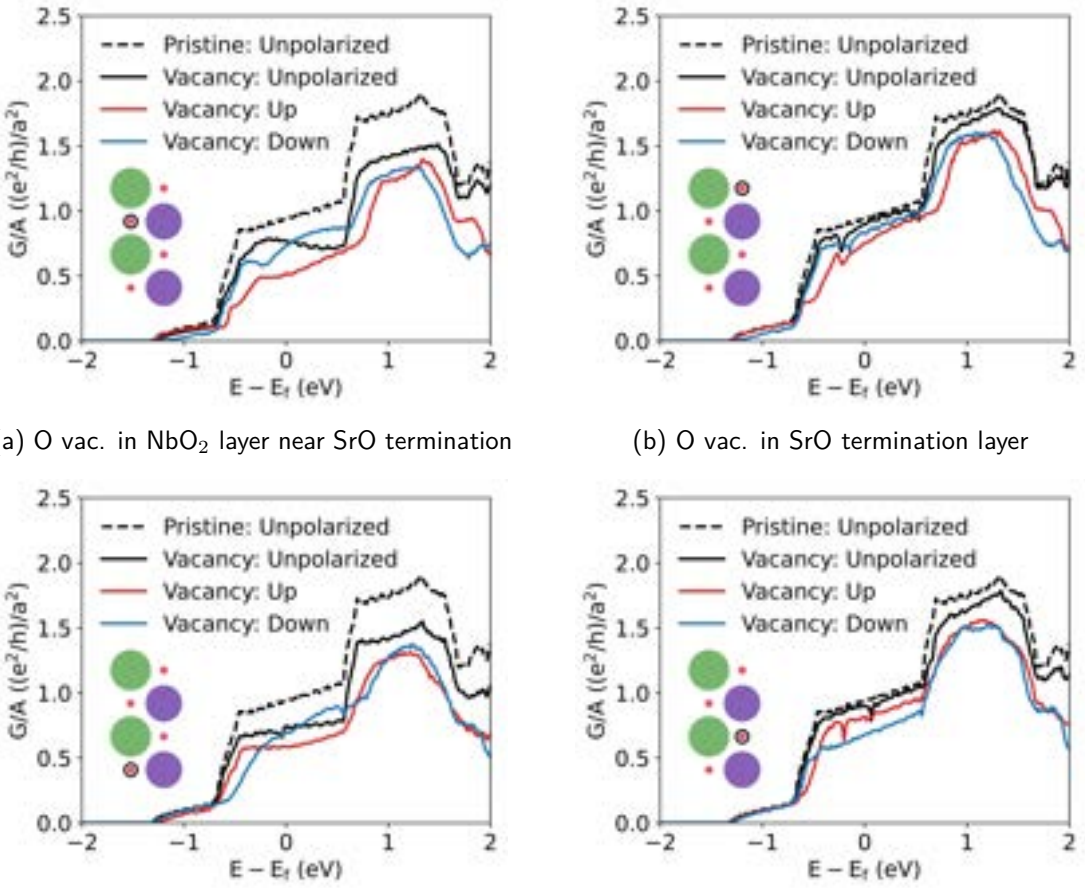

(a) O vac. in NbO_2 layer near SrO termination

(b) O vac. in SrO termination layer

(c) O vac. in NbO_2 termination layer

(d) O vac. in SrO layer near NbO_2 termination

Figure 5.6: Conductance per unit cell area for different configurations of 2 u.c. thick $SrNbO_3$. Both spin polarized and unpolarized results are shown. The pristine calculation is always without spin polarization. The black circles denotes which oxygen ion is removed.

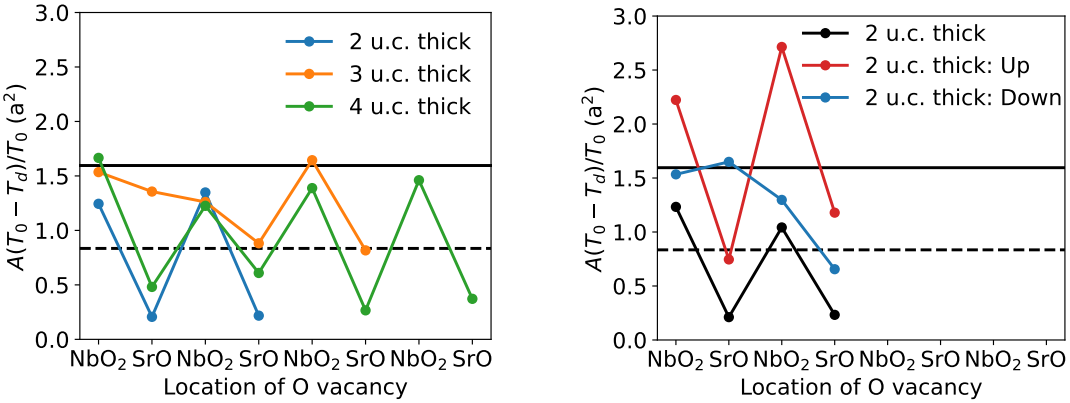

(a) Unpolarized cross sections

(b) Effect of spin on cross sections

Figure 5.7: Scattering cross sections due to O vacancies in units of lattice constant squared at the Fermi level. Unpolarized (polarized) results are shown to the left (right). The solid (dashed) horizontal line represent the cross section for vacancy in NbO_2 (SrO) layer in bulk. The bulk results are all unpolarized for simplicity.

much cross sectional area is lost due to the defect, and a value of $1a^2$, where a is the lattice parameter, means that one unit cell area is effectively lost. This is useful for understanding the scattering mechanism in real space, e.g., by comparing the scattering cross section with the geometrical cross section of a potential device. The cross sections at the Fermi levels are presented in Figure 5.7. There is a clear layer dependency, as seen previously, and the scattering cross sections are larger when the oxygen vacancy is placed in the NbO_2 layers compared to SrO layers (except for one outlier in the 3 u.c. thick film). Overall, the scattering cross section of one O vacancy is ca. $1.5a^2$ when located in a NbO_2 layer. In this case bulk and slab results are quite similar. When the vacancy is placed in a SrO layer, the scattering cross section is ca. $0.8a^2$ in bulk, while it is noticeably lower in the 2 u.c. and 4 u.c. thick films. Overall, these values are reasonable, and they indicate that oxygen vacancies essentially ruins the electronic transport in the unit cell they are located in.

Next, the spin resolved scattering cross sections are analysed in Figure 5.7b. Here only results from 2 u.c. $SrNbO_3$ are available due to the computational complexity. A large systematic increase in the scattering cross sections is observed when spin is introduced. Oxygen vacancies placed in a NbO_2 layer still leads to the strongest scattering. Increases with factors of ca. 2 is observed between spin polarized and unpolarized scattering cross sections. This is a surprising result, since in bulk the effect of spin was very minor. Overall, it seems that the scattering mechanism becomes more rich in ultra thin $SrNbO_3$ compared to bulk $SrNbO_3$, and that the spin degree of freedom becomes more influential in slab $SrNbO_3$.

5.7 Real space transmission eigenchannels

The total transmissions (or conductances) calculated previously originate from individual transmission eigenchannels that contribute to the transmission as $T(E) = \sum_n T_n(E)$. [79] The eigenchannels, $|\Psi_n\rangle$, describe how incoming Bloch waves from the electrodes scatters and interacts with the central device region. Furthermore, the corresponding eigenvalues quantify the transmission of the eigenchannel, i.e., T_n.

In this section, the eigenchannels are analyzed in real space. I only present the eigenchannels that originate from the left electrode and the transport is always in z-direction. Moreover,

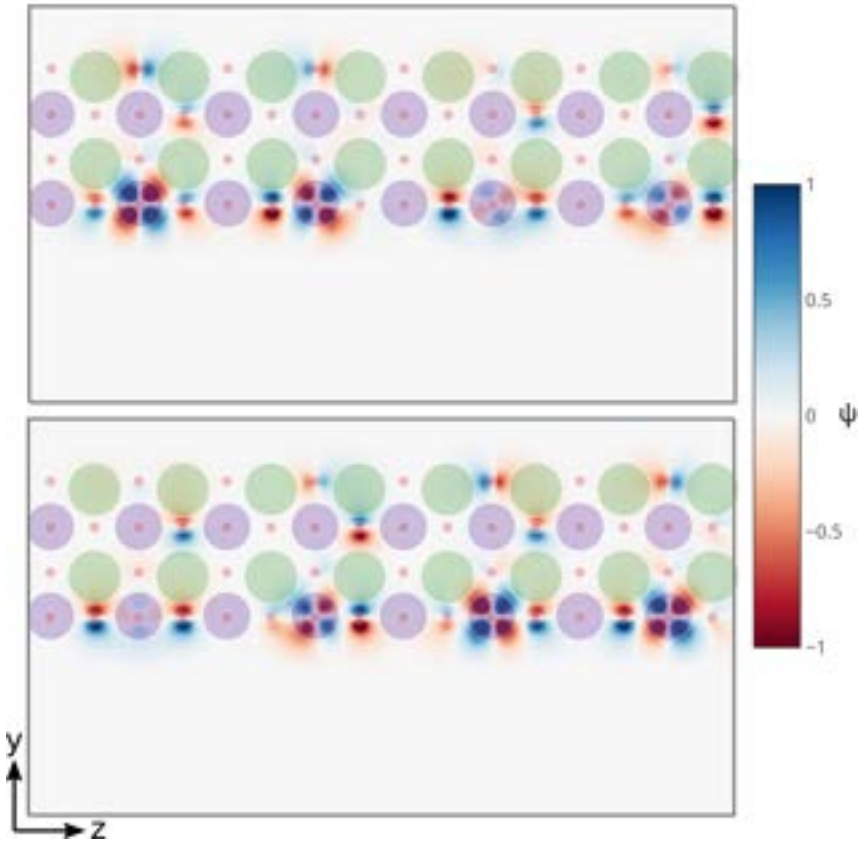

Figure 5.8: Transmission channel in pristine 2 u.c. $SrNbO_3$ visualized in yz-plane cutting through the Nb ions (purple circles). The upper (lower) figure shows the real (imaginary) part of the wavefunction, $\Psi(\vec{r})$. The red circles denotes oxygen ions and green circles denotes strontium.

I focus on the transport at the Fermi level with $k_x = k_y = 0$, i.e., the Γ-point. Finally, there can be multiple eigenchannels that contribute to the transport, and I here only visualize "representative" eigenchannels with substantial transmission eigenvalues. This is not intended to be quantitative, but rather aid with the understanding of how the electrons are transported in these systems.

In Figure 5.8 and Figure 5.9 two eigenchannels for pristine 2 u.c. $SrNbO_3$ are visualized. For these systems the presented channels have $T_n = 1$, i.e., they are perfect transmission channels. Figure 5.8 shows an eigenchannel with large magnitude in a yz-plane cutting through the Nb ions. The real and imaginary parts of the wavefunction is visualized in separate subfigures. The symmetry of the Nb t_{2g} and O $2p$ states are clearly observed (compare with Fig. 3.1). Moreover, the wavefunction is large in the whole domain in the z-direction, which indicates that this eigenchannel indeed has a high transmission and is conductive. Figure 5.9 tells a similar story, but here an eigenchannel with large magnitude in the xz-plane cutting through the NbO_2 termination layer is shown. Now the wavefunction has t_{2g} character in the xz-plane, i.e., perpendicular to the yz-plane. Moreover, the wavefunction is spread out over the whole domain and there is no sign of scattering as expected. From Figure 5.8 and Figure 5.9, the contribution from 2 out of 3 t_{2g} states are observed. This is reasonable, since the last t_{2g} state lives to majority in the xy-planes which is unlikely to lead to any significant transport in the z-direction. It is also interesting to note that to a large extent, the wavefunctions live on the NbO_2 termination layer.

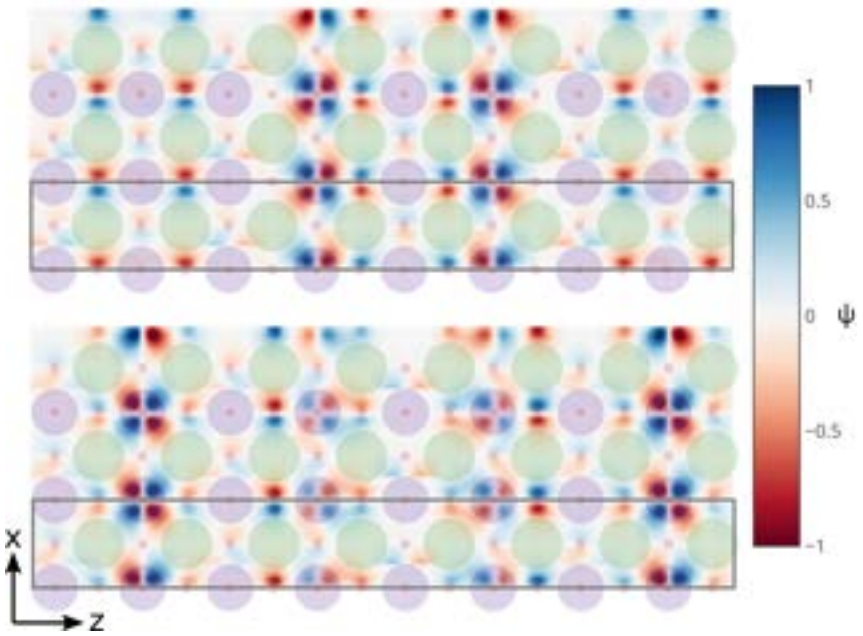

Figure 5.9: Transmission channel in pristine 2 u.c. $SrNbO_3$ visualized in xz-plane cutting through the Nb ions at NbO_2 terminated layer. The notations are the same as in Figure 5.8. The grey box is the computational unit cell, which here is repeated in x-direction for visualization purposes.

Next, selected transmission eigenchannels of 2 u.c. $SrNbO_3$ with oxygen vacancies are presented. Only the real part is shown here. In Figure 5.10, an eigenchannel is shown for 2 u.c. $SrNbO_3$ with O vacancy in NbO_2 termination layer. This eigenchannel has a transmission of ca. 0.79. In the side view (i.e. yz-plane cutting through the oxygen vacancy), the real part of the wavefunction to the left of the vacancy looks quite similar to the eigenchannel in the pristine system (Fig. 5.8). Moreover, in the xz-plane cutting through the oxygen vacancy, it is seen that the channel is concentrated to a line (i.e., the yz-plane through the vacancy). In contrast to the pristine system, here the wavefunction is strongly attenuated to the right of the defect. In other words, the incoming waves from left are scattered at the defect, thereby reducing the transmission of electrons from left to right. This is expected from the total transmission presented in Figure 5.6c, but now it is seen in real space.

A transmission eigenchannel in 2 u.c. $SrNbO_3$ with an oxygen vacancy in the SrO termination layer is shown in Figure 5.11. For this system, the eigenchannels all have large transmissions. The wavefunction extends out through the whole domain and there are no signs of scattering. There is, however, is a minor intensity centered around the oxygen vacancy seen in the xz-plane cutting through the vacancy. This is complete agreement what was found in Figure 5.6b, i.e., the scattering on oxygen vacancies in the SrO termination layer is very weak.

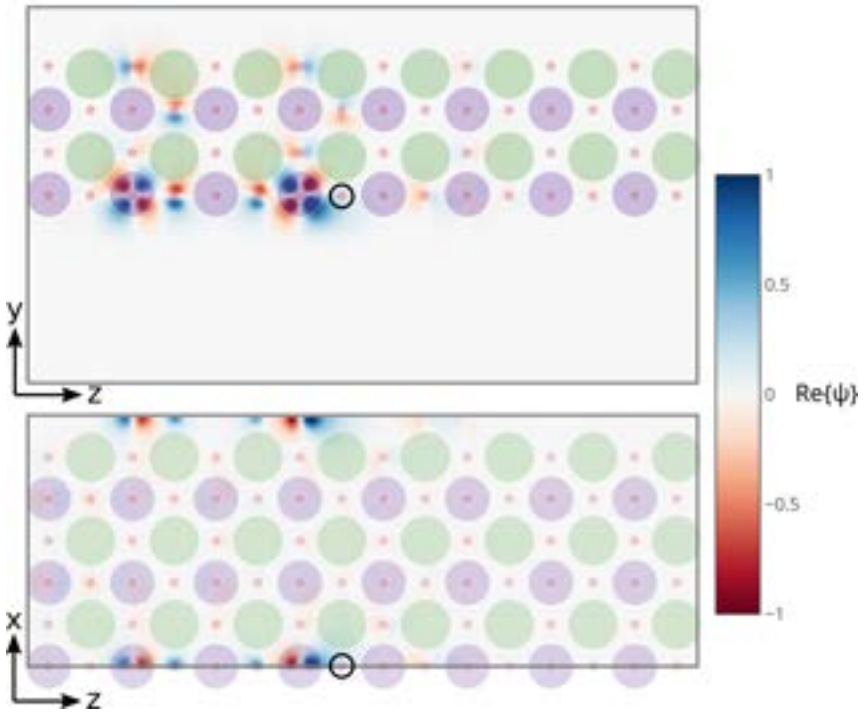

Figure 5.10: Transmission eigenchannel ($T_n \approx 0.79$) at Fermi level for 2 u.c. $SrNbO_3$ with O vacancy in the NbO_2 termination layer. The circle marks the vacancy. Both the yz-plane and xz-plane goes through the vacancy. The real part of the wavefunction is shown. This eigenchannel represents one of the channels that results in the total transmission seen in Fig 5.6c.

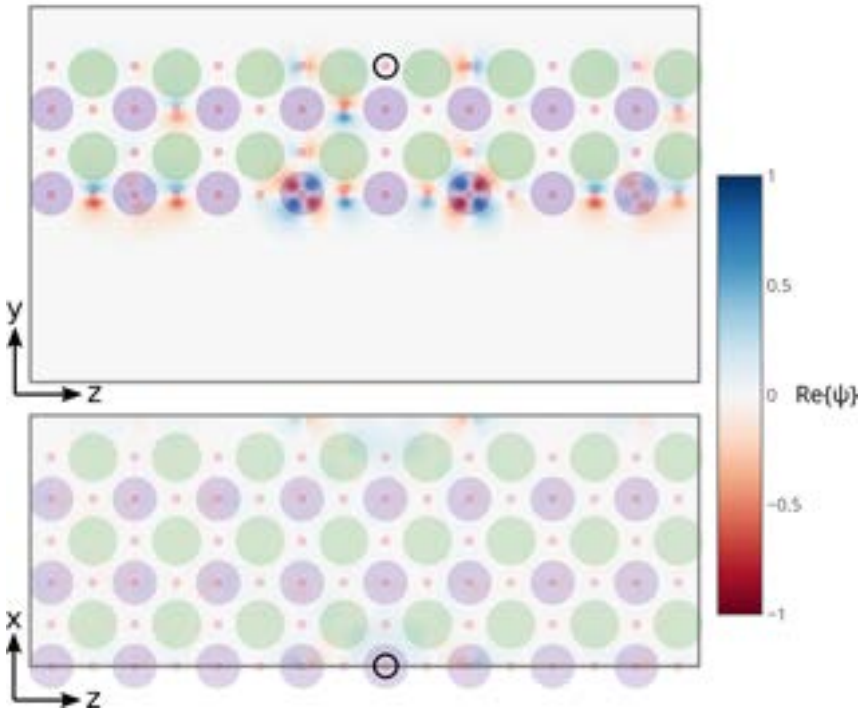

Figure 5.11: Transmission eigenchannel ($T_n \approx 0.99$) at Fermi level for 2 u.c. $SrNbO_3$ with O vacancy in the SrO termination layer. The circle marks the vacancy. Both the yz-plane and xz-plane goes through the vacancy. The real part of the wavefunction is shown. This eigenchannel represents one of the channels that results in the total transmission seen in Fig 5.6b.

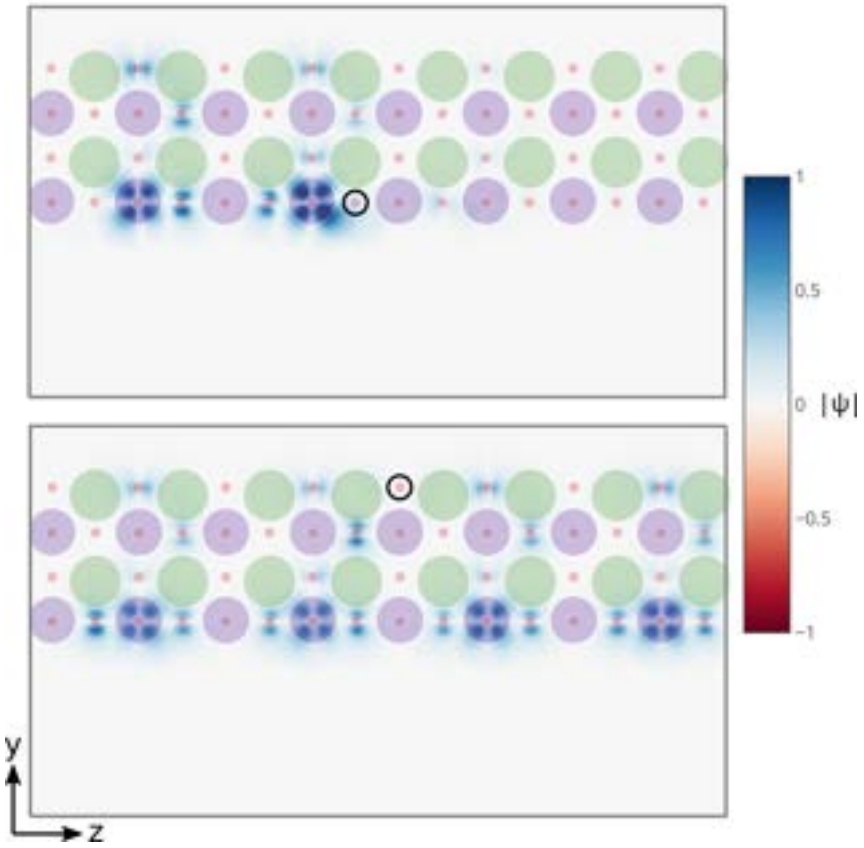

Figure 5.12: Comparison of the magnitude of the wavefunctions from Figure 5.10 and Figure 5.11. The upper figure shows an eigenchannel ($T_n \approx 0.79$) when the O vacancy is in the NbO_2 termination layer. The lower figure shows an eigenchannel ($T_n \approx 0.99$) when the O vacancy is placed in the SrO termination layer.

To further illustrate how the wavefunction decays to the right of the oxygen vacancies, the absolute value of the wavefunctions in Figure 5.10 and Figure 5.11 are visualized together in Figure 5.12. The upper figure shows an eigenchannel with $T_n \approx 0.79$ when the O vacancy is placed in the NbO_2 termination layer (i.e. eigenchannel from Figure 5.10). In the bottom figure, a highly conducting eigenchannel with $T_n \approx 0.99$ when the O vacancy is placed in SrO termination layer is shown (i.e. eigenchannel in Figure 5.11). The figures clearly show how the eigenchannel with lower tranmission decays to the right of the vacancy, while the highly conductive channel has a large magnitude to the right of the vacancy. In both cases, the NbO_2 termination layer shows the largest values of the wavefunction.

In summary, it is found that the transmission eigenchannels of 2 u.c. $SrNbO_3$ have the symmetries of the Nb t_{2g} and O $2p$ states as expected from the conduction band of $SrNbO_3$. Furthermore, the eigenchannels have large values near the NbO_2 termination layer, compared to the other layers. Introducing an oxygen vacancy, causes the electrons to scatter, which leads to a smaller wavefunction to the right of the defect (when left-to-right transport is considered), this was most clearly seen when the oxygen vacancy was placed in the NbO_2 termination layer. The scattering leads to a reduction in the channel resolved transmission, $T_n(E)$, which in the end results in a lower transmission $T(E) = \sum_n T_n(E)$ and conductance $G(E) = \frac{e^2}{h} T(E)$.

5.8 Summary

Having investigated the scattering of electrons on oxygen vacancies in $SrNbO_3$ the key points can be summarized:

- Oxygen vacancies scatter electrons and reduces the conductance of $SrNbO_3$
- Due to confinement, slabs show steps in the energy resolved conductance
- In slabs, the impact of the vacancy location increases. A vacancy in a NbO_2 layer scatters electrons substantially stronger than a vacancy in a SrO layer
- While bulk $SrNbO_3$ shows a rather small difference between the spin channels, 2 u.c. thick $SrNbO_3$ shows a noticeable spin filtering
- The scattering cross sections increase when the spin degree of freedom is included
- Typical scattering cross sections were below ca $1.5a^2$ without spin, with spin polarization values above $2.5a^2$ were observed
- Transmission eigenchannels in $SrNbO_3$ have clear Nb $4d$ t_{2g} and O $2p$ characters
- In 2 u.c. $SrNbO_3$, the eigenchannels are attenuated by the oxygen vacancies, especially when placed in NbO_2 layers in agreement with the total transmissions

Chapter 6

Non-diffusive phonon transport in Si

Silicon is used extensively in semiconductor industries, e.g., to create transistors and solar cells. The abundancy combined with the Czochralski process enables for industrial scale manufacturing of affordable high quality semiconducting devices. Furthermore, the electrical, mechanical, and thermal properties of intrinsic or doped silicon is hard to beat. In crystalline semiconductors, like silicon, the lattice vibrations or phonons conduct the majority of the heat. In silicon, the phonons have very long mean free paths (MFPs) and group velocities, resulting in a very high thermal conductivity. [80, 81] The long MFPs of the phonons makes it very relevant to ask what happens if the system size is of the length scale as the MFPs or even smaller? Precisely this question was asked and partially answered in Gang Chen's paper from 1996. [12] By solving the more general Boltzmann transport equation (BTE), compared to solving Fourier´s law of conduction, he showed that the thermal transport is reduced in the vicinity of a small heat source. Here, small or big is always relative to the average length between the phonon interactions, i.e., the MFP. Furthermore, the findings in Reference [12] suggested that the temperature rise of nanoscopic heaters will be underestimated by Fourier's law of conduction, due to the overestimation of the thermal transport. While the analytical solution in Reference [12] is relatively simple, it inspired a lot of research in the field of nanoscale thermal transport.

In this chapter, I will outline how phonon properties can be extracted from DFT and how to use said properties to calculate the temperature rise from a small heater by solving the BTE. Results of doped silicon will be presented and comparisons will be made against diffusive models. Finally, the predictions will be compared to experimental thermal measurements of doped silicon at the microscale. I want to emphasize that, while silicon phonon transport has been studied extensively previously [80, 81, 82, 83], I here expand the findings to doped silicon and also connect the predictions to an experimental technique.

This chapter is based on the manuscript "Observation of diffusive-to-ballistic phonon transport in boron doped silicon". The manuscript is appended in Section B.4. The experiments were conducted by Neetu Lamba and Benny Guralnik.

6.1 Theory

Here, I will describe what phonons are and how one can study them using DFT. Furthermore, I will define the Boltzmann transport equation (BTE) and illustrate how it can be efficiently solved for phonons in certain geometries following the recipe of Hua and Minnich [82].

6.1.1 Phonons and how to calculate them

Crystalline solids are more interesting than just electrons sitting in a static periodic potential. With temperature the nuclei will start to move around their equilibrium positions. This motion

is called lattice vibrations, and is crucial for mechanisms such as heat transport, thermal expansion and electrical resistance. Furthermore, any lattice vibration can be decomposed into individual modes, and when quantized they are called *phonons*. [84]

Within the Born-Oppenheimer approximation (see Chapter 2), it is possible to decouple the electrons from the nuclei of the system. Each set of positions for the nuclei will result in a new electronic problem with a new ground state and energy. A map of the potential energy landscape can be calculated, e.g., using DFT, where the local minima for the nuclei can be found. The energy landscape in the vicinity of these minima defines the lattice vibrations. A Taylor expansion of the energy can be made and stopping at the second term results in the harmonic approximation. The harmonic approximation is reasonable at lower temperatures, when there are few phonons and the interaction is weak, but at higher temperatures anharmonic terms must be included. The anharmonic, i.e., higher than 2nd order, terms describes the phonon-phonon interaction. Below this type of expansion will outlined and described how to calculate them from first principles. This is based on References [84, 85, 86, 87].

The expansion of the potential near the equilibrium positions can be written as:

$$U = U_0 + U_1 + U_2 + U_3 + U_4 + ..., \tag{6.1}$$

where U_0 is a free constant and $U_1 = 0$ since the forces are zero in equilibrium. The rest of the terms can be written as:

$$U_n = \frac{1}{n!} \sum_{l_1\kappa_1,...,l_n\kappa_n} \sum_{\alpha_1,...,\alpha_n} \Phi_{\alpha_1...\alpha_n}(l_1\kappa_1;...;l_n\kappa_n) u_{\alpha_1}(l_1\kappa_1) \cdots u_{\alpha_n}(l_n\kappa_n), \tag{6.2}$$

with $u_\alpha(l\kappa)$ denoting a displacement of nucleus κ in unit cell l along a direction α in the Cartesian coordinate system. The so-called interatomic force constants (IFCs) are denoted $\Phi_{\alpha_1...\alpha_n}(l_1\kappa_1;...;l_n\kappa_n)$ and have the form:

$$\Phi_{\alpha_1...\alpha_n}(l_1\kappa_1;...;l_n\kappa_n) = \left. \frac{\partial^n U}{\partial u_{\alpha_1}(l_1\kappa_1) \cdots \partial u_{\alpha_n}(l_n\kappa_n)} \right|_{u_{\alpha_i}(l_i\kappa_i)=0} \tag{6.3}$$

Within the harmonic approximation, the equations of motion is analogous to Hooke's law which turns into a eigenvalue if the displacements are expanded in a plane wave basis. The equations of motion then takes the form:

$$\vec{D}(\vec{q})\vec{e}_{\vec{q}j} = \omega^2_{\vec{q}j}\vec{e}_{\vec{q}j}, \tag{6.4}$$

with $\bar{D}$ being the dynamical matrix and $\vec{e}_{\vec{q}j}$ being the polarization vector of phonon with momentum $\vec{q}$ and index j. The harmonic frequencies are denoted $\omega_{\vec{q}j}$ which define the phonon dispersion. The dynamical matrix contains the Fourier transforms of the harmonic IFCs:

$$D_{\alpha\beta}(\kappa\kappa';\vec{q}) = \frac{1}{\sqrt{m_\kappa m_{\kappa'}}} \sum_{l'} \Phi_{\alpha\beta}(l\kappa;l'\kappa') e^{i\vec{q}\cdot(\vec{r}(l')-\vec{r}(l))} \tag{6.5}$$

Furthermore, using the anharmonic IFCs, one can also evaluate the imaginary part of the phonon self-energy, which in turn is inversely proportional to the phonon lifetimes.

There are many ways of actually calculating the IFCs. The procedure proposed in the Alamode [86] package is followed here. In short, DFT is used to calculate the atomic forces in supercell structures with ionic displacements. Doing this for a set of displacements one can then regress the IFCs against the forces from DFT. The harmonic IFCs are calculated using a small displacement, to reduce the anharmonicity, while the anharmonic IFCs are calculated using larger displacements to increase the effect of the anharmonicity. From the symmetries of the crystal, it is possible reduce the number unique IFCs. This is done by Alamode.

Phonon lifetimes
The imaginary part of the phonon self-energy is given by [86]:

$$\Gamma_{\vec{q}n}(\omega) = \frac{\pi}{2}\sum_{\vec{q}_1,\vec{q}_2}\sum_{n_1,n_2}\left|V_{-\vec{q}n,\vec{q}_1n_1,\vec{q}_2n_2}\right|^2\Big[(f_{\vec{q}_1n_1}+f_{\vec{q}_2n_2}+1)\delta(\omega-\omega_{\vec{q}_1n_1}-\omega_{\vec{q}_2n_2})+ \\ -(f_{\vec{q}_1n_1}-f_{\vec{q}_2n_2})\delta(\omega-\omega_{\vec{q}_1n_1}+\omega_{\vec{q}_2n_2})+ \\ +(f_{\vec{q}_1n_1}-f_{\vec{q}_2n_2})\delta(\omega+\omega_{\vec{q}_1n_1}-\omega_{\vec{q}_2n_2})\Big], \tag{6.6}$$

where $V_{-\vec{q}n,\vec{q}_1n_1,\vec{q}_2n_2}$ is the three-phonon scattering potential and can be written as:

$$V_{\vec{q}n,\vec{q}_1n_1,\vec{q}_2n_2} = \left(\frac{\hbar}{2N_q}\right)^{\frac{3}{2}}\frac{1}{\sqrt{\omega_{\vec{q}n}\omega_{\vec{q}_1n_1}\omega_{\vec{q}_2n_2}}}\sum_{l,l_1,l_2}e^{i(\vec{q}\cdot\vec{r}(l)+\vec{q}_1\cdot\vec{r}(l_1)+\vec{q}_2\cdot\vec{r}(l_2))} \tag{6.7}$$

$$\times\sum_{\kappa,\kappa_1,\kappa_2}\sum_{\alpha,\beta,\gamma}\Phi_{\alpha\beta\gamma}(l\kappa;l_1\kappa_1;l_2\kappa_2) \tag{6.8}$$

$$\times\frac{e^{\alpha}_{\vec{q}n,\kappa}e^{\beta}_{\vec{q}_1n_1,\kappa_1}e^{\gamma}_{\vec{q}_2n_2,\kappa_2}}{\sqrt{m_\kappa m_{\kappa_1}m_{\kappa_2}}}, \tag{6.9}$$

where the first sum vanishes unless $\vec{q}+\vec{q}_1+\vec{q}_2=\vec{G}$, where $\vec{G}$ is a reciprocal lattice vector, which in turn kills one of the sums over momentum in Equation 6.6.

From the imaginary part of the self-energy, $\Gamma_{\vec{q}n}(\omega)$, the phonon lifetime can be evaluated as $\tau = 1/(2\Gamma_{\vec{q}n}(\omega))$.

6.1.2 Boltzmann transport equation

The motion of classical particles in non-equilibrium conditions can be described using the Boltzmann transport equation (BTE). [88] Particles move, or are transported, to establish a global equilibrium. Hence, transport phenomena is a reaction to the non-equilibrium landscape created by the forces applied to the system. Transport is a very broad term and ranges from electrical current, dynamics of fluids, to heat transport, just to name a few. Example of forces in the previously mentioned transport problems are electric and magnetic fields, pressure gradients, and temperature gradients. The BTE treats the particles as classical objects with definable position and momentum, i.e., a distribution function $f(\vec{r},\vec{p},t)$ is defined that describes the probability of finding a particle at position $\vec{r}$ with momentum $\vec{p}$ at time t. Therefore, in the BTE formalism, quantum mechanical effects are neglected. This, however, does not mean that the transport regimes described by the BTE is lacking interesting features, as we will see. It simply limits us to the world at larger length scales than the de Broglie wavelength.

The BTE can be written:

$$\frac{\partial f(\vec{r},\vec{p},t)}{\partial t}+\underbrace{\dot{\vec{r}}\cdot\nabla_{\vec{r}}f(\vec{r},\vec{p},t)+\dot{\vec{p}}\cdot\nabla_{\vec{p}}f(\vec{r},\vec{p},t)}_{\text{stream}}+\underbrace{\mathcal{S}(\vec{r},\vec{p},t)}_{\text{source}}=\underbrace{\mathcal{I}\left[f(\vec{r},\vec{p},t)\right]}_{\text{collision}}, \tag{6.10}$$

where $\mathcal{I}\left[f(\vec{r},\vec{p},t)\right]$ is the collision functional that describes the interaction between the particles and $\mathcal{S}(\vec{r},\vec{p},t)$ is a source for the particles. The BTE describes the time evolution of the distribution function in phase space by a streaming term and collision term. The collisions drive the system towards equilibrium and give time a direction, where the system goes from more order to less. The collision integral can be complex and depends on which processes are involved, but I will here resort to the simple RTA:

$$\mathcal{I}\left[f(\vec{r},\vec{p},t)\right]\approx-\frac{f(\vec{r},\vec{p},t)-f_0(\vec{r},\vec{p})}{\tau}, \tag{6.11}$$

where $f_0(\vec{r},\vec{p})$ denotes a local equilibrium distribution function, e.g. Bose-Einstein or Fermi-Dirac distributions for bosons and fermions, respectively. The relaxation time is denoted τ and is generally momentum and energy dependent. Even within the RTA the BTE is difficult to solve (due to its high dimensionality) and numerical methods are essential, with the exception of a few simple systems. When the non-equilibrium distribution function is known one can calculate measurable quantities such as heat and charge current, $\vec{q}$ and $\vec{j}$, respectively, through:

$$\vec{q} = \int d^3\vec{p}(\varepsilon - \mu)\frac{\vec{p}}{m}f(\vec{r},\vec{p},t) \tag{6.12}$$

$$\vec{j} = \int d^3\vec{p}e\frac{\vec{p}}{m}f(\vec{r},\vec{p},t) \tag{6.13}$$

Here the energy, chemical potential and charge is introduced as ε, μ and e, respectively. While the BTE is challenging to solve for general geometries it is possible analytically for some simple problems. An example of such a problem is a temperature (or potential) gradient. This problem reduces to the Fourier's law of conduction (or Ohm's law) within the linear response regime, as will be demonstrated for phononic heat transport below.

Phonon BTE

Phonons are bosons and they are unaffected by forces (such as electric fields), hence phonons are described by the Bose-Einstein distribution when in equilibrium and $\vec{F} = \dot{\vec{p}} = \vec{0}$. Using this knowledge one can write the phonon BTE within the RTA:

$$\frac{\partial n_\nu}{\partial t} + \vec{v}_\nu \cdot \nabla_{\vec{r}} n_\nu + Q_\nu = -\frac{n_\nu - n_0(T)}{\tau_\nu} \tag{6.14}$$

Here, I have also changed the notation to distinguish a general distribution function and the phonon distribution function, n_ν, for phonon mode ν. The Bose-Einstein distribution is denoted $n_0(T)$. I have also dropped the position and momentum variables.

Thermal conductivity from micro to macroscale

I begin by assuming steady state ($\partial_t n_\nu = 0$) and no phonon generation ($Q_\nu = 0$) which simplifies the phonon BTE:

$$\vec{v}_\nu \cdot \nabla_{\vec{r}} n_\nu = -\frac{n_\nu - n_0(T)}{\tau_\nu} \tag{6.15}$$

Next I define the distribution function that describes the deviation from the the equilibrium $n_\nu^{'} = n_\nu - n_0(T)$. Furthermore, it is assumed that this deviation is small, i.e., the distribution function is linear. The gradient of the distribution function can be written as:

$$\nabla_{\vec{r}} n_\nu = \frac{\partial n_\nu}{\partial T}\nabla_{\vec{r}} T = \left(\frac{\partial n_0(T)}{\partial T} + \frac{\partial n_\nu^{'}}{\partial T}\right)\nabla_{\vec{r}} T \approx \frac{\partial n_0(T)}{\partial T}\nabla_{\vec{r}} T \tag{6.16}$$

Substituting Eq. 6.16 into Eq. 6.15, one can write the linearized BTE:

$$-\vec{v}_\nu \cdot \frac{\partial n_0(T)}{\partial T}\nabla_{\vec{r}} T = \frac{n_\nu^{'}}{\tau_\nu} \Rightarrow -\tau_\nu \vec{v}_\nu \cdot \frac{\partial n_0(T)}{\partial T}\nabla_{\vec{r}} T = n_\nu^{'} \tag{6.17}$$

Hence, an expression for the non-equilibrium distribution function has been found. Finally, one can write down the heat current:

$$\vec{q} = \frac{1}{V}\sum_\nu \hbar\omega_\nu \vec{v}_\nu n_\nu = \underbrace{\frac{1}{V}\sum_\nu \hbar\omega_\nu \vec{v}_\nu n_0(T)}_{\text{equilibrium}} + \frac{1}{V}\sum_\nu \hbar\omega_\nu \vec{v}_\nu n_\nu^{'}, \tag{6.18}$$

where the summation is over all phonons in the 1st BZ. The first sum is zero, since the summation is over an odd function over an even domain. Using the linearized BTE in Eq. 6.17 the current in α direction can be expressed as:

$$q^{\beta} = -\frac{1}{V}\sum_{\nu} \hbar\omega_{\nu} v_{\nu}^{\beta} \tau_{\nu} v_{\nu}^{\alpha} \frac{\partial n_0(T)}{\partial T} \frac{\partial T}{\partial r^{\alpha}} \tag{6.19}$$

Comparing this with Fourier's law ($q^{\beta} = -\kappa^{\alpha\beta}\frac{\partial T}{\partial r^{\alpha}}$), one finally gets:

$$\kappa^{\alpha\beta} = \sum_{\nu} \frac{\hbar\omega_{\nu}}{V} v_{\nu}^{\beta} \tau_{\nu} v_{\nu}^{\alpha} \frac{\partial n_0(T)}{\partial T} = \sum_{\nu} c_{\nu} v_{\nu}^{\beta} \tau_{\nu} v_{\nu}^{\alpha} \tag{6.20}$$

Where $c_{\nu} = \frac{\hbar\omega_{\nu}}{V}\frac{\partial n_0(T)}{\partial T}$, is the mode specific heat capacity. The thermal conductivity is now connected to the underlying microscopic properties of the material, namely phonon heat capacity, group velocity and relaxation time.

Having found the connection between the microscopic description of phonons and the macroscopic thermal conductivity enables for deeper understanding of how heat is transported in crystalline solids. A phonon with heat capacity c, group velocity v and relaxation time τ, will conduct heat according to:

$$\kappa \propto cv\tau v = c\lambda v \tag{6.21}$$

Here the MFP, λ, is introduced and it is a measure of how far the phonon travels (on average) before scattering. The MFP is mode dependent and can be very complex depending on what scattering mechanisms are involved. Eq. 6.21 is powerful, but it has its limitations. What happens when the system size is on the order of, or even below, the phonon MFP? Similar questions arise when the characteristic time scale is on the order of the relaxation time.

To answer these questions one must solve the BTE without the limiting assumption of a linear distribution function. The linearized BTE is based on the assumption that one can expand the distribution function around some local equilibrium. Furthermore, it is assumed that the deviation from the local equilibrium is small. A small deviation from (local) equilibrium means that the frequency of the scattering events is high, which is questionable in systems with long MFP and relaxation times. Systems that exhibit few scattering events (with respect to either length or time scale of the system) are called *ballistic* compared to *diffusive* systems which show an abundance of scattering events.

6.1.3 Solution of the Boltzmann transport equation for non-diffusive systems

The full phonon BTE can in principle be solved using techniques such as finite difference methods or stochastic Monte-Carlo methods [89, 90]. While these methods are very general, they are computationally heavy and require elaborate codes, even for rather simple geometries. It is important to stress that one cannot rely on the linearized BTE when studying non-diffusive transport, but must solve the full BTE without the assumption about high scattering rates.

In this section, the method for solving the phonon BTE is outlined. The method was developed by Hua and Minnich [82], and is remarkably simple. It can handle frequency dependent phonon properties (i.e. there is no assumption about gray phonons) and the scattering integral is treated using the RTA. Furthermore, it covers transport in the whole ballistic-to-diffusive range. The main limitation of the method is the requirement that the geometry must be Fourier transformable. If the phonon parameters are known and the heater profile is Fourier transformable, the resulting temperature rise can be calculated, with no restriction to diffusive versus ballistic transport.

Hua's and Minnich's BTE solution

The starting point is the (phonon) BTE:

$$\frac{\partial g_\omega}{\partial t} + \vec{v}_\omega \cdot \nabla_{\vec{r}} g_\omega - \frac{Q_\omega}{4\pi} = -\frac{g_\omega - g_0(T)}{\tau_\omega} \tag{6.22}$$

Where, $g_\omega = \hbar\omega D(\omega)(n_\omega(\vec{r},\theta,\phi,t) - n_0(T_0))$, is the unknown distribution function with respect to a reference distribution. For convenience, the phonons are parametrized in frequency and now the direction is described using the angles θ, ϕ. It is assumed that the phonons are is isotropic, which is reasonable for crystals such as Si. The equilibrium deviation distribution function is defined as:

$$g_0(T) = \frac{\hbar\omega}{4\pi} D(\omega)(n_0(T) - n_0(T_0)) \approx \frac{1}{4\pi} c_\omega \Delta T, \tag{6.23}$$

where it is assumed that the temperature deviation is small. The mode specific heat capacity is also introduced as $c_\omega = \hbar\omega D(\omega)\partial_T n_0(T)$. The first important step is to make use of the conservation of energy. After a integration over phonon frequency and solid angle, the left hand side of Eq. 6.22 takes the form:

$$\frac{\partial E}{\partial t} + \boldsymbol{\nabla} \cdot \vec{q} - Q \equiv 0 \tag{6.24}$$

This allows us to detangle the unknown temperature from the unknown distribution function since, under the same integration, the right hand side of Eq. 6.22 must be equal to zero:

$$-\int\int \left[\frac{g_\omega}{\tau_\omega} - \frac{1}{\tau_\omega}\frac{1}{4\pi} c_\omega \Delta T\right] d\omega d\Omega \equiv 0 \tag{6.25}$$

To actually calculate one of the unknowns, a Fourier transform of Eq. 6.22 is made in both spatial and temporal dimensions. This turns the problem into an algebraic equation from a differential equation. By taking the Fourier transform of Eq. 6.22 and using the result of the distribution function together with Eq. 6.25, one get the following expression for the temperature rise in Fourier space:

$$\Delta\tilde{T}(\eta,\xi) = \frac{\int d\omega \frac{\tilde{Q}_\omega}{\lambda_\omega \xi} \arctan\left(\frac{\lambda_\omega \xi}{1 + i\eta\tau_\omega}\right)}{\int d\omega \frac{c_\omega}{\tau_\omega}\left[1 - \frac{1}{\lambda_\omega \xi}\arctan\left(\frac{\lambda_\omega \xi}{1+i\eta\tau_\omega}\right)\right]} \tag{6.26}$$

Here, $\sim$ denotes Fourier transformed quantities, and η and $\xi = \sqrt{\xi_x^2 + \xi_y^2 + \xi_z^2}$ denotes the temporal and spatial frequencies, respectively. Here the MFP is introduced as $\lambda_\omega = v_\omega \tau_\omega$. If the phonon parameters and heater profile (described by $\tilde{Q}_\omega$) are known, the temperature rise in real space can be calculated by taking the inverse Fourier transform of Eq. 6.26:

$$\begin{aligned}\Delta T_{\mathsf{BTE}}(\eta, r) &= \frac{1}{(2\pi)^3}\int \exp\left(i\vec{\xi}\cdot\vec{r}\right)\Delta\tilde{T}(\eta,\vec{\xi})d\vec{\xi} \\ &= \frac{4\pi}{(2\pi)^3}\int_0^\infty \frac{\sin(\xi r)}{r}\Delta\tilde{T}(\eta,\xi)\xi d\xi\end{aligned} \tag{6.27}$$

To make realistic predictions of phonon transport it is necessary to have high quality phonon parameters such as group velocity, heat capacity, and finally the scattering rates. In Section 6.1.1, it was decsribed how one can evaluate these properties from DFT calculations.

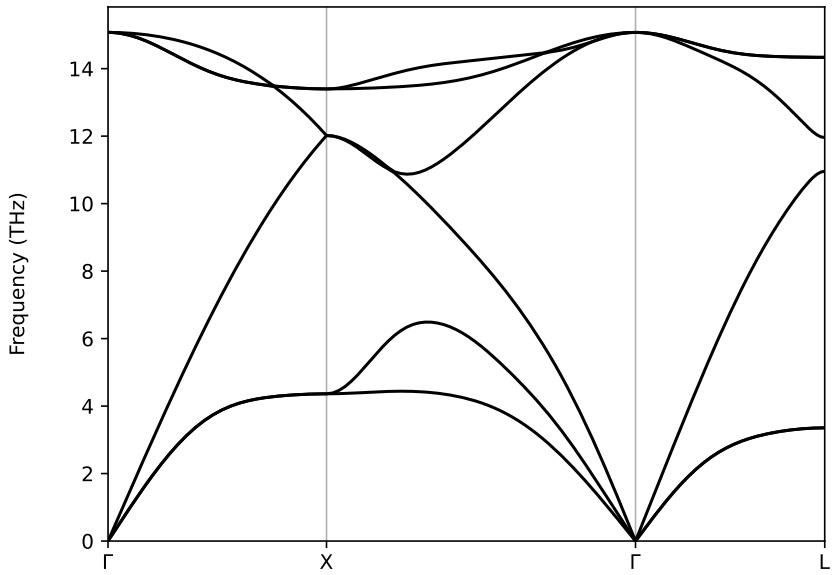

Figure 6.1: Calculated phonon dispersion of silicon.

6.2 Calculated doped silicon phonons

To simulate the thermal response of any system, properties such as the thermal conductivity must be known for the given material. Furthermore, if the BTE is solved one need the phonon mode resolved properties, i.e., the lifetimes, group velocities and specific heat capacities, that result in a mode specific thermal conductivity, $\kappa \propto c\lambda v$. In this study, these properties were calculated (partially) from first principles using DFT. The intrinsic Si phonon properties are calculated directly from DFT, while the effects of doping is modelled using analytical phonon-electron and phonon-mass scattering terms.

ALAMODE [86] was used to evaluate the Si phonon dispersion and anharmonic phonon-phonon lifetimes. The quantities were evaluated based on first principles forces predicted using VASP [37], and the PBE [74] functional was used. A plane-wave cutoff of 245 eV was used and the self-consistent solution was converged below 1×10^{-6} eV. The conventional silicon unit cell was used with a fixed lattice constant of 5.46 Å. The force constants were calculated by doing ionic displacements (as instructed by ALAMODE) within a $3 \times 3 \times 3$ supercell of the conventional unit cell. The magnitudes of the displacements were set to $\Delta u = 0.01$ Å and $\Delta u = 0.03$ Å, for the harmonic and anharmonic force constants, respectively. For these supercells, the DFT calculations were performed using a Γ-centered $3 \times 3 \times 3$ k-grid. Finally, using the force constants, the phonon dispersion and phonon-phonon scattering rates were evaluated on a k-grid of $30 \times 30 \times 30$. From the momentum resolved properties, I then collapsed all parameters on to one frequency dependent phonon mode. Here, 101 frequency bins were used. In each bin, the number of states are counted which results in a density of states. Furthermore, the group velocity is averaged in the ith bin as $v^2_{avg}(\omega_i) = \langle |\vec{v}(\omega_i)|^2 \rangle$. Similarly, the anharmonic lifetime is averaged as $\langle \tau(\omega_i) |\vec{v}(\omega_i)|^2 \rangle / v^2_{avg}(\omega_i)$. This transformation averages out all anisotropy of the crystal, but since Si is quite isotropic the loss in information is minimal. [82]

Figure 6.1 shows the harmonic phonon dispersion of (intrinsic) silicon. The three acoustic and three optical phonon modes can be observed and good agreement is observed with literature dispersions.

In Figure 6.2, the calculated frequency resolved phonon lifetimes at 300 K is presented. The blue line denotes the lifetimes only due to phonon-phonon interaction, the other cases will be

discussed later. The low frequency acoustic phonons have long lifetimes and therefore carry heat effectively, as expected. [91, 86] Furthermore, to the right in Figure 6.2, the cumulative thermal conductivity is presented. The cumulative thermal conductivity is defined as $\kappa(\lambda) = \sum_{\nu}^{\lambda_\nu<\lambda} c_\nu \lambda_\nu v_\nu$, where $\lambda_\nu = v_\nu \tau_\nu$ is the MFP of mode ν, i.e., the sum only included phonon modes with MFP shorter than λ. Again, the blue line denotes the intrinsic cumulative thermal conductivity of Si at 300 K. The MFP distribution clearly shows that phonon MFPs up to a couple of micrometers are relevant for the heat conduction, as expected. [80, 81, 82]

Next, the influence of doping on the phonons is investigated. This is done in two stages, since doping both changes the atomic masses, which results in so-called mass difference or isotope scattering [92], and introduces free charges to the semiconductor leading to phonon-electron scattering [93].

The phonon scattering due to a mass difference is described by Tamura's isotope scattering model [92]:

$$\tau_M^{-1} = \frac{\pi}{6} V g \omega^2 D(\omega), \tag{6.28}$$

where V is the volume and $D(\omega)$ is the phonon density of states. The strength of the scattering is governed by the dimensionless parameter:

$$g = \sum_i c_i (1 - m_i/\bar{m})^2, \tag{6.29}$$

that depends on the concentration c_i and mass m_i of atom i, compared to the average mass $\bar{m} = \sum_i c_i m_i$. Here I use the mass of silicon and boron. Boron is taken since this creates a large mass difference, and hence strong scattering, compared to, e.g., phosphorus which has a mass more comparable with silicon. The resulting lifetime, τ_M, is presented in Figure 6.2. Furthermore, by combining the mass difference scattering with the intrinsic anharmonic scattering rates using Matthiessen's rule the reduction in thermal conductivity can be evaluated. This is shown to the right in Figure 6.2. As expected, the thermal conductivity is reduced due to the additional scattering channel. Matthiessen's rule is an approximate way of combining different scattering mechanisms:

$$\tau^{-1}(\omega) = \sum_i \tau_i^{-1}, \tag{6.30}$$

where sum is over the considered scattering mechanisms, e.g., anhmarmonic and mass difference scattering. This is of course a very simple model, that only works if the different mechanisms are independent. Furthermore, the treatment here neglects any impact of the doping on the silicon phonon dispersion. It is assumed that the dopants only modifies the scattering of the phonons, but not their other properties. This is likely reasonable, since even though I am interested in highly doped Si, the doping concentration is below 1 %, which should put the system in the doping regime and not alloying regime.

To model the scattering of the phonons on the free charges, I used an asymptotic limit of the deformation potential approximation proposed in [93]:

$$\tau_{pe}^{-1} = \frac{(2\pi m^*)^{1/2} D^2}{(k_B T)^{3/2} g_d \rho v(\omega)} \exp\left(-\frac{m^* v(\omega)^2}{2 k_B T}\right) n\omega, \tag{6.31}$$

where m^* and g_d is the effective mass and valley degeneracy of the bands, respectively. The mass density is denoted ρ and doping concentration is denoted n. Furthermore, the phonon frequency and speed is denoted ω and $v(\omega)$. The strength of the interaction is parametrized by the deformation potential, D, with dimension energy. The expression in Equation 6.31

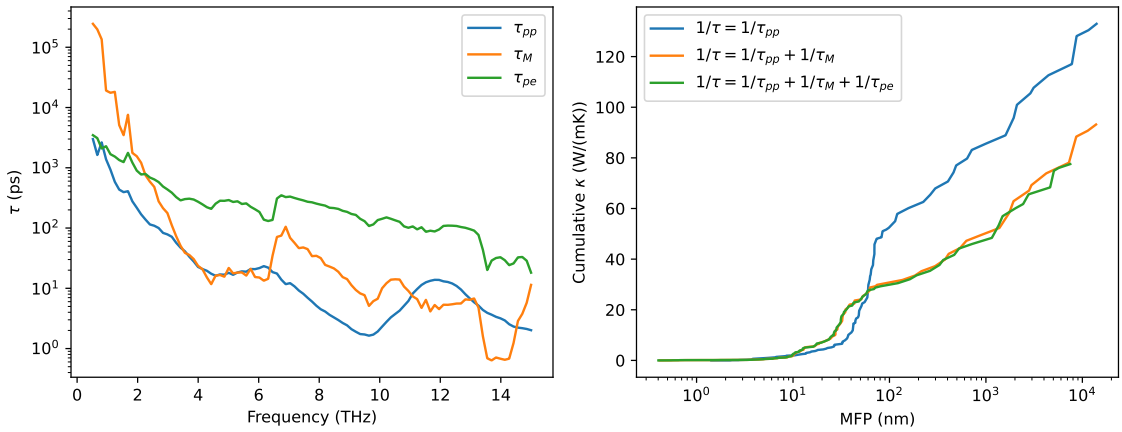

Figure 6.2: Left: Relaxation lifetimes due to different scattering mechanisms. Right: Cumulative thermal conductivity as a function of MFP for different combinations of scattering mechanisms. The indices pp, M, and pe denotes phonon-phonon, phonon-mass, and phonon-electron scattering, respectively. The values are for Si at 300 K and with a boron mass scattering with doping concentration of $1 \times 10^{20}\,\mathrm{cm}^{-3}$. The deformation potential, defining the phonon-electron interaction, was set to $D = 0.5\,\mathrm{eV}$.

is only applicable for the acoustic phonons, but since the optical phonons conduct a rather small fraction of the total heat, I here neglect the scattering of optical phonons on electrons. The effective mass was set to the free electron mass $m^* = m_e$ and the degeneracy was set to $g_d = 6$. However, these values are not hugely important, since the deformation potential, D, was used a free parameter in this work. To find the value for the deformation potential, the predicted total thermal conductivity was benchmarked against experimental values of the thermal conductivity of boron doped silicon [94]. This comparison is shown in Figure 6.3, and good agreement is found between experimental values and predicted values with D values around ca. 0.50 eV. Here, the mass difference scattering is also included. It should be noted, that while the agreement is good, the comparison is only of the *total* thermal conductivity, and it does not necessarily mean that the spectral composition of the phonons is modelled correctly.

6.3 Predicted temperature profiles in doped silicon

Using the frequency resolved phonon heat capacities, velocities, and lifetimes it is now possible to calculate the temperature rise from a nanoscopic heater by solving the BTE. The BTE was solved as outlined in Section 6.1.3. [82] The nanoscopic heater geometry is sketched in Figure 6.4, and the heater is a sphere with radius $R = 50\,\mathrm{nm}$. Theoretically, the semi-infinite geometry is identical to fully infinite system, since surface effects are neglected here. This representation is chosen to make the connection with experiments such as the micro four-point probe (M4PP), where nanoscopic electrodes are placed at a surface which causes Joule heating. More specifically, the heating is constant in time and the heating profile is defined as:

$$Q_\omega(\vec{r}) = \begin{cases} Ap(\omega) & \text{for } r \leq R \\ 0 & \text{for } r > R \end{cases}, \tag{6.32}$$

with A being the volumetric heat generation and the spectral distribution, $p(\omega)$, defined as [83, 95]:

$$p(\omega) = \frac{c_\omega/\tau_\omega}{\sum_p \int_0^{\omega_{\max}} d\omega c_\omega/\tau_\omega} \tag{6.33}$$

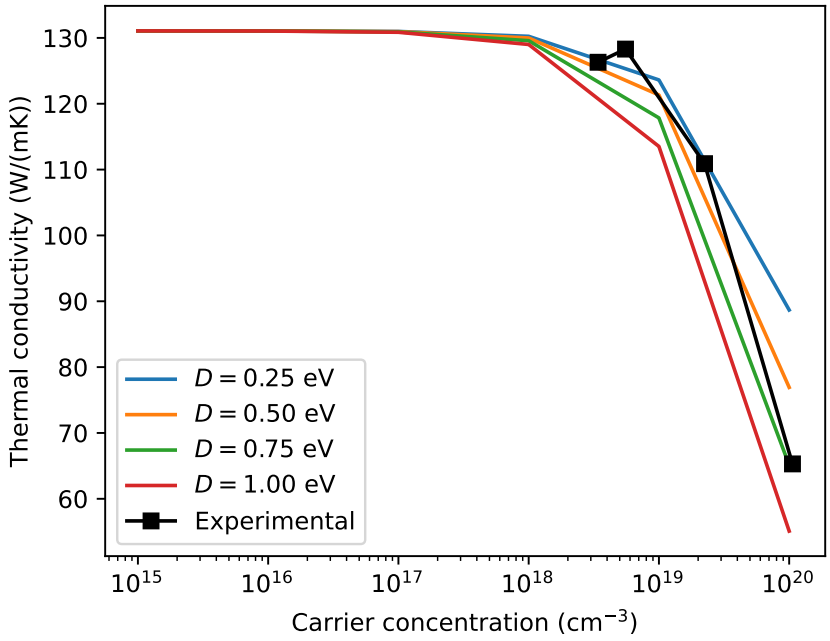

Figure 6.3: Benchmarking of the calculated total thermal conductivity and experimental thermal conductivity of boron doped Silicon from Reference [94].

To make the real space heating profile useful in the BTE solution, the real space heating profile must be Fourier transformed:

$$\tilde{Q}_\omega(\vec{\xi}) = \int \exp\left(-i\vec{\xi}\cdot\vec{r}\right) Q_\omega(\vec{r}) d\vec{r} = \tag{6.34}$$
$$= \frac{4\pi}{\xi^3} Ap(\omega) \left[\sin(\xi R) - \xi R \cos(\xi R)\right]$$

Furthermore, a diffusive model is used as a benchmark, and the quantity of interest is the deviation between the BTE solution and the diffusive model. The spherical heater geometry results in the following diffusive temperature profile:

$$\Delta T_{\text{Fourier}}(r) = \frac{1}{3}\frac{AR^3}{\kappa r}, \tag{6.35}$$

This expression is found by taking the steady-state limit of the more general solution by Carslaw and Jaeger [96].

Finally, the predicted temperature rises for doped silicon at 300 K from a nanoscopic heater is presented in Figure 6.5. The ratio between the BTE prediction and the diffusive model is shown as a function of distance from the center of the heater. Furthermore, different doping concentrations are shown. It is observed that the diffusive model underestimates the temperature rise, as expected. [12, 82, 83]. At the boundary of the heater, $r = 50$ nm, the error is above 100 %. Far away from the heater the agreement between the two models increases, and the error decreases. Furthermore, increasing the doping leads to a reduction in the apparent error, indicating that the thermal transport becomes more diffusive. This is further illustrated in Figure 6.6, where the doping concentration is fixed to $n = 1 \times 10^{20}$ cm^{-3}, while the deformation potential, D, is varied. A stronger phonon-electron interaction, i.e., larger deformation potential, leads to a more diffusive phonon transport due to the shorter MFPs. However, for reasonable doping concentrations and phonon-electron interactions, the

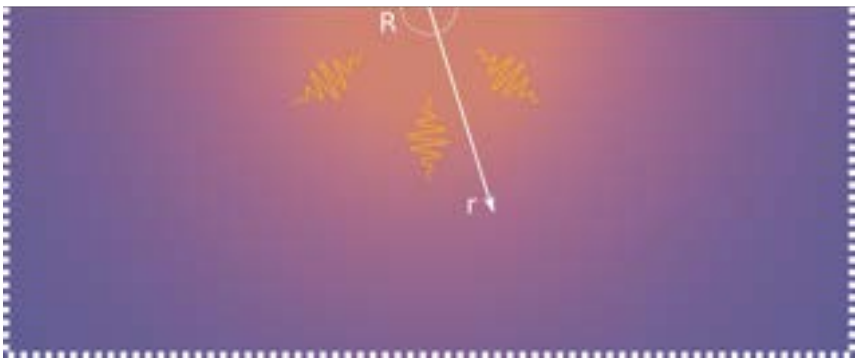

Figure 6.4: Geometry of the nanoscopic heater system. The vacuum is above the doped Si and phonons are generated within the hemisphere with radius $R = 50\,\text{nm}$. The dashed lines represent directions extend to infinity.

diffusive model underestimates the temperature rise by more than 10 %, perhaps up to 40 %, at a distance of 1 µm. While the modelling of the doping is quite simple here, it still shows that the non-diffusive transport is likely relevant in Si, *even* with high doping concentrations relevant to industry. This indicates that Fourier's law of conduction should be used with care, not only in intrinsic silicon, but also in highly doped systems.

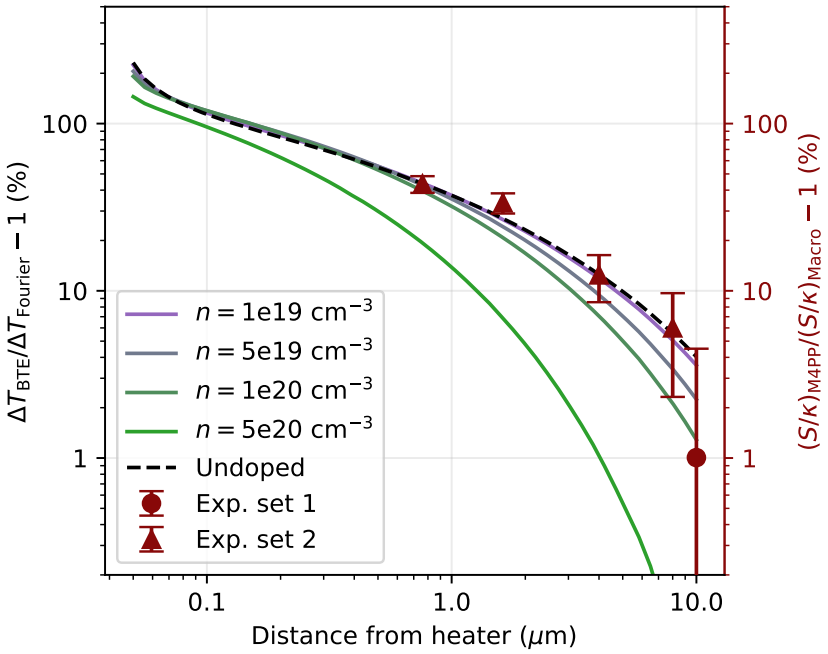

Figure 6.5: Comparison between the temperature rise predicted using the BTE and the diffusive model. The heater radius is $R = 50\,\text{nm}$, the ambient temperature is 300 K, and the deformation potential is $D = 0.5\,\text{eV}$. Thermal properties of boron doped Si ($n = 5.54 \times 10^{18}\,\text{cm}^{-3}$) are included from measurements with different characteristic length scales. Here, "Exp. set 1" denotes measurements from Ref. [94] and "Exp. set 2" refers to unpublished results gathered using the same method but smaller probes. Note, that the experimental data is preliminary and the data treatment is subject to change (see main text).

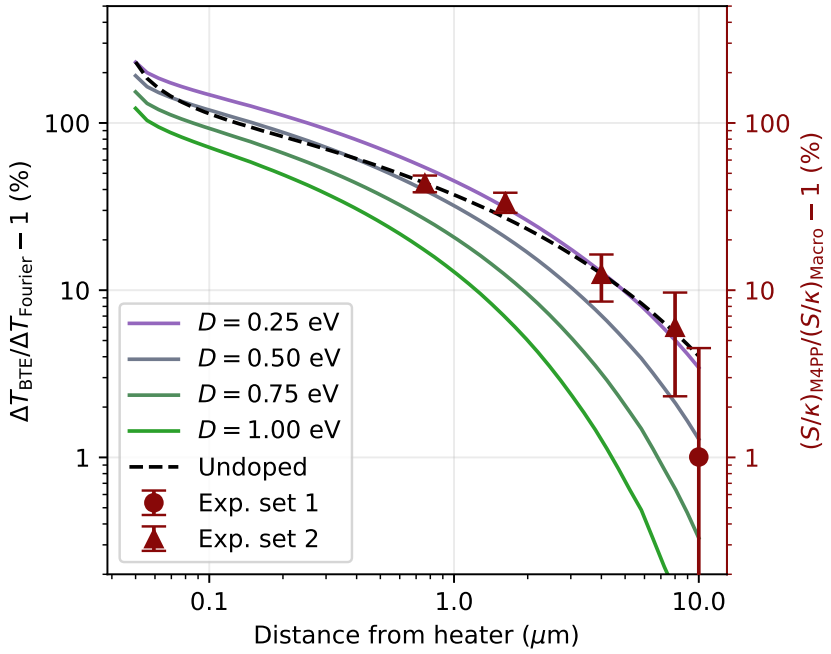

Figure 6.6: Same as Fig. 6.5, but now the predictions are done using $n = 1 \times 10^{20}\,\mathrm{cm}^{-3}$ and D is varied.

6.4 Experimental thermal response of boron doped silicon

Traditionally, the M4PP is a technique employed to measure electrical properties of metals or doped semiconductors. However, recent developments have enabled the study of thermal and thermoelectric properties using the same tool. [94, 97] This extension allows for extraction of Seebeck over thermal conductivity ratios, S/κ. By assuming that the thermal conductivity purely originates from the phonons in doped Si and that the Seebeck is due to purely diffusive electrons, the ratio S/κ can be used as a quantity to study non-diffusive phonon transport. In a linear M4PP, the four probes are separated by distances at the micrometer scale. The two current pins will act as two small point heaters, giving rise to a temperature profile governed by the thermal conductivity, and the two voltage pins will measure a voltage proportional to the temperature difference due to the Seebeck effect. Doing these measurements using probes with different probe separations, it is possible to extract S/κ at different characteristic length scales. When the pin separations are large, I expect the thermal transport to be diffusive and S/κ should converge to the macroscale values. However, when small probe separations are used, I expect non-diffusive thermal transport to be relevant leading to a *suppression* of the thermal conductivity and therefore an *increase* in S/κ. Thanks to my experimental colleagues, Neetu Lamba and Benny Guralnik, I have access to this type of M4PP measurements of boron doped silicon. The S/κ ratios measured using the M4PP with different probe separations are compared to macroscale values of S/κ of the same sample. The boron doping concentration was $n = 5.54 \times 10^{18}\,\mathrm{cm}^{-3}$. These values are overlain in Figures 6.5 and 6.6. It should be noted, that there could be errors in the estimated power deposited into the sample, which would affect the shape experimental of the experimental trends. Furthermore, the macroscale references might have errors which could shift the absolute deviations. Hence, this data is preliminary and might change. Nonetheless, it is observed that the microscale measurements show overestimation of S/κ, compared to the macroscale values. Furthermore, the overestimation increases for smaller probe separations, as predicted using BTE. At 10 µm, the error between the M4PP value and macroscale value is negligible. However, at probe

separations of ca. 0.8 µm the deviation from macroscale values is ca. 40 $\%$, in good agreement with the error between BTE and the diffusive model. While there could be other effects in play, it seems that the BTE is a good predictor of these observed length dependent deviations.

6.5 Summary

The key findings from the study of phonons in doped silicon are that:

- BTE calculations show that non-diffusive phonon transport lead to even hotter hotspots
- Phonons in highly doped silicon remains non-diffusive at the microscale when treating the doping as a simple perturbation that increases the phonon scattering rate
- Deviations between measurements of S/κ at microscale and macroscale might be due to non-diffusive thermal transport

Chapter 7

Conclusion and outlook

In this thesis, I have described how first principles computational tools can be employed to understand materials from the atomic structure and upwards. By numerically solving the electronic structure problem using density functional theory (DFT), it is possible to *efficiently* get direct insight into the quantum mechanical states of materials such as $SrNbO_3$ and Si. From the electronic structure, many related material properties can be extracted, such as optical, electrical, and thermal properties.

In $SrNbO_3$, quantities such as the dielectric function, the Seebeck coefficient, and the electrical conductance were obtained with various distortions, such as octahedral rotations and oxygen vacancies. These properties are important, since $SrNbO_3$ has been discussed in the literature as a transparent conductor. [8, 49] Furthermore, the electronic states were also investigated directly, and Dirac nodal lines were observed near the Fermi level for the energetically favorable octahedral rotation ($a^0a^0c^+$). The predicted band structures of $SrNbO_3$ with various octahedral rotations were compared with bands from angle-resolved photoemission spectroscopy (ARPES) measurements. A side-by-side comparison of DFT and ARPES data further indicated the stabilization of $a^0a^0c^+$. This is surprising since $a^0a^0c^+$ is an uncommon tilt in perovskite oxides. [42, 43] Moreover, it highlights how complex these oxides are, i.e., there exists a plethora of distortions with competing local minima, and to find the global minimum one has to sample all candidates.

From the oxygen vacancy study, it was shown, as expected, that oxygen vacancies causes electrical resistance in $SrNbO_3$. Furthermore, the scattering strength is sensitive to the location of the oxygen vacancy, especially in slabs of $SrNbO_3$. Interestingly, in ultra thin $SrNbO_3$, the resistance due to an oxygen vacancy increases when spin is considered. Moreover, a noticeable spin splitting was found. Typical scattering cross sections were between ca. $0.5a^2$ and $1.5a^2$ without spin polarization, and with spin polarization values above $2a^2$ were observed. Here, a is the lattice constant. By studying the transmission eigenchannels in real space it was seen they have a clear t_{2g} character. Furthermore, they indicate that it is largely the NbO_2 layers that are conducting in 2 u.c. $SrNbO_3$, which explains the layer sensitivity of the electron-vacancy scattering. Overall, these findings indicate that the electrical degradation of thin conducting oxides might be related to electron-oxygen vacancy scattering. [64, 65, 66] Interestingly, the spin dependent scattering adds complexity, and perhaps it could be leveraged in spintronics.

Phonon transport was studied in doped Si at length scales comparable to the phonon mean free paths (MFPs). DFT calculations were performed to get the intrinsic Si phonon dispersion and phonon-phonon scattering rates, and the effect of doping was modelled using simple analytical formulas. The temperature rise due to a nanoscopic heater was then calculated for doped Si by

solving the Boltzmann transport equation (BTE). As expected from the literature, intrinsic Si phonons are transported in a non-diffusive manner at length scales up to the micrometer scale at room temperature. However, surprisingly, the additional scattering due to doping did not push the thermal transport into a diffusive regime as efficiently as anticipated. The phonons in doped Si remained noticeably non-diffusive at the microscale, even with doping concentrations of $1 \times 10^{20}\,\mathrm{cm}^{-3}$. Furthermore, room temperature micro four-point probe (M4PP) measurements of doped Si showed length-dependent thermal properties at the microscale, perhaps due to non-diffusive thermal transport. To summarize, the study indicates that diffusive models, such as Fourier's law of conduction, should be used with caution when phonon transport in Si is considered, even in highly doped Si.

Bibliography

[1] A. S. Bhalla, Ruyan Guo, and Rustum Roy. "The perovskite structure - A review of its role in ceramic science and technology". In: *Materials Research Innovations* 4 (2000), pp. 3–26. DOI: 10.1007/s100190000062.

[2] J. F. Schooley, W. R. Hosler, and Marvin L. Cohen. "Superconductivity in semiconducting $SrTiO_3$". In: *Phys. Rev. Lett.* 12 (1964), pp. 474–475. DOI: 10.1103/PhysRevLett.12.474.

[3] Ronald E Cohen. "Origin of ferroelectricity in perovskite oxides". In: *Nature* 358 (1992), pp. 136–138. DOI: 10.1038/358136a0.

[4] Julien Varignon, Manuel Bibes, and Alex Zunger. "Origin of band gaps in 3d perovskite oxides". In: *Nature Communications* 10 (2019). DOI: 10.1038/s41467-019-09698-6.

[5] Lei Zhang et al. "Correlated metals as transparent conductors". In: *Nature materials* 15 (2016), pp. 204–210. DOI: 10.1038/nmat4493.

[6] James M. Rondinelli, Steven J. May, and John W. Freeland. "Control of octahedral connectivity in perovskite oxide heterostructures: An emerging route to multifunctional materials discovery". In: *MRS Bulletin* 37 (2012), pp. 261–270. DOI: 10.1557/mrs.2012.49.

[7] F. Gunkel et al. "Oxygen vacancies: The (in)visible friend of oxide electronics". In: *Applied Physics Letters* 116 (2020), p. 120505. DOI: 10.1063/1.5143309.

[8] Yoonsang Park et al. "$SrNbO_3$ as a transparent conductor in the visible and ultraviolet spectra". In: *Communications Physics* 3 (2020). DOI: 10.1038/s42005-020-0372-9.

[9] Jong Mok Ok et al. "Correlated oxide Dirac semimetal in the extreme quantum limit". In: *Science Advances* 7 (2021), p. 235121. DOI: 10.1126/sciadv.abf9631.

[10] Narayan Mohanta et al. "Semi-Dirac and Weyl fermions in transition metal oxides". In: *Phys. Rev. B* 104 (2021). DOI: 10.1103/PhysRevB.104.235121.

[11] Arden L. Moore and Li Shi. "Emerging challenges and materials for thermal management of electronics". In: *Materials Today* 17 (2014), pp. 163–174. DOI: 10.1016/j.mattod.2014.04.003.

[12] G. Chen. In: *Journal of Heat Transfer* 118 (1996), pp. 539–545. DOI: 10.1115/1.2822665.

[13] David J. Griffiths and Darrell F. Schroeter. *Introduction to Quantum Mechanics*. 3rd ed. Cambridge University Press, 2018. DOI: 10.1017/9781316995433.

[14] M. Born and R. Oppenheimer. "Zur Quantentheorie der Molekeln". In: *Annalen der Physik* 389 (1927), pp. 457–484. DOI: https://doi.org/10.1002/andp.19273892002.

[15] B.H. Bransden and C.J. Joachain. *Physics of Atoms and Molecules*. Pearson Education. Prentice Hall, 2003.

[16] D.S. Sholl and J.A. Steckel. *Density Functional Theory: A Practical Introduction*. Wiley, 2011.

[17] P. Hohenberg and W. Kohn. "Inhomogeneous Electron Gas". In: *Phys. Rev.* 136 (1964), B864–B871. DOI: 10.1103/PhysRev.136.B864.

[18] W. Kohn and L. J. Sham. "Self-Consistent Equations Including Exchange and Correlation Effects". In: *Phys. Rev.* 140 (1965), A1133–A1138. DOI: 10.1103/PhysRev.140.A1133.

[19] Pedro Borlido et al. "Large-Scale Benchmark of Exchange–Correlation Functionals for the Determination of Electronic Band Gaps of Solids". In: *Journal of Chemical Theory and Computation* 15 (2019), pp. 5069–5079. DOI: 10.1021/acs.jctc.9b00322.

[20] Richard M. Martin. *Electronic Structure: Basic Theory and Practical Methods*. Cambridge University Press, 2004. DOI: 10.1017/CBO9780511805769.

[21] Ralf Stowasser and Roald Hoffmann. "What Do the Kohn−Sham Orbitals and Eigenvalues Mean?" In: *Journal of the American Chemical Society* 121 (1999), pp. 3414–3420. DOI: 10.1021/ja9826892.

[22] John P. Perdew, Kieron Burke, and Matthias Ernzerhof. "Generalized Gradient Approximation Made Simple". In: *Phys. Rev. Lett.* 77 (1996), pp. 3865–3868. DOI: 10.1103/PhysRevLett.77.3865.

[23] John P. Perdew et al. "Restoring the Density-Gradient Expansion for Exchange in Solids and Surfaces". In: *Phys. Rev. Lett.* 100 (2008), p. 136406. DOI: 10.1103/PhysRevLett.100.136406.

[24] Gábor I. Csonka et al. "Assessing the performance of recent density functionals for bulk solids". In: *Phys. Rev. B* 79 (2009), p. 155107. DOI: 10.1103/PhysRevB.79.155107.

[25] Burak Himmetoglu et al. "Hubbard-corrected DFT energy functionals: The LDA+U description of correlated systems". In: *International Journal of Quantum Chemistry* 114 (2014), pp. 14–49. DOI: https://doi.org/10.1002/qua.24521.

[26] Yubo Zhang et al. "Symmetry-breaking polymorphous descriptions for correlated materials without interelectronic U". In: *Phys. Rev. B* 102 (2020), p. 045112. DOI: 10.1103/PhysRevB.102.045112.

[27] Antoine Georges et al. "Dynamical mean-field theory of strongly correlated fermion systems and the limit of infinite dimensions". In: *Rev. Mod. Phys.* 68 (1996), pp. 13–125. DOI: 10.1103/RevModPhys.68.13.

[28] Gabriel Kotliar and Dieter Vollhardt. "Strongly Correlated Materials: Insights From Dynamical Mean-Field Theory". In: *Physics Today* 57 (2004), pp. 53–59. DOI: 10.1063/1.1712502.

[29] Victor Rosendal et al. "Octahedral distortions in $\mathrm{SrNbO_3}$: Unraveling the structure-property relation". In: *Phys. Rev. Materials* 7 (2023), p. 075002. DOI: 10.1103/PhysRevMaterials.7.075002.

[30] T. Okuda et al. "Large thermoelectric response of metallic perovskites: $\mathrm{Sr_{1-}}_x\mathrm{La}_x\mathrm{TiO_3}(0 < x < 0.1)$". In: *Phys. Rev. B* 63 (2001), p. 113104. DOI: 10.1103/PhysRevB.63.113104.

[31] Tong Zhao et al. "Highly conductive Nb doped $SrTiO_3$ epitaxial thin films grown by laser molecular beam epitaxy". In: *Journal of Crystal Growth* 212 (2000), pp. 451–455. DOI: https://doi.org/10.1016/S0022-0248(00)00307-9.

[32] James M. Rondinelli and Nicola A. Spaldin. "Structure and Properties of Functional Oxide Thin Films: Insights From Electronic-Structure Calculations". In: *Advanced Materials* 23 (2011), pp. 3363–3381. DOI: https://doi.org/10.1002/adma.201101152.

[33] Daichi Oka et al. "Intrinsic high electrical conductivity of stoichiometric $SrNbO_3$ epitaxial thin films". In: *Phys. Rev. B* (2015). DOI: 10.1103/PhysRevB.92.205102.

[34] DY Wan et al. "Electron transport and visible light absorption in a plasmonic photocatalyst based on strontium niobate". In: *Nature communications* 8 (2017), p. 15070. DOI: 10.1038/ncomms15070.

[35] M. Gajdoš et al. "Linear optical properties in the projector-augmented wave methodology". In: *Phys. Rev. B* 73 (2006), p. 045112. DOI: 10.1103/PhysRevB.73.045112.

[36] Georg K.H. Madsen, Jesús Carrete, and Matthieu J. Verstraete. "BoltzTraP2, a program for interpolating band structures and calculating semi-classical transport coefficients". In:

Computer Physics Communications 231 (2018), pp. 140–145. DOI: 10.1016/j.cpc.2018.05.010.

[37] G. Kresse and J. Furthmüller. "Efficient iterative schemes for ab initio total-energy calculations using a plane-wave basis set". In: *Phys. Rev. B* 54 (1996). DOI: 10.1103/PhysRevB.54.11169.

[38] Alim B. Alchagirov et al. "Energy and pressure versus volume: Equations of state motivated by the stabilized jellium model". In: *Phys. Rev. B* 63 (2001), p. 224115. DOI: 10.1103/PhysRevB.63.224115.

[39] A. M. Glazer. "The classification of tilted octahedra in perovskites". In: *Acta Crystallographica Section B* 28 (1972), pp. 3384–3392. DOI: 10.1107/s0567740872007976.

[40] Vei Wang et al. "VASPKIT: A user-friendly interface facilitating high-throughput computing and analysis using VASP code". In: *Computer Physics Communications* 267 (2021), p. 108033. DOI: 10.1016/j.cpc.2021.108033.

[41] Ulrich Aschauer and Nicola A. Spaldin. "Competition and cooperation between antiferrodistortive and ferroelectric instabilities in the model perovskite $SrTiO_3$". In: *Journal of Physics: Condensed Matter* 26 (2014), p. 122203. DOI: 10.1088/0953-8984/26/12/122203.

[42] Joshua Young and James M. Rondinelli. "Octahedral Rotation Preferences in Perovskite Iodides and Bromides". In: *Journal of Physical Chemistry Letters* 7 (2016), pp. 918–922. DOI: 10.1021/acs.jpclett.6b00094.

[43] H. J. Xiang et al. "Rules and mechanisms governing octahedral tilts in perovskites under pressure". In: *Phys. Rev. B* 96 (2017), p. 054102. DOI: 10.1103/PhysRevB.96.054102.

[44] Kazuyuki Uchida, Shinji Tsuneyuki, and Tatsuo Schimizu. "First-principles calculations of carrier-doping effects in $SrTiO_3$". In: *Phys. Rev. B* (2003), p. 174107. DOI: 10.1103/PhysRevB.68.174107.

[45] V. M. Goldschmidt. "Die Gesetze der Krystallochemie". In: *Die Naturwissenschaften* 14 (1926), pp. 477–485. DOI: 10.1007/BF01507527.

[46] Moritz M. Hirschmann et al. "Symmetry-enforced band crossings in tetragonal materials: Dirac and Weyl degeneracies on points, lines, and planes". In: *Phys. Rev. Materials* 5 (2021), p. 054202. DOI: 10.1103/PhysRevMaterials.5.054202.

[47] Zhi Wang et al. "Mass enhancement in 3d and s-p perovskites from symmetry breaking". In: *Phys. Rev. B* 103 (2021), p. 165110. DOI: 10.1103/PhysRevB.103.165110.

[48] Tao Zhu et al. "Generation of multiple plasmons in strontium niobates mediated by local field effects". In: *Phys. Rev. B* 98 (2018), p. 235115. DOI: 10.1103/PhysRevB.98.235115.

[49] Mathieu Mirjolet et al. "Optical Plasmon Excitation in Transparent Conducting $SrNbO_3$ and $SrVO_3$ Thin Films". In: *Advanced Optical Materials* 9 (2021), p. 2100520. DOI: 10.1002/adom.202100520.

[50] J. Harl et al. "Ab initio reflectance difference spectra of the bare and adsorbate covered Cu(110) surfaces". In: *Phys. Rev. B* 76 (2007), p. 035436. DOI: 10.1103/PhysRevB.76.035436.

[51] Voicu Popescu and Alex Zunger. "Extracting E versus $\vec{k}$ effective band structure from supercell calculations on alloys and impurities". In: *Phys. Rev. B* 85 (2012), p. 085201. DOI: 10.1103/PhysRevB.85.085201.

[52] Di Xiao, Ming-Che Chang, and Qian Niu. "Berry phase effects on electronic properties". In: *Rev. Mod. Phys.* 82 (2010), pp. 1959–2007. DOI: 10.1103/RevModPhys.82.1959.

[53] M Zahid Hasan et al. "Weyl, Dirac and high-fold chiral fermions in topological quantum matter". In: *Nature Reviews Materials* 6 (2021), pp. 784–803. DOI: 10.1038/s41578-021-00301-3.

[54] Nicola Marzari et al. "Maximally localized Wannier functions: Theory and applications". In: *Rev. Mod. Phys.* 84 (2012), pp. 1419–1475. DOI: 10.1103/RevModPhys.84.1419.
[55] Giovanni Pizzi et al. "Wannier90 as a community code: new features and applications". In: *Journal of Physics: Condensed Matter* 32 (2020), p. 165902. DOI: 10.1088/1361-648x/ab51ff.
[56] Xin Gang Zhao et al. "Effect of static local distortions vs. dynamic motions on the stability and band gaps of cubic oxide and halide perovskites". In: *Materials Today* 49 (2021), pp. 107–122. DOI: 10.1016/j.mattod.2021.05.021.
[57] Maxwell Thomas Dylla, Stephen Dongmin Kang, and G. Jeffrey Snyder. "Effect of Two-Dimensional Crystal Orbitals on Fermi Surfaces and Electron Transport in Three-Dimensional Perovskite Oxides". In: *Angewandte Chemie International Edition* 58 (2019), pp. 5503–5512. DOI: https://doi.org/10.1002/anie.201812230.
[58] Paolo Giannozzi et al. "QUANTUM ESPRESSO: a modular and open-source software project for quantum simulations of materials". In: *Journal of Physics: Condensed Matter* 21 (2009), p. 395502. DOI: 10.1088/0953-8984/21/39/395502.
[59] QuanSheng Wu et al. "WannierTools: An open-source software package for novel topological materials". In: *Computer Physics Communications* 224 (2018), pp. 405–416. DOI: https://doi.org/10.1016/j.cpc.2017.09.033.
[60] Guo-Xiang Zhi et al. "WannSymm: A symmetry analysis code for Wannier orbitals". In: *Computer Physics Communications* 271 (2022), p. 108196. DOI: https://doi.org/10.1016/j.cpc.2021.108196.
[61] Tomáš Bzdušek et al. "Nodal-chain metals". In: *Nature* 538 (2016), pp. 75–78. DOI: 10.1038/nature19099.
[62] Chen Fang et al. "Topological nodal line semimetals with and without spin-orbital coupling". In: *Phys. Rev. B* 92 (2015), p. 081201. DOI: 10.1103/PhysRevB.92.081201.
[63] Byungmin Sohn et al. "Sign-tunable anomalous Hall effect induced by two-dimensional symmetry-protected nodal structures in ferromagnetic perovskite thin films". In: *Nature materials* 20 (2021), pp. 1643–1649. DOI: 10.1038/s41563-021-01101-4.
[64] Gaomin Wang et al. "Role of disorder and correlations in the metal-insulator transition in ultrathin $SrVO_3$ films". In: *Phys. Rev. B* 100 (2019), p. 155114. DOI: 10.1103/PhysRevB.100.155114.
[65] Hikaru Okuma et al. "Transport properties around the metal-insulator transition for $SrVO_3$ ultrathin films fabricated by electrochemical etching". In: *Phys. Rev. B* 105 (2022), p. 045138. DOI: 10.1103/PhysRevB.105.045138.
[66] Arindom Chatterjee et al. "On the thermoelectric properties of Nb-doped $SrTiO_3$ epitaxial thin films". In: *Phys. Chem. Chem. Phys.* 24 (2022), pp. 3741–3748. DOI: 10.1039/D1CP03679C.
[67] Gianaurelio Cuniberti, Giorgos Fagas, and Klaus Richter. *Introducing molecular electronics: A brief overview*. Springer, 2005.
[68] M. Paulsson. *Non Equilibrium Green's Functions for Dummies: Introduction to the One Particle NEGF equations*. 2006. arXiv: cond-mat/0210519 [cond-mat.mes-hall].
[69] Dmitry A Ryndyk et al. *Theory of quantum transport at nanoscale*. Vol. 184. Springer, 2016, p. 9.
[70] M P Lopez Sancho, J M Lopez Sancho, and J Rubio. "Quick iterative scheme for the calculation of transfer matrices: application to Mo (100)". In: *Journal of Physics F: Metal Physics* 14 (1984), p. 1205. DOI: 10.1088/0305-4608/14/5/016.
[71] Mads Brandbyge et al. "Density-functional method for nonequilibrium electron transport". In: *Phys. Rev. B* 65 (2002), p. 165401. DOI: 10.1103/PhysRevB.65.165401.
[72] Alberto García et al. "Siesta: Recent developments and applications". In: *The Journal of Chemical Physics* 152 (2020), p. 204108. DOI: 10.1063/5.0005077.

[73] Nick Papior et al. "Improvements on non-equilibrium and transport Green function techniques: The next-generation transiesta". In: *Computer Physics Communications* 212 (2017), pp. 8–24. DOI: https://doi.org/10.1016/j.cpc.2016.09.022.

[74] John P. Perdew, Kieron Burke, and Matthias Ernzerhof. "Generalized Gradient Approximation Made Simple". In: *Phys. Rev. Lett.* 77 (1996), pp. 3865–3868. DOI: 10.1103/PhysRevLett.77.3865.

[75] Nick Papior. *sisl: v13.0*. 2023. DOI: 10.5281/zenodo.597181. URL: https://doi.org/10.5281/zenodo.597181.

[76] Chiara Ricca et al. "Self-consistent site-dependent DFT+U study of stoichiometric and defective $SrMnO_3$". In: *Phys. Rev. B* 99 (2019), p. 094102. DOI: 10.1103/PhysRevB.99.094102.

[77] Troels Markussen et al. "Scaling Theory Put into Practice: First-Principles Modeling of Transport in Doped Silicon Nanowires". In: *Phys. Rev. Lett.* 99 (2007), p. 076803. DOI: 10.1103/PhysRevLett.99.076803.

[78] Troels Markussen et al. "Scattering cross section of metal catalyst atoms in silicon nanowires". In: *Phys. Rev. B* 81 (2010), p. 125307. DOI: 10.1103/PhysRevB.81.125307.

[79] Magnus Paulsson and Mads Brandbyge. "Transmission eigenchannels from nonequilibrium Green's functions". In: *Phys. Rev. B* 76 (2007), p. 115117. DOI: 10.1103/PhysRevB.76.115117.

[80] A. J. Minnich et al. "Thermal conductivity spectroscopy technique to measure phonon mean free paths". In: *Phys. Rev. Lett.* (2011), p. 095901. DOI: 10.1103/PhysRevLett.107.095901.

[81] Yongjie Hu et al. "Spectral mapping of thermal conductivity through nanoscale ballistic transport". In: *Nature Nanotechnology* 10 (2015), pp. 701–706. DOI: 10.1038/nnano.2015.109.

[82] Chengyun Hua and Austin J. Minnich. "Analytical Green's function of the multidimensional frequency-dependent phonon Boltzmann equation". In: *Phys. Rev. B* 90 (2014), p. 214306. DOI: 10.1103/PhysRevB.90.214306.

[83] Chengyun Hua and Austin J. Minnich. "Heat dissipation in the quasiballistic regime studied using the Boltzmann equation in the spatial frequency domain". In: *Phys. Rev. B* 97 (2018), p. 014307. DOI: 10.1103/PhysRevB.97.014307.

[84] J.M. Ziman. *Electrons and Phonons: The Theory of Transport Phenomena in Solids*. Oxford University Press, 2001. DOI: 10.1093/acprof:oso/9780198507796.001.0001.

[85] Brent Fultz. "Vibrational thermodynamics of materials". In: *Progress in Materials Science* 55 (2010), pp. 247–352. DOI: https://doi.org/10.1016/j.pmatsci.2009.05.002.

[86] T. Tadano, Y. Gohda, and S. Tsuneyuki. "Anharmonic force constants extracted from first-principles molecular dynamics: Applications to heat transfer simulations". In: *Journal of Physics: Condensed Matter* 26 (2014), p. 225402. DOI: 10.1088/0953-8984/26/22/225402.

[87] Terumasa Tadano and Shinji Tsuneyuki. "Self-consistent phonon calculations of lattice dynamical properties in cubic $SrTiO_3$ with first-principles anharmonic force constants". In: *Phys. Rev. B* 92 (2015), p. 054301. DOI: 10.1103/PhysRevB.92.054301.

[88] Mark Lundstrom. *Fundamentals of Carrier Transport*. 2nd ed. Cambridge University Press, 2000. DOI: 10.1017/CBO9780511618611.

[89] Jean Philippe M. Péraud and Nicolas G. Hadjiconstantinou. "Efficient simulation of multidimensional phonon transport using energy-based variance-reduced Monte Carlo formulations". In: *Phys. Rev. B* 84 (2011), p. 205331. DOI: 10.1103/PhysRevB.84.205331.

[90] Jean-Philippe M. Peraud, Colin D. Landon, and Nicolas G. Hadjiconstantinou. "Monte Carlo Methods for Solving the Boltzmann Transport Equation". In: *Annual Review of Heat Transfer* (2014), pp. 205–265. DOI: 10.1615/annualrevheattransfer.2014007381.

[91] Arpit Mittal and Sandip Mazumder. "Monte Carlo Study of Phonon Heat Conduction in Silicon Thin Films Including Contributions of Optical Phonons". In: *Journal of Heat Transfer* 132 (2010), p. 052402. DOI: 10.1115/1.4000447.

[92] Shin Ichiro Tamura. "Isotope scattering of dispersive phonons in Ge". In: *Phys. Rev. B* 27 (1983), pp. 858–866. DOI: 10.1103/PhysRevB.27.858.

[93] Bolin Liao et al. "Significant reduction of lattice thermal conductivity by the electron-phonon interaction in silicon with high carrier concentrations: A first-principles study". In: *Phys. Rev. Lett.* 114 (2015), p. 115901. DOI: 10.1103/PhysRevLett.114.115901.

[94] Benny Guralnik et al. "Determination of thermoelectric properties from micro four-point probe measurements". In: *Measurement Science and Technology* 33 (2022), p. 125001. DOI: 10.1088/1361-6501/ac88ea.

[95] Vazrik Chiloyan et al. "Thermal transport exceeding bulk heat conduction due to nonthermal micro/nanoscale phonon populations". In: *Applied Physics Letters* (2020), p. 163102. DOI: 10.1063/1.5139069.

[96] H.S. Carslaw and J.C. Jaeger. *Conduction of Heat in Solids*. Clarendon Press, 1959.

[97] Neetu Lamba et al. *Deconvolution of Heat Sources for Application in Thermoelectric Micro Four-Point Probe Measurements*. DOI: 10.2139/ssrn.4243742.

Appendix A

Band folding and Brillouin zones

In Figure A.1 the 1st BZ of $a^0a^0c^-$ and $a^0a^0c^+$ are shown within the 1st BZ of $a^0a^0a^0$. The arrows indicate how the bands are folded from the larger BZ of $a^0a^0a^0$ to the smaller BZ of the tilted structures.

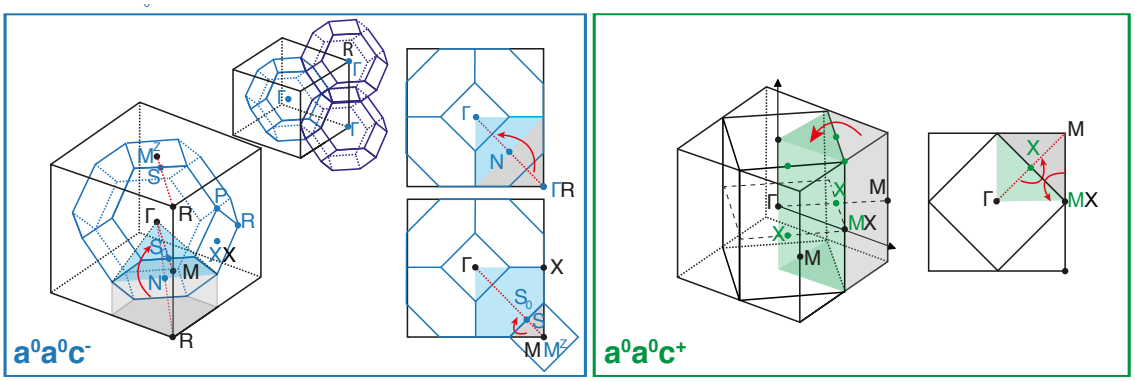

Figure A.1: Illustration of the folding of $a^0a^0c^-$ and $a^0a^0c^+$ in the $a^0a^0a^0$ 1st BZ. Figure created by Alla Chikina and taken from manuscript appended in Section B.2.

Appendix B

Paper and manuscripts

In this chapter the paper and manuscripts that this thesis is based on are appended. Each paper or manuscript has its own section.

B.1 Octahedral distortions in $SrNbO_3$: Unraveling the structure-property relation

This paper is a purely theoretical study about how biaxial strain couples to the octahedral rotations in $SrNbO_3$. The optical loss function and the Seebeck coefficient is calculated as a function of octahedral rotation. This was done to get insight into how these distortions affect important material properties. Fascinatingly, a pure in-phase rotation is found to be lower in energy, compared to the common out-of-phase rotation. Compressive biaxial strain stabilizes this rotation, which indicates its relevance for practical purposes since $SrNbO_3$ has a rather large lattice constant, compared to, e.g., $SrTiO_3$ which is a common substrate. I performed all calculations except for the DMFT calculations (they were performed by Walber Hugo Brito). This paper is published and can be found as Reference [29].

Octahedral distortions in $SrNbO_3$: Unraveling the structure-property relation

Victor Rosendal [1,*] Walber H. Brito [2] Milan Radovic,[3] Alla Chikina [3] Mads Brandbyge [4] Nini Pryds [1,†] and Dirch H. Petersen [1]

[1]*Department of Energy Conversion and Storage, Technical University of Denmark, 2800 Kgs. Lyngby, Denmark*
[2]*Departamento de Física, Universidade Federal de Minas Gerais, C. P. 702, 30123-970, Belo Horizonte, MG, Brazil*
[3]*Swiss Light Source, Paul Scherrer Institut, CH-5232 Villigen, Switzerland*
[4]*Department of Physics, Technical University of Denmark, 2800 Kgs. Lyngby, Denmark*

(Received 1 March 2023; revised 1 June 2023; accepted 20 June 2023; published 20 July 2023)

Strontium niobate has triggered a lot of interest as a transparent conductor and as a possible realization of a correlated Dirac semimetal. Using the lattice parameters as a tunable knob, the energy landscape of octahedral tilting was mapped using density functional theory calculations. We find that biaxial compressive strain induces tilting around the out-of-plane axis, while tensile strain induces tilting around the two in-plane axes. The two competing distorted structures for compressive strain show semi-Dirac dispersions above the Fermi level in their electronic structure. Our density functional theory calculations combined with dynamical mean field theory reveal that dynamical correlations downshift these semi-Dirac-like cones towards the Fermi energy. More generally, our study reveals that the competition between the *in-phase* and *out-of-phase* tilting in $SrNbO_3$ provides a new degree of freedom that allows for tuning the thermoelectric and optical properties. We show how the tilt angle and mode are reflected in the behavior of the Seebeck coefficient and the plasma frequency due to changes in the band structure.

DOI: 10.1103/PhysRevMaterials.7.075002

I. INTRODUCTION

The perovskite (oxide) structure, ABO_3, is a versatile structure relevant in many existing and emerging applications [1] including piezoelectricity [2], thermoelectricity [3], oxygen separation, and solid oxide fuel cells [4]. It is also a platform where the coupling of charge, spin, and orbital degrees of freedom takes place, giving rise to numerous materials with interesting electronic and magnetic properties such as superconductivity [5], colossal magnetoresistance [6], metal-insulator transitions [7,8], and more recently the realization of correlated Dirac semimetallic states [9].

One possible way of changing the properties of perovskite oxides is to apply strain to the crystal [10,11]. This can be achieved by epitaxial growth of films on substrates with different lattice parameters. The lattice mismatch between the substrate and the film will induce strain in the system. The compression (tension) induced by the substrate will shrink (expand) the in-plane B-O bond length from its equilibrium value. As a response, the oxygen ions can displace and alter the B-O-B bond angle and bond lengths, and in this way relieve stress. This displacement will be referred to as *octahedral tilt* or *octahedral rotation*, and it is visualized in Fig. 1.

Strontium niobate, $SrNbO_3$, is a conducting perovskite oxide that has gained interest in recent years [9,12–14]. $SrNbO_3$ has a larger lattice parameter in comparison to the prototypical $SrTiO_3$, i.e., 4.023 and 3.905 Å, respectively [12]. Park *et al.* investigated $SrNbO_3$ as a potential transparent conductor due to its large gap between the (filled) conduction and valence states [14]. The energy gap between the valence-band maximum and the conduction-band minimum is ∼2.3 eV, predicted with density functional theory in Ref. [14]. Further interest has been related to the emerging Dirac states in heavily strained $SrNbO_3$ thin films. Both theoretical and experimental work suggests that light electrons emerge in strained $SrNbO_3$ films due to the induced octahedral tilting [9].

Yet, there has been no systematic investigation of the atomic and electronic structure of $SrNbO_3$ under biaxial stress, e.g., found in epitaxial thin films, especially including octahedral tilting. Theoretical calculations provide a fast and unique way to investigate the local distortions, which are difficult to access using experimental techniques [15]. This has been shown to be important for explaining metal-insulator behavior in $3d$ perovskite oxides using standard density functional theory (DFT) methods [16]. Distortions such as octahedral tilting alter the electronic configuration, specifically the orbital overlaps and bandwidths, W. The ratio between the interelectronic Coulomb interaction and the bandwidth, U/W, describes the strength of the electron correlation. Furthermore, a large ratio can result in a localization of the electrons, i.e., U/W governs the Mott metal-insulator transition [17]. Hence, the electrical properties are dependent on the bandwidth, which is connected to distortions such as octahedral tilting. Similarly, there is a connection between the bandwidth and the optical response of a material. The plasma

*vicros@dtu.dk
†nipr@dtu.dk

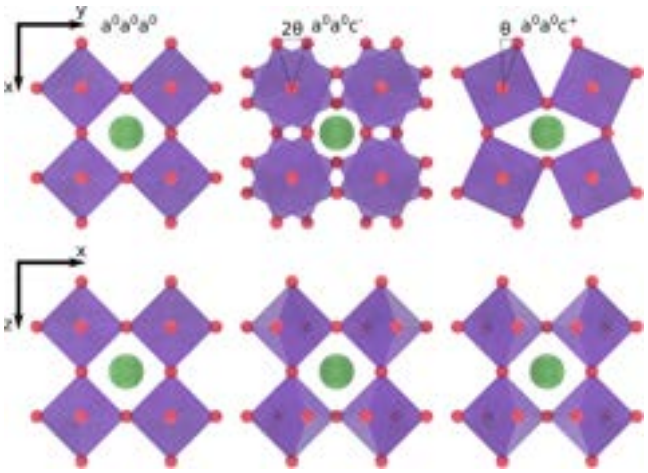

FIG. 1. Illustration of different octahedral tilting modes. The left column shows $a^0a^0a^0$ (no tilt), the middle column shows $a^0a^0c^-$ (*out-of-phase* tilting), and the right column shows $a^0a^0c^+$ (*in-phase* tilting). The upper (lower) row shows the structures in the xy-plane (zx-plane). In the $SrNbO_3$ structure, the octahedra are formed by oxygen (red) centered around niobium atoms. The green spheres correspond to strontium atoms.

frequency that governs the optical response can be written as $\omega_p = e\sqrt{n/(m^*\varepsilon)}$, with e being the elemental charge, n is the carrier concentration, m^* is the effective mass, and ε is the permittivity [13,18]. The plasma frequency is then related to the bandwidth through the effective mass $m^* \propto 1/W$. Therefore, a reduction of the bandwidth (or increase in effective mass) results in a redshift of the plasma frequency. Due to the connection between atomic structure and electrical and optical properties discussed here, it is worthwhile to consider the influence of octahedral tilting on the material properties of $SrNbO_3$.

In this study, we first address the atomic and electronic structure for $SrNbO_3$ as a function of epitaxial strain using DFT. Since $SrTiO_3$ is a very common substrate for growing perovskite oxides and has been investigated extensively before, we used it as a reference for all calculations. Both compressive and tensile biaxial strain is considered, and the applied strain is always in the (001)-plane of $SrTiO_3$ and $SrNbO_3$. Different octahedral tilts have been investigated with respect to the imposed strain, and the stabilization of the different octahedral tilts with respect to doping was analyzed. Furthermore, we investigate how the excitation spectra and degree of electronic correlations of $SrNbO_3$ evolve as a function of octahedral tilting. The Seebeck coefficient and the optical loss function have been studied for relevant octahedral tilting modes and angles. We aimed at establishing a complete picture of octahedral tilting in $SrNbO_3$ for various strains.

II. COMPUTATIONAL METHODS

Density functional theory (DFT) [19] was used to investigate the atomic and electronic structures of $SrNbO_3$ (and $SrTiO_3$). Our DFT calculations were performed using the exchange-correlation functional PBEsol, and projector augmented wave (PAW) potentials [20,21] as implemented in *Vienna Ab initio Simulation Package* (VASP) [22]. The PBEsol functional was chosen due to its ability to predict accurate lattice parameters as pointed out in Refs. [23,24]. The total energies were calculated with Γ-centered k-point meshes $8 \times 8 \times 8$ and $4 \times 4 \times 4$ for the primitive (5-atom) cell and $2 \times 2 \times 2$ (40-atom) supercell, respectively. The self-consistent loops were converged below 1×10^{-6} eV and the plane-wave energy cutoff was set to 550 eV. A force tolerance of 0.01 eV/Å was set during the relaxations. Octahedral tilts were introduced to the $2 \times 2 \times 2$ supercells by moving the oxygen ions according to $\delta = \tan(\theta)(a/2)$, where δ is the displacement due to a rotation and $a/2$ is the B-O distance, expressed by the lattice parameter, a. A rotation around, e.g., the z-axis would result in a shift $\pm\delta$ in x for the oxygen ions on the y-axis, and vice versa. The sign alternates between each adjacent octahedra in the xy-plane (and also between each layer in the z-direction for out-of-phase tilting). The space groups of the tilted structures were checked using spglib [25].

Using the DFT obtained relaxed structures, we performed DFT plus dynamical mean field theory (DMFT) calculations at 200 K for $SrNbO_3$ using the *state-of-the-art* fully charge self-consistent implementation [26]. The DFT part was done within the Perdew-Burke-Ernzerhof generalized gradient approximation (PBE-GGA) [27] as implemented in the WIEN2K package [28]. Within our implementation, we take into account all the itinerant and correlated states (Nb-t_{2g}) within a large energy window (20 eV) around the chemical potential. This is done using a projector that preserves both causality and spectral weight as proposed in Ref. [26]. The DMFT impurity problem was solved by using continuous-time quantum Monte Carlo (CTQMC) calculations [29], with a Hubbard $U = 6.0$ eV and Hund's coupling $J = 0.8$ eV. These values are chosen since they are similar to the ones used in previously published DFT+DMFT studies of $SrNbO_3$ [13,14]. To compute the spectral functions, we performed the analytical continuation of the self-energy using the maximum entropy method [26].

The Seebeck coefficient was predicted within the constant relaxation-time approximation employing BOLTZTRAP2 [30]. This was done using a charge density calculated with a k-point density corresponding to $15 \times 15 \times 15$ for the 5-atom cubic unit cell. Non-self-consistent calculations were performed using a k-point mesh of $50 \times 50 \times 50$ for the 5-atom cubic unit cell. The electronic states were then interpolated on a grid 15 times as dense using BOLTZTRAP2. The temperature was set to 300 K.

The complex dielectric function was calculated using the independent-particle random phase approximation (RPA) as implemented in VASP. This implies that the excitations are assumed to be independent, given by the bare Kohn-Sham band structure and neglect of the local field effects [31]. A phenomenological Drude term was added to model the contribution of intraband transitions; see Appendix B. The imaginary part was set to 0.3 eV, which creates good agreement with experimental loss functions in Ref. [18].

III. RESULTS AND DISCUSSIONS

A. Energy landscape of octahedral tilts

The lattice parameters for varying degrees of biaxial strain were calculated for $SrNbO_3$. This was done

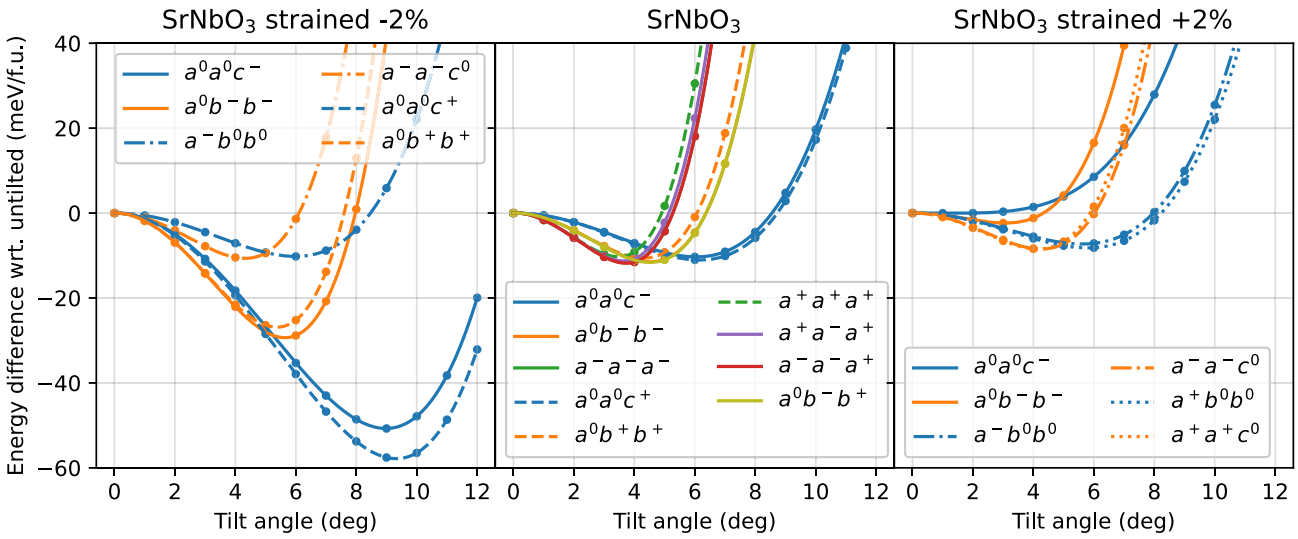

FIG. 2. Energy landscapes of octahedral tilting in $SrNbO_3$ under different amounts of biaxial strain. The energy shown is the difference in total internal energy between the tilted structure and untilted structure. The middle plot is the case of no biaxial strain. Compressive strain stabilizes the tilts around the out-of-plane axis, while tensile strain leads to preferred rotations around the in-plane axes. The *in-phase* tilt $a^0a^0c^+$ is found to have the largest energy gain in compressively strained $SrNbO_3$.

using the high-symmetry 5-atom unit cells, i.e., excluding any symmetry-breaking octahedral tilting. The relative difference, $(a_{\mathrm{DFT}} - a_{\mathrm{exp}})/a_{\mathrm{exp}}$, was $\sim -0.15\%$ for unstrained $SrNbO_3$. Here, $a_{\mathrm{DFT}} = 4.0182$ Å and $a_{\mathrm{exp}} = 4.023$ Å [12] are the predicted and experimental unstrained lattice parameters, respectively. A table of the relaxed out-of-plane lattice parameters for different biaxial strains between -3% and $+3\%$ can be found in Appendix A. These lattice parameters were fixed throughout the rest of the study.

Using the calculated lattice parameters, we predicted the energy landscapes of the octahedral tilting for varying degrees of strain. In the case of unstrained $SrNbO_3$ (and $SrTiO_3$) the following pure octahedral tilts were investigated (using Glazer's notation [32]): $a^0a^0c^-$, $a^0a^0c^+$, $a^0b^-b^-$, $a^0b^+b^+$, $a^-a^-a^-$, and $a^+a^+a^+$. Combined *in-phase* and *out-of-phase* tilts were also sampled, e.g., $a^+a^-a^+$, $a^-a^-a^+$, and $a^0b^-b^+$. The letters a, b, and c correspond to the rotation angles around the x, y, and z axis, respectively, and the $+/-$ signs denote *in-phase* and *out-of-phase* rotation between two adjacent octahedra; see Fig. 1. The superscript 0 denotes that no rotation is performed around that Cartesian axis. For the strained systems, we examined octahedral tilts around both the *in-plane* and *out-of-plane* axes, since they are no longer symmetrically equivalent. These calculations were performed on fixed tilts, i.e., for each structure the energy was only evaluated once (self-consistently) without any update of the atomic positions. In this work, we generally did not consider tilts with different angles around different axes, i.e., it is assumed that the rotation angles are the same around all axes (except if one or more is zero). However, since neutron diffraction studies of $SrNbO_3$ have shown indications of the $a^-a^-c^+$ tilt mode [33], this mode was investigated additionally. To check if $a^-a^-c^+$ is preferred over $a^-a^-a^+$, we varied the rotation angles θ_a and θ_c for $a^-a^-c^+$. The energy was never below the $a^-a^-a^+$ mode with tilt angle 4°, i.e., $a^-a^-c^+$ is not preferred over $a^-a^-a^+$. However, since the energy landscape of unstrained $SrNbO_3$ is rather shallow, it is possible that $SrNbO_3$ might condense into any of the competing modes, including more general modes such as $a^-a^-c^+$ with different rotation angles around the different axes. Furthermore, the stability of $a^0a^0c^+$ and $a^0a^0c^-$ was confirmed in the case of compressive strain by including a small rotation around the x and the y axis. Minimizing the ionic forces led to a suppression of these rotations, which suggests that the lowest energies are in fact found for systems with rotation *only* around the *out-of-plane* axis in the case of compressive strain.

Figure 2 shows the total internal energy landscapes for different octahedral tilts in $SrNbO_3$ under varying degrees of strain. The reference energy is the total internal energy of the untilted structures, so that the energy goes to zero at zero tilt angle (each strain has its own reference energy). For unstrained $SrNbO_3$, all octahedral tilts show an energy reduction, including the *in-phase* tilting modes. This is not the case for the unstrained $SrTiO_3$ (see Fig. 3 or Appendix F). This is a notable feature, since the *in-phase* tilting is rare in oxide perovskites [34]. Furthermore, the energy gain is larger than in $SrTiO_3$ and the optimal tilt angles are also slightly larger. For -2% strained $SrNbO_3$ ($SrTiO_3$) the $a^0a^0c^-$ tilt mode shows a gain of $\sim$50 meV f.u.$^{-1}$ (30 meV f.u.$^{-1}$) compared to the untilted phase, and the optimal tilt angle is $\sim 9^\circ$ (7.5°). The complete data set for $SrTiO_3$ and $SrNbO_3$ with additional strain values can be found in Appendix F.

By biaxially compressing the oxides (while relaxing the out-of-plane lattice parameter) the B-O bond length in the octahedral structure is contracted in-plane and extended out-of-plane. As a result, the oxygen network is distorted by octahedral tilting. This phenomenon can be seen in the left plot in Fig. 2, where the crystals are biaxially strained by -2% (with the out-of-plane lattice parameters relaxed; further details are given in Table I in Appendix A). The key messages

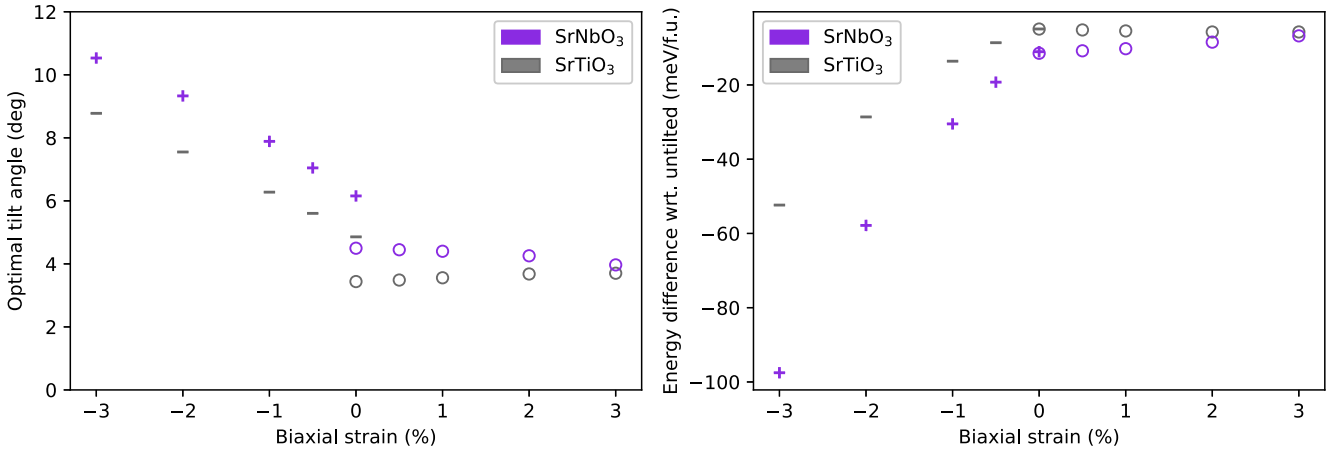

FIG. 3. Optimal tilt angles for $SrNbO_3$ and $SrTiO_3$ with varying biaxial strain. A plus (minus) sign means that the $a^0a^0c^+$ ($a^0a^0c^-$) tilt mode is lowest in energy, i.e., for $SrNbO_3$ the $a^0a^0c^+$ mode is lowest in energy under compressive strain. The circle marker denotes the $a^-a^-c^0$ tilting mode, which is the stable tilt under tensile strain. For 0% we include multiple data points, since the energies are very similar and it helps with understanding the limit from compressive to unstrained and tensile to unstrained.

are (i) due to the tetragonality, octahedral tilting is preferred around the (longer) out-of-plane axis, (ii) tilts around one and two axes are no longer degenerate (likely due to competition between B-O and A-O bond lengths, e.g., the A-O bond length is shorter for $a^0b^-b^-$ than $a^0a^0c^-$ and the B-O bond lengths are only slightly longer for $a^0b^-b^-$ than $a^0a^0c^-$), and (iii) *in-phase* tilts are energetically favorable for strained $SrNbO_3$, in contrast to $SrTiO_3$ where *out-of-phase* tilting is favorable. The energy gain for *in-phase* tilting relative to *out-of-phase* tilting in $SrNbO_3$ increases with larger biaxial compressive strain; see Appendix F. This behavior is interesting, because perovskite oxides typically show preference for *out-of-phase* tilting [34]. Furthermore, in a recent study where $SrNbO_3$ thin film was grown on $SrTiO_3$, x-ray diffraction experiments suggested that the $a^0a^0c^-$ tilting mode is stabilized under compressive strain [9].

Biaxial tensile stress elongates the lattice in-plane while the lattice contracts out-of-plane; see Table I. The resulting energy landscapes with respect to octahedral tilting for +2% biaxially strained $SrNbO_3$ is shown in Fig. 2. The calculated wells are quite shallow compared to the case of compressive strain; instead their depths are similar to the unstrained case. During tensile strain, the two in-plane lattice parameters are found to increase and the out-of-plane lattice parameter decreases. Therefore, oxygen octahedral tilting can only alleviate stress in one direction (out-of-plane) by octahedral rotation around the two in-plane axes. In other words, tensile biaxial strain leads to octahedral tilting around the in-plane axes, in contrast with compressive biaxial strain, which leads to tilting around the out-of-plane axis, in agreement with investigations of other perovskite oxides [35,36]. Due to the small energy gains observed here for tensile strained $SrNbO_3$, the possibility of stabilizing octahedral tilting by tensile strain is quite small, especially at elevated temperatures.

The overall optimal tilt modes and their magnitudes are shown in Fig. 3. Here we include $SrTiO_3$ as a reference. It is seen that the octahedral tilting is energetically more stable in the case of $SrNbO_3$ than for the case of $SrTiO_3$ (see also Appendix F). The optimal tilt angles are ∼25% larger in $SrNbO_3$ than $SrTiO_3$, which is true under compressive strain and small tensile strains. For larger tensile strains, the two materials show similar tilting behavior. It is interesting to note that the trends are reversed in tensile strained $SrNbO_3$ and $SrTiO_3$. Larger tensile strain is found to destabilize the tilting (both smaller energy gains and rotation angles) in $SrNbO_3$. The opposite is found in $SrTiO_3$.

In perovskite oxides, *out-of-phase* tilting (or tilts with both *in-phase* and *out-of-phase* components) is the most prevalent tilting mode. Young and Rondinelli [34] studied bromide and iodide perovskites and linked the octahedral tilt stability to electrostatic interactions, bond valency sums of the *A*-site ions, and charge distribution between the *A*-site ions and the cations. Here, the *A*-site ions are not displaced during octahedral tilting, hence the bond valency remains constant when comparing *out-of-phase* ($a^0a^0c^-$) and *in-phase* ($a^0a^0c^+$) tilts. This is because the bond valency is a function of the nearest-neighbor distances only.

To understand what stabilizes the *in-phase* tilt in $SrNbO_3$ and $SrTiO_3$, we controlled the doping by creating holes in $SrNbO_3$ and adding electrons in the case of $SrTiO_3$. We added (or removed) charge in steps of 0.25 electrons per formula unit up to 1 electron per formula unit. This was achieved using the background charge method, which allows for modeling of doping without having to introduce impurities by the use of supercells. Charge neutrality is kept by the introduction of a homogeneous background charge. While this method has its flaws, such as inaccurate lattice relaxations [37], it allows us to get some insight into the stability of tilting without more elaborate calculations. The lattice is kept fixed while analyzing the influence of doping, and only the oxygen ions are displaced. Additional electrons can increase the energy gain by octahedral tilting in $SrTiO_3$, as indicated in Ref. [38]. Hence, octahedral tilting is stabilized with the addition of electrons in $SrTiO_3$. Uchida *et al.* [38] attribute the stabilization of the tilting to the increase in size of the Ti ion, hence decreasing the Goldschmidt factor. The Goldschmidt tolerance factor,

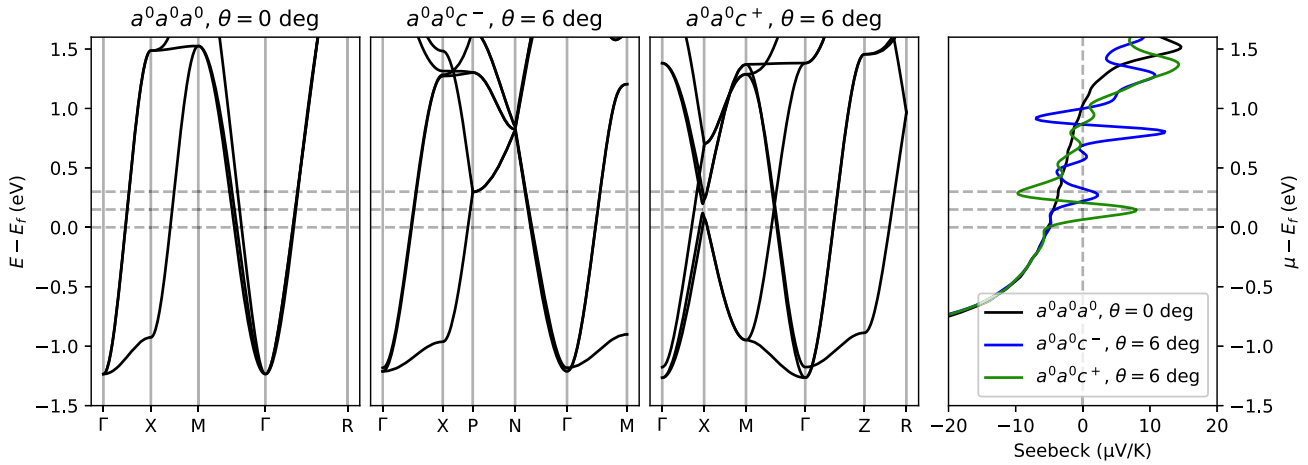

FIG. 4. Conduction bands of unstrained $SrNbO_3$ with $a^0a^0a^0$, $a^0a^0c^-$, and $a^0a^0c^+$ tilt modes. The tilt angle, θ, is set to 6°. To the right, the in-plane Seebeck coefficient as a function of chemical potential at 300 K is shown. The peaks in the Seebeck coefficient align with the (avoided) band crossings at P for $a^0a^0c^-$ and at X as well as along M-Γ for $a^0a^0c^+$. The Γ-point t_{2g} split is sensitive to the tilting mode. For $a^0a^0a^0$, the t_{2g} states are degenerate at Γ. The degeneracy is lifted for $a^0a^0c^-$ and $a^0a^0c^+$. The Brillouin zones, with sampled high-symmetry points, for the different tilting modes can be found in Appendix C.

$t = (r_A + r_O)/[\sqrt{2}(r_B + r_O)]$, where r_i denotes the ionic radius of ion i, indicates the stability of octahedral distortions in perovskite oxides [39]. In the following, we will focus only on −2% strained system since it is a relevant strain observed in thin films. The resulting energy landscapes are shown in Fig. 10 in Appendix D. By analyzing both the $a^0a^0c^-$ and the $a^0a^0c^+$ tilting modes, it is evident that including electrons reduces the energy difference between the two tilt modes. To the best of our knowledge, this has not been considered in earlier works. On the contrary, introducing holes to $SrNbO_3$ is found to destabilize the two tilt modes. Here, as in the case of $SrTiO_3$, changing the number of electrons (by addition of holes) also changes the energy difference between the two tilt modes. Interestingly, there is a critical point at which $a^0a^0c^-$ is stabilized over $a^0a^0c^+$ in $SrNbO_3$ (see Fig. 10). Adding 0.5 holes per formula unit, i.e., 0.5 holes per Nb ion, to $SrNbO_3$ makes the two tilt modes almost degenerate with a slight preference for $a^0a^0c^-$ over $a^0a^0c^+$.

This suggests that the stability of the *out-of-phase* ($a^0a^0c^-$) and *in-phase* ($a^0a^0c^+$) tilting modes is connected to the number of electrons and the size of the A ion (e.g., Nb and Ti). Further investigations by doping with different ion sizes could benefit our understanding of the stability of the various tilting modes in more complex scenarios. These results also suggest that the so-called rigid-band assumption should be used with caution for perovskites. In other words, it is possible that electron doping affects the octahedral tilting stability, hence the assumption that doping can be captured by a simple shift of Fermi level is questionable. In summary, these predictions suggest that it is possible to tune the stability of octahedral tilting by doping and/or gating.

The effect of dynamical correlations on the octahedral tilting was briefly investigated by calculating the total energy landscape of −2% strained $SrNbO_3$ using DFT+DMFT. We note that the free energy and total energy landscapes are very similar, and therefore we focus only on the latter. Here, we limited ourselves to $a^0a^0c^-$ and $a^0a^0c^+$. The total energy landscapes are qualitatively similar to the ones predicted using DFT, i.e., both tilt modes show stabilization and $a^0a^0c^+$ is preferred over $a^0a^0c^-$. However, the energy gains and optimal tilt angles are larger for DFT+DMFT compared to DFT. The $a^0a^0c^+$ mode shows an energy gain of ∼100 meV f.u.$^{-1}$ with a tilt angle of ∼10° within the DFT+DMFT framework. This is a substantial increase compared to DFT, and it is something to consider in future work related to octahedral tilting in oxides. However, since the qualitative trends are similar, we do not consider this further in this work.

B. Effects of tilt and strain on band structure and spectral function

We then moved over to the electronic structure of $SrNbO_3$. The electronic band structure of $SrNbO_3$ was studied with different octahedral tiltings. Here, we focus on $a^0a^0c^-$ and $a^0a^0c^+$ since they are both stabilized under compressive biaxial strain. The reference in these cases was the untilted ($a^0a^0a^0$) $SrNbO_3$.

In Fig. 4 the conduction bands for unstrained $SrNbO_3$ are shown for different octahedral tilts. The band structures are calculated along high-symmetry points of the first Brillouin zone for the different crystals (see Appendix C for Brillouin zones). Here, the rotation angle is set to 6°, which is close to the minima for $a^0a^0c^-$ and $a^0a^0c^+$ in the unstrained case. The untilted system shows the heavy and light bands which originate from the t_{2g}-like niobium orbitals. Since the tilts require repetitions of the minimal unit cell, there are additional bands in $a^0a^0c^-$ and $a^0a^0c^+$. The *out-of-phase* tilt $a^0a^0c^-$ shows a semi-Dirac point at P, in agreement with Ref. [9]. This tilt mode has been further investigated theoretically illustrating the tunability of the Berry phase and the anomalous Hall coefficient [40]. A similar dispersion is found at the X-point in $a^0a^0c^+$, albeit at a substantially higher energy. Both tilt modes

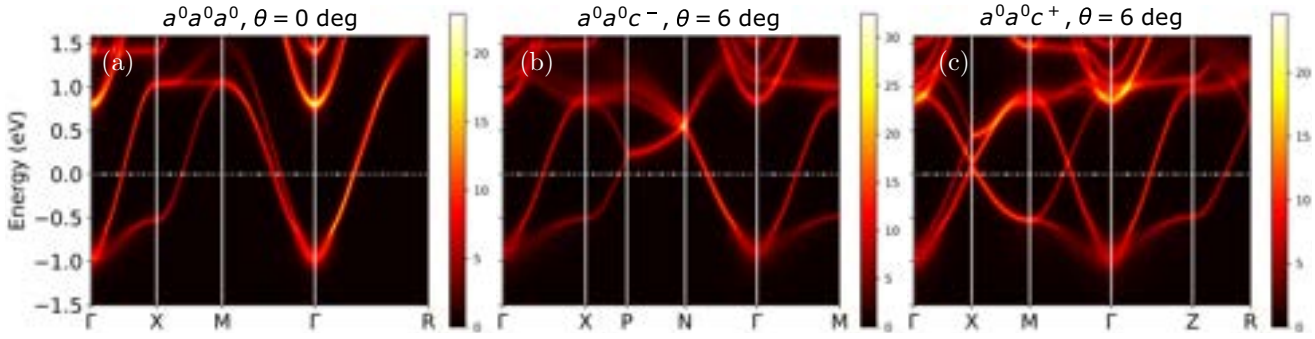

FIG. 5. DFT+DMFT calculated spectral functions at 200 K of unstrained $SrNbO_3$ with $a^0a^0a^0$ (a), $a^0a^0c^-$ (b), and $a^0a^0c^+$ (c) tilt modes.

create t_{2g} splitting at the Γ-point, however for $a^0a^0c^-$ with 6° rotation angle the splitting is quite small. The *in-phase* tilt $a^0a^0c^+$ shows a gap opening at the X-point slightly above the Fermi level. The band velocities are low at the bottom of the conduction bands and higher near the Fermi level, as can be seen from the slope of the bands ($\hbar v_{\mathbf{k}} = \partial_{\mathbf{k}}\epsilon_{\mathbf{k}}$). Moreover, the bands near the Dirac points show both mobile and slow carriers, as indicated by the slopes of the bands. As an example, the states from P to X show high velocities, while the opposite is true for the states from P towards N in the case of $a^0a^0c^-$.

The qualitative picture of the band structure is rather similar for compressively strained $SrNbO_3$ (see Appendix G). There are, however, a few noteworthy changes. Straining introduces t_{2g} splitting in the untilted system, due to a symmetry lowering from cubic to tetragonal. Inclusion of octahedral tilting further splits the t_{2g} states. For −2% strained $SrNbO_3$, the split is ∼0.15 and 0.3 eV for $a^0a^0c^-$ and $a^0a^0c^+$, respectively, both with a 9° tilt angle. By examining the splitting for different strain-tilt combinations, it is observed that the large t_{2g} splitting in strained $SrNbO_3$ originates from both the strain alone and from the increase in tilt angle with strain. The t_{2g} splitting at the Γ point can be found in Appendix E. As an example, the t_{2g} splitting in −1% strained $a^0a^0a^0$ is ∼0.05 eV and is of similar magnitude to the splitting in unstrained $a^0a^0c^+$ with a 6° tilt angle. Furthermore, the Dirac point at P is shifted closer to the Fermi level for $a^0a^0c^-$ with compressive strain, while the gapping at X is larger in the case of −2% strained $a^0a^0c^+$ with a 9° rotation angle than unstrained $a^0a^0c^+$ with 6°. The increase in the gap at X is dominated by the enhancement of the tilt angle with strain, i.e., the gap is not so sensitive to the strain alone. We speculate that it in fact may be the t_{2g} splitting that stabilizes the $a^0a^0c^+$ tilt mode by decreasing the lowest conduction-band energies at the Γ-point and creating a gap at X, compared to the other modes; see Fig. 4.

In Fig. 5, we present the DFT+DMFT obtained spectral functions. As can be noticed, the dynamical correlations downshift the Dirac-like points toward the Fermi level. The P and N crossing points exhibited in the $a^0a^0c^-$ structure are ∼0.25 and 0.55 eV above the Fermi energy, compared to 0.30 and 0.75 eV, respectively, in the DFT band structure. Furthermore, we observe an additional crossing point at 0.27 eV along Γ-X in $a^0a^0c^+$ structure. The Dirac point between M-Γ appears around 0.15 eV.

Overall, these findings indicate that the interplay of lattice distortions and electronic correlations is a key factor for the topology properties of strained $SrNbO_3$ thin films. This analysis also illustrates the tunability of the electronic states in $SrNbO_3$ with biaxial compressive strain. The tunability has two components: there is an effect from straining alone, but also an effect from the tilt that is induced by the strain. Furthermore, since the stability of the octahedral tilting modes seems to be connected to the number of electrons, it could also act as a turning knob for the atomic structure and hence electronic structure in addition to a shift of Fermi level.

C. Seebeck coefficient and optical properties

We further investigated the influence of the octahedral tilting on the Seebeck coefficient. The Seebeck coefficient was selected as a useful probe of the electronic structure of the material. In comparison to the conductivity or mobility, the Seebeck coefficient is less sensitive to the scattering rate. Specifically, in the constant relaxation-time approximation, the Seebeck coefficient is independent of the scattering rate [30]. Therefore, changes in the band structure could have an effect on the Seebeck coefficient, which could act as a fingerprint for the octahedral tilting. In Fig. 6, the in-plane (i.e., $xx = yy$ component) Seebeck coefficient is shown for the two tilts as a function of octahedral rotation angle. The results are shown for unstrained $SrNbO_3$ at a temperature of 300 K. The qualitative trends are the same for −2% strained $SrNbO_3$. Below ∼ − 100 meV all configurations show a negative Seebeck coefficient lower than $-5\ \mu V\ K^{-1}$, corresponding to n-type transport. The typical Seebeck coefficients for metals or heavily doped semiconductors are $\pm 10\ \mu V\ K^{-1}$ [41]. Interestingly, near the Fermi level and slightly above, the Seebeck coefficient varies and can even become positive when octahedral tilting is included. Furthermore, this behavior is different for $a^0a^0c^-$ and $a^0a^0c^+$. The positive values occur at lower energies for $a^0a^0c^+$ than $a^0a^0c^-$. In the case of $a^0a^0c^+$ there is also a sharp decrease in the Seebeck coefficient after the increase with higher chemical potential. These features can be connected to the band crossings in Fig. 4. The semi-Dirac point at P coincides with the first Seebeck peak in the case of $a^0a^0c^-$. Similarly, in the case of $a^0a^0c^+$ the first peak coincides with the gapped bands at X and the cluster of bands along M-Γ. The sign of the Seebeck coefficient is sensitive to

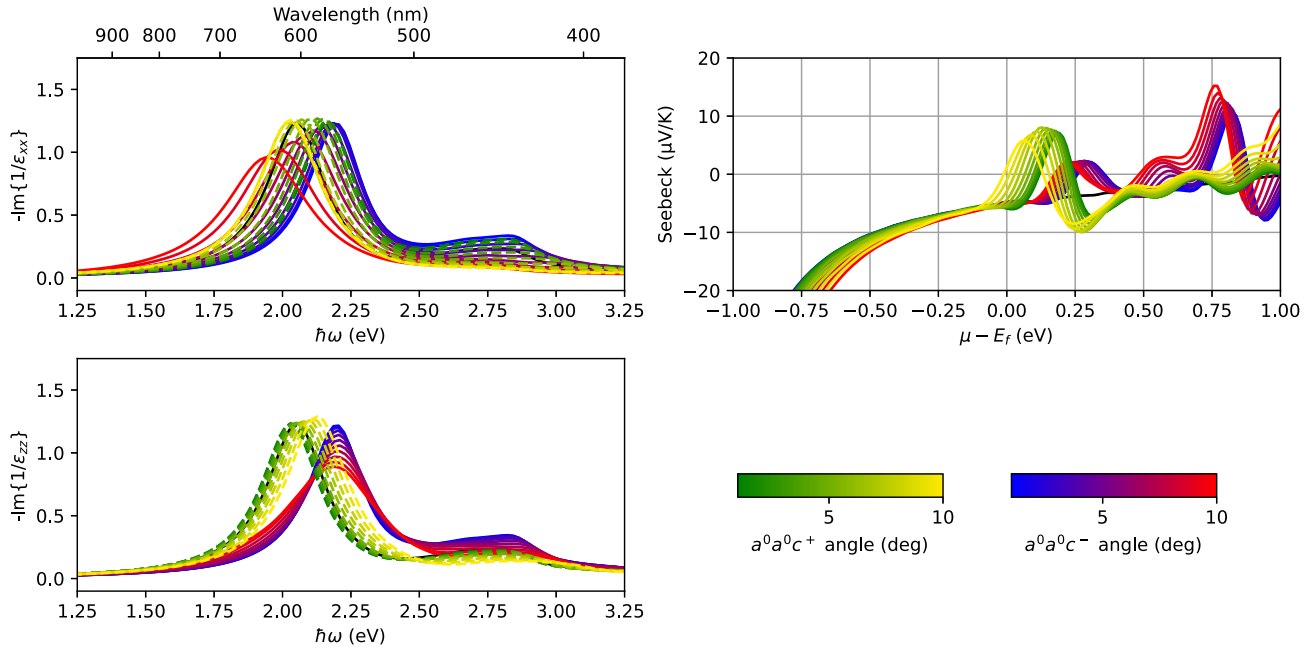

FIG. 6. Influence of octahedral tilting on the optical loss function (top left and bottom left) and on the room-temperature in-plane Seebeck coefficient (top right) in unstrained $SrNbO_3$. The black lines correspond to the response of untilted $SrNbO_3$. In the upper left (lower left) figure, the xx (zz) component of the optical loss function is shown. For visibility, the $a^0a^0c^+$ tilts are drawn with a dashed line. A systematic redshift with a tilt angle is observed in the loss peak of the xx component, while the zz component shows a blueshift with a tilt angle of $a^0a^0c^+$ and an almost constant peak position for $a^0a^0c^-$. Due to the (avoided) band crossings related to octahedral tilting, the Seebeck coefficient shows sign changes over a small range of chemical potentials.

the character of the dispersion, such as nonparabolic features and band crossings, as indicated in Ref. [42] for graphene. This highlights the difference between the effects of strain and octahedral tilting, since strain alone does not create new features such as band crossings and gapping near the Fermi level. The Seebeck values are, of course, small, i.e., not relevant for thermoelectric generator purposes, but they could be valuable as fingerprints of octahedral tilting. Measurements of the Seebeck coefficient, with varying gate voltage, of $SrNbO_3$ could be used as an indirect probe of the electronic structure. Abrupt sign changes, with respect to chemical potential, could be used as a fingerprint of octahedral tilting and an indication of change in the topology of the bands, compared to the bands of untilted $SrNbO_3$ that show a much flatter change in Seebeck with respect to chemical potential.

We then examined the optical properties of $SrNbO_3$ for different octahedral tilting by calculating the optical loss function. The optical loss function, which describes the interaction between electromagnetic fields and matter, is an indirect probe of the electronic states. The optical loss function can be written as $\mathrm{LF}(\omega) = -\mathrm{Im}\{\epsilon(q \to 0, \omega)^{-1}\}$, where the optical limit $q \to 0$ of the dielectric function, $\epsilon(\omega)$, results in no momentum transfer between the applied field and the electrons. The loss function exhibits a peak when the real part of the dielectric function changes sign (a slight energy shift can occur due to the frequency-dependent imaginary part). Therefore, the loss function peak position is a good indication of the plasma frequency defined by $\mathrm{Re}\{\epsilon(\omega_p)\} = 0$. The optical loss functions given by the independent-particle random phase approximation are shown in Fig. 6 for unstrained $SrNbO_3$. Both xx and zz components of the loss functions are shown. A clear loss peak is observed in the visible regime for each tilt configuration, in agreement with Refs. [14,18]. Therefore, the plasma frequencies are in the visible regime. Increasing the rotation angle in $a^0a^0c^-$ decreases the peak height for the xx and zz components. Furthermore, there is a redshift of the peak (and hence plasma frequency) of the xx component, while this is not true for the zz component. Contrary to this, the peak height seems not to be sensitive to variations of the $a^0a^0c^+$ rotation angle. There is also a redshift of the peak and plasma frequency for $a^0a^0c^+$ with larger rotation angles when the xx component is considered. The opposite is true in the zz component, i.e., there is a blueshift of the plasma frequency with respect to larger rotation angles for $a^0a^0c^+$. For smaller octahedral rotations, there is also a secondary peak at ∼2.75 eV. This peak has been connected to the excitations from t_{2g} to e_g bands [13,14], and it is weakened with a larger rotation angle, especially for the xx component. The peaks vanish for large rotations for both $a^0a^0c^-$ and $a^0a^0c^+$. It has been noted that the small peak is absent in experiments, while it is present in DFT. This fits well with our predictions, since octahedral tilting breaks the octahedral crystal field, i.e., the t_{2g} and e_g states are altered by octahedral tilting. One should, however, further analyze the transmission matrix elements between these states, with various tilting, for a complete picture. To our knowledge, octahedral tilting was not included in the DFT analysis by Park and co-workers [14]. It is possible that the missing secondary peak in spectroscopic ellipsometry

at room temperature is due to thermally fluctuating oxygen ions in the $SrNbO_3$ rather than stabilization of a tilting mode. Furthermore, it is possible that correlation effects, such as finite lifetimes and renormalization, could influence the details of the optical response, including the peak at ∼2.75 eV. In any case, temperature-dependent spectroscopic ellipsometry could be valuable for understanding the stabilization of the octahedral tilting modes, given the strong signals due to tilting predicted here and the energy scale involved, which is comparable to the thermal energy.

The effect of biaxial strain on the optical properties of $SrNbO_3$ (and other oxides) was investigated previously by Paul and Birol [13]. They showed that the plasma frequency is almost constant in zz, while there is a systematic blueshift of the xx component with compressive strain. Furthermore, Paul and Birol showed how renormalization of the effective mass due to correlations can redshift the plasma frequency according to the expression $\omega_p = e\sqrt{n/(m^*\varepsilon)}$. Our predictions show that octahedral tilting could shift the plasma frequency substantially (between 2.0 and 2.25 eV), which could be interpreted as a mass renormalization, not due to dynamic correlations but due to octahedral tilting. Here, the sign (i.e., redshift or blueshift) is sensitive to what octahedral tilting mode is present and which component of the dielectric function one is sensing, i.e., xx or zz. This further illustrates the need for systematic temperature-dependent spectroscopic ellipsometry of $SrNbO_3$ under varying strain.

The independent particle assumption used in the calculation of the dielectric function is relatively crude, but it has been shown to qualitatively reproduce the experimental plasmon peak in $SrNbO_3$ when intraband transitions are included [43]. We modeled intraband transitions by using a phenomenological Drude term (see Appendix B). Although these calculations involve serious approximations, they indicate how some typical experimental quantities can give a fingerprint of the underlying octahedral tilting.

These observations call for further *ab initio* modeling of $SrNbO_3$ (and other perovskites), not only by assuming highly symmetric unit cells, but also allowing for deviations from highly symmetric cells by the use of supercells [15]. Further investigations of the stabilization of octahedral tilting with respect to strain under finite temperatures will be highly relevant for application purposes. Our results show that octahedral tilting can have a significant effect on thermoelectric and optical properties. The Seebeck coefficient exhibits sign changes due to the new band features appearing from the octahedral tilting. Moreover, the optical loss function peak position and plasma frequency are tuneable by octahedral tilting over a range of ∼100 nm in the visible regime. Therefore, octahedral tilting should be considered when analyzing strained perovskite oxides like $SrNbO_3$.

IV. CONCLUSIONS

A first-principles investigation of the atomic and electronic structure of $SrNbO_3$ under biaxial strain has been performed with emphasis on the relation between octahedral tilting and strain. This was done by using supercells to allow for the symmetry-breaking octahedral tilting, while the biaxial strain was applied in the (001) plane. By methodically sampling different tilt modes and magnitudes, the optimal octahedral tilting could be found for the different strain conditions. Compressive (tensile) strain was found to induce octahedral tilting around the out-of-plane (in-plane) axis. Interestingly, the *in-phase* tilt $a^0a^0c^+$ was energetically favorable for $SrNbO_3$ under compressive strain. This is in contrast to $a^0a^0c^-$, which has been reported in a recent experimental study of $SrNbO_3$ [9]. The *in-phase* tilt, $a^0a^0c^+$, shows larger t_{2g} splitting compared to the *out-of-phase* tilt $a^0a^0c^-$. The electronic dispersion is also gapped slightly above the Fermi level at the X-point, in the case of $a^0a^0c^+$. DFT+DMFT calculations show that the (avoided) band crossings due to octahedral tilting are shifted towards the Fermi level by correlations, hence making these points easier to reach experimentally. The DFT+DMFT calculations also suggest that octahedral tilting could stabilize further due to electron correlations. The energy gain due to tilting increased from ∼60 to 100 meV f.u.$^{-1}$ when going from DFT to DFT+DMFT. We note that the stabilization and description of octahedral rotations in $SrMoO_3$, which is a correlated metal, were recently addressed by Hampel and co-workers [44], where it was found that dynamic electronic correlations are important for obtaining the correct ground state. Furthermore, the Seebeck coefficient shows positive values slightly above the Fermi level for $a^0a^0c^-$ and $a^0a^0c^+$, as compared with the untilted $SrNbO_3$ that only displays negative values. Interestingly, the tilts are distinguishable due to the difference in the required chemical potential needed to observe positive values of the Seebeck coefficient. The peak in the optical loss function shows tunability with respect to octahedral tilting. Furthermore, the trends in peak position (and hence plasma frequency) and heights are different for the two tilts. We also show that the small feature around 2.75 eV is sensitive to octahedral tilting, which could explain the absence of this peak in experiments; see Ref. [14].

With the recent interest in $SrNbO_3$ we hope to give guidance for how the octahedral tilting behaves in the material but also suggest that tilting modes other than $a^0a^0c^-$ should be considered and investigated further in perovskite oxides. The pronounced features in thermoelectric and optical properties with respect to octahedral tilting could be used as an indication of tilting in $SrNbO_3$, and of the changes in the electronic structure therein.

ACKNOWLEDGMENTS

This work has been supported by Independent Research Fund Denmark Grant No. 8048-00088B and Innovation Fund Denmark Grant No. 1045-00029B. This project has received funding from the European Union's Horizon 2020 research and innovation programme under the Marie Skłodowska-Curie Grant Agreement No. 884104 (PSI-FELLOW-III-3i). W.H.B. acknowledges the National Laboratory for Scientific Computing (LNCC/MCTI, Brazil) for providing HPC resources of the SDumont supercomputer [45] and CENAPAD-SP, which have contributed to the research results.

TABLE I. Predicted lattice parameters using PBEsol in units of Å. In the strained cases, the relaxed out-of-plane parameter is presented.

Biaxial strain (%)	$SrNbO_3$	$SrTiO_3$
−3.0	4.095	3.974
−2.0	4.073	3.947
−1.0	4.047	3.922
−0.5	4.033	3.910
0.0	4.018	3.896
+0.5	4.007	3.887
+1.0	3.997	3.876
+2.0	3.979	3.855
+3.0	3.964	3.836

APPENDIX A: LATTICE PARAMETERS FOR A 5-ATOM CELL

The equilibrium lattice parameters were calculated for $SrNbO_3$ and $SrTiO_3$ with varying degrees of biaxial strain. This was done using the high-symmetry 5-atom unit cells. The objective is to find lattice parameters that can be used for all the following DFT calculations. For biaxial strain, the lattice parameters are given by $a = b = a_0(\epsilon + 1)$, where $a_0 = b_0$ is the relaxed unstrained lattice parameter and ϵ is the biaxial strain. The results are shown in Table I.

As expected, the lattice parameter of $SrNbO_3$ is substantially larger than that of $SrTiO_3$ [12]. Our predicted unstrained lattice parameters were 3.8958 and 4.0182 Å, which is in excellent agreement with the experimental values 3.905 and 4.023 Å for the titanate and niobate, respectively [12]. The difference between our predicted unstrained lattice parameter and the literature value is −0.009 and −0.005 Å for $SrTiO_3$ and $SrNbO_3$, respectively. In the following, the lattice parameters presented in Table I are kept fixed for a given strain value.

APPENDIX B: DRUDE TERM FOR INTRABAND TRANSITIONS

A phenomenological Drude intraband term was included in the calculation of the dielectric function:

$$\epsilon_{\text{intra}}(\omega) = \epsilon^{(1)}_{\text{intra}}(\omega) + i\epsilon^{(2)}_{\text{intra}}(\omega), \tag{B1}$$

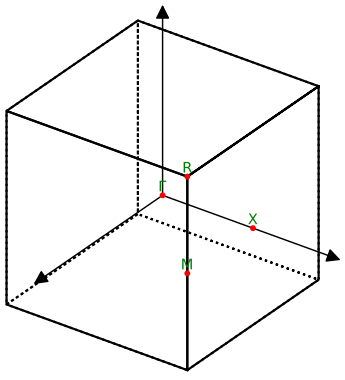

FIG. 7. BZ for $a^0a^0a^0$.

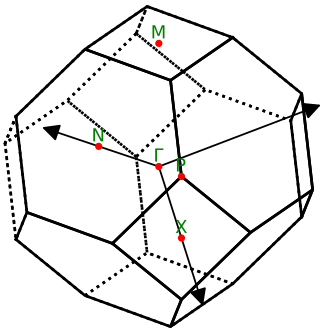

FIG. 8. BZ for $a^0a^0c^-$.

where the real and imaginary parts are given by

$$\epsilon^{(1)}_{\text{intra}}(\omega) = 1 - \frac{\omega^2_{p,\text{intra}}}{\omega^2 + \gamma^2}, \tag{B2}$$

$$\epsilon^{(2)}_{\text{intra}}(\omega) = \frac{\gamma\omega^2_{p,\text{intra}}}{\omega^3 + \omega\gamma^2}. \tag{B3}$$

Here $\omega_{p,\text{intra}}$ is the intraband plasma frequency [46] and $\gamma = 0.3$ eV is the inverse lifetime chosen in this work to reproduce the broadening in Ref. [18].

APPENDIX C: FIRST BRILLOUIN ZONE FOR DIFFERENT TILTS

In Figs. 7–9 the first Brillouin zones of $a^0a^0a^0$, $a^0a^0c^-$, and $a^0a^0c^+$ are shown. Note that the coordinate systems for the tilted structures are rotated 45° around the z-axis of the untilted structure.

APPENDIX D: STABILITY OF TILTS WITH CHARGE

The effect of electron (hole) doping on the tilting stability is presented in Fig. 10.

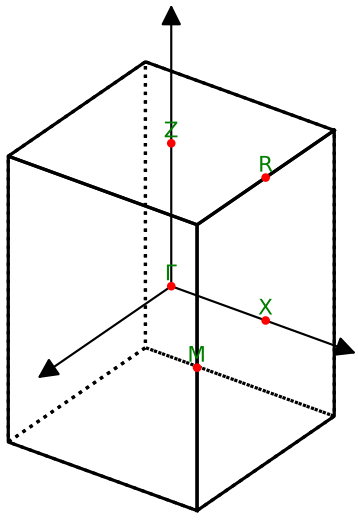

FIG. 9. BZ for $a^0a^0c^+$.

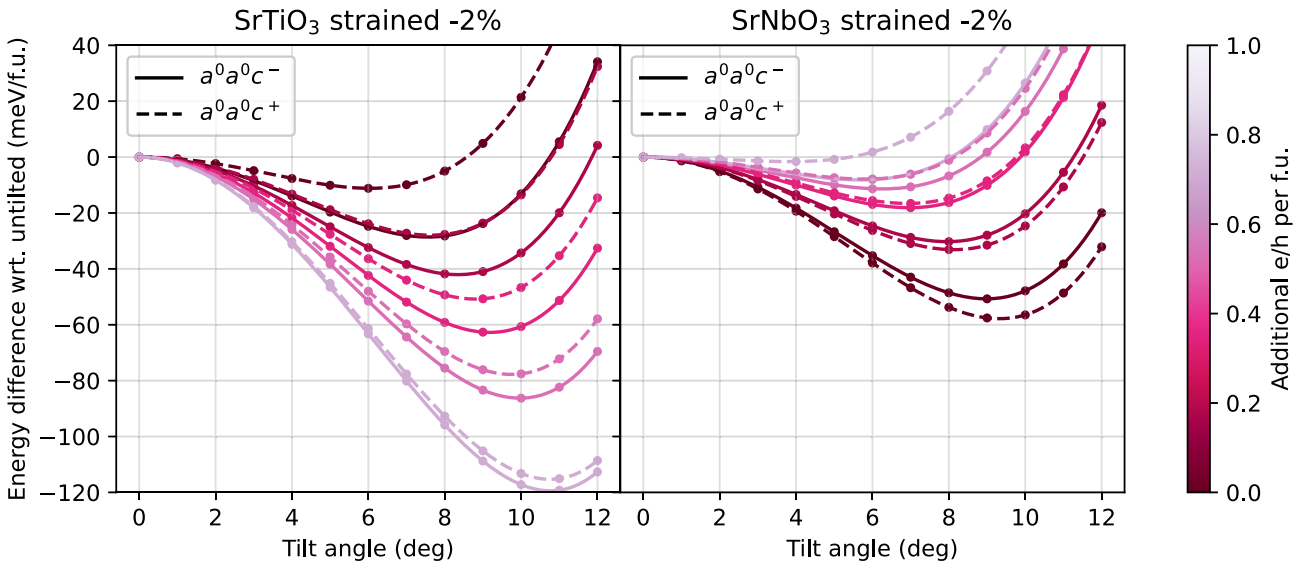

FIG. 10. Effect of electron (hole) doping on tilting stability of $SrTiO_3$ ($SrNbO_3$) under -2° biaxial strain. $SrTiO_3$ to the left and $SrNbO_3$ to the right. The darkest purple lines correspond to undoped systems, and lighter lines correspond to more electrons (or holes). Adding electrons to $SrTiO_3$ causes the two tilt modes to stabilize. Furthermore, the addition of an electron reduces the difference in energy between *in-phase* and *out-of-phase* tilting. $SrNbO_3$ shows destabilization of tilts with the addition of holes. For $SrNbO_3$ there is a critical point at which the optimal tilt transitions from *in-phase* to *out-of-phase*.

APPENDIX E: t_{2g} SPLITTING MAP

A map of the t_{2g} splitting can be found in Fig. 11.

APPENDIX F: ALL OCTAHEDRAL TILTS

Figures 12 and 13 show the energy landscapes for the octahedral tilt modes in $SrNbO_3$ and $SrTiO_3$ over a wide range of strain values.

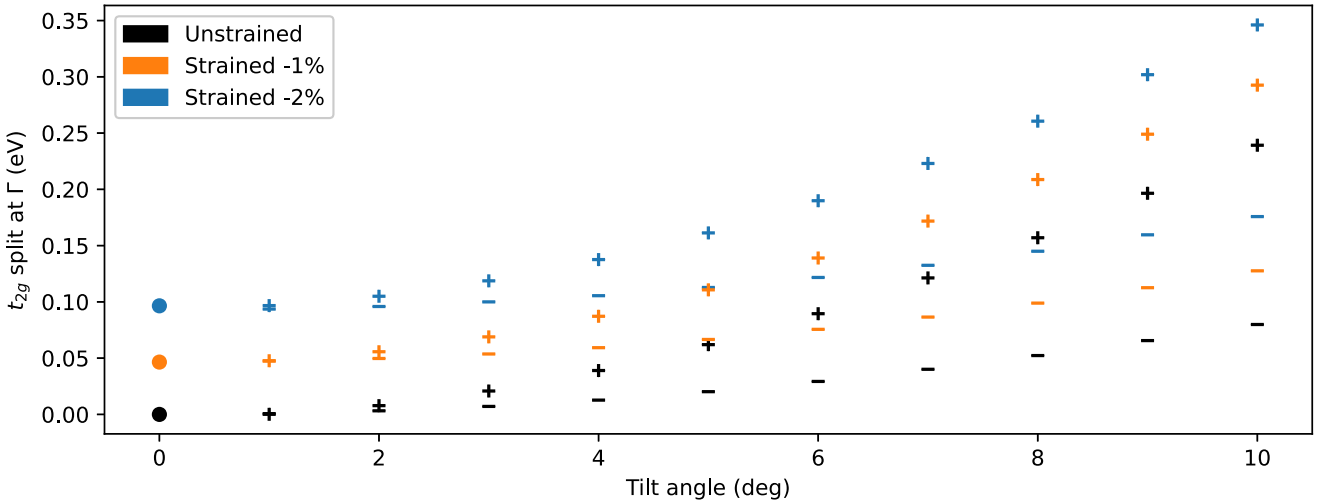

FIG. 11. Splitting between the t_{2g} orbitals at Γ. Circles denote untilted, plus signs denote $a^0a^0c^+$, and minus signs denote $a^0a^0c^-$.

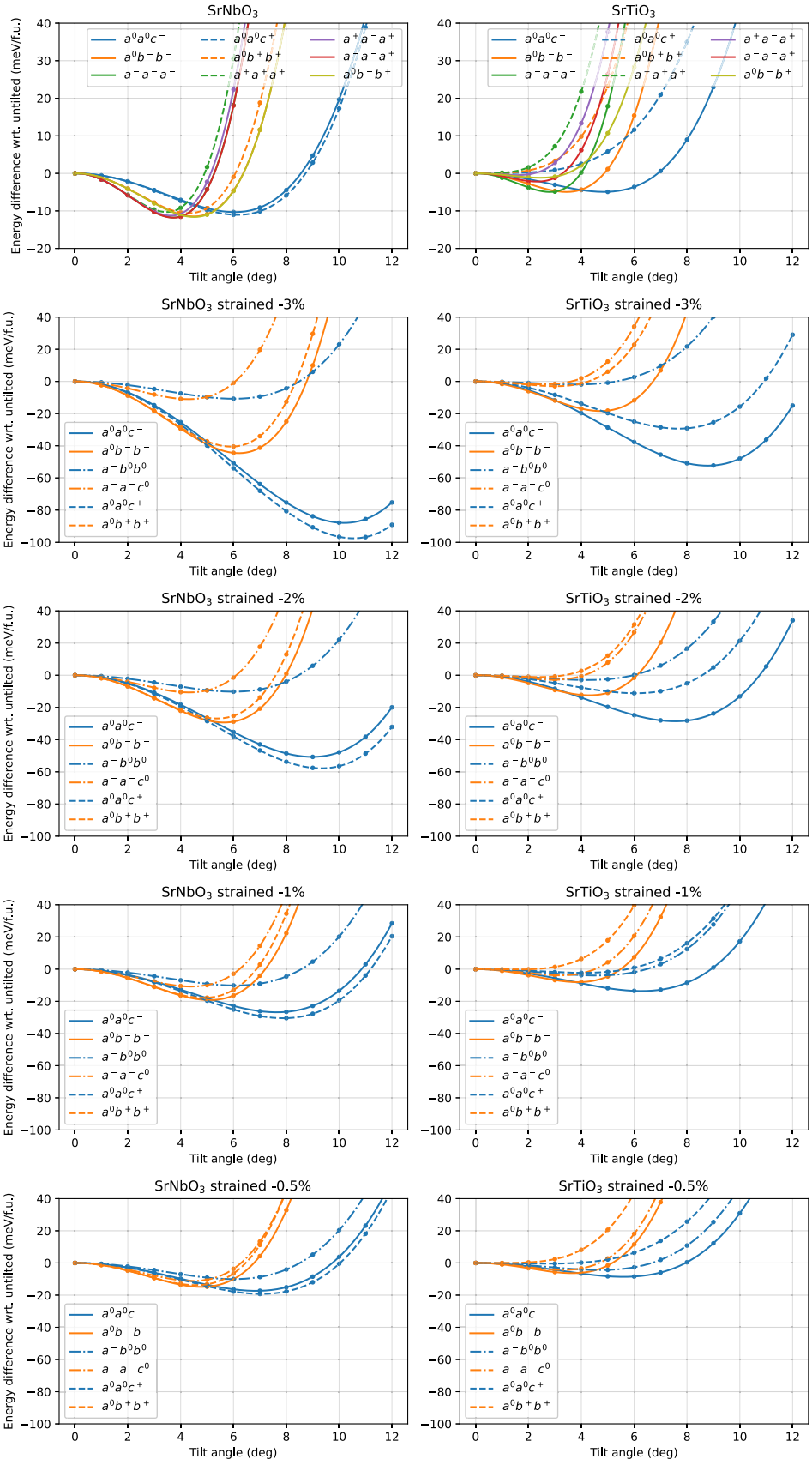

FIG. 12. Octahedral tilting for $SrNbO_3$ and $SrTiO_3$ under various strains.

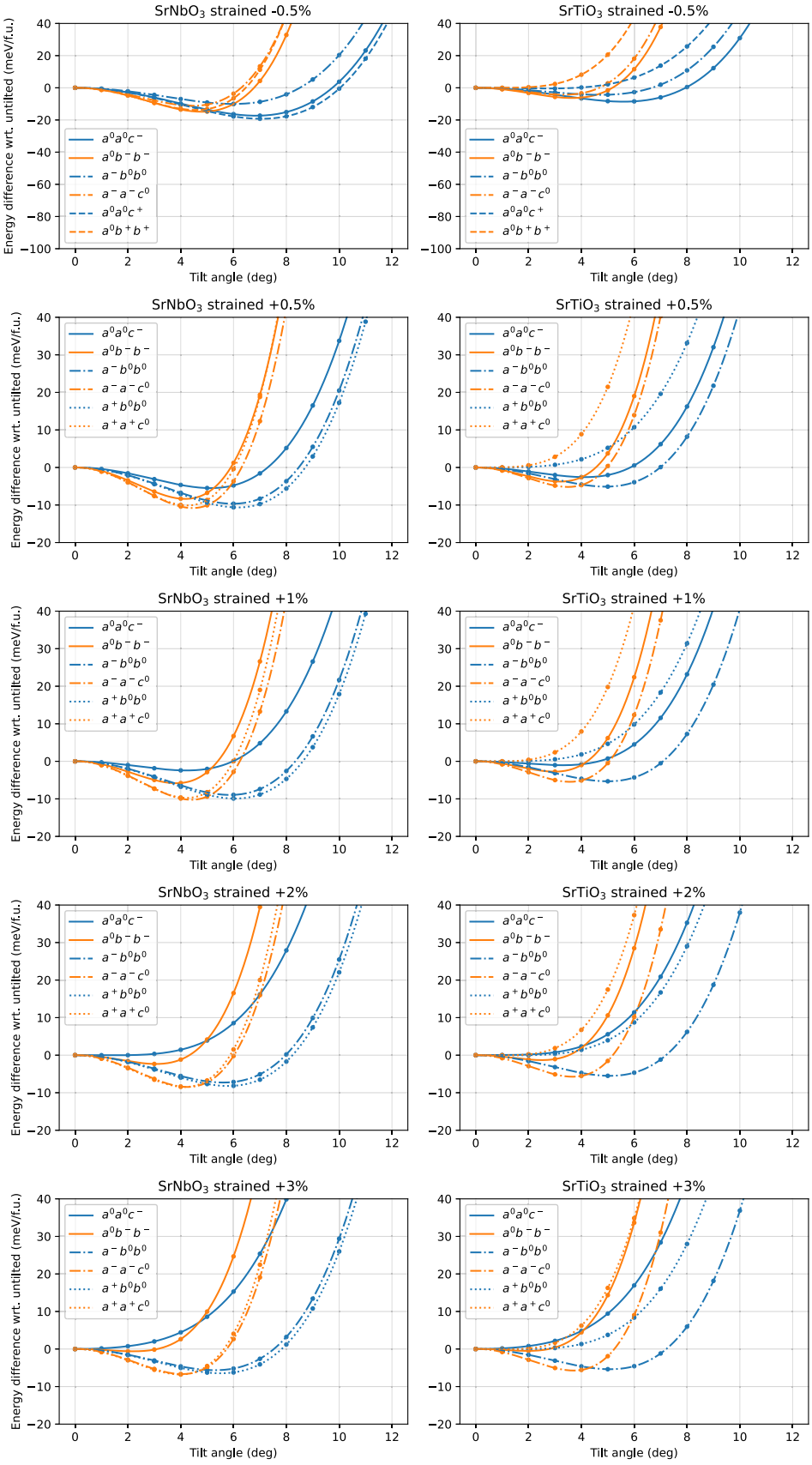

FIG. 13. Octahedral tilting for $SrNbO_3$ and $SrTiO_3$ under various strains.

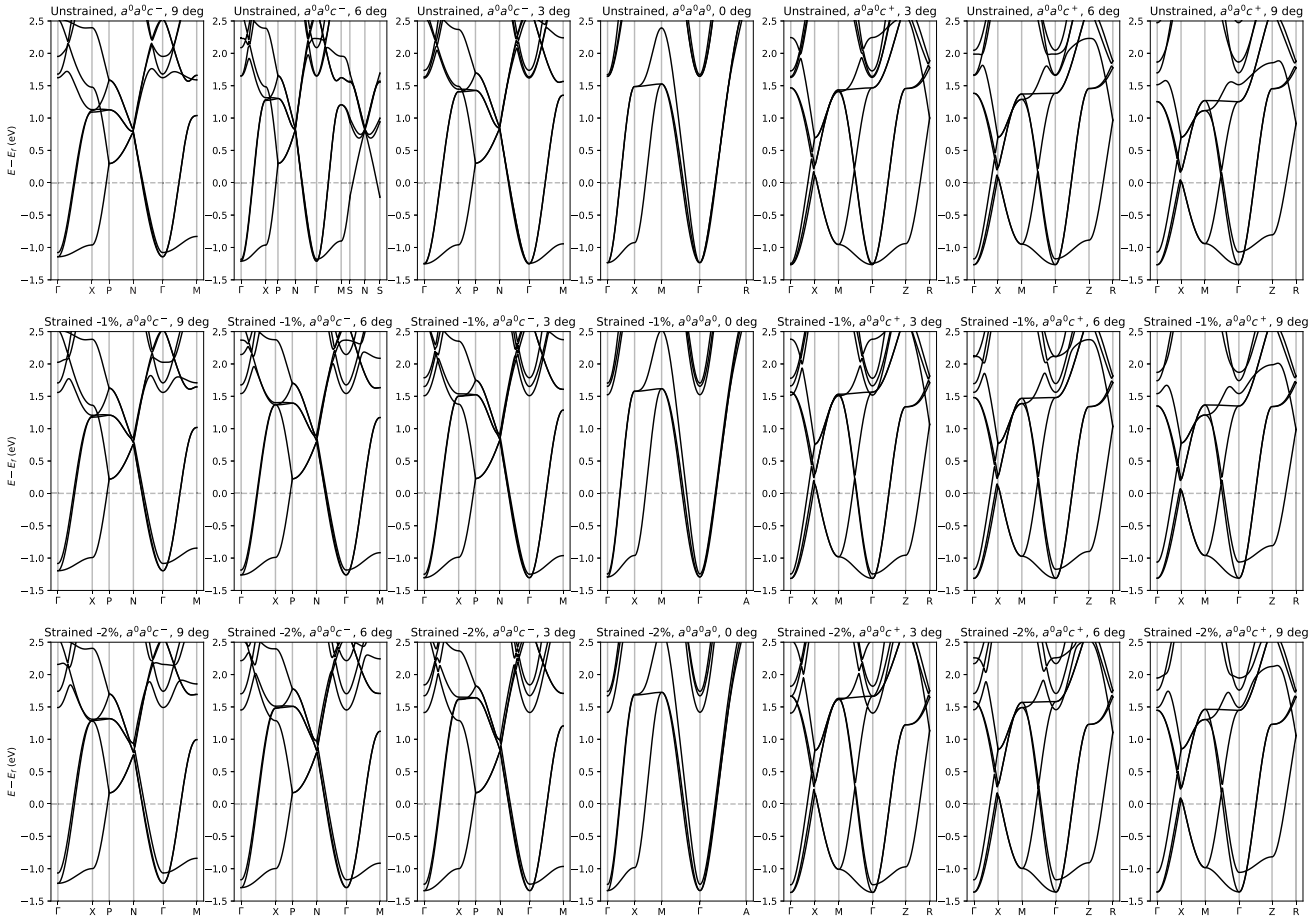

FIG. 14. Map of the band structure of $SrNbO_3$ for different tilt angles under compressive strain.

APPENDIX G: ALL BAND STRUCTURES

A map of the band structure of $SrNbO_3$ for various strains can be found in Fig. 14. Both in-phase and out-of-phase tilting modes are shown.

[1] A. S. Bhalla, R. Guo, and R. Roy, The perovskite structure - A review of its role in ceramic science and technology, Mater. Res. Innovations **4**, 3 (2000).

[2] P. K. Panda and B. Sahoo, PZT to lead free piezo ceramics: A review, Ferroelectrics **474**, 128 (2015).

[3] Y. Yin, B. Tudu, and A. Tiwari, Recent advances in oxide thermoelectric materials and modules, Vacuum **146**, 356 (2017).

[4] J. Sunarso, S. S. Hashim, N. Zhu, and W. Zhou, Perovskite oxides applications in high temperature oxygen separation, solid oxide fuel cell and membrane reactor: A review, Prog. Energy Combust. Sci. **61**, 57 (2017).

[5] J. F. Schooley, W. R. Hosler, and M. L. Cohen, Superconductivity in Semiconducting $SrTiO_3$, Phys. Rev. Lett. **12**, 474 (1964).

[6] M. Baldini, T. Muramatsu, M. Sherafati, H. Kwang Mao, L. Malavasi, P. Postorino, S. Satpathy, and V. V. Struzhkin, Origin of colossal magnetoresistance in $LaMnO_3$ manganite, Proc. Natl. Acad. Sci. USA **112**, 10869 (2015).

[7] F. J. Wong, S. H. Baek, R. V. Chopdekar, V. V. Mehta, H. W. Jang, C. B. Eom, and Y. Suzuki, Metallicity in $LaTiO_3$ thin films induced by lattice deformation, Phys. Rev. B **81**, 161101(R) (2010).

[8] M. Gu, J. Laverock, B. Chen, K. E. Smith, S. A. Wolf, and J. Lu, Metal-insulator transition induced in $CaVO_3$ thin films, J. Appl. Phys. **113**, 133704 (2013).

[9] J. M. Ok, N. Mohanta, J. Zhang, S. Yoon, S. Okamoto, E. S. Choi, H. Zhou, M. Briggeman, P. Irvin, A. R. Lupini, Y. Y. Pai, E. Skoropata, C. Sohn, H. Li, H. Miao, B. Lawrie, W. S. Choi, G. Eres, J. Levy, and H. N. Lee, Correlated oxide Dirac semimetal in the extreme quantum limit, Sci. Adv. **7**, eabf9631 (2021).

[10] J. M. Rondinelli and N. A. Spaldin, Structure and properties of functional oxide thin films: Insights from electronic-structure calculations, Adv. Mater. **23**, 3363 (2011).

[11] J. M. Rondinelli, S. J. May, and J. W. Freeland, Control of octahedral connectivity in perovskite oxide heterostructures: An emerging route to multifunctional materials discovery, MRS Bull. **37**, 261 (2012).

[12] D. Oka, Y. Hirose, S. Nakao, T. Fukumura, and T. Hasegawa, Intrinsic high electrical conductivity of stoichiometric $SrNbO_3$ epitaxial thin films, Phys. Rev. B **92**, 205102 (2015).

[13] A. Paul and T. Birol, Strain tuning of plasma frequency in vanadate, niobate, and molybdate perovskite oxides, Phys. Rev. Mater. **3**, 085001 (2019).

[14] Y. Park, J. Roth, D. Oka, Y. Hirose, T. Hasegawa, A. Paul, A. Pogrebnyakov, V. Gopalan, T. Birol, and R. Engel-Herbert, $SrNbO_3$ as a transparent conductor in the visible and ultraviolet spectra, Commun. Phys. **3**, 102 (2020).

[15] X. G. Zhao, Z. Wang, O. I. Malyi, and A. Zunger, Effect of static local distortions vs. dynamic motions on the stability and band gaps of cubic oxide and halide perovskites, Mater. Today **49**, 107 (2021).

[16] J. Varignon, M. Bibes, and A. Zunger, Origin of band gaps in 3d perovskite oxides, Nat. Commun. **10**, 1658 (2019).

[17] N. Mott, *Metal-Insulator Transitions* (CRC, Boca Raton, FL, 2004).

[18] M. Mirjolet, M. Kataja, T. K. Hakala, P. Komissinskiy, L. Alff, G. Herranz, and J. Fontcuberta, Optical plasmon excitation in transparent conducting $SrNbO_3$ and $SrVO_3$ thin films, Adv. Opt. Mater. **9**, 2100520 (2021).

[19] W. Kohn and L. J. Sham, Self-consistent equations including exchange and correlation effects, Phys. Rev. **140**, A1133 (1965).

[20] P. E. Blöchl, Projector augmented-wave method, Phys. Rev. B **50**, 17953 (1994).

[21] G. Kresse and D. Joubert, From ultrasoft pseudopotentials to the projector augmented-wave method, Phys. Rev. B **59**, 1758 (1999).

[22] G. Kresse and J. Furthmüller, Efficient iterative schemes for ab initio total-energy calculations using a plane-wave basis set, Phys. Rev. B **54**, 11169 (1996).

[23] J. P. Perdew, A. Ruzsinszky, G. I. Csonka, O. A. Vydrov, G. E. Scuseria, L. A. Constantin, X. Zhou, and K. Burke, Restoring the Density-Gradient Expansion for Exchange in Solids and Surfaces, Phys. Rev. Lett. **100**, 136406 (2008).

[24] U. Aschauer and N. A. Spaldin, Competition and cooperation between antiferrodistortive and ferroelectric instabilities in the model perovskite $SrTiO_3$, J. Phys.: Condens. Matter **26**, 122203 (2014).

[25] A. Togo and I. Tanaka, spglib: A software library for crystal symmetry search, arXiv:1808.01590.

[26] K. Haule, C.-H. Yee, and K. Kim, Dynamical mean-field theory within the full-potential methods: Electronic structure of $CeIrIn_5$, $CeCoIn_5$, and $CeRhIn_5$, Phys. Rev. B **81**, 195107 (2010).

[27] J. P. Perdew, K. Burke, and M. Ernzerhof, Generalized Gradient Approximation Made Simple, Phys. Rev. Lett. **77**, 3865 (1996).

[28] P. Blaha, G. K. H. Madsen, D. Kvasnicka, and J. Luitz, *WIEN2K, An Augmented Plane Wave + Local Orbitals Program for Calculating Crystal Properties* (Karlheinz Schwarz, Techn. Universität Wien, Austria, 2001).

[29] K. Haule, Quantum monte carlo impurity solver for cluster dynamical mean-field theory and electronic structure calculations with adjustable cluster base, Phys. Rev. B **75**, 155113 (2007).

[30] G. K. Madsen, J. Carrete, and M. J. Verstraete, BoltzTraP2, a program for interpolating band structures and calculating semi-classical transport coefficients, Comput. Phys. Commun. **231**, 140 (2018).

[31] M. Gajdoš, K. Hummer, G. Kresse, J. Furthmüller, and F. Bechstedt, Linear optical properties in the projector-augmented wave methodology, Phys. Rev. B **73**, 045112 (2006).

[32] A. M. Glazer, The classification of tilted octahedra in perovskites, Acta Crystallogr. Sect. B **28**, 3384 (1972).

[33] H. Hannerz, G. Svensson, S. Y. Istomin, and O. G. D'Yachenko, Transmission Electron Microscopy and Neutron Powder Diffraction Studies of $GdFeO_3$ Type $SrNbO_3$, J. Solid State Chem. **147**, 421 (1999).

[34] J. Young and J. M. Rondinelli, Octahedral rotation preferences in perovskite iodides and bromides, J. Phys. Chem. Lett. **7**, 918 (2016).

[35] R. L. Johnson-Wilke, D. Marincel, S. Zhu, M. P. Warusawithana, A. Hatt, J. Sayre, K. T. Delaney, R. Engel-Herbert, C. M. Schlepütz, J. W. Kim, V. Gopalan, N. A. Spaldin, D. G. Schlom, P. J. Ryan, and S. Trolier-Mckinstry, Quantification of octahedral rotations in strained $LaAlO_3$ films via synchrotron x-ray diffraction, Phys. Rev. B **88**, 174101 (2013).

[36] M. Moreau, A. Marthinsen, S. M. Selbach, and T. Tybell, Strain-phonon coupling in (111)-oriented perovskite oxides, Phys. Rev. B **96**, 094109 (2017).

[37] F. Bruneval, C. Varvenne, J. P. Crocombette, and E. Clouet, Pressure, relaxation volume, and elastic interactions in charged simulation cells, Phys. Rev. B **91**, 024107 (2015).

[38] K. Uchida, S. Tsuneyuki, and T. Schimizu, First-principles calculations of carrier-doping effects in $SrTiO_3$, Phys. Rev. B **68**, 174107 (2003).

[39] V. M. Goldschmidt, Die Gesetze der Krystallochemie, Naturwissenschaften **14**, 477 (1926).

[40] N. Mohanta, J. M. Ok, J. Zhang, H. Miao, E. Dagotto, H. N. Lee, and S. Okamoto, Semi-Dirac and Weyl fermions in transition metal oxides, Phys. Rev. B **104**, 235121 (2021).

[41] D. M. Rowe, *CRC Handbook of Thermoelectrics* (CRC, Boca Raton, FL, 2018).

[42] P. Wei, W. Bao, Y. Pu, C. N. Lau, and J. Shi, Anomalous Thermoelectric Transport of Dirac Particles in Graphene, Phys. Rev. Lett. **102**, 166808 (2009).

[43] T. Zhu, P. E. Trevisanutto, T. C. Asmara, L. Xu, Y. P. Feng, and A. Rusydi, Generation of multiple plasmons in strontium niobates mediated by local field effects, Phys. Rev. B **98**, 235115 (2018).

[44] A. Hampel, J. Lee-Hand, A. Georges, and C. E. Dreyer, Correlation-induced octahedral rotations in $SrMoO_3$, Phys. Rev. B **104**, 035102 (2021).

[45] http://sdumont.lncc.br.

[46] J. Harl, G. Kresse, L. D. Sun, M. Hohage, and P. Zeppenfeld, Ab initio reflectance difference spectra of the bare and adsorbate covered Cu(110) surfaces, Phys. Rev. B **76**, 035436 (2007).

B.2 Band topology induced by octahedral rotation in $SrNbO_3$

This manuscript is inspired by our findings from Reference [29]. Here, experimentally obtained bands are compared with theoretically predicted bands of octahedral rotated $SrNbO_3$. The puzzle of "which tilt is present" is played by comparing expected fingerprints for the different rotations and experimental bands. The fingerprints of the in-phase rotation is found in the experiment. Here, it was also shown theoretically that the in-phase rotation hosts Dirac nodal lines that upon time reversal symmetry breaking results in large Berry curvatures. This indicates that $SrNbO_3$ likely exhibits the rare in-phase rotation, and that this rotation has interesting band features. The ARPES measurements were done by Alla Chikina, and I performed all calculations, i.e. DFT and analysis of the bands (nodal line search and Berry phase-related quantities). This manuscript is to be submitted to Science Advance.

Band topology induced by octahedral rotation in $SrNbO_3$

Alla Chikina[1,*], Victor Rosendal[2], Hang Li[1], Eduardo B. Guedes[1], Marco Caputo[3], Nicholas Clark Plumb[1], Ming Shi[1], Dirch Hjorth Petersen[2], Mads Brandbyge[4], Walber Hugo Brito[5], Ekaterina Pomjakushina[6], Valerio Scagnoli[6,7], Jike Lyu[6], Marisa Medarde[6], Elizabeth Marie Skoropata[1], Urs Staub[1], Shih-Wen Huang[1], Felix Baumberger[1,8], Nini Pryds[2,*], and Milan Radovic[1,*]

[1]Photon Science Division, Paul Scherrer Institut, CH-5232 Villigen, Switzerland
[2]Department of Energy Conversion and Storage, Technical University of Denmark, 2800 Kgs. Lyngby, Denmark
[3]MAX IV Laboratory, Lund University, P.O. Box 118, 22100, Lund, Sweden
[4]Department of Physics, Technical University of Denmark, 2800 Kgs. Lyngby, Denmark
[5]Departamento de Física, Universidade Federal de Minas Gerais, C. P. 702, 30123-970, Belo Horizonte, MG, Brazil
[6]Laboratory for Multiscale Materials Experiments, Paul Scherrer Institut, CH-5232 Villigen, Switzerland
[7]Department of Materials, Laboratory for Mesoscopic Systems, ETH Zurich, 8093 Zurich, Switzerland
[8]Department of Quantum Matter Physics, University of Geneva, 24 Quai Ernest-Ansermet,1211 Geneva 4, Switzerland
[*]Corresponding authors. Email: chikina.alla@gmail.com, nipr@dtu.dk, milan.radovic@psi.ch

September 27, 2023

Transition metal oxides with a wide variety of electronic and magnetic properties offer an extraordinary possibility to be a platform for developing future electronics based on unconventional quantum phenomena, for instance, the topology. The formation of topologically non-trivial states is related to crystalline symmetry, spin-orbit coupling, and magnetic ordering. Here, we demonstrate how lattice distortions and octahedral rotation in $SrNbO_3$ films induce the band topology. By employing angle-resolved photoemission spectroscopy (ARPES) and density functional theory (DFT) calculations, we verify the presence of in-phase $a^0a^0c^+$ octahedral rotation in ultra-thin $SrNbO_3$ films, which causes the formation of topologically-protected Dirac band crossings. Our study illustrates that octahedral engineering can be effectively exploited for implanting and controlling quantum topological phases in transition metal oxides.

1 Introduction

The physical properties of perovskite-type ABO_3 transition metal oxides (TMOs) are largely determined by BO_6 octahedra that form a three-dimensional network. Variations in the size, symmetry, and orientation of octahedra open the possibility of creating new properties due to the strong coupling between the lattice, charge, spin, and orbital degrees of freedom in TMOs (*1–7*). In recent years, there has been a growing interest in exploring topological phases in TMOs, which requires to the breaking of certain symmetries, such as inversion or time-reversal symmetries (*1, 8, 9*). In this regard, TMO thin films possess great potential for creating novel quantum phases by tailoring structural distortions (*10*). For instance, it was predicted that cubic perovskite oxides could be transformed into a tetragonal structure with non-symmorphic symmetry in epitaxially-strained thin films (*1, 9, 11*). This induced octahedral rotations, which

lower the symmetry, cause a band folding and may give rise to a Dirac crossing near the Fermi level. These massless fermions are protected (*8*), leading to higher carrier mobility, which is a key property for high-speed electronics (*12–15*).

Band structure analysis of tetragonal perovskite oxides (*9*), including $CaNbO_3$, $SrRuO_3$, $SrMoO_3$, $SrTiO_3$, and $SrNbO_3$ suggests that the non-trivial Dirac crossing is located closest to the Fermi level in $SrNbO_3$ with out-of-phase $a^0a^0c^-$ octahedral rotation (using the Glazer notation (*16*), see Fig.1C). Another theoretical study predicts that in-phase $a^-a^-c^+$ octahedral rotation also induces a topological band structure in $SrNbO_3$ (*17*). While both in-phase and out-of-phase octahedral rotations lead to the formation of symmetry-protected Dirac crossings, the position in energy and reciprocal space are different due to the specific band folding. A recent study of $SrNbO_3$ thin films found out-of-phase $a^0a^0c^-$ octahedral rotation and reported evidence for a non-zero Berry curvature from an analysis of quantum oscillations (*18*). Generally conveying, understanding how the structural change in TMOs affects the band structure is of utmost importance to utilize topological phases in this material. The most direct method to reveal the band structure topology in relation to crystal symmetry is angle-resolved photoemission spectroscopy (ARPES). In our study, we combine ARPES and density functional theory (DFT) calculations to investigate the influence of octahedral rotations on the band topology and the evolution of the electronic structure in $SrNbO_3$ films.

2 Results and discussion

$SrNbO_3$ is a transparent conductor in the visible and ultraviolet range (*19, 20*). The stoichiometric material has one electron in the Nb $4d$ states distributed over the three almost degenerate t_{2g} orbitals. Each orbital forms a cylindrical Fermi surface sheet along a principal axis, and weak hybridization results in the three Fermi surfaces (illustrated in Fig.1A for the cubic phase $a^0a^0c^0$ $SrNbO_3$.) In our previous work, we analyzed possible, stable configurations of

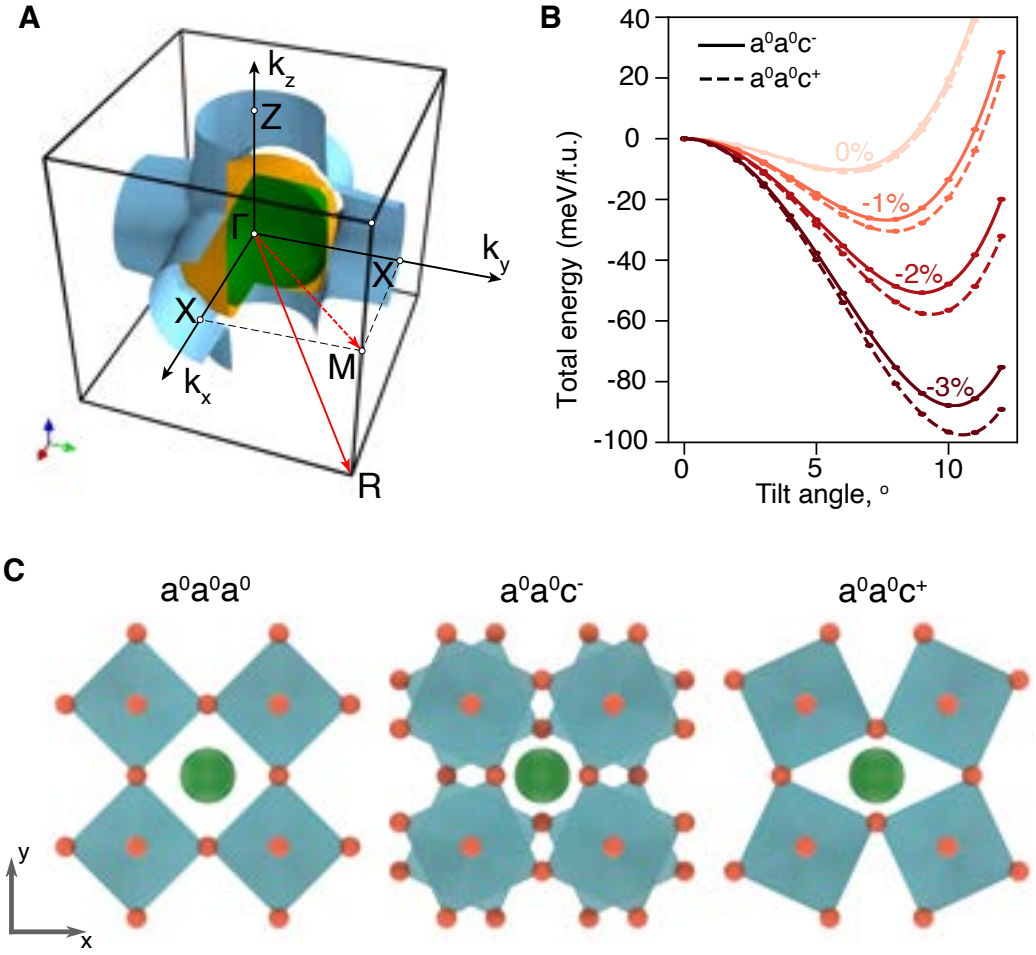

Figure 1: (**A**) Rendering of the DFT 3D Fermi surface of the cubic phase determined by DFT calculations. Red arrows are reciprocal lattice vectors of the supercell arising from the $a^0a^0a^+$(dashed line) and $a^0a^0a^-$(solid line) tilting modes. They illustrate the band folding for both configurations. (**B**) Strain-tilt energy landscape. The strain of -2 % is applied in the xy-plane. The total energy difference is relative to the $a^0a^0a^0$ structure and is normalized to the unit cell. (**C**) Sketches of rotation modes with exaggerated angles.

the strained $SrNbO_3$ by performing first-principles DFT calculations (*21*). Among the various studied octahedral configurations (*21*), this study is focused on $a^0a^0c^+$ and $a^0a^0c^-$, which are the most stabilized under compressive biaxial strain (Fig. 1B, C). Interestingly, DFT calculations show that both studied octahedral configurations of $SrNbO_3$ are near-degenerate with the cubic one while getting more stable with increasing the strain (Fig. 1B). The energetic stabilization of the distorted structures is further favorable by the moderate electronic correlations raised in $SrNbO_3$, as pointed out in our previous study (*21*) based on DFT+DMFT calculations.

The calculated band structures for the pseudocubic $a^0a^0c^0$ and two out-of-phase $a^0a^0c^-$ and in-phase $a^0a^0c^+$ modes are presented in Fig. 2. To simplify the comparison, we unfold the phases onto the cubic $a^0a^0a^0$ lattice and use this notation of the Brillouin zone (BZ). Below, we investigate the distinction in the band structure of both phases, using the cubic notation of BZ.

In order to capture the band structure of $a^0a^0c^-$, the a, b, and c lattice parameters of the cubic need to be multiplied by a factor of $\sqrt{2}$. This new periodicity causes band folding (translation vector indicated by the solid arrow in Fig.1A). Consequently, the new pocket at the M-point is formed by folding the pocket at the $Z(X)$-point. In addition, due to a mirror folding of the band structure in the cubic BZ inside the smaller tetragonal BZ, a Dirac-like crossing is formed along X - M and Γ - M directions. More details regarding band foldings are presented in the Supplementary Information.

In the case of $a^0a^0c^+$ in-phase octahedral rotation, the cubic cell needs to multiply by a factor $\sqrt{2} \times \sqrt{2} \times 1$ (see Supplementary information). That results in reducing and 45^o rotation of the BZ (P4/mbm (127) space group) and the folding of the "cubic" band structure over the $X - X$ diagonal plane (dashed red arrow in fig.1A). This folding results also in Dirac-like band crossings along Γ - M, X - M and Γ - X directions (Fig 2C,F) and translation of the band structure from the Γ-point to the M-point (dashed arrow in Fig.3A). Importantly, the new pocket at M-point either corresponds to the original band from Γ- or X- points, depending on

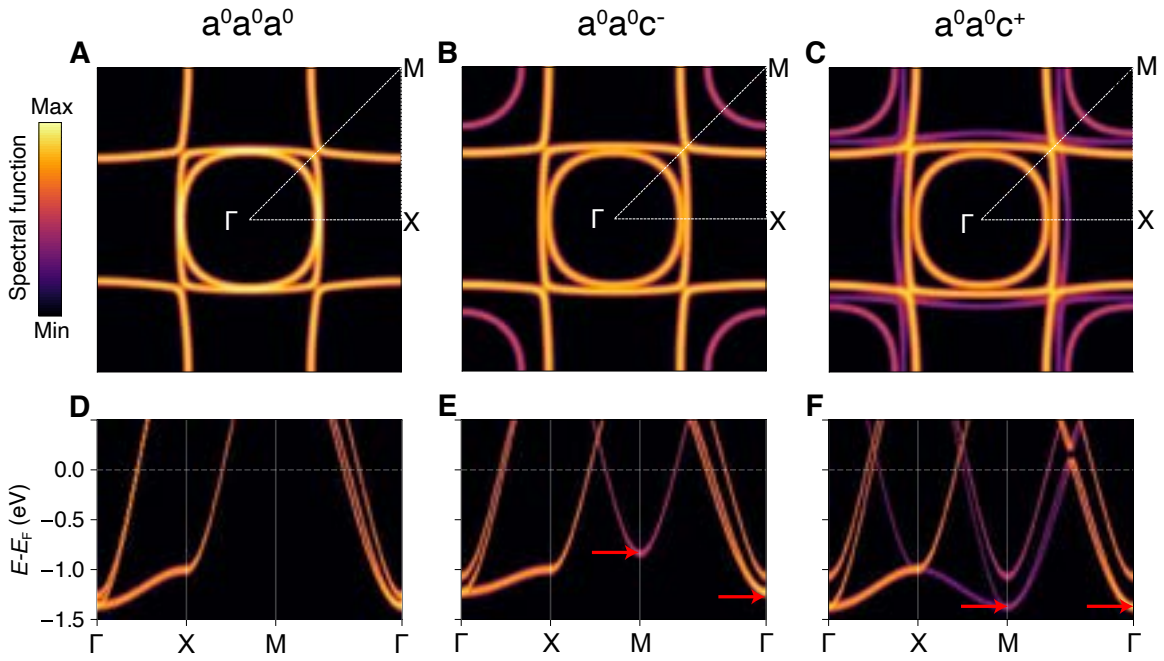

Figure 2: Evolution of the DFT Fermi surface slices and band structures of $SrNbO_3$ with octahedral rotation for (**A,D**) $a^0a^0a^0$, (**B,E**) $a^0a^0c^-$ and (**C,F**) $a^0a^0c^+$ phases. Calculations are done for a -2 $\%$ strained films with a 9 $^\circ$ rotation. Panels (**A-B**) present unfolded Fermi surface slices at $k_z = 0$, and panels (**D-F**) show unfolded band structures of the different tilt modes under -2$\%$ in-plane biaxial strain. Note that we use the cubic BZ notation and a logarithmic color map. Note that the spectral function here is a measure of the Bloch character of the states smeared using a Gaussian (*22, 23*). Furthermore, the smearing is arbitrary and does not reflect any finite lifetimes due to many-body effects.

the octahedral rotation phase. According to the calculations, the folded band at the M-point is located at lower energy for the in-phase $a^0a^0c^+$ (indicated by arrows in Fig 2E,F). Therefore, the position of the band bottom at M-point and the presence of the heavy band along X - M direction are fingerprints of the octahedral configuration type, allowing us to distinguish them.

To identify which phase is stabilized, we measured the band structure of $SrNbO_3$ films using ARPES (Fig. 3). All measured films were grown by pulsed laser deposition at the Swiss Light Source's Surface/Interface Spectroscopy (SIS) beamline at the Paul Scherrer Institut in Villigen, Switzerland. The films were grown on TiO_2-terminated $SrTiO_3$ (001) substrates at T = 650°C and P(O_2) $< 5 \times 10^{-7}$ mbar, resulting in single-phase epitaxial films (see Supplementary Information). The lattice mismatch between the $SrNbO_3$ film and $SrTiO_3$ (001) substrate induces a compressive strain of about 2 % in the film and presumably octahedral rotations (*18*). After the growth, the films were transferred *in situ* to the ARPES station at the SIS beamline via an ultra-high vacuum transfer line.

Previous photoemission studies of the electronic structure of 15 nm (around 38 unit cells) $SrNbO_3$ films grown on $DyScO_3$ (110) showed no indications of deviation from the cubic $SrNbO_3$ structure (*24*). Nevertheless, $SrNbO_3$ film grown on $DyScO_3$ (110) should experience compressive strain, but it can relax after several tens of unit cells (*25, 26*). Therefore, to observe the conceivable strain effect, we studied the band structure evolution for $SrNbO_3$ films of different thicknesses: 7, 12, 25, and 325 unit cells (u.c.). In the following part, we focus on two $SrNbO_3$ films: ultra-thin 7 u.c. film, where the strain should have a more significant effect, and a thick film of 325 u.c. (130 nm), where the strain effect is minimized through relaxation. Indeed, X-ray reciprocal space mapping confirmed that 25 u.c. film is fully strained (see Supplementary Information). Based on that, we assume that the SNO films with lower thicknesses are also fully strained. Nevertheless, the X-ray reciprocal space mapping shows that 325 u.c. thick (bulk-like) film is fully relaxed (see Supplementary Information). Fig. 3 displays ARPES

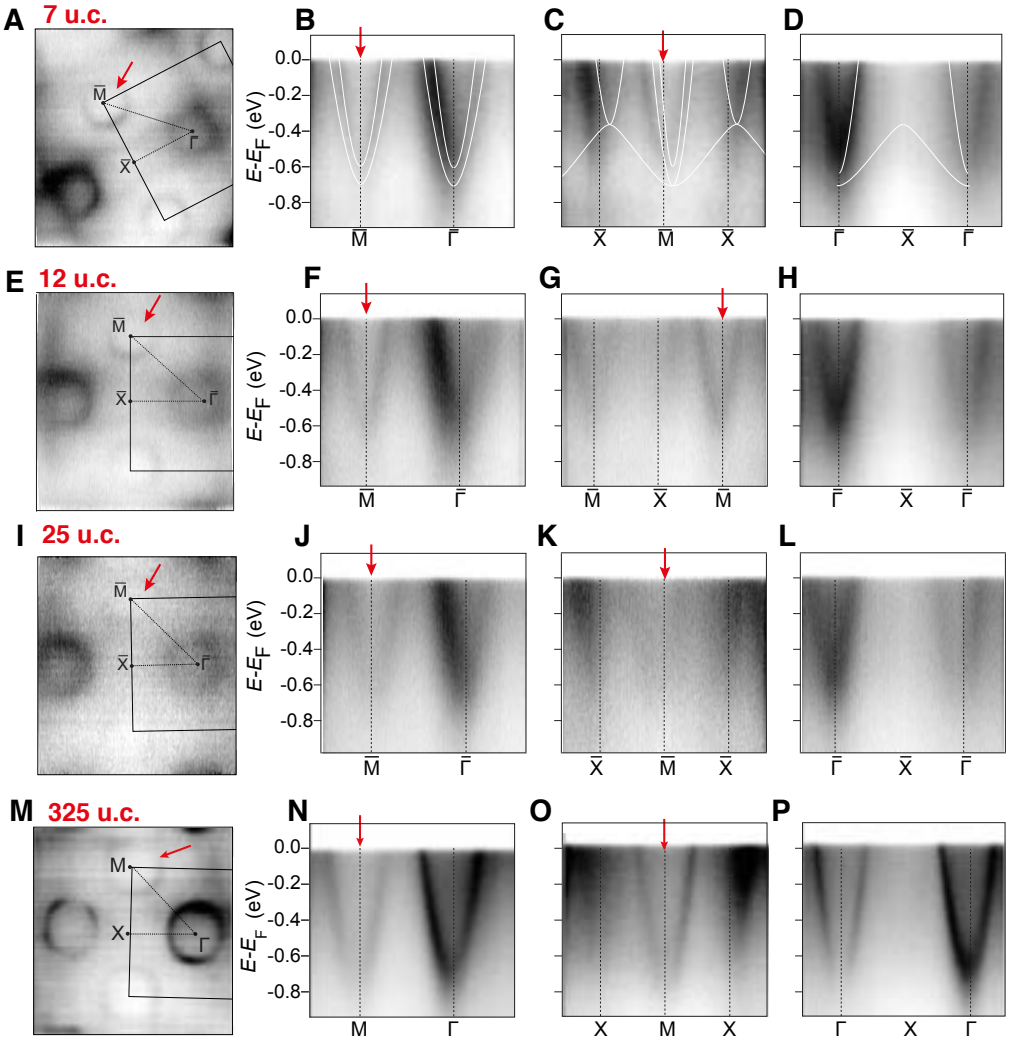

Figure 3: Spectra taken at 106 eV photon energy and circular polarisation of **(A-D)** 7 u.c., **(E-H)** 12 u.c., **(I-L)** 25 u.c. and **(M-O)** 325 u.c. thick $SrNbO_3$ films. DFT band structure shifted toward Fermi level by 0.6 eV is presented by thin white lines in panels (**B-D**). Surface-projected symmetry points are marked with a dashed line. The red arrow marks an additional pocket around M-point, which appears due to the octahedral rotations.

spectra taken along high-symmetry directions with circularly polarized light of $h\nu = 106$ eV photon energy. Fig. 3(A,E,I,M) shows the Fermi surface maps in the Γ-X-M plane for the films. Besides one spherical and two cylindrical Fermi surface sheets near the Γ-point, the data reveal a new pocket around the M-point for both films. Since the band structure folding occurs for the ultra-thin films and the thick, relaxed film, it is obvious that octahedral rotations are inherent in the $SrNbO_3$ film. However, there is still the question of which type of tilting phase, out-of-phase ($a^0a^0c^-$) or in-phase ($a^0a^0c^+$), is present.

Differences in the band structure between $a^0a^0c^+$ or $a^0a^0c^-$ configurations allow a more detailed understanding of the crystal structure in $SrNbO_3$ films. The most noticeable distinctions (in Fig.2 between panels D and F) are the position of the band bottom at the M point, and the presence of a weak dispersive folded band along X - M direction in the $a^0a^0c^+$ configuration. However, we do not observe this band in ARPES spectra, probably due to the matrix element effect. In fact, this band, primarily of d_{yz} character, was noted to be scarcely visible in the ARPES spectra of comparable perovskite transition metal oxides (*27–30*). Therefore, we concentrate on the relative positions of the band minima at the Γ and M-points. In our DFT calculations of $a^0a^0c^-$, the conduction band minimum at the M-point is located $\sim$ 0.35 eV above the Γ-point minimum, whereas $a^0a^0c^+$ phase, the band minimum at M and Γ have the same energy (red arrows in Fig.2F). Accordingly, the relative position of band minima at the M and X points of $a^0a^0c^-$ and $a^0a^0c^+$ is distinguishable.

In the ARPES spectra of the 7 u.c. film (Fig. 3B), which is highly strained (see Supplementary Information), we find that the conduction band minima at Γ and M are around -0.52 ± 0.05 and -0.54 ± 0.05 eV, respectively. At the same time, the band minima at X is located around -0.37 ± 0.05 eV (see Fig. 3(B-D)). Comparing DFT calculations with experimental results where the band minima at Γ and M points coincide, we deduce that band structure reconstruction originates from $a^0a^0c^+$ in-phase octahedral rotation. This observation is in agreement with

our calculation, which predicts that $a^0a^0c^+$ configuration of $SrNbO_3$ under 2% compressive strain is slightly energetically favorable (see Fig. 1B). Nevertheless, we performed synchrotron-based X-ray diffraction measurements to examine the type of phases present in relaxed 325 u.c. thick film. Interestingly, the data analyses of superstructure peaks (See Supplementary Information) reveal the existence of both in-phase and out-of-phase octahedral rotations. Since ARPES is a predominantly surface-sensitive method, we argue that the $a^0a^0c^-$ configuration is not encountered within the surface region.

In Fig. 3 (B-D), we show the DFT band structure of $a^0a^0c^+$ phase superimposed with experimental spectra of 7u.c. $SrNbO_3$ film. We find that the calculated bands need to be shifted by 0.6 eV towards the Fermi level to overlap with the experimental data. DFT-based estimation suggests that such a shift corresponds to $\sim 0.58\ \bar{e}$ hole doping and thus Nb $4d^{0.42}$ configuration, instead of Nb $4d^1$ (see Supplementary Information). Indeed, X-ray photoemission spectrum of core levels obtained using 650 eV photon energy shows the existence of mixed Nb^{5+} and Nb^{4+} state (see Supplementary Information). This experimental observation indicates a significant depletion of electrons at the Nb site of $SrNbO_3$ (*24*). Nevertheless, X-ray diffraction data from 25 u.c. thick films do not show the presence of any other phases (see Supplementary Information). Therefore, the observed hole doping is likely related to self-doping or non-stoichiometry, either from Sr-vacancies or excess oxygen, which is known to exist in $SrNbO_3$ thin film (*24,31*). However, the conduction band minimum in 320 u.c spectra (See Fig. 3(F,G)) is located at lower binding energy than for the ultra-thin film. As a result, Fermi surface pockets at Γ and M point are larger in the case of 325 u.c. film (Fig.3 M vs A). This can be because the thick film is less hole-doped and probably closer to the stoichiometric composition. Nevertheless, the matching position of the conduction band minima at Γ and M points suggests that $a^0a^0c^+$ phase subsists in the relaxed 130 nm thick film.

To investigate the topological properties of the Dirac-like crossings in distorted $SrNbO_3$

($a^0a^0c^+$ tilt mode), we analyzed the calculated band structure more closely employing the calculation of Berry curvatures and phases, as similarly performed by Mohanta and co-workers (*9*). Such examination is done in two steps: first, by keeping time-reversal symmetry, and second by breaking the time-reversal symmetry through the introduction of an artificial magnetic ordering (without any external magnetic field).

Within the first step, we examine the properties of the nodal lines in the presence of time-reversal symmetry. Fig. 4A displays Dirac nodal lines for two bands, showing energy distribution close to the Fermi level. We considered bands that are populated by the 6 Nb t_{2g} states (2 Nb ions and 3 states per ion). We do not consider other bands with nodal lines since they are further away from the Fermi level. The small circles enclosing the nodal lines with a fourfold degeneracy in Fig. 4A show a π Berry phase, which indicates a non-trivial topology of these bands (*32*). Furthermore, since the $a^0a^0c^+$ structure belongs to the P4/mbm (127) space group, symmetry-enforced Dirac nodal lines are located along the edge of the BZ (*33*). In this space group, the protected nodal lines are on the $\overline{\mathrm{MX}}$, $\overline{\mathrm{AM}}$ and $\overline{\mathrm{AR}}$ lines (*8*) (in the notation of the P4/mbm (127) space group). An example of such a Dirac nodal line is shown in Fig. 4B. Note that the nodal lines protected by the time-reversal symmetry and the nonsymmorphic symmetry are robust even in the presence of SOC (*8, 33*).

Next, we break the time-reversal symmetry by creating a magnetic ordering. Fig. 4C shows the Wannier interpolated band structure of $a^0a^0c^+$ together with the z-component of the Berry curvature. It reaches the most significant values in regions where the folded bands (due to octahedral tilting) are crossing. Here, we constrained a spin polarization in the DFT calculation with a ferromagnetic ordering where each Nb ion has 20% spin polarization, as conducted in Ref. (*9*). Experimentally, this might be achievable by doping with magnetic impurities or applying an external magnetic field. As expected, the magnetization lifts the spin-degeneracy and breaks time-reversal symmetry, which is necessary for a non-zero Berry curvature in centrosym-

metric crystals (*34*). The finite Berry curvature can give rise to features such as the anomalous Hall effect (*35*). One of the non-trivial Dirac crossings appears at -0.09 eV below the Fermi level in Fig. 4C. It could be used for the realization of novel correlated topological phases. Although our calculations show that the non-trivial Dirac crossing is occupied, a slight deviation in stoichiometry leads to doping. Bringing the Dirac crossings to the Fermi level is an essential aspect of the broader application of this system. The additional electrons, which assist in bringing the Dirac point to the Fermi level, could be provided by chemical substitution (for example, $Sr_xLa_{1-x}NbO_3$), by gating or by charge transfer due to the proximity effect. Another option to move the crossing points closer to the Fermi level is to drive $SrNbO_3$ to be more correlated.

3 Summary

We studied the effect of octahedral rotations on electronic structure in $SrNbO_3$ films. Our DFT calculations show that two types of octahedral tilting, $a^0a^0c^+$ and $a^0a^0c^-$, are possible and degenerated with the non-tilted phase but favored by compressive strain. Both of them result in the emergence of symmetry-protected Dirac crossings near the Fermi level. Through the analysis of ARPES spectra, we identify that $SrNbO_3$ films exhibit in-phase $a^0a^0c^+$ octahedral tilting, which gives rise to symmetry-protected Dirac nodal lines in the band structure. Furthermore, the first principles-based calculations show that when time reversal symmetry is broken (with the magnetic field), the electronic structure of $a^0a^0c^+$ phase hosts considerable Berry curvatures. Our study demonstrates the potential of engineering octahedral rotation to create and alter the topology of transition metal oxides.

4 Computational methods

The VIENNA AB INITIO SIMULATION PACKAGE (VASP) (*36*) was used to perform DFT calculations within the projector-augmented-wave method (*37, 38*). PBEsol was chosen as the

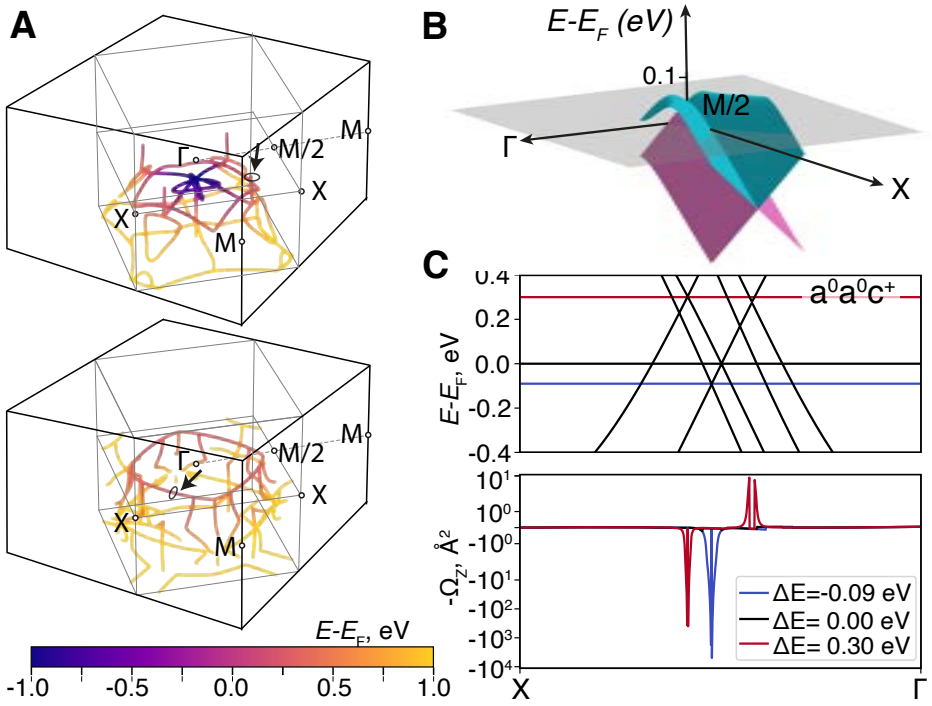

Figure 4: Topology of the $SrNbO_3$ $a^0a^0c^+$ band structure. The BZ is drawn within the BZ of the untilted structure and we use the notation of the untilted structure. (A) Nodal lines (without SOC) of two bands close to Fermi level. A Berry phase of π is observed around the drawn circles enclosing the nodal lines. (B) Symmetry protected Dirac nodal line on the boundary of the $a^0a^0c^+$ BZ with SOC included. (C) Bands and Berry curvatures, when time-reversal symmetry is broken by magnetic ordering and SOC, is included. The different lines correspond to different energies relative to the Fermi level.

exchange-correlation functional for its accuracy of predicting the lattice parameter (*39*). The electronic convergence criteria was set to $10^{-6}\,\mathrm{eV}$ and the plane-wave energy cutoff was set to $550\,\mathrm{eV}$. K-point meshes corresponding to the Γ-centered $8 \times 8 \times 8$ mesh in the case of the 5 atom unit cell was chosen for the ionic relaxations. For band structure calculations, the k-point sampling was increased to $16 \times 16 \times 16$ corresponding to the 5 atom unit cell. While the effect of spin-orbit coupling (SOC) is present in $SrNbO_3$, the energy scale involved is not resolvable in the experiments. Therefore, we neglect SOC in the main text of this paper. For reference, the band structures with and without SOC can be found in the Supplementary information. Band structure unfolding (*22,23*) was performed onto the cubic BZ as implemented in VASPKIT (*40*). This was done with a Gaussian smearing with standard deviation $\sigma_\epsilon = 0.02\,\mathrm{eV}$. This artificial smearing was done to create a smooth electronic structure and should not be interpreted as a broadening due to finite lifetimes. Unfolding of the Fermi slices was done by including a Gaussian smearing in both energy *and* momentum. The standard deviations of the Gaussians were set to $\sigma_\epsilon = 0.04\,\mathrm{eV}$ and $\sigma_{\mathbf{k}} = 0.005$ in units of the primitive reciprocal lattice in the case of energy and momentum, respectively. Integration of the states at Γ and M was performed by taking weighted sums over all sampled electronic states. Gaussians were used to weight the states in both energy and momentum, and the standard deviations were increased to $\sigma_\epsilon = 0.2\,\mathrm{eV}$ and $\sigma_{\mathbf{k}} = 0.1$ in units of the primitive reciprocal in energy and momentum, respectively. The additional broadening here was used to form continuous energy distribution curves comparable to the experiment. The Fermi surface of the cubic phase of $SrNbO_3$ was visualized using the Python code `VASPFermiSurface` (*41*).

To investigate the effects of octahedral tilting on the topology of the band structure, we constructed Wannier functions using Wannier90 (*42*) based on the electronic structure calculated with Quantum Espresso(QE) (*43*). Nb d_{xy}, d_{xz}, and d_{yz} atomic-centered orbitals were used as projectors for the Wannierization. The atomic structures were fixed in this analysis, and

the PBE (*44*) exchange-correlation was applied. SOC was neglected for the calculation of the nodal structures and Berry phase, while for the Berry curvature calculation, SOC was included. Furthermore, in the calculation of Berry curvature, the time-reversal symmetry was broken by constraining a spin polarization of $0.2\,\%$ on the Nb ions, as in Reference (*9*). WannSymm (*45*) was used to symmetrize the Wannier Hamiltonian, which is useful since the Wannierization typically fails to preserve lattice symmetries. WannierTools (*46*) was used to search for nodal structures and calculate the $k_x k_y$-resolved band structures. The `postw90.x` (*42*) program was used to calculate the Berry curvature.

5 Acknowledgments

This project has been supported by the European Union's Horizon 2020 research and innovation program under the Marie Skłodowska-Curie grant agreement No 884104 (PSI-FELLOW-III-3i).N.P. acknowledges the support of Novo Nordisk Foundation Challenge Program 2021: Smart nanomaterials for applications in life-science, BIOMAG Grant NNF21OC0066526, the support from the ERC Advanced "NEXUS" Grant 101054572 and the Danish Council for Independent Research Technology and Production Sciences for the DFF- Research Project 3 (grant No 00069B). W.H.B. acknowledges the financial support from CNPq (in particular Grant 402919/2021-1) and the computational centers: National Laboratory for Scientific Computing (Santos Dumont - LNCC/MCTI, Brazil) and the Brazilian National Center of High Processing Computing (CENAPAD-SP).

References

1. J. M. Rondinelli, N. A. Spaldin, *Phys. Rev. B* **82**, 113402 (2010).

2. J. M. Rondinelli, N. A. Spaldin, *Advanced Materials* **23**, 3363 (2011).

3. J. Liu, *et al.*, *Nature Communications* **4**, 2714 (2013).

4. E. J. Moon, *et al.*, *Nature Communications* **5**, 5710 (2014).

5. D. Kan, *et al.*, *Nature Materials* **15**, 432 (2016).

6. Z. Liao, *et al.*, *Nature Materials* **15**, 425–431 (2016).

7. Z. Liao, *et al.*, *Proceedings of the National Academy of Sciences* **115**, 9515 (2018).

8. M. M. Hirschmann, A. Leonhardt, B. Kilic, D. H. Fabini, A. P. Schnyder, *Phys. Rev. Mater.* **5**, 054202 (2021).

9. N. Mohanta, *et al.*, *Phys. Rev. B* **104**, 235121 (2021).

10. J. M. Rondinelli, S. J. May, J. W. Freeland, *MRS Bulletin* **37** (2012).

11. A. Herklotz, *et al.*, *Scientific Reports* **6**, 26491 (2016).

12. T. Liang, *et al.*, *Nature Materials* **14**, 280 (2015).

13. L. M. Schoop, *et al.*, *Nature Communications* **7**, 11696 (2016).

14. F. Arnold, *et al.*, *Nature Communications* **7**, 11615 (2016).

15. T. Y. Yang, *et al.*, *Nature Materials* **19**, 27–33 (2020).

16. A. M. Glazer, *Acta Crystallographica Section B Structural Crystallography and Crystal Chemistry* **28** (1972).

17. T. Zhang, *et al.*, *Nature* **566**, 475–479 (2019).

18. J. M. Ok, *et al.*, *Science Advances* **7**, eabf9631 (2021).

19. Y. Park, *et al.*, *Communications Physics* **3**, 102 (2020).

20. D. Oka, Y. Hirose, S. Nakao, T. Fukumura, T. Hasegawa, *Phys. Rev. B* **92**, 205102 (2015).

21. V. Rosendal, *et al.*, *Phys. Rev. Mater.* **7**, 075002 (2023).

22. V. Popescu, A. Zunger, *Physical Review Letters* **104**, 236403 (2010).

23. V. Popescu, A. Zunger, *Physical Review B - Condensed Matter and Materials Physics* **85**, 085201 (2012).

24. C. Bigi, *et al.*, *Phys. Rev. Materials* **4**, 025006 (2020).

25. T. K. Truttmann, F. Liu, J. Garcia-Barriocanal, R. D. James, B. Jalan, *ACS Applied Electronic Materials* **3**, 1127 (2021).

26. P. Siwakoti, *et al.*, *Phys. Rev. Mater.* **5**, 114409 (2021).

27. S. Backes, *et al.*, *Physical Review B* **94**, 241110 (2016).

28. E. Cappelli, *et al.*, *Phys. Rev. Mater.* **6**, 075002 (2022).

29. H. Takatsu, *et al.*, *Journal of Crystal Growth* **543**, 125685 (2020).

30. T. Yoshida, *et al.*, *Phys. Rev. B* **82**, 085119 (2010).

31. S. Thapa, *et al.*, *APL Materials* **10** (2022). 091112.

32. C. Fang, Y. Chen, H.-Y. Kee, L. Fu, *Phys. Rev. B* **92**, 081201 (2015).

33. S.-Y. Yang, *et al.*, *Advances in Physics: X* **3**, 1414631 (2018).

34. D. Xiao, M.-C. Chang, Q. Niu, *Rev. Mod. Phys.* **82**, 1959 (2010).

35. N. Nagaosa, J. Sinova, S. Onoda, A. H. MacDonald, N. P. Ong, *Rev. Mod. Phys.* **82**, 1539 (2010).

36. G. Kresse, J. Furthmüller, *Physical Review B - Condensed Matter and Materials Physics* **54** (1996).

37. P. E. Blöchl, *Physical Review B* **50**, 17953 (1994).

38. D. Joubert, *Physical Review B - Condensed Matter and Materials Physics* **59**, 1758 (1999).

39. J. P. Perdew, *et al.*, *Physical Review Letters* **100**, 136406 (2008).

40. V. Wang, N. Xu, J. C. Liu, G. Tang, W. T. Geng, *Computer Physics Communications* **267**, 108033 (2021).

41. VASPFermiSurface, https://github.com/QijingZheng/VASP_FermiSurface (2023).

42. G. Pizzi, *et al.*, *Journal of Physics: Condensed Matter* **32**, 165902 (2020).

43. P. Giannozzi, *et al.*, *Journal of Physics Condensed Matter* **21** (2009).

44. J. P. Perdew, K. Burke, M. Ernzerhof, *Phys. Rev. Lett.* **77**, 3865 (1996).

45. G.-X. Zhi, C. Xu, S.-Q. Wu, F. Ning, C. Cao, *Computer Physics Communications* **271**, 108196 (2022).

46. Q. Wu, S. Zhang, H.-F. Song, M. Troyer, A. A. Soluyanov, *Computer Physics Communications* **224**, 405 (2018).

Supplementary Information: Band topology induced by octahedral rotation in $SrNbO_3$

Alla Chikina[1,*], Victor Rosendal[2], Hang Li[1], Eduardo B. Guedes[1], Marco Caputo[3], Nicholas Clark Plumb[1], Ming Shi[1], Dirch Hjorth Petersen[2], Mads Brandbyge[4], Walber Hugo Brito[5], Ekaterina Pomjakushina[6], Valerio Scagnoli[6,7], Jike Lyu[6], Marisa Medarde[6], Elizabeth Marie Skoropata[1], Urs Staub[1], Shih-Wen Huang[1], Felix Baumberger[1,8], Nini Pryds[2,*], and Milan Radovic[1,*]

[1]Photon Science Division, Paul Scherrer Institut, CH-5232 Villigen, Switzerland

[2]Department of Energy Conversion and Storage, Technical University of Denmark, 2800 Kgs. Lyngby, Denmark

[3]MAX IV Laboratory, Lund University, P.O. Box 118, 22100, Lund, Sweden

[4]Department of Physics, Technical University of Denmark, 2800 Kgs. Lyngby, Denmark

[5]Departamento de Física, Universidade Federal de Minas Gerais, C. P. 702, 30123-970, Belo Horizonte, MG, Brazil

[6]Laboratory for Multiscale Materials Experiments, Paul Scherrer Institut, CH-5232 Villigen, Switzerland

[7]Department of Materials, Laboratory for Mesoscopic Systems, ETH Zurich, 8093 Zurich, Switzerland

[8]Department of Quantum Matter Physics, University of Geneva, 24 Quai Ernest-Ansermet,1211 Geneva 4, Switzerland

[*]Corresponding authors. Emails: chikina.alla@gmail.com, nipr@dtu.dk, milan.radovic@psi.ch

September 27, 2023

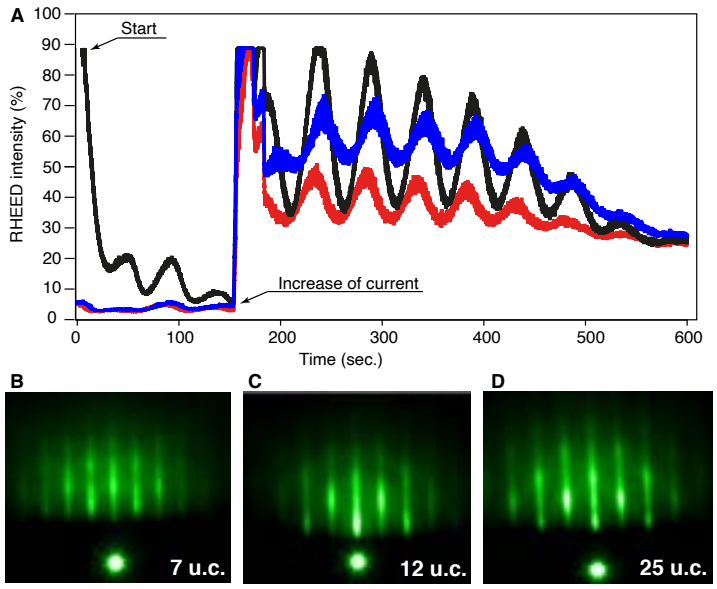

Figure S1: RHEED characterisation of $SrNbO_3$ films. (**A**) RHEED oscillations observed during the growth of 25 u.c. $SrNbO_3$ layer on top of $SrTiO_3$ (001) substrate, indicating a layer-by-layer growth mode. (**B-D**) RHEED patterns for 7, 12 and 25 unit cells.

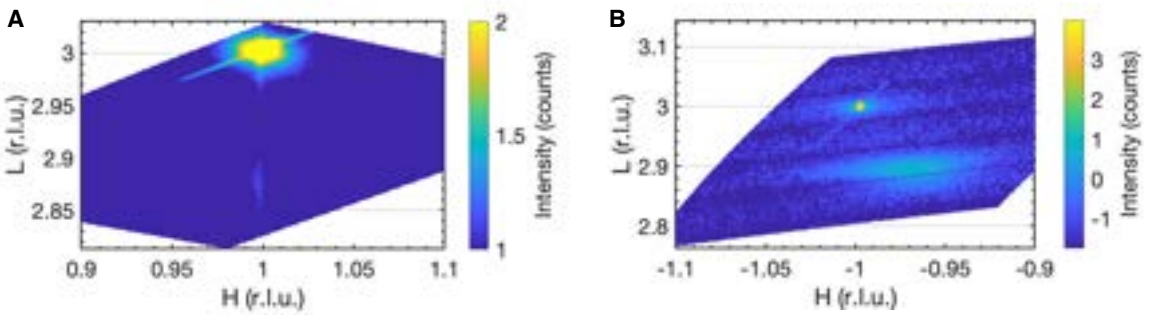

Figure S2: The XRD reciprocal-space maps taken around the $SrTiO_3$ (002) and (001) reciprocal-lattice points for (**A**) 25 and (**B**) 235 u.c. thick $SrNbO_3$ films. The alignment of peaks for thin films confirms the film strain.

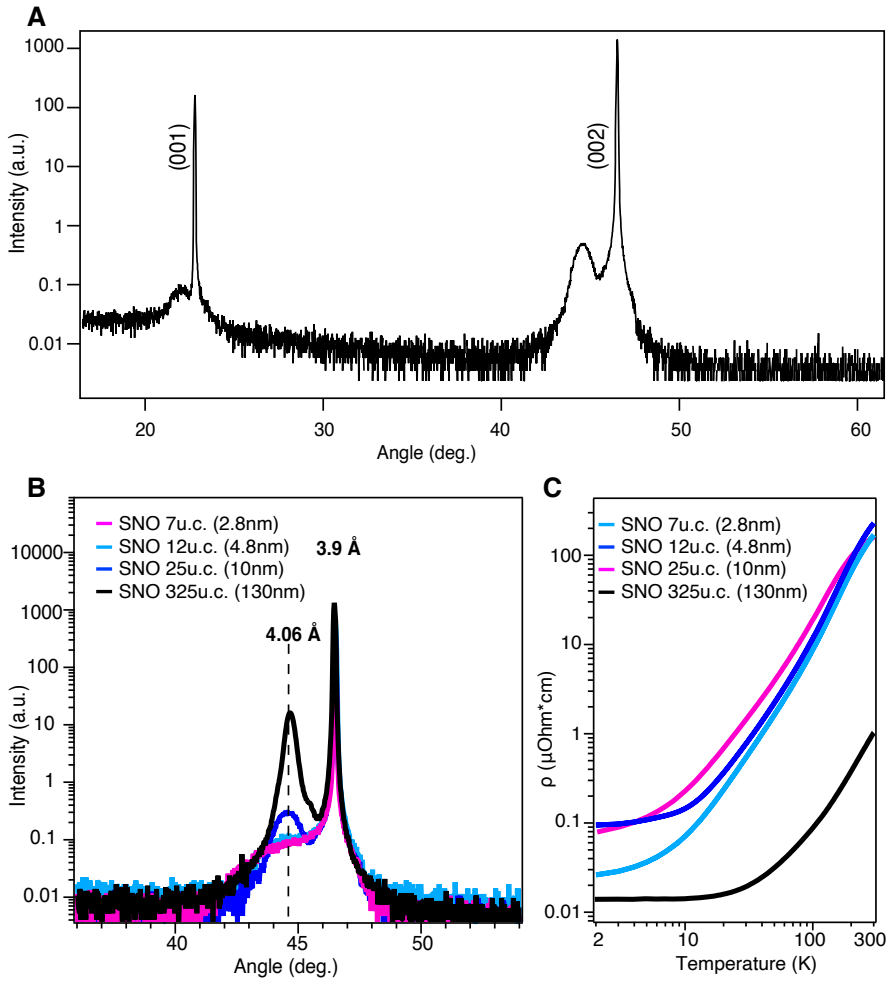

Figure S3: (**A**) X-ray diffraction $2\theta - \theta$ patterns for 25 u.c. thick $SrNbO_3$ film and (**B**) comparison of X-ray diffraction $2\theta - \theta$ for 7, 12, 25 and 325 u.c. thick $SrNbO_3$ films. (**C**) Temperature dependence of resistivity of $SrNbO_3$ thin films with different film thicknesses.

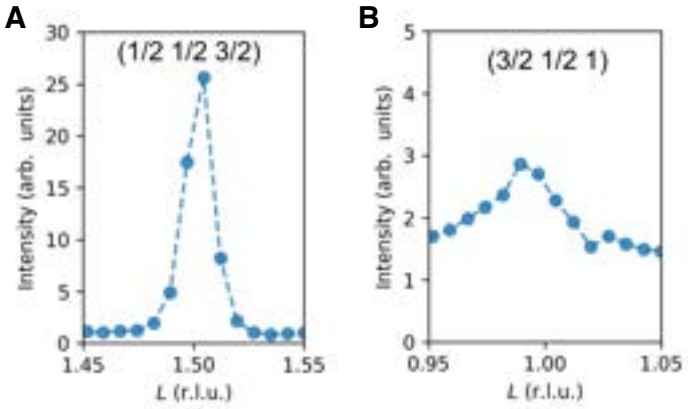

Figure S4: Octahedral rotation-induced half-order superstructure diffraction peaks of (**A**) (1/2 1/2 3/2) and (**B**) (3/2 1/2 1) for fully relaxed 130 nm thick SrNbO3 film. The presence of both peaks typical for (**A**) $a^0a^0c^+$ and (**B**) $a^0a^0c^-$ tilt modes show the co-existance of both phases. X-Ray diffraction also shows that $a^0a^0c^+$ phase has more two-dimentional character, which together with the ARPES findings would support the view that the $a^0a^0c^+$ is localised more at the surface.

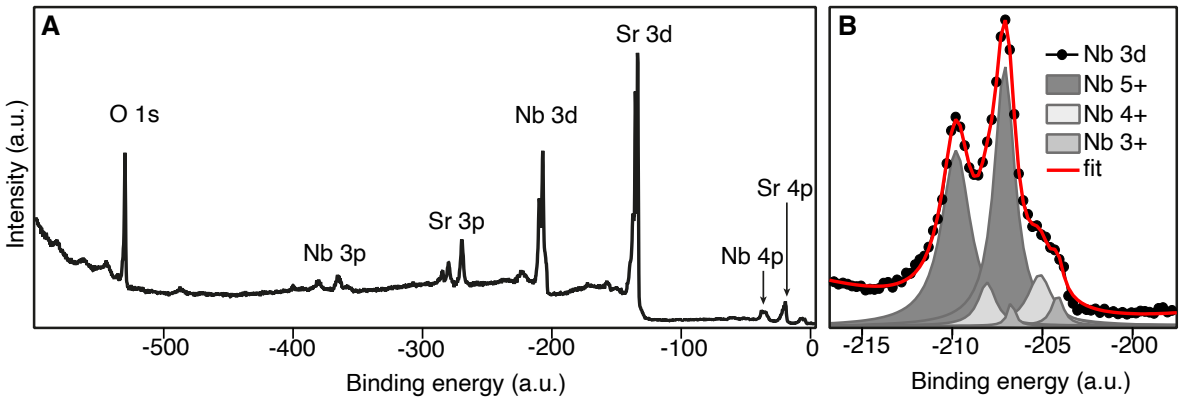

Figure S5: (**A**) Photoemission spectra taken at $h\nu$= 650 eV photon energy for 25u.c. thick $SrNbO_3$. (**B**) Nb 3d peaks. Nd 3d spectra shows 3d $\frac{3}{2}$ and $\frac{5}{2}$ contributions from several valence states.

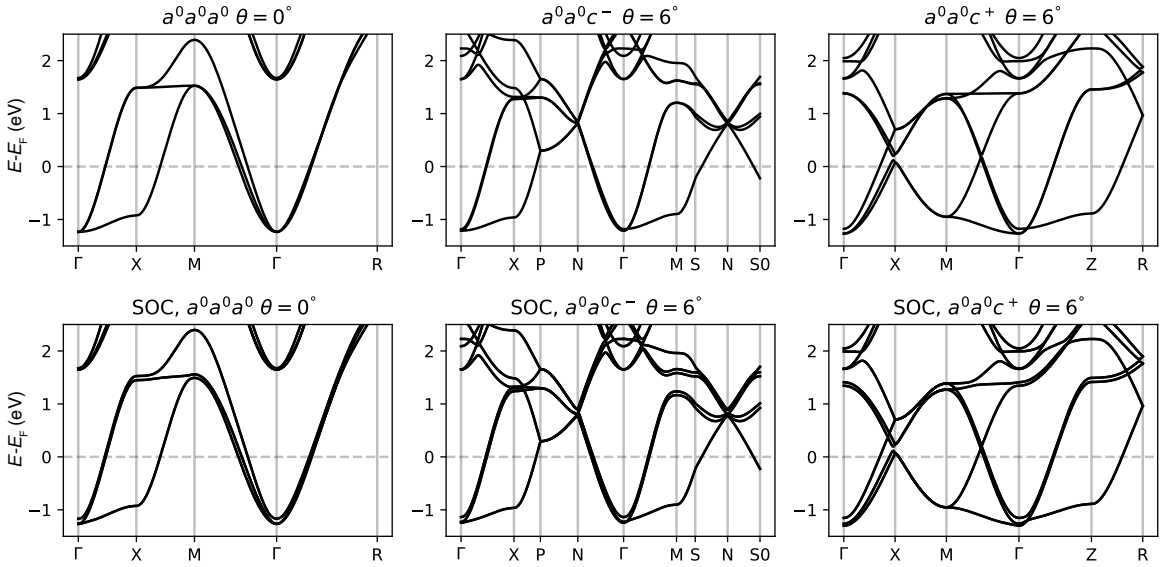

Figure S6: Upper (lower) row shows the band structures without (with) SOC. Here the bands are shown along the paths in the respective 1st BZ of the primitive structures and no unfolding is performed. Octahedral tilting and SOC split the t_{2g} orbitals.

1 Effect of spin-orbit coupling

Niobium is a relatively heavy atom, hence the spin-orbit coupling (SOC) could be sizeable in $SrNbO_3$. Fig. S6 shows the band structures without and with SOC. Note, the band structures are shown in the 1st BZ of the primitive structures, hence the notations are not the same as in the main text. The SOC splits the previously degenerate t_{2g} states at Γ in $a^0a^0a^0$. Furthermore, the SOC and octahedral tilting in combination split the t_{2g} orbitals further in $a^0a^0c^-$ and $a^0a^0c^+$. The t_{2g} split at Γ is circa 100 meV for $a^0a^0a^0$, i.e. substantial but likely too small to be relevant in the ARPES analysis.

2 Brillouin zones and band folding

Figure S7 shows the band folding due to change from the cubic lattice to the lattices describing $a^0a^0c^-$ and $a^0a^0c^+$. For simplicity we here use a tilt angle of 0 degrees, so that the changes seen are only due to the increase in the sizes of the cells. A non-zero rotation will lift the degeneracy of the t_{2g} states at, e.g., Γ. Furthermore, a rotation will break the cubic symmetry hence lifting the degeneracy of the $\vec{k}_1 = (\pi/a, 0, 0)$ and $\vec{k}_2 = (0, 0, \pi/a)$ points at the Brillouin zone edges. As an example, a finite rotation in the $a^0a^0c^-$ mode will lift the degeneracy of the $X = (\pi/a, 0, 0)$ and $M = (0, 0, \pi/a)$ points (given in the Cartesian system), which can be seen in Figure S6. A larger rotation angle increases the energy difference between these points. This

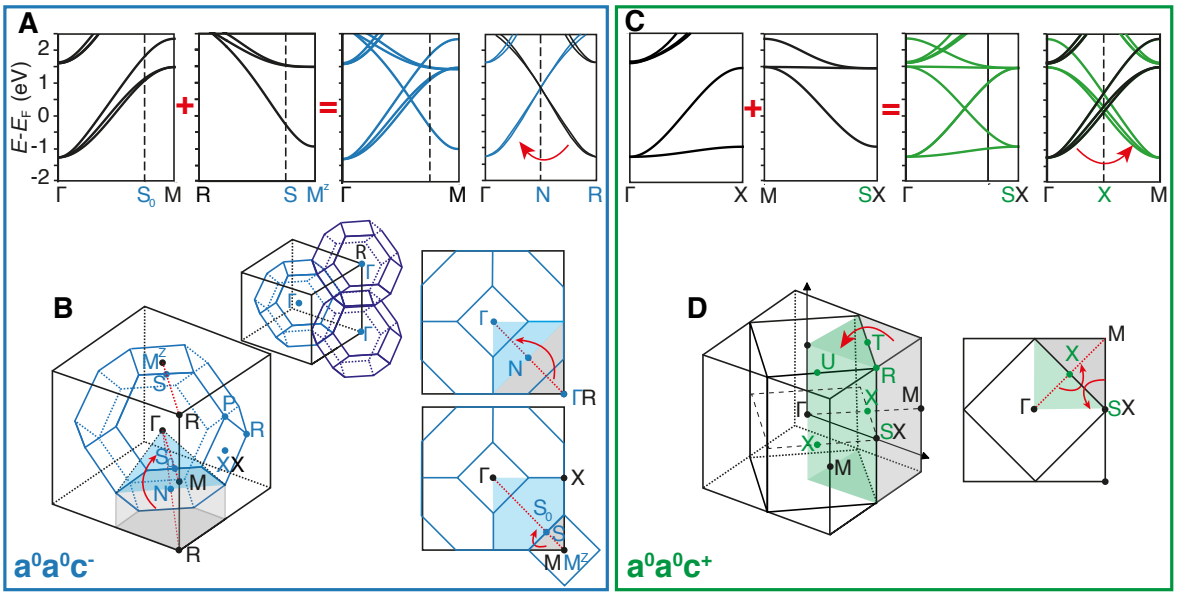

Figure S7: (**A, C**) Folding of bands due to the octahedral tilting and (b,d)schemes of the 1st Brillouin zones of $a^0a^0c^-$ **(A, B)** and $a^0a^0c^+$ **(C, D)** in the Brillouin zone of $a^0a^0a^0$(black notation). Dispersions along selected high symmetry directions are shown for $a^0a^0a^0$ in black, in blue for $a^0a^0c^-$ and in green $a^0a^0c^+$. This presents 0 deg tilt. Folding of bands are highlighted with a red arrow.

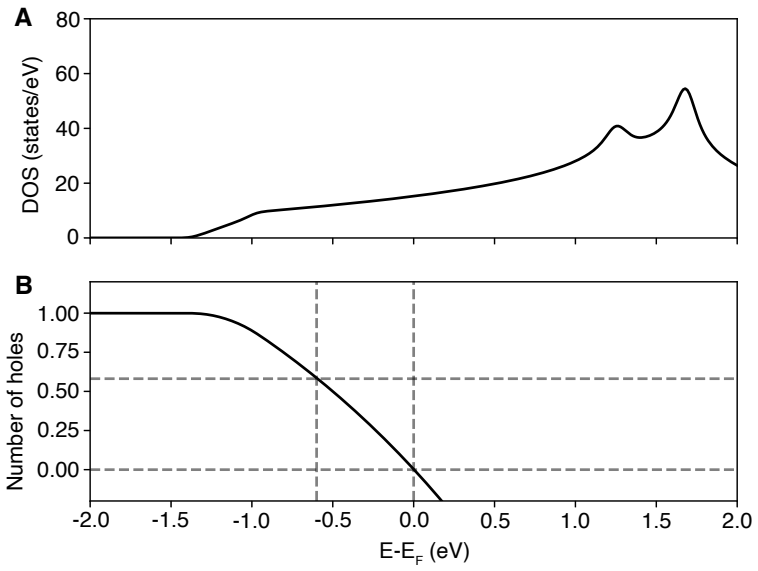

Figure S8: (A) Density of states of $SrNbO_3$ near the Fermi level. (B) Number of holes necessary to dope the system to shift the Fermi level to match experimental data.

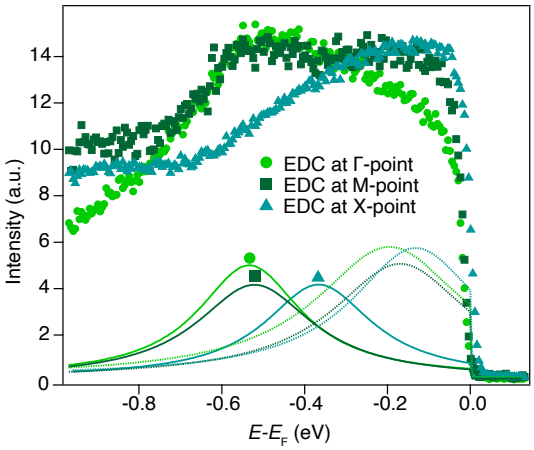

Figure S9: Energy distribution curves at the M, Γ and X points of the Brillouin zone.

is the origin of the energy difference between the conduction band minimum at (cubic) X and M in the unfolded band structure of $a^0a^0c^-$ in the main text. The reason is the following, the unfolded states around the cubic M point originate from M (of the $a^0a^0c^-$ lattice), which no longer is equivalent with the X point in the cubic and $a^0a^0c^-$ lattice, hence, there is a lifting of the degeneracy at unfolded X and M in the case of $a^0a^0c^-$. In the case of $a^0a^0c^+$, the unfolded bands around cubic M originate from the Γ point. Therefore, any changes in the bands due to a change of tilt angle will be identical at cubic M and Γ, with a mirror symmetry around cubic X, as shown in Figure S7. To summarize, due to the nature of the band folding presented in Figure S7, a degeneracy in conduction band minima at cubic M and Γ in the unfolded band structure (or ARPES) is a strong indication for the presence of $a^0a^0c^+$. For the minima to be equivalent at cubic M and Γ in the case of $a^0a^0c^-$, the heavy t_{2g} state must in fact be dispersionless, furthermore $X = (\pi/a, 0, 0)$ and $M = (0, 0, \pi/a)$ (in Cartesian system) must be degenerate, which is only true in the absence of tilt. Hence, to observe identical minima at cubic M and Γ with a $a^0a^0c^-$ tilt mode, the tilt angle must be vanishingly small and the t_{2g} orbitals must essentially be planar, which seems unlikely.

3 ARPES

In order to understand what type of octahedral tilting we need to evaluate the position of the conduction band minimum at Γ, M and X points of Brillouin zone. Figure S9 shows energy distribution curves taken at Γ, X and M points from the spectra of 7 u.c. thick $SrNbO_3$ films. The fit of EDCs showed that the position of conduction band maximum is $\sim -0.52 \pm 0.05$ eV at M point, $\sim -0.54 \pm 0.05$ eV at Γ- point and $\sim -0.37 \pm 0.05$ eV at X point. The fitted peaks presented on the FigureS9 below where markers point out the position of the peaks.

B.3 Influence of oxygen vacancies on charge and spin transport in $SrNbO_3$: A DFT-NEGF based study

In this manuscript the electron-oxygen vacancy scattering in bulk and slab $SrNbO_3$ is studied computationally. This is motivated by the theme that conducting oxides often lose their conductive properties with smaller thickness and that oxygen vacancies are common in oxides. The loss in conductance due to one oxygen vacancy is estimated as a function of vacancy location. Furthermore, the importance spin polarization is investigated. The findings here are (to my knowledge) a first attempt at trying to theoretically quantify the effect of oxygen vacancies on the transport in conducting oxides. In this study I performed all calculations and wrote the manuscript with help from co-authors.

Influence of oxygen vacancies on charge and spin transport in $SrNbO_3$: A DFT-NEGF based study

Victor Rosendal,[1] Nini Pryds,[1] Dirch H. Petersen,[1] and Mads Brandbyge[2]

[1] *Department of Energy Conversion and Storage, Technical University of Denmark, 2800 Kgs. Lyngby, Denmark*

[2] *Department of Physics, Technical University of Denmark, 2800 Kgs. Lyngby, Denmark*

(Dated: September 29, 2023)

The existence of oxygen atoms in perovskite oxides is, of course, essential to its material properties. Hence, a lack of oxygen atoms, or precense of oxygen vacancies, will likely play a role in how the oxide behaves. In this article, we investigate how oxygen vacancies affect the electronic transport in bulk and slabs of $SrNbO_3$. This is done using density functional theory (DFT) and non-equilibrium Green's function calculations (NEGF). Strontium niobate has previously shown promise as a transparent conductor, but also a potential semi-Dirac metal, making it an interesting platform for studying various transport phenomena. We show how oxygen vacancies scatter electrons and thereby increasing the electrical resistance, as expected. Furthermore, if the O vacancy is between two Nb ions in the direction of transport, the resistance is substantially larger than if the vacancy is placed between two Nb ions perpendicular to the transport. Finally, we show, by performing spin polarized calculations, that the O vacancy scatters the two spin channels with different strengths. The spin filtering is seemingly enhanced in ultra thin slabs compared to bulk $SrNbO_3$. This could indicate that the O vacancies are more than just cause for resistance, but potentially useful in spintronic applications in conducting oxides like $SrNbO_3$.

I. INTRODUCTION

The plethora of material properties that perovskite oxides offer is rewarding both for applications, but also from a fundamental point-of-view. The behaviour of these materials is a result of the interplay between the atomic, electronic and lattice degrees of freedom. By tuning the stochiometry of perovskite oxides one can alter the material properties. More specifically, it has been shown both experimentally and theoretically that the oxygen content is crucial for the electronic structure and properties of oxides.[1–3] Disorder due to oxygen vacancies have also been connected to the poor or even insulating electronic behaviour of thin film oxides. [4–6]

An oxide of recent interest is $SrNbO_3$. The interest stems from the potential of using $SrNbO_3$ as a transparent conductor [7] or even to realise extremely mobile electrons by forming semi-Dirac dispersions [8]. These findings make it worthwhile to ask what the effect of oxygen vacancies is on the electronic transport properties in a material such as $SrNbO_3$.

We here examine the influence of oxygen vacancies on the electronic transport in $SrNbO_3$ using density functional theory (DFT) based calculations. We employ non-equilibrium Green's functions (NEGFs) to study open quantum transport problems, in comparison to the periodic boundary condition often used in DFT studies of both pristine and defective systems. Both bulk and slabs are considered and different oxygen vacancy positions are sampled. We show that oxygen vacancies reduce the electron transmission, as expected. More interestingly, we are able to differentiate the importance of the different vacancy positions. Furthermore, by doing both spin unpolarized and polarized calculations we get insight into significance of the oxygen vacancy on the spin dependent transport. A substantial spin splitting is observed, indicating that oxygen vacancies are not simply bad for all purposes, but could be important and useful for spin transport where the O vacancy might act as a spin filter.

II. METHOD

To study the electron transport we use NEGF, in which one separates the "scatter" region (colorful circles in Figure 1) from the semi-infinite "electrode" regions (transparent circles in Figure 1). The electrodes are pristine (bulk or slabs) of $SrNbO_3$ and act as infinite reservoirs where the electrons are in (local) equilibrium described by some temperature and chemical potential. The central or scatter region contains $SrNbO_3$ with an oxygen vacancy, and this is where the periodic translational symmetry of the lattice is broken and a resistance emerges. Periodic boundary condition is applied in x and y-direction. In the NEGF technique the electrodes are coupled to the central region as a self-energy, i.e. the Green's function of the device is the Green's function of the central region with the addition of self-energies from the left and right electrodes. In this study, we solved the electronic structure problem using DFT coupled with the NEGF formalism. In practice this was done using Siesta [9] and TranSiesta [10, 11] which use linear combination of atomic orbitals (LCAO) basis sets. A comparison between the LCAO and a plane-wave band structure can be found in Appendix A. The oxygen vacancies were introduced as ghost atoms. Transmission functions were calculated based on the self-consistent electronic structure using TBtrans [11] and post-processing was done using SISL [12]. The PBE [13] functional was used throughout the work. In the directions with peri-

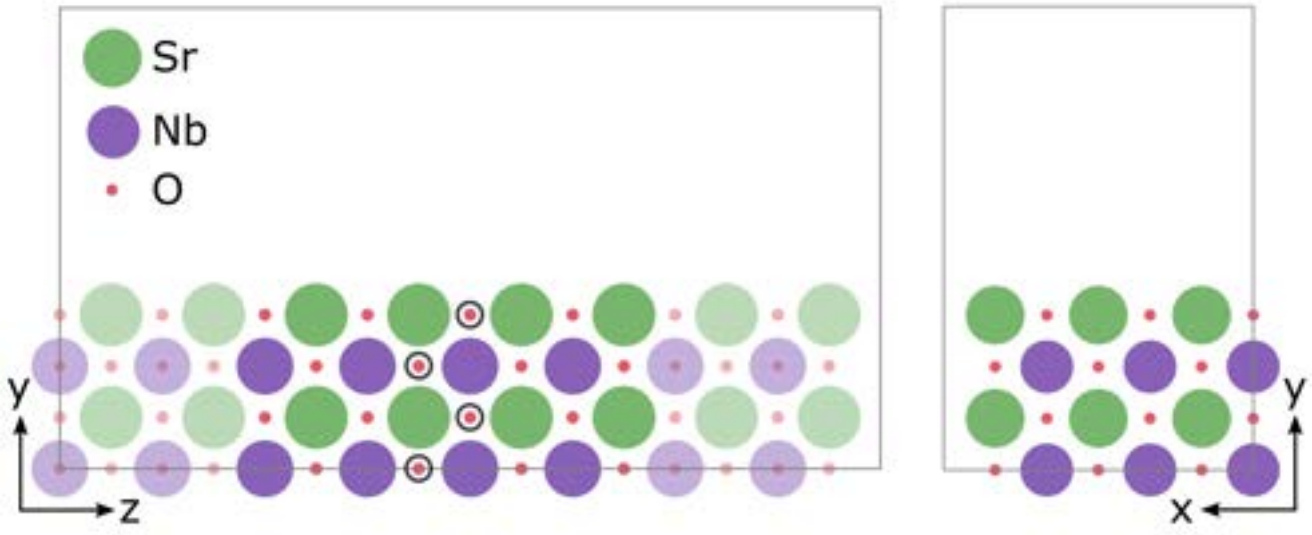

FIG. 1: Schematic of the transport problem of the 2 u.c. slab of $SrNbO_3$. The transport is in the z-direction and repitition of 3 u.c. is used in x-direction to reduce the vacancy-image interaction. The transparent circles denote the electrode regions. The locations for the O vacancies are drawn as circles, we refer them as located in NbO_2 or SrO layers in the text, since they appear in different layers in the y-direction.

odic boundary conditions, 12 k-points (per unit cell) were used for the calculation of self-consistent charge densities and then the transmission functions were calculated with 60 k-points (per unit cell).

The electrodes were two unit cells in transport direction, which is necessary to make sure there are no orbitals overlapping with orbitals in second (and so on) nearest neighbour electrode cells. Furthermore, the NEGF formalism requires that the connection between the electrodes and the first layer in the transport direction of the central region is "bulk-like" and not perturbed by the defect. In other words, there should be a extension of the central region that is identical to the the electrode region where the perturbation caused by the defect can vanish. For this reason, we chose to use a central region of 4 unit cells in the transport direction, see Fig. 1. Furthermore, to reduce the interaction between the defect and its images, we used 3 repetitions of the unit cells in the periodic directions as depicted in Fig. 1 in the x-direction. This was a compromise between the cost and accurate description of *local* point defects. In the slab calculations, a vacuum of 10 Å was introduced to separate the slab from its images. The slabs were also chosen to be asymmetric. Due to the asymmetry of the slabs we employed a dipole correction to compensate for the artificial electrostatic interaction between the two sides of the slabs.

The cubic phase of $SrNbO_3$ was used with a lattice parameter of 4.0182 Å as predicted using DFT in Reference [14]. There is an excellent agreement between the used and experimental value 4.023 Å [15]. The ion positions were relaxed in the slabs below a max force of 0.04 eV Å^{-1}. This was, however, only done for the 2 u.c. thick slab. The oxygen vacancy is created in the relaxed structures (unrelaxed for 3 and 4 u.c. thick slabs), and no further relaxation is done. This is done with the motivation that the conductance is almost unaffected by the initial relaxation, as seen in Appendix C, i.e., we do not expect that further relaxation will affect the conclusions.

In this work we limit ourselves to zero bias conditions, i.e., the two electrodes are in equilibrium with each other. The transmission function from the left electrode to right electrode takes the form:

$$T_{LR} = \mathrm{Tr}\left[\mathbf{G}\mathbf{\Gamma}_L\mathbf{G}^\dagger\mathbf{\Gamma}_R\right] \tag{1}$$

where $\mathbf{G}$ is the Green's function:

$$\mathbf{G} = \left[(E+i0^+)\mathbf{S} - \mathbf{H} - \mathbf{\Sigma}_L - \mathbf{\Sigma}_R\right]^{-1} \tag{2}$$

and $\mathbf{\Gamma}_{L/R}$ is the broadening matrix due to the left or right electrode:

$$\mathbf{\Gamma}_{L/R} = i\left[\mathbf{\Sigma}_{L/R} - \mathbf{\Sigma}_{L/R}^\dagger\right] \tag{3}$$

We have skipped the energy and momentum variables for simplicity. In Eqs. 2 and 3, the electrode self-energy is denoted $\mathbf{\Sigma}_{L/R}$ and the overlap and Hamiltonian matrices of the central region is denoted $\mathbf{S}$ and $\mathbf{H}$, respectively. We present our results using the conductance function, $G(E) = \frac{e^2}{h}T_{LR}(E)$, normalised with the interface area, A, in units of number of unit cells. The conductance is given per spin channel, hence in the spin unpolarized cases there are two identical channels with equal conductances.

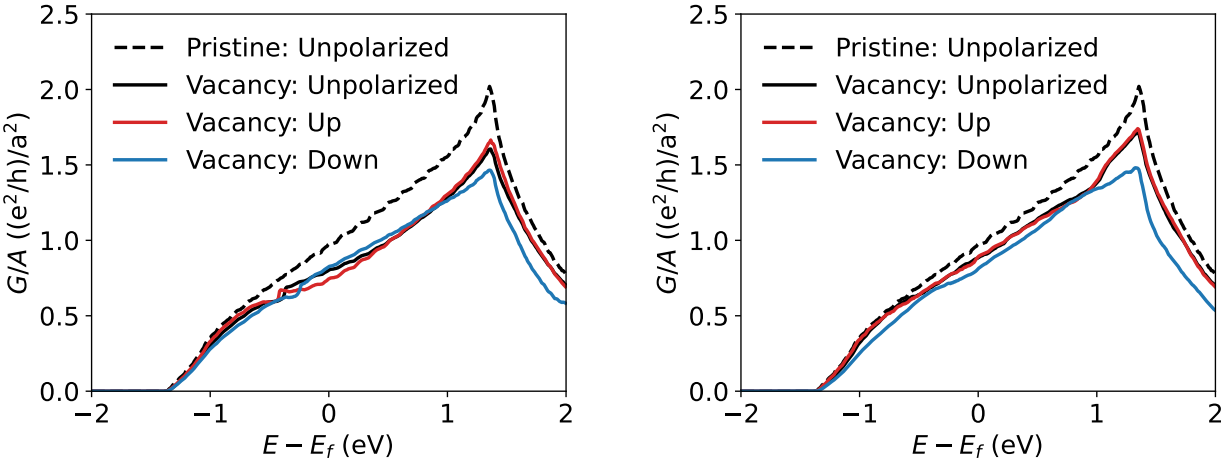

(a) O vacancy in NbO_2 layer

(b) O vacancy in SrO layer

FIG. 2: Conductance per unit cell area for different configurations of bulk $SrNbO_3$.

III. RESULTS AND DISCUSSION

A. Bulk conductance

First, the bulk electron transmission was calculated for $SrNbO_3$. This was done for both the spin polarized and unpolarized case. Due to the symmetry of the transport problem, there are two unique oxygen vacancy positions, either between two Nb ions in the transport direction or above the Nb ion perpendicular to the transport direction. We call the first scenario "O vacancy in NbO_2 layer" and the latter scenario "O vacancy in SrO layer", by the appearance in Fig. 1. Furthermore, the results shown for the defective systems are for unrelaxed structures, i.e., we have not relaxed the structures after the vacancies are introduced.

Figure 2 shows the conductance per unit cell area of bulk $SrNbO_3$ without and with O vacancies. Figure 2(a) shows the transport properties when the vacancy is placed in the NbO_2 layer, while Figure 2(b) shows the results when the vacancy is located in the SrO layer. It is clear that both types of vacancies come at a loss of electronic transport, i.e., the vacancies contribute to the electrical resistance. Furthermore, the resistance due to the O vacancy in the NbO_2 layer is slightly larger compared to the O vacancy in the SrO layer. This is understandable from the orbital picture of the perovskite, where the oxygen p-states bridges the niobium d-states that forms the conduction bands. [16] Therefore, removing this "bridge" is more disruptive if it occurs between two Nb ions in the transport direction, as in the case of O vacancy in NbO_2 layer. Enabling spin polarization, we observe a small spin splitting in the conductance, i.e., the two spin channels are no longer equivalent. The electrodes are always without spin polarization, i.e., the electrons injected from the electrodes are unpolarized. This effect is very small in bulk, and likely negligible for experimental purposes.

B. Confinement effects in slabs

Next, we create asymmetric slabs of $SrNbO_3$ with varying thickness. The results for 2, 3, and 4 u.c. thick $SrNbO_3$ is presented in Figure 3. Due to the confinement effect the conductance of the slabs shows abrupt jumps, and the thicker films shows more frequent steps. The reason for the non-zero slopes of the steps is the existing periodicity perpendicular to the transport direction within the slabs. Hence, the states are dispersed in said direction. Increasing the thickness to infinity must result in the same conductance as the bulk case, as shown in Figure 2, and this seems reasonable.

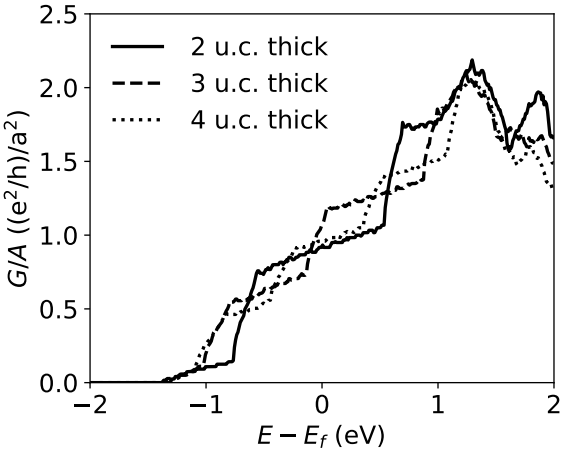

FIG. 3: Thickness dependency of conductance in ultra thin $SrNbO_3$.

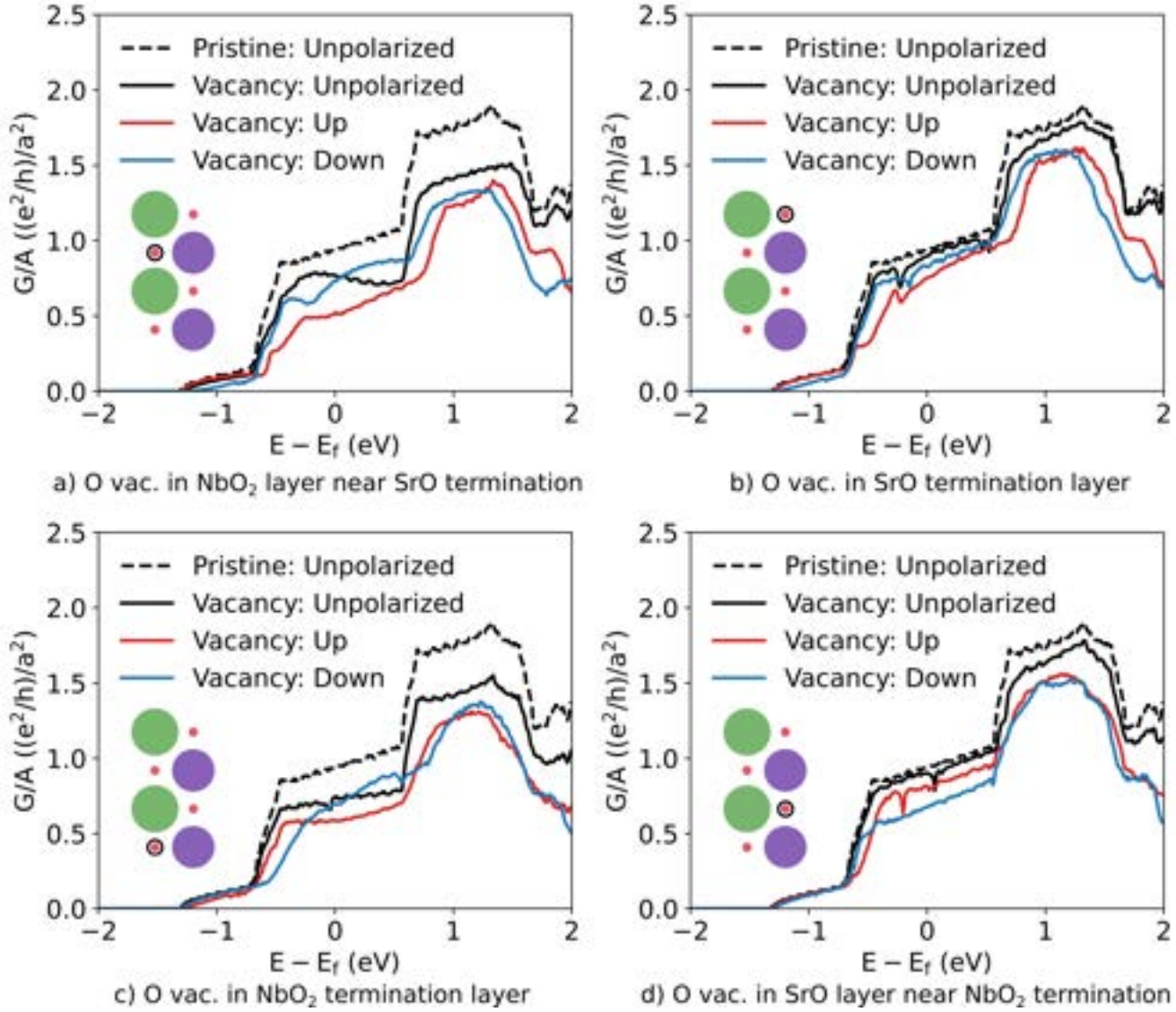

FIG. 4: Conductance per unit cell area for different configurations of 2 u.c. thick $SrNbO_3$. Both spin polarized and unpolarized results are shown. The pristine calculation is always without spin polarization

C. Conductance in defective slabs

Then oxygen vacancies are introduced to the slabs of $SrNbO_3$ at the different unique positions. We here focus on the 2 u.c. thick slab, since for this thickness we have performed spin polarized calculations additional to the unpolarized calculations. These results are shown in Figure 4. The left (right) column shows the conductance when the O vacancy is placed in the NbO_2 (SrO) layer. The upper (lower) row shows the conductance the the vacancy is placed in a layer near (or at) the SrO (NbO_2) terminated surface. Comparing the conductance of the pristine system with the conductance of the defective systems in the unpolarized case, it is evident that all O vacancies are not equal. Like in the bulk case, the vacancies give rise to a larger resistance when placed between the Nb ions in the transport direction, compared to when they are placed above the Nb ions perpendicular to the transport direction. This is true both near (or at) the SrO and NbO_2 terminated surfaces. Interestingly, the difference between the resistance due to the vacancies in the different layers is larger than in bulk. By introducing the (collinear) spin degree of freedom, the electron transmission now becomes dependent of the spin. The electronic states of the electrodes are treated as spin degenerate. Like in the unpolarized case, the vacancies are more resistive when placed in the NbO_2 layers, compared to when placed in the SrO layers. However, now the conductance is larger (at least around the Fermi level) for one of the spin channels. Interestingly, the po-

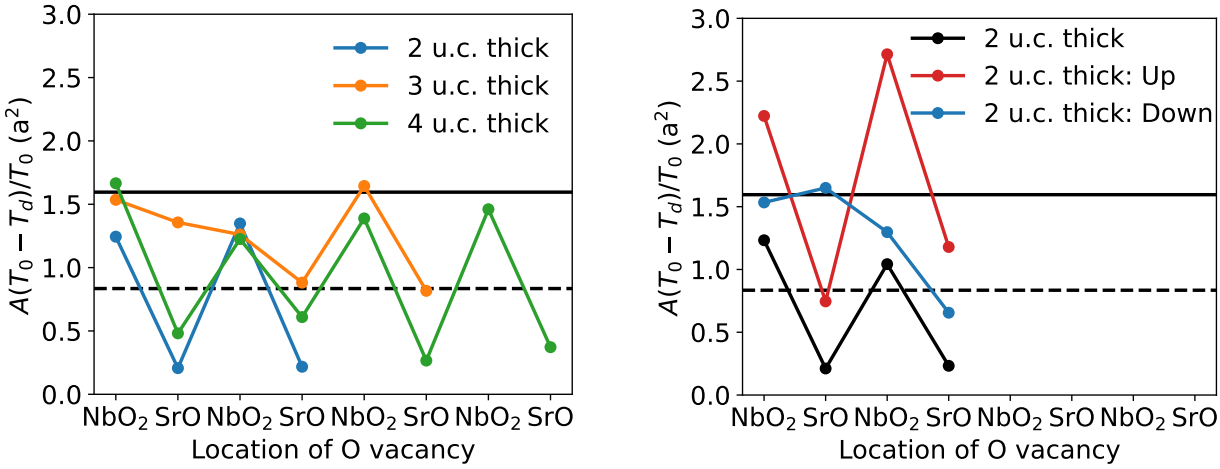

(a) Unpolarized cross sections

(b) Effect of spin on cross sections

FIG. 5: Scattering cross sections due to O vacancies in units of lattice constant squared at the Fermi level. Unpolarized (polarized) results are shown to the left (right). The solid (dashed) horizontal line represent the cross section for vacancy in NbO_2 (SrO) layer in bulk. The bulk results are all unpolarized for simplicity.

larization of the electron transmission is larger compared to the bulk counterparts. Furthermore, the polarization of the transmitted electrons is slightly larger for the systems where the O vacancy is placed between Nb ions in the transport direction, i.e., in the NbO_2 layers. In this case, segments (e.g. between 0 and 0.5 eV) of the conductance function of the spin up channel is higher than the spin unpolarized case. In other words, the spin polarization reduces the resistivity of the vacancy in these cases. This illustrates how oxygen vacancies could filter the spin of the electrons in $SrNbO_3$ that is normally non-magnetic. To check that the change in conductance between the two spins is related to the vacancy, and not a slab effect alone, we performed spin polarized calculation of the pristine 2 u.c. slab. The result is shown in Appendix B, and it shows that while the conductances are slightly lower than the unpolarized case, the two spin channels are almost identical, especially near the Fermi level.

D. Scattering cross sections of O vacancies

Finally, we evaluate so called scattering cross sections using the transmission functions of the pristine and defective systems. We define the scattering cross section as: [17, 18]

$$\sigma(E) = A\frac{T_0(E) - T_d(E)}{T_0(E)}, \tag{4}$$

where A is the cross sectional area of the defective system, and T_0 and T_d is the transmission functions of the pristine and defective systems, respectively. The scattering cross section is a measure of how much effective cross sectional area is removed due to the presence of the defect. The scattering cross sections for the different oxygen vacancy locations is presented in Figure 5. All cross sections are evaluated at the Fermi levels. We present both spin polarized data, extracted from Figure 4, but also unpolarized data with additional data for 3 and 4 u.c. thick films. From the unpolarized data, in Fig. 5(a), it is again clear that the scattering is sensitive to where the O vacancies are placed, even for thicker films. A typical scattering cross section for O vacancies placed in NbO_2 layers is circa 1.5 a^2, while vacancies in SrO layers contribute to a scattering cross section of circa 0.8 a^2. The cross sections are slightly lower in the slab cases compared to the bulk counterparts. The addition of spin polarization systematically increases the scattering strengths, as seen in Fig. 5(b). Furthermore, there is a clear difference between the cross sections of the two spin channels, as discussed previously in relation to Figure 4. In this case, the cross section can reach above 2.5 a^2. This is a clear difference compared to the bulk response: the spin dependent transport becomes more rich and the the scattering strengths of the two spin channels increases when one considers slabs.

IV. SUMMARY

The effect of oxygen vacancies on the electronic transport in bulk and ultra thin slabs of $SrNbO_3$ has been investigated. The transport problem was investigated numerically using DFT-NEGF. We find that pristine bulk and slabs of $SrNbO_3$ are conductive and the inclusion of an oxygen vacancy reduces the conductance, as expected. Furthermore, the resistance due to an O vacancy is larger

if the vacancy is placed between the Nb ions in the transport direction, compared to when placed between Sr ions. In any case, by this knowledge, the oxygen vacancies are unwanted in the conducting perovskite. However, by letting the spins vary freely, we observe that the two spin channels have different conductive properties. In other words, the oxygen vacancy could act as as a spin filter in $SrNbO_3$. Furthermore, there is a clear difference between the bulk and slab behaviour. In bulk the spin filtering is rather small, while in the 2 u.c. slabs the difference between the spin up and down channels is up to $10 - 20\,\%$ near the Fermi level. These findings suggests that oxygen vacancies are not all bad, but that they could potentially be leveraged in spintronics applications to filter spins, especially in ultra thin films.

[1] F. Gunkel, D. V. Christensen, Y. Z. Chen, and N. Pryds, Oxygen vacancies: The (in)visible friend of oxide electronics, Applied Physics Letters **116**, 120505 (2020).

[2] D.-S. Park, A. Rata, I. Maznichenko, S. Ostanin, Y. Gan, S. Agrestini, G. Rees, M. Walker, J. Li, J. Herrero-Martin, *et al.*, The emergence of magnetic ordering at complex oxide interfaces tuned by defects, Nature communications **11**, 3650 (2020).

[3] H. O. Jeschke, J. Shen, and R. Valentí, Localized versus itinerant states created by multiple oxygen vacancies in srtio3, New Journal of Physics **17**, 023034 (2015).

[4] G. Wang, Z. Wang, M. Meng, M. Saghayezhian, L. Chen, C. Chen, H. Guo, Y. Zhu, E. W. Plummer, and J. Zhang, Role of disorder and correlations in the metal-insulator transition in ultrathin $srvo_3$ films, Phys. Rev. B **100**, 155114 (2019).

[5] Y. Ha and S. Lee, Oxygen-vacancy-endurable conductors with enhanced transparency using correlated 4d2 srmoo3 thin films, Advanced Functional Materials **30**, 2001489 (2020).

[6] H. Okuma, Y. Katayama, K. Otomo, and K. Ueno, Transport properties around the metal-insulator transition for $srvo_3$ ultrathin films fabricated by electrochemical etching, Phys. Rev. B **105**, 045138 (2022).

[7] Y. Park, J. Roth, D. Oka, Y. Hirose, T. Hasegawa, A. Paul, A. Pogrebnyakov, V. Gopalan, T. Birol, and R. Engel-Herbert, Srnbo3 as a transparent conductor in the visible and ultraviolet spectra, Communications Physics **3**, 102 (2020).

[8] J. M. Ok, N. Mohanta, J. Zhang, S. Yoon, S. Okamoto, E. S. Choi, H. Zhou, M. Briggeman, P. Irvin, A. R. Lupini, Y.-Y. Pai, E. Skoropata, C. Sohn, H. Li, H. Miao, B. Lawrie, W. S. Choi, G. Eres, J. Levy, and H. N. Lee, Correlated oxide dirac semimetal in the extreme quantum limit, Science Advances **7**, eabf9631 (2021).

[9] A. García, N. Papior, A. Akhtar, E. Artacho, V. Blum, E. Bosoni, P. Brandimarte, M. Brandbyge, J. I. Cerdá, F. Corsetti, R. Cuadrado, V. Dikan, J. Ferrer, J. Gale, P. García-Fernández, V. M. García-Suárez, S. García, G. Huhs, S. Illera, R. Korytár, P. Koval, I. Lebedeva, L. Lin, P. López-Tarifa, S. G. Mayo, S. Mohr, P. Ordejón, A. Postnikov, Y. Pouillon, M. Pruneda, R. Robles, D. Sánchez-Portal, J. M. Soler, R. Ullah, V. W.-z. Yu, and J. Junquera, Siesta: Recent developments and applications, The Journal of Chemical Physics **152**, 204108 (2020).

[10] M. Brandbyge, J.-L. Mozos, P. Ordejón, J. Taylor, and K. Stokbro, Density-functional method for nonequilibrium electron transport, Phys. Rev. B **65**, 165401 (2002).

[11] N. Papior, N. Lorente, T. Frederiksen, A. García, and M. Brandbyge, Improvements on non-equilibrium and transport green function techniques: The next-generation transiesta, Computer Physics Communications **212**, 8 (2017).

[12] N. Papior, sisl: v13.0 (2023).

[13] J. P. Perdew, K. Burke, and M. Ernzerhof, Generalized gradient approximation made simple, Phys. Rev. Lett. **77**, 3865 (1996).

[14] V. Rosendal, W. H. Brito, M. Radovic, A. Chikina, M. Brandbyge, N. Pryds, and D. H. Petersen, Octahedral distortions in $srnbo_3$: Unraveling the structure-property relation, Phys. Rev. Mater. **7**, 075002 (2023).

[15] D. Oka, Y. Hirose, S. Nakao, T. Fukumura, and T. Hasegawa, Intrinsic high electrical conductivity of stoichiometric $SrNbo_3$ epitaxial thin films, Phys. Rev. B **92**, 205102 (2015).

[16] M. T. Dylla, S. D. Kang, and G. J. Snyder, Effect of two-dimensional crystal orbitals on fermi surfaces and electron transport in three-dimensional perovskite oxides, Angewandte Chemie International Edition **58**, 5503 (2019).

[17] T. Markussen, R. Rurali, A.-P. Jauho, and M. Brandbyge, Scaling theory put into practice: First-principles modeling of transport in doped silicon nanowires, Phys. Rev. Lett. **99**, 076803 (2007).

[18] T. Markussen, R. Rurali, X. Cartoixà, A.-P. Jauho, and M. Brandbyge, Scattering cross section of metal catalyst atoms in silicon nanowires, Phys. Rev. B **81**, 125307 (2010).

Appendix A: Basis set benchmark

To generate a good Siesta LCAO basis set, we benchmarked our band structures against a VASP plane-wave solution. The VASP calculation was done as described in Reference [14]. The resulting band structures are shown in Figure 6. Excellent agreement is observed. To get good agreement between the two solutions, it was necessary to use triple-zeta polarized basis functions for oxygen. For niobium and strontium double-zeta polarized was sufficient.

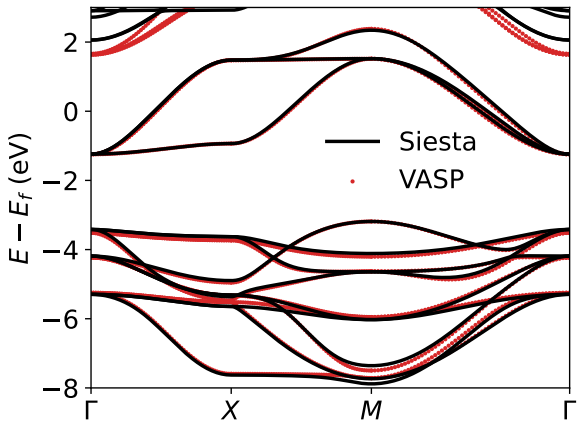

FIG. 6: Comparison between the $SrNbO_3$ band structure as calculated using Siesta and VASP. The VASP calculations were performed as described in Reference [14]. Note, the valence bands from VASP where shifted to fit the Siesta bands.

Appendix B: Spin polarization in pristine slab

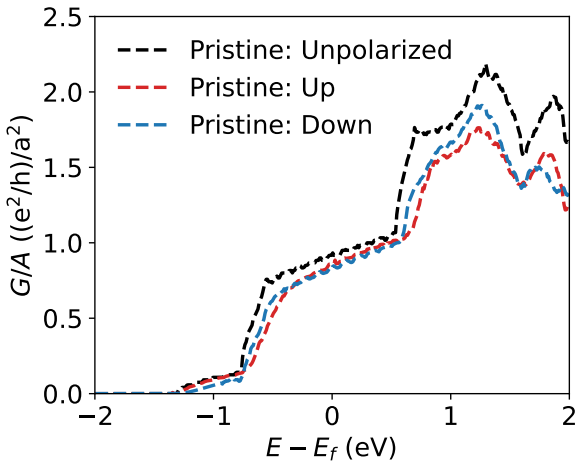

FIG. 7: Influence of spin polarization on the conductance in 2 u.c. thick $SrNbO_3$. A minor reduction in conductance is observed. However, close to Fermi level the two channels are almost identical.

Appendix C: Effect of relaxation on transport

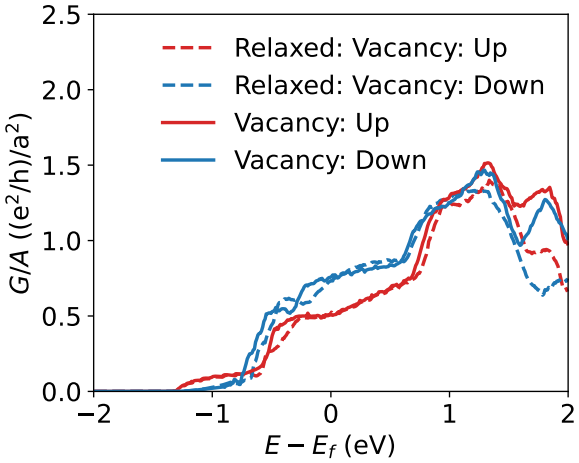

FIG. 8: Comparison between the conductance of 2 u.c. thick $SrNbO_3$ without and with ionic relaxation. The oxygen vacancy is placed between the Nb ions in transport direction closest to the SrO terminated surface. The relaxation only includes ionic relaxation of the pristine system, then the vacancy is introduced without further relaxation.

B.4 Observation of diffusive-to-ballistic phonon transport in boron doped silicon

The last manuscript included in this thesis is about how phonons behave at the microscale in doped silicon. Theoretical predictions are made by solving the general Boltzmann transport equation (BTE) and the results are compared with a diffusive model. While intrinsic silicon has been studied previously using BTE, I have not seen studies that include scattering due to the doping. Surprisingly, it is found that the doping has a rather small impact on the non-diffusive phonon transport. This indicates that diffusive models should be used with caution for describing the thermal transport of doped Si at the microscale. Preliminary measurements of thermal properties of doped Si at the microscale are included. They show length dependent deviations from macroscale references, which could indicate non-diffusive phonon transport as predicted using BTE. I performed the calculations (DFT and BTE), and the experiments were done by Neetu Lamba and Benny Guralnik. I wrote theoretical part of the manuscript, and Neetu Lamba and Benny Guralnik wrote the experimental details.

Observation of diffusive-to-ballistic phonon transport in boron doped silicon

Victor Rosendal,[1] Neetu Lamba,[1] Benny Guralnik,[1,2] Braulio Beltrán-Pitarch,[1,2] Mads Brandbyge,[3] Nini Pryds,[1] and Dirch H. Petersen[1]

[1] *Department of Energy Conversion and Storage, Technical University of Denmark, 2800 Kgs. Lyngby, Denmark*
[2] *CAPRES - a KLA Company, Diplomvej 373B, 2800 Kgs. Lyngby, Denmark*
[3] *Department of Physics, Technical University of Denmark, 2800 Kgs. Lyngby, Denmark*

(Dated: September 21, 2023)

Thermal transport in silicon, the primary material within the semiconductor industry, is characterized by long (up to 10 µm) phonon mean free paths (MFPs) at room temperature. When the system size is comparable to the MFP of the phonons, the thermal transport is ballistic, compared to diffusive as in macroscopic systems. In this work, we quantify the error in the predicted temperature profile by assuming Fourier's law in doped silicon at room temperature. The intrinsic Si phonon properties were predicted using density functional theory (DFT) methods. To model the effects of doping, isotope and phonon-electron scattering were introduced using analytical models. Using these phonon parameters, the Boltzmann transport equation (BTE) was solved for a nanoscopic heater geometry. A difference up to ca. 40 % is found between BTE and Fourier's law at a distance of 1 µm from the heater, even in the case of highly doped (1×10^{20} cm^{-3}) silicon. These predictions are further supported by thermal measurements of boron-doped silicon using a micro four-point probe (M4PP). The M4PP measurements exhibit length-dependent deviations from the expected macroscale thermal properties. Good agreement is found between the experimental and theoretical predictions, indicating a diffusive-to-ballistic transition at the micrometer length scale.

I. INTRODUCTION

Thermal transport describes the flow of heat through different mechanisms such as advection, convection, radiation, and conduction. A complete understanding of these mechanisms is crucial for optimal engineering and designing of thermal systems, especially in the era of nanoscale electronic devices with large power densities that must be dissipated quickly [1]. Phonons are the major heat carriers in semiconductors. Therefore, phonon transport is a topic of great relevance to the electronics industry. Fourier's law of conduction describes heat transport in the diffusive regime and is typically applicable in macroscopic systems. However, understanding the limitations of Fourier's law is essential, otherwise, the thermal response might be inadequately modeled. Similar to electrons, phonons can also display ballistic/non-diffusive transport. This occurs under the condition $\lambda_{MFP} \geq L$, where λ_{MFP} is the mean free path (MFP) and L is a characteristic length scale of the system [2]. However, unlike electrons, phonons can have a broad spectrum MFPs [3, 4], which further complicates the heat transport since some phonons might be transported diffusively while others are ballistic. In References [3, 4], the phonon MFP spectrum is measured by varying the heater sizes and evaluating the suppression in thermal transport.

Recently, it has been demonstrated that micro four-point probe (M4PP) measurements at the microscale induce sufficient Joule heating in the sample to enable probing of the ratio, S/κ, where S is the Seebeck coefficient and κ is the thermal conductivity [5]. While ballistic transport was briefly mentioned in References [5, 6], the contribution to heat transport was considered negligible and thus left unquantified. Inspired by the findings from microscopic thermal transport and the recent expansion of the M4PP method to thermoelectric properties, we were motivated to further analyse the thermal transport at the microscale using a combination of theory and M4PP experiments.

The Boltzmann transport equation (BTE) describes the transport of classical particles, including both diffusive and ballistic transport. Hence a solution of BTE, without limiting assumptions, is ideal for modeling phonon transport in the classical limit. However, such solutions are computationally intensive for general geometries and frequency-dependent phonon parameters, and often Monte Carlo approaches are necessary [7, 8]. For certain heater geometries, Hua and Minnich showed that it is possible to efficiently solve the BTE by taking advantage of Fourier transforms. [9] Their solution is valid for non-gray (frequency-dependent) phonons, in both ballistic and diffusive transport regimes. The method described by Hua and Minnich has been applied to various heater geometries, ranging from Gaussian heaters to periodic heater structures. [9–11] When the heater size and/or spatial separation becomes sufficiently small compared to the phonon MFP, the diffusive Fourier's law of conduction starts to overestimate the heat transport, and hence underestimate the temperature rise. In these papers, silicon was been studied by the use of *ab initio* predicted phonon dispersions and phonon-phonon scattering lifetimes. However, the effect of doping on the phonon lifetimes has not been included previously, there is therefore an opportunity to study the influence of doping on the phonon transport at the microscale.

In this work, we estimate the potential error made by assuming Fourier's law of conduction, compared to

a BTE solution, in doped silicon. We calculate silicon phonon dispersion and phonon-phonon lifetimes using density functional theory (DFT). Furthermore, we model the effects of doping on the phonon lifetimes by including mass scattering and phonon-electron scattering using analytical formulas. This is done using Tamura's isotope scattering and phonon-electron interaction within the deformation potential approximation, respectively. These parameters are used as input for the numerical solution of the phonon BTE describing a nanoscopic heater. Here, the method proposed by Hua and Minnich in Ref. [9] is applied. The temperature rise predicted using the BTE is compared to a diffusive Fourier-type model at length scales up to 10 µm. The error by assuming diffusive heat transport is evaluated and compared to state-of-the-art M4PP thermoelectric measurements on doped silicon [5, 6]. Good agreement between the predicted error and observed deviations in microscale measurements is presented. Deviations above 30 % are observed at a length scale of 1 µm, both in theory and experiment.

The findings here show that Fourier's law should be used with caution, even in highly doped silicon at room temperature. The results also indicate that the M4PP could potentially be used to study the characteristic length scales of heat transport.

II. BOLTZMANN TRANSPORT EQUATION

Our numerical solution of the BTE follows the recipe proposed by Hua and Minnich [9] and is introduced briefly below. In short, the method solves the full frequency-dependent phonon-BTE in 3D using the relaxation time approximation (RTA). This can be done for systems where the Fourier transform is known for the heater geometry. The main assumption, in addition to the RTA, is that the temperature deviation is small compared to some reference temperature. Furthermore, it is implicitly assumed that the boundary in the semi-infinite system does not contribute to additional phonon scattering.

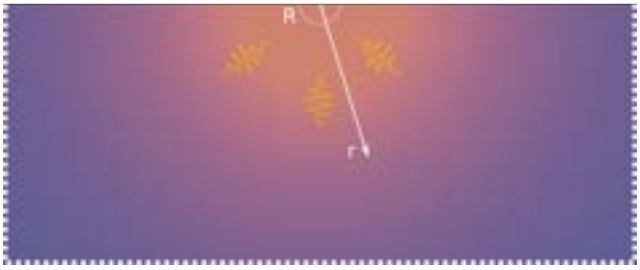

FIG. 1: Cross-sectional view of the simulated domain. The uniform heater has a radius $R = 50\,\text{nm}$ and is marked by the dashed semicircle. It is assumed that the system is semi-infinite with a vacuum above the heater. The dashed line around the domain represents the infinite directions. This geometry mimics a small heater present in, e.g., the M4PP setup.

The phonon-BTE can be written as [9]:

$$\frac{\partial g_\omega}{\partial t} + \mathbf{v}_\omega \cdot \nabla_\mathbf{r} g_\omega - \frac{Q_\omega}{4\pi} = -\frac{g_\omega - g_0(T)}{\tau_\omega} \tag{1}$$

Here the BTE is in an energy-deviational form, i.e. instead of solving for the phonon distribution function, $f_\omega(t, \mathbf{r}, \theta, \phi)$, it is solved for the deviational energy distribution function, $g_\omega = \hbar\omega D(\omega)(f_\omega(t, \mathbf{r}, \theta, \phi) - f_0(T_0))$. Spatial and temporal coordinates are denoted by $\mathbf{r}$ and t, respectively. The direction of a phonon is parametrized by the polar and azimuthal angles θ and ϕ. The density of states is denoted $D(\omega)$. The reference temperature is denoted as T_0 and the distribution $f_0(T)$ is the Bose-Einstein distribution. The phonon frequency, group velocity, and relaxation time is denoted ω, $\mathbf{v}_\omega$, and τ_ω, respectively. The phonon generation, due to the heater, is described by $Q_\omega(\mathbf{r})$.

The heat equation emerges by summing the left-hand side of Equation 1 over all states in the first Brillouin zone. Since energy must be conserved, the sum over all states of the left-hand side must equal to zero. Therefore, the sum over all states of the right-hand side must also equal to zero:

$$-\sum_p \int \int_0^{\omega_\text{max}} \left[\frac{g_\omega}{\tau_\omega} - \frac{1}{\tau_\omega}\frac{1}{4\pi} C_\omega \Delta T\right] d\omega d\Omega = 0, \tag{2}$$

where the summation is over all phonon polarizations. Here the assumption regarding the small magnitude of the temperature rise is employed and the phonon heat capacity, C_ω, is introduced. In this work, it is assumed that the phonon dispersion is isotropic. Therefore, instead of summing over states in 3D reciprocal space, we integrate over frequency (up to some maximum value ω_max) and solid angle, Ω. Equation 2 makes it possible to detangle the unknown temperature rise and the unknown energy-deviation distribution.

By Fourier transforming Equation 1 in spatial and temporal space, the differential equation is transformed into an algebraic equation. Fourier transformed quantities are marked using $\sim$ and the Fourier transform of x and t is ξ_x and η, respectively. Then, by re-arranging the algebraic equation one can get an expression for the Fourier transformed distribution function as a function of the Fourier transformed temperature, $\Delta\tilde{T}$. Using this equation together with Equation 2, one can solve for the Fourier transformed temperature:

$$\Delta\tilde{T}(\eta, \xi) = \frac{\sum_p \int_0^{\omega_\text{max}} d\omega \frac{\tilde{Q}_\omega}{\lambda_\omega \xi} \arctan\left(\frac{\lambda_\omega \xi}{1 + i\eta\tau_\omega}\right)}{\sum_p \int_0^{\omega_\text{max}} d\omega \frac{C_\omega}{\tau_\omega}\left[1 - \frac{1}{\lambda_\omega \xi}\arctan\left(\frac{\lambda_\omega \xi}{1 + i\eta\tau_\omega}\right)\right]}, \tag{3}$$

where $\xi = \sqrt{\xi_x^2 + \xi_y^2 + \xi_z^2}$ and the phonon mean free path is denoted as $\lambda_\omega = v_\omega \tau_\omega$. This expression for the temperature rise is used in this work.

The temperature rise can be calculated in Fourier space given the Fourier transformed heater profile $\tilde{Q}_\omega$ and phonon parameters evaluated at the reference temperature. By doing an (numerical) inverse-Fourier transform the real space temperature rise can be calculated. At this point, everything is specified by the phonons present in the material and the heater geometry, i.e., it is possible to solve the BTE for a temperature profile.

The geometry of the examined system is shown in Figure 1. To predict the temperature rise, the volumetric heating (in real space) must be Fourier transformed into reciprocal space. We consider a small hemispherical heater of radius $R = 50\,\mathrm{nm}$ at the origin, delivering power $Ap(\omega)$ over its volume, where A is power density, and $p(\omega)$ is the spectral distribution of the generated phonons:

$$Q_\omega(\mathbf{r}) = \begin{cases} Ap(\omega) & \text{for } r \leq R \\ 0 & \text{for } r > R \end{cases}, \tag{4}$$

The spectral distribution, $p(\omega)$, is defined as [10, 12]:

$$p(\omega) = \frac{C_\omega/\tau_\omega}{\sum_p \int_0^{\omega_{\max}} d\omega C_\omega/\tau_\omega} \tag{5}$$

By taking the Fourier transform of Equation 4 using the spherical symmetry of the heater, the following expression is obtained:

$$\begin{aligned} \tilde{Q}_\omega(\boldsymbol{\xi}) &= \int \exp(-i\boldsymbol{\xi}\cdot\mathbf{r}) Q_\omega(\mathbf{r}) d\mathbf{r} = \\ &= \frac{4\pi}{\xi^3} Ap(\omega)\left[\sin(\xi R) - \xi R\cos(\xi R)\right] \end{aligned} \tag{6}$$

The Fourier transform of the heater profile can now be used to predict the temperature rise in Fourier space.

To calculate the temperature rise in real space, as a function of r, an inverse Fourier transform is performed. Since the heater is considered to be stationary (i.e. $\eta = 0$), we omit the η-variable here.

$$\begin{aligned} \Delta T_{\mathrm{BTE}}(r) &= \frac{1}{(2\pi)^3}\int \exp(i\boldsymbol{\xi}\cdot\mathbf{r})\Delta\tilde{T}(\xi_x,\xi_y,\xi_z)d\boldsymbol{\xi} \\ &= \frac{4\pi}{(2\pi)^3}\int_0^\infty \frac{\sin(\xi r)}{r}\Delta\tilde{T}(\xi)\xi d\xi \end{aligned} \tag{7}$$

Note that the function $\Delta\tilde{T}(\xi)$ contains the (phonon) frequency integral, see Equation 3, which must be evaluated for each ξ. We here choose to talk about temperatures, while we note that in weakly interacting systems even the presence of a local equilibrium is in question.

III. DIFFUSIVE MODEL

The diffusive solution to the time-dependent uniform heater problem can be found in the work by Carslaw and Jaeger [13]. At steady-state the temperature rise above a reference temperature can be written as:

$$\Delta T_{\mathrm{Fourier}}(r) = \frac{1}{3}\frac{AR^3}{\kappa r}, \tag{8}$$

where $\kappa = \sum_p \int_0^{\omega_{\max}} d\omega \frac{1}{3} C_\omega v_\omega \lambda_\omega$ is the thermal conductivity. Eq. 8 describes thermal transport in the diffusive limit, and the BTE solution should converge to this function far away from the heater.

IV. PHONONS IN DOPED SILICON

The phonon (harmonic) dispersion, and derived parameters, is relatively straightforward to calculate from density functional theory. However, the anharmonicity and phonon scattering rates are more challenging to evaluate. In the following, we show how we calculated the total phonon scattering rates, based on ab initio phonon-phonon scattering together with analytical phonon-isotope and phonon-electron scattering models.

Matthiessen's rule can be used to evaluate the total scattering rate of the phonons:

$$\tau_\omega^{-1} = \sum_i \tau_i^{-1} = \tau_{pp}^{-1} + \tau_M^{-1} + \tau_{pe}^{-1}, \tag{9}$$

where the sum is over different scattering mechanisms. The rule is valid under the assumption that the scattering mechanisms are independent of each other. In general, there is no guarantee for the validity of this assumption. However, the largest doping concentration sampled here is ca. 1 %, i.e., it is reasonable to assume that the phonons can be described as silicon phonons perturbed by the doping, as described by Matthiessen's rule. To model the total scattering rate we combine phonon-phonon scattering, τ_{pp}^{-1}, mass-difference scattering (or isotope scattering), τ_M^{-1}, and phonon-electron scattering τ_{pe}^{-1}. In the following subsections, we will go through each term. A summary of all effects can be found in Figure 2. The figure shows the silicon phonon lifetimes and cumulative thermal conductivity when different scattering mechanisms are included.

A. Phonon-phonon scattering rates

The phonon-phonon scattering rate, τ_{pp}^{-1}, is the major contribution to the total scattering rate at elevated temperatures. Phonon density of states, velocities, and anharmonic phonon-phonon scattering rates were predicted using ALAMODE [14] based on the forces calculated using Vienna Ab initio Simulation Package[15] (VASP). PBE [16] was used as the xc-functional. A plane-wave cutoff of 245 eV was used and the self-consistent solution was converged below $1 \times 10^{-6}\,\mathrm{eV}$. A $3 \times 3 \times 3$ supercell of the conventional silicon unit cell was used and the

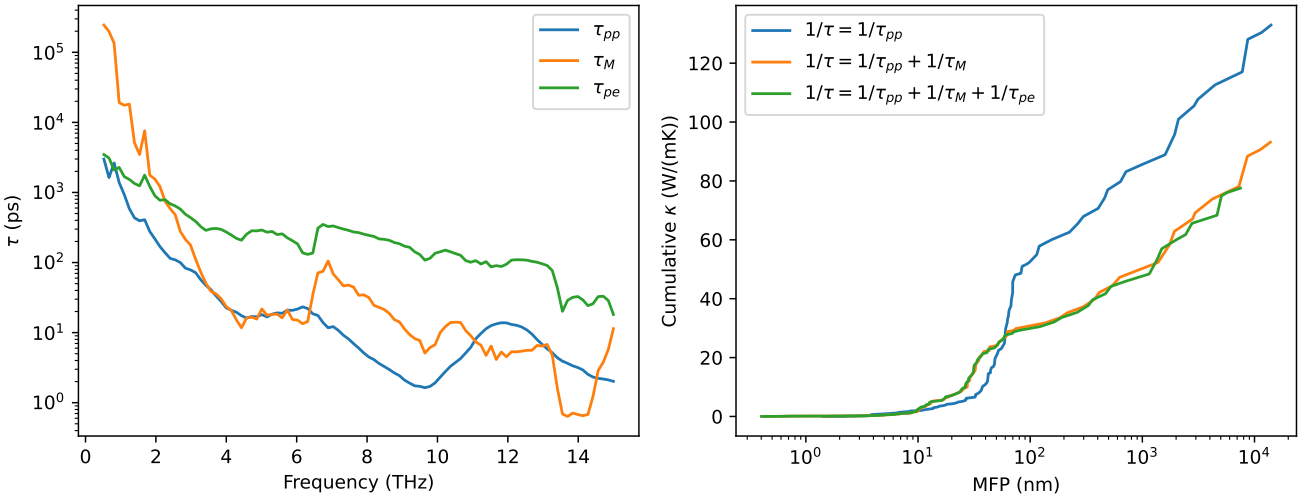

FIG. 2: Left: Phonon lifetimes due to different scattering mechanisms. Right: Thermal conductivity vs. MFP spectra with different combinations of scattering rates. The data is for 300 K and boron mass scattering with doping concentration of $1 \times 10^{20}\,\mathrm{cm}^{-3}$. The deformation potential was set to $D = 0.5\,\mathrm{eV}$.

lattice parameter was set to 5.46 Å. The supercell calculations were sampled with a $3 \times 3 \times 3$ k-mesh. The force constants were evaluated by performing displacement of $\Delta u = 0.01$ Å and $\Delta u = 0.03$ Å, in the case of harmonic and cubic force constants, respectively. The phonon-phonon scattering rate and phonon dispersion was predicted using these force constants on a k-mesh of $30 \times 30 \times 30$.

The momentum-resolved phonon modes were collapsed onto a single frequency-dependent phonon model. This treatment averages out any anisotropy in the phonon properties but is reasonable for silicon since there is no strong anisotropy in the material. The phonons were placed in 101 equal bins from the smallest to largest phonon frequency.

B. Isotope scattering

The atomic mass difference by doping acts as phonon scattering centers and we model this effect using Tamura's isotope scattering model [17]:

$$\tau_M^{-1} = \frac{\pi}{6} V g_2 \omega^2 D(\omega), \tag{10}$$

where V and $D(\omega)$ are the volume and phonon density of states, respectively. The dimensionless factor, g_2, describing the doping concentration is defined as:

$$g_2 = \sum_i c_i (1 - m_i/\bar{m})^2, \tag{11}$$

where i runs over the elements, e.g., Si and B. Specifically, we performed calculations only for boron doping, since the mass difference, and hence scattering, is very small between phosphorus and silicon. Furthermore, m_i and c_i is the mass and fraction of the atoms, respectively. The weighted average mass is denoted $\bar{m} = \sum_i c_i m_i$.

C. Phonon-electron scattering

To model the influence of phonon-electron scattering, which becomes important in highly doped semiconductors, we use an asymptotic limit of the deformation potential approximation as derived in Reference [18]:

$$\tau_{pe}^{-1} = \frac{(2\pi m^*)^{1/2} D^2}{(k_B T)^{3/2} g_d \rho v_s} \exp\left(-\frac{m^* v_s^2}{2 k_B T}\right) n\omega \tag{12}$$

In the above equation, m^* is the electron effective mass, g_d is the degeneracy of the bands, n is the carrier concentration, ρ is the mass density, v_s and ω is the speed and frequency of the phonons, respectively. The effective mass was set to $m^* = m_e$ and the valley degeneracy to $g_d = 6$. The deformation potential, D, was used as a free parameter to fit the total thermal conductivity to the experimental values, see Figure 6. Good agreement was found using $D = 0.5\,\mathrm{eV}$. Note, that Equation 12 is only applicable to the acoustic phonon modes, however, since acoustic phonons are the dominant heat carriers in silicon, we neglect the phonon-electron scattering on the optical phonon modes.

V. RESULTS AND DISCUSSION

A. Predicted thermal response of doped Si

Solving the phonon BTE with varying carrier concentrations, and comparing the results to the diffusive limit

(Eq. 8), we can get an indication of how the ballistic-to-diffusive transition behaves in conditions relevant to semiconductor devices. In Figure 3, the error by assuming diffusive transport instead of the full BTE solution is shown. The error, calculated for representative doping concentrations, is shown as a function of the distance from the heater. Here the carrier concentration also defines the doping fraction in the mass scattering. To be representative of M4PP measurements [5], the heater radius was 50 nm and the reference temperature was $T_0 = 300\,\mathrm{K}$. The ballistic transport is most prominent in the undoped case, resulting in ca. 40 % higher temperature at 1 µm away from the heater relative to a purely diffusive thermal transport. Interestingly, doping concentrations below ca. $1 \times 10^{19}\,\mathrm{cm}^{-3}$ is negligible, and can be treated as undoped. The introduction of more dopants shortens the phonon relaxation time due to the scattering at the dopant itself and at the generated charge carriers (Figure 2). This reduction in phonon lifetimes causes the MFP to decrease, hence a larger amount of the heat is then conducted by phonons that experience diffusive transport at a given length scale. Since the phonon transport becomes increasingly diffusive, the Fourier's law of conduction becomes more accurate and the difference between Boltzmann transport and the diffusive model vanishes. While our treatment of the additional phonon scattering due to doping is simple, and by no means a complete representation of the intricate details in phonon-electron interaction, it is interesting to note that the ballistic nature of silicon phonons remains at surprisingly high dopant concentrations. In Appendix A the sensitivity of the deformation potential on the ballistic-diffusive transition is presented. From this, it is clear that the transition is sensitive to the deformation potential. It is therefore challenging to accurately define a doping concentration at which the ballistic nature of the phonons has vanished at the microscale. However, it is reasonable to assume that a very high dopant concentration ($> 1 \times 10^{21}\,\mathrm{cm}^{-3}$) is necessary to safely justify the use of Fourier's law in room temperature silicon at the microscale. Furthermore, at length scales sub 100 nm, the error is beyond 100 % and the validity of Fourier's law is very questionable.

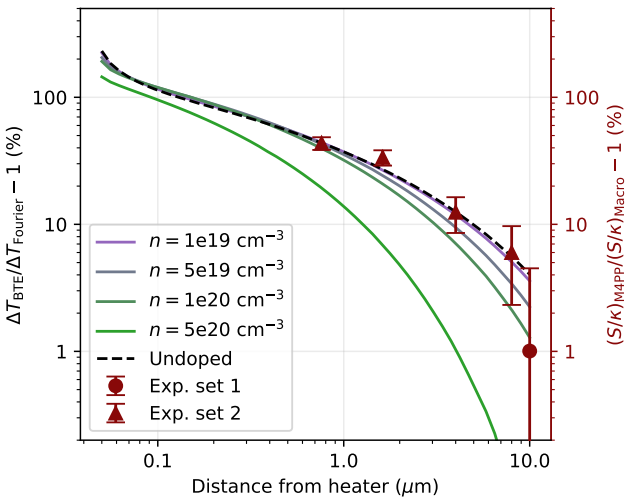

FIG. 3: Temperature rise comparison between BTE solution and Fourier's law as a function of distance from the heater. The different lines correspond to different doping concentrations and the black dashed line is the undoped case with only phonon-phonon scattering included. Experimental points correspond to apparent deviations of thermal properties measured using the M4PP. The "Exp. set 1" is from data published in Ref. [5], while "Exp. set 2" is new data following the same recipe but with smaller probe pitches.

B. Experimental observations with M4PP

In an M4PP measurement an alternating current with frequency ω is forced between two current pins. This causes Joule heating in proximity of the contacts and results in a temperature increase in the sample at the second harmonic frequency, 2ω. This results in a thermoelectric voltage, $\Delta V = -S\Delta T$, measurable between two other electrodes, also at the second harmonic frequency. Here S is the difference in Seebeck coefficient between the sample and electrode. Under the assumption of diffusive heat transport, it is possible to determine the ratio, S/κ, from the second harmonic voltage. [5] If the thermal transport becomes partially ballistic, the estimated ratio S/κ will increase, due to a suppression of the effective thermal conductivity. By assuming that the Sebeeck coefficient is independent of length, the ratio of the M4PP S/κ with corresponding macroscale value is a measure of the suppression of the thermal conductivity. In other words, $(S/\kappa)_{\mathrm{M4PP}}/(S/\kappa)_{\mathrm{Macro}} = \kappa_{\mathrm{Macro}}/\kappa_{\mathrm{M4PP}}$, which is directly comparable to $\Delta T_{BTE}/\Delta T_{Fourier}$. M4PP measurements were performed on boron-doped Si with $N_B = 5.54 \times 10^{18}\,\mathrm{cm}^{-3}$ (sample 4790 in [5, 19]) and was collected using probes with pitches ranging from 0.8–10 µm. The data was analyzed exactly as in Ref. [5] and the relative difference between M4PP measured S/κ and the macroscale reference value is shown in Figure 3. The estimated ratio, S/κ, depends on four distances, i.e., the distances between current and voltage electrodes. Since the shortest distance contributes to the majority of the signal, we here choose to define the characteristic transport length as the shortest distance between current and voltages electrodes. This length defines the horizontal axis in Figure 3. The M4PP data from "Exp. set 2" closely follows the prediction obtained from BTE across an order of magnitude of distances. For 10 µm electrode spacing ("Exp. set 1"), even the predicted BTE offset (3-4 %) is within experimental error, rendering the original assessment in Reference [5] rather intact. However, it is clear that the 10 µm is a cusp: even at marginally smaller probe pitches, the thermal M4PP measurements begin to

noticeably deviate from the material's macroscale reference value, and it appears that BTE is a good predictor for the thermal transport. Moreover, we believe that under more favorable conditions (e.g. cryogenic temperature) M4PP could be leveraged to extract length scale-dependent phonon properties, such as MFP spectra [3, 4]. While our results focus on the M4PP tool, the key findings are applicable to other systems that involve nanoscopic heaters.

VI. CONCLUSION

In this work, we have solved the phonon BTE for doped silicon at room temperature for a geometry relevant to micro four-point probe measurements of thermoelectric properties. Phonon-phonon scattering rates are predicted from first principles, while the effect of doping is modelled using Tamura's isotope scattering and deformation potential approximation for the phonon-electron scattering. The phonon-electron doping parametrization is benchmarked to (macroscopic) thermal conductivities of boron-doped silicon. As expected, doping reduces the total thermal conductivity, and in highly doped silicon at large length scales the phonon transport becomes diffusive and the Fourier's law of conduction is justifiable. However, the phonon transport remains significantly ballistic up to a very large doping concentration ($> 1 \times 10^{21}\,\mathrm{cm}^{-3}$) at a length scale of circa 1 µm. Under these conditions, the error by assuming Fourier's law could still be on the order of tens of percent. On shorter length scales ($< 5\,\mu\mathrm{m}$), M4PP measurements show significant deviations with respect to macroscale references. The deviations grow with smaller probe pitches, in agreement with the theoretical predictions. These findings demonstrate the potential inaccuracy by assuming Fourier's law in thermal measurements on doped silicon at the nano- and microscale. On the other hand, this implies that the M4PP could be leveraged to study the phonon mean free paths in industrially relevant systems.

ACKNOWLEDGEMENTS

This work has been supported by Independent Research Fund Denmark grant 8048-00088B and Innovation Fund Denmark grant 1045-00029B.

[1] A. L. Moore and L. Shi, Emerging challenges and materials for thermal management of electronics, Materials Today **17**, 10.1016/j.mattod.2014.04.003 (2014).
[2] G. Chen, Journal of Heat Transfer 10.1115/1.2822665 (1996).
[3] A. J. Minnich, J. A. Johnson, A. J. Schmidt, K. Esfarjani, M. S. Dresselhaus, K. A. Nelson, and G. Chen, Thermal conductivity spectroscopy technique to measure phonon mean free paths, Physical Review Letters 10.1103/PhysRevLett.107.095901 (2011).
[4] Y. Hu, L. Zeng, A. J. Minnich, M. S. Dresselhaus, and G. Chen, Spectral mapping of thermal conductivity through nanoscale ballistic transport, Nature Nanotechnology **10**, 10.1038/nnano.2015.109 (2015).
[5] B. Guralnik, O. Hansen, A. R. Stilling-Andersen, S. E. Hansen, K. A. Borup, B. M. Mihiretie, B. Beltrán-Pitarch, H. H. Henrichsen, R. Lin, L. Shiv, B. B. Iversen, P. F. Nielsen, and D. H. Petersen, Determination of thermoelectric properties from micro four-point probe measurements, Measurement Science and Technology **33**, 10.1088/1361-6501/ac88ea (2022).
[6] N. Lamba, B. Guralnik, B. Beltrán-Pitarch, V. Rosendal, N. Pryds, O. Hansen, and D. H. Petersen, Deconvolution of Heat Sources for Application in Thermoelectric Micro Four-Point Probe Measurements.
[7] J. P. M. Péraud and N. G. Hadjiconstantinou, Efficient simulation of multidimensional phonon transport using energy-based variance-reduced monte carlo formulations, Physical Review B - Condensed Matter and Materials Physics **84**, 10.1103/PhysRevB.84.205331 (2011).
[8] J.-P. M. Peraud, C. D. Landon, and N. G. Hadjiconstantinou, Monte carlo methods for solving the boltzmann transport equation, Annual Review of Heat Transfer 10.1615/annualrevheattransfer.2014007381 (2014).
[9] C. Hua and A. J. Minnich, Analytical Green's function of the multidimensional frequency-dependent phonon Boltzmann equation, Physical Review B - Condensed Matter and Materials Physics 10.1103/PhysRevB.90.214306 (2014).
[10] C. Hua and A. J. Minnich, Heat dissipation in the quasiballistic regime studied using the Boltzmann equation in the spatial frequency domain, Physical Review B **97**, 10.1103/PhysRevB.97.014307 (2018).
[11] X. Chen, C. Hua, H. Zhang, N. K. Ravichandran, and A. J. Minnich, Quasiballistic thermal transport from nanoscale heaters and the role of the spatial frequency, Physical Review Applied **10**, 10.1103/PhysRevApplied.10.054068 (2018).
[12] V. Chiloyan, S. Huberman, A. A. Maznev, K. A. Nelson, and G. Chen, Thermal transport exceeding bulk heat conduction due to nonthermal micro/nanoscale phonon populations, Applied Physics Letters 10.1063/1.5139069 (2020).
[13] H. Carslaw and J. Jaeger, *Conduction of Heat in Solids* (Clarendon Press, 1959).
[14] T. Tadano, Y. Gohda, and S. Tsuneyuki, Anharmonic force constants extracted from first-principles molecular dynamics: Applications to heat transfer simulations, Journal of Physics Condensed Matter **26**, 10.1088/0953-8984/26/22/225402 (2014).
[15] G. Kresse and J. Furthmüller, Efficient iterative schemes for ab initio total-energy calculations using a plane-wave basis set, Physical Review B - Condensed Matter and Materials Physics **54**, 10.1103/PhysRevB.54.11169 (1996).
[16] J. P. Perdew, K. Burke, and M. Ernzerhof, Generalized gradient approximation made simple, Physical Review

Letters **77**, 10.1103/PhysRevLett.77.3865 (1996).
[17] S. I. Tamura, Isotope scattering of dispersive phonons in Ge, Physical Review B **27**, 10.1103/PhysRevB.27.858 (1983).
[18] B. Liao, B. Qiu, J. Zhou, S. Huberman, K. Esfarjani, and G. Chen, Significant reduction of lattice thermal conductivity by the electron-phonon interaction in silicon with high carrier concentrations: A first-principles study, Physical Review Letters **114**, 10.1103/PhysRevLett.114.115901 (2015).
[19] B. Guralnik, P. F. Nielsen, D. H. Petersen, O. Hansen, L. Shiv, W. Wei, T. A. Marangoni, J. D. Buron, F. W. Østerberg, R. Lin, H. H. Henrichsen, and M. F. Hansen, Review of micro- and nanoprobe metrology for direct electrical measurements on product wafers, in *2022 China Semiconductor Technology International Conference (CSTIC)* (2022) pp. 1–3.

Appendix A: Sensitivity of temperature rise error

Figure 4 and 5 show the error by assuming Fourier's law as a function of distance from heater (as in the main text), but here the dopant concentration is fixed and the deformation potential is varied.

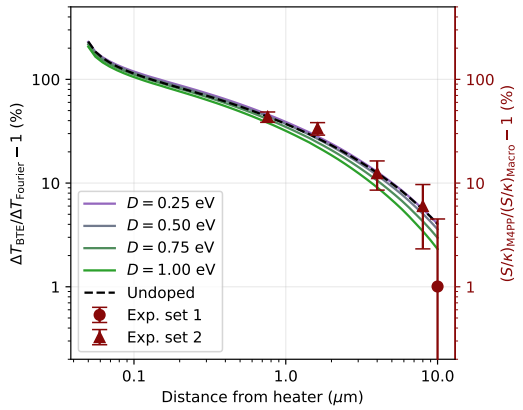

FIG. 4: Similar to the figure in the main text, but here the carrier concentration is fixed to $1 \times 10^{19}\,\mathrm{cm}^{-3}$ and the deformation potential, D, is varied.

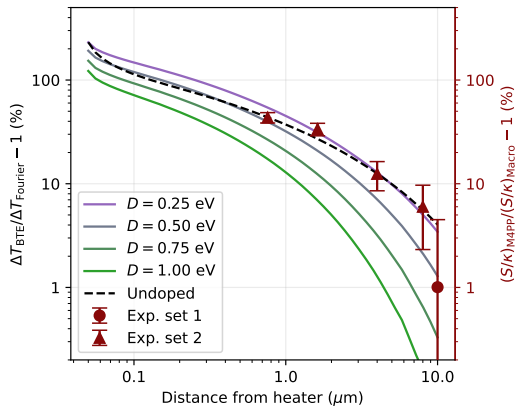

FIG. 5: Similar to the figure in the main text, but here the carrier concentration is fixed to $1 \times 10^{20}\,\mathrm{cm}^{-3}$ and the deformation potential, D, is varied.

Appendix B: Thermal conductivity of doped silicon

The phonon-electron interaction model used is parametrized by the deformation potential, D. To estimate the value of D we compare the predicted thermal conductivity with experimental thermal conductivities of doped Si from Ref. [5]. The comparison is shown in Figure 6, and good agreement is found when $D \sim 0.5\,\mathrm{eV}$.

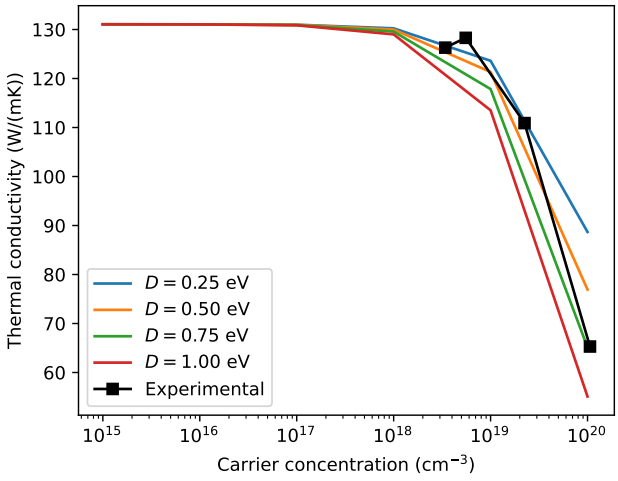

FIG. 6: Influence of doping on the total lattice thermal conductivity at 300 K. The phonon-electron scattering is parametrized by D, which is varied. Experimental values for doped silicon are included from Reference [5].

Technical
University of
Denmark

2800 Kgs. Lyngby

www.energy.dtu.dk